

## **INFORMATION TO USERS**

This manuscript has been reproduced from the microfilm master. UMI films the text directly from the original or copy submitted. Thus, some thesis and dissertation copies are in typewriter face, while others may be from any type of computer printer.

**The quality of this reproduction is dependent upon the quality of the copy submitted.** Broken or indistinct print, colored or poor quality illustrations and photographs, print bleedthrough, substandard margins, and improper alignment can adversely affect reproduction.

In the unlikely event that the author did not send UMI a complete manuscript and there are missing pages, these will be noted. Also, if unauthorized copyright material had to be removed, a note will indicate the deletion.

Oversize materials (e.g., maps, drawings, charts) are reproduced by sectioning the original, beginning at the upper left-hand corner and continuing from left to right in equal sections with small overlaps. Each original is also photographed in one exposure and is included in reduced form at the back of the book.

Photographs included in the original manuscript have been reproduced xerographically in this copy. Higher quality 6" x 9" black and white photographic prints are available for any photographs or illustrations appearing in this copy for an additional charge. Contact UMI directly to order.

# **UMI**

A Bell & Howell Information Company  
300 North Zeeb Road, Ann Arbor MI 48106-1346 USA  
313/761-4700 800/521-0600



STUDY OF NUMERICAL METHODOLOGIES FOR  
MULTI-PASS WELDING ANALYSIS

DISSERTATION

Presented in Partial Fulfillment of the Requirements for  
the Degree Doctor of Philosophy in the Graduate  
School of The Ohio State University

By

Jeong Kyun Hong, B.S., M.S.

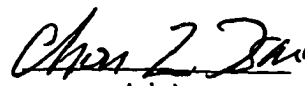
\* \* \* \* \*

The Ohio State University  
1996

Dissertation Committee:

Dr. Chon L. Tsai, Advisor  
Dr. June K. Lee  
Dr. Pingsha Dong

Approved by



Chon L. Tsai  
Advisor

Welding Engineering Graduate Program

**UMI Number: 9710581**

---

**UMI Microform 9710581  
Copyright 1997, by UMI Company. All rights reserved.**

**This microform edition is protected against unauthorized  
copying under Title 17, United States Code.**

---

**UMI**  
**300 North Zeeb Road**  
**Ann Arbor, MI 48103**

## ABSTRACT

Fusion welding processes are generally used to join structural members. Welding processes produce residual stresses and distortion as a result of the large nonlinear thermal loading created by a moving heat source. Moreover, multi-pass welding of thick sections subjects the components to multiple thermal cycles and inelastic strain patterns, creating a more severe and complex residual stress distribution through the plate thickness. Residual stresses increase crack driving force and largely affect the strength and resistance to brittle fracture. Distortion can make it difficult to maintain dimensional tolerances and cause misalignment of welded joints. Thus, accurate prediction of residual stresses and distortion is very important.

The study of appropriate finite element analysis (FEA) procedure addresses the element rebirth technique to predict the residual stresses and/or distortion for multi-pass welding. The FEA procedure is integrated with the commercial code ABAQUS. In order to establish the appropriate FEA procedure, the characteristics of thermal and mechanical analyses for welding simulation are investigated. The lumping techniques are employed for a five-pass welded plate and a six-pass girth welded pipe. The modified Gaussian heat input model for surface heat flux is developed. It is concluded that the body heat input is helpful to accommodate the weld shape and that prescribed initial temperature of

the weld metal does not affect final residual stress distributions. It is also found that the weld zone size and shape determine the final residual stress distributions. In order to include thermal and mechanical mismatch conditions, the interface element technique is employed for a three-pass welded plate model. The preparation of FEA model and input files is cumbersome, and the interface element technique provides a good alternative for the prediction of residual stresses, but not accurate enough for the prediction of distortion.

The plastic strain relaxation effect is also considered for numerical simulations. In nature, the accumulated plastic strains are relieved when the weld reaches melting point. The plastic strain accumulation may resume when the weld temperature falls below the melting temperature. However, in the numerical analysis, the plastic strain accumulation continues even if the weld exceeds the melting temperature. Consequently, the accumulated plastic strains are large where the plastic strains are non-existent, especially in the weld area. The overestimated plastic strains affect the prediction of residual stresses and/or distortion. Therefore, the plastic strain relaxation effect is studied theoretically and compared with FEA models. A computer program which incorporates the plastic strain relaxation effect is developed. It is shown that, by considering the plastic strain relaxation effect, the stress variation becomes small and the stresses are smoothly distributed inside and near fusion zone. The consideration of plastic strain relaxation effect improves the final out-of-plane distortion when compared with the experiments. Incorporating the plastic strain relaxation effect into numerical analyses helps to reduce the CPU time in multi-pass weld models as well.

Dedicated to

My lovely wife, Jieun, and daughters, Youngjoo and Youngeun

## ACKNOWLEDGMENTS

God has blessed me with an opportunity to study at The Ohio State University and kept my family together in peace, for which I am most grateful.

I wish to thank Professor Chon L. Tsai, my advisor, for his invaluable advice, intellectual support, guidance, and encouragement throughout the study. His knowledge and insight have greatly contributed the research, leading to this dissertation.

I would like to express my appreciations to Dr. Pingsha Dong at Battelle, for giving me a chance to work with him and for the endless discussion during the dissertation work. I am also grateful to Professor June K. Lee for his helpful comments and assistance.

I would also acknowledge all my colleagues in the welding design group for their assistances. I thank Dr. Jimmio Zhang at Battelle for helping me with his mechanics expertise. I also thank Roberta Gerlach who has proofread the dissertation.

Finally, but not the least I sincerely appreciate Jieun's pray, sacrifice, patience, encouragement, and emotional support which made the research more enjoyable.

## VITA

January 9, 1965	Born, Kyungi-Do, Korea
1987	B.S., Mechanical Engineering, Yonsei University, Seoul, Korea
1989	M.S., Mechanical Engineering, Yonsei University, Seoul, Korea
1990 - 1991	Research Assistant Yonsei University, Seoul, Korea
1993 - Present	Graduate Research Associate The Ohio State University, Columbus, Ohio

## PUBLICATIONS

1. C. L. Tsai, P. Dong, and J. K. Hong, " An Effective Finite Element Procedure for Residual Stress Predictions in Multi-Pass Welds," Research Report, MR9505, Edison Welding Institute, Columbus, Ohio, 1995.
2. J. K. Hong, P. Dong, and C. L. Tsai, "Finite Element Simulation of Residual Stresses in Multi-Pass Welds," Research Brief, B9404, Edison Welding Institute, Columbus, Ohio, 1994.
3. J. K. Hong, P. Dong, and C. L. Tsai, "Finite Element Simulation of Residual Stresses in Multi-Pass Welds," in International Conference Proceedings on Modeling and Control of Joining Processes, Edited by T. Zacharia, held at December 8 - 10, 1993, Orlando, Florida, pp. 470 - 476, American Welding Society, 1994.

4. K. Y. Lee, and J. K. Hong, "Boundary Element Analysis of Thermal Stress Intensity Factors for Cusp Crack in Transient State," *Engineering Fracture Mechanics*, Vol. 45, No. 3, pp. 309 - 320, 1993.
5. J. K. Hong, "Determination of Transient Thermal Stress Intensity Factors for Cusp Cracks by Boundary Element Method," M.S. Thesis, Department of Mechanical Engineering, Yonsei University, Seoul, Korea, 1987.

## FIELDS OF STUDY

Major Field: Welding Engineering  
Welding Design, Finite Element Analysis

## TABLE OF CONTENTS

	<u>Page</u>
Dedication .....	iv
Acknowledgments .....	v
Vita .....	vi
List of Tables .....	xi
List of Figures .....	xiii
Chapters:	
1. Introduction .....	1
1.1 Background .....	1
1.2 Research Issues .....	5
1.3 Objectives .....	7
2. Literature review .....	10
2.1 Welding heat flow analysis .....	10
2.1.1 Analytical studies .....	11
2.1.2 Numerical studies .....	13
2.2 Residual stress analysis .....	15
2.2.1 Causes of residual stresses .....	16
2.2.2 Numerical studies .....	17
2.3 Distortion analysis .....	24
2.3.1 Experimental studies .....	25
2.3.2 Numerical studies .....	26

3. Finite element modeling techniques for thermal and mechanical welding analysis .....	30
3.1 Uncoupled thermo-mechanical analysis .....	31
3.2 Numerical model types .....	33
3.3 Thermal model .....	34
3.3.1 Heat source model .....	34
3.3.2 Ramp heat input model .....	39
3.3.3 Initial temperature conditions for welding model .....	40
3.4 Temperature insensitivity for residual stress analysis .....	41
3.5 Non-linear thermo-mechanical modeling .....	42
3.6 Element rebirth technique .....	44
3.7 Mismatch effects .....	45
3.7.1 Thermal mismatch .....	45
3.7.2 Mechanical mismatch .....	46
3.8 Generalized plane strain assumption .....	48
3.9 Lumping (grouping) techniques .....	49
3.10 Meshing .....	51
4. Assessments of numerical procedures .....	60
4.1 Effect of weld lumping technique .....	61
4.1.1 Five-pass welded plate (Non lumping and lumping modeling techniques) .....	62
4.1.1.1 Model definition .....	62
4.1.1.2 Finite element modeling .....	63
4.1.1.3 Results .....	68
4.1.2 Six-pass girth welded pipe (Lumping modeling technique) .....	70
4.1.2.1 Model definition .....	70
4.1.2.2 Finite element modeling .....	71
4.1.2.3 Results .....	73
4.2 Effect of interface mismatch .....	76
4.2.1 Model definition .....	76
4.2.2 Finite element modeling .....	77
4.2.3 Results .....	78
4.3 Discussion .....	81
5. Plastic strain relaxation effect .....	126
5.1 Thermo-elastic-plastic material behaviors .....	127
5.1.1 Constitutive Equations for thermo-elastic-plastic materials .....	127
5.1.2 Thermo-mechanical material properties .....	136

5.1.3 Calculation of stress increments with the plastic strain relaxation effect .....	138
5.2 Theoretical development .....	142
5.2.1 Model without the plastic strain relaxation effect .....	143
5.2.2 Model with the plastic strain relaxation effect .....	144
5.3 Verification .....	146
5.4 Examples .....	147
6. Numerical examples with the plastic strain relaxation effect .....	162
6.1 Bead-on-plate welding .....	163
6.2 Partial penetration butt welding .....	167
6.3 One-pass single V groove butt welding .....	168
6.4 Three-pass single V groove butt welding .....	170
6.5 Tee joint with fillet welds .....	172
6.6 Discussion .....	173
7. Conclusions .....	213
List of references .....	215

## LIST OF TABLES

<u>Table</u>	<u>Page</u>
4.1 Pass sequences and welding parameters of each pass for a five-pass welded plate model [1] .....	85
4.2 Temperature-independent material properties and initial conditions for a five-pass welded plate model .....	85
4.3 Pass sequences and welding parameters of each pass for a six-pass girth welded pipe model [80] .....	86
4.4 Combination of heat inputs for a six-pass girth welded pipe model .....	86
4.5 Pass sequences and welding parameters of each pass for a three-pass welded plate .....	87
4.6 Comparison of CPU time and distortion for a three-pass welded plate with and without the mismatch effects .....	88
6.1 Welding parameters for a one-pass bead-on-plate weld on a 1/2" thick plate model .....	175
6.2 Comparison of CPU time and distortion for a one-pass bead-on-plate weld on a 1/2" thick plate .....	175
6.3 Welding parameters for a one-pass partial penetration butt welded plate model .....	176
6.4 Comparison of CPU time and distortion for a one-pass partial penetration welded plate .....	176
6.5 Welding parameters for a one-pass butt welded plate model with a single V groove .....	177

6.6	Comparison of CPU time and distortion for a one-pass butt welded plate model with a single V groove .....	177
6.7	Welding parameters for a three-pass butt welded plate model with a single V groove .....	178
6.8	Comparison of CPU time and distortion for a three-pass butt welded plate model with a single V groove .....	178
6.9	Welding parameters for a tee-joint with fillet welds .....	179
6.10	Comparison of CPU time and distortion for a tee-joint with fillet welds .....	179

## LIST OF FIGURES

<u>Figure</u>	<u>Page</u>
2.1	27
Some assumed geometries for solutions of heat flow during welding ..	
(a) Semi-infinite body	
(b) Two-dimensional infinite body	
(c) Finite thickness plate with point heat source	
2.2	28
Gaussian circular heat input model [28] .....	
2.3	28
Double ellipsoidal heat source configuration together with the power distribution function along the $\xi$ axis [35] .....	
2.4	29
Types of welding distortion [65] .....	
(a) Transverse shrinkage	
(b) Angular change	
(c) Rotational distortion	
(d) Longitudinal shrinkage	
(e) Longitudinal bending distortion	
(f) Buckling distortion	
3.1	54
Numerical procedures for an uncoupled thermo-mechanical analysis ...	
3.2	55
Definition of Cross sectional plane model and In-plane section model in two-dimensional analysis .....	
3.3	56
Modified Gaussian heat input scheme .....	
3.4	56
Shape of ramp heat input function .....	
3.5	57
Two schemes of discretization for weld deposit (d) and workpiece (w) materials [7] .....	
(a) Element rebirth (use *MODEL CHANGE)	
(b) Interface element shown schematically with broken line (use *GAPCON user subroutine)	

3.6	Concept of the generalized plane strain theory [19]	58
3.7	Definition of ramp functions of heat input before and after lumping [62]	59
	(a) Ramp functions of welding passes before lumping	
	(b) Ramp function after lumping (RAMP 1)	
	(c) Ramp function after lumping (RAMP 2)	
4.1	Temperature-dependent material properties of ASTM A36 mild steel for finite element analysis [6]	89
	(a) Thermal material properties	
	(b) Mechanical material properties	
4.2	Strain hardening effect used for ASTM A36 mild steel	90
4.3	Finite element models for a five-pass welded plate	91
	(a) Weld detail - 5 pass model (non-lumped model)	
	(b) Weld detail - 3 pass model (lumped model)	
4.4	View of entire model and mechanical boundary conditions for a five-pass welded plate model	92
4.5	Comparison of the numerical and experimental temperature changes at two locations during welding (first weld pass, a five-pass welded plate model)	93
	(a) On top surface, 1/4" from the weld toe	
	(b) On top surface, 1/2" from the weld toe	
4.6	Definitions of stress directions	95
4.7	Residual transverse stress distributions after final weld pass for a five-pass welded plate model	96
	(a) On top surface	
	(b) On bottom surface	
4.8	Residual longitudinal stress distributions after final weld pass for a five-pass welded plate model	98
	(a) On top surface	
	(b) On bottom surface	
4.9	Through-thickness residual stress distributions after final weld pass at 2/5" from the weld toe for a five-pass welded plate model	100
	(a) Transverse stress distributions	
	(b) Longitudinal stress distributions	

4.10	Residual stress distributions on top surface after first weld pass for a five-pass welded plate model .....	102
4.11	Residual stress distributions on top surface after second weld pass for a five-pass welded plate model .....	103
4.12	Residual stress distributions on top surface after third weld pass for a five-pass welded plate model .....	104
4.13	Residual stress distributions on top surface after fourth weld pass for a five-pass welded plate model .....	105
4.14	Finite element model for a six-pass girth welded pipe .....	106
	(a) View of weld area	
	(b) Entire view of the axisymmetric pipe model	
4.15	Temperature dependent material properties of 304 stainless steel for finite element stress analysis .....	107
4.16	Residual axial stresses for different heat inputs (a six-pass girth welded pipe) .....	108
	(a) On outer surface	
	(b) On inner surface	
4.17	Residual circumferencial (hoop) stresses for different heat inputs (a six-pass girth welded pipe) .....	110
	(a) On outer surface	
	(b) On inner surface	
4.18	Distortion changes with different heat inputs at two locations during welding (a six-pass girth welded pipe) .....	112
	(a) 5.0" from weld centerline on outer surface	
	(b) 0.375" from weld centerline on inner surface	
4.19	Comparison of the numerical (Case 1 heat input) and experimental residual axial stress distributions (a six-pass girth welded pipe) .....	114
	(a) On inner surface	
	(b) On outer surface	
4.20	Comparison of the numerical(Case 1 heat input) and experimental residual circumferencial (hoop) stress distributions (a six-pass girth welded pipe) .....	116
	(a) On inner surface	
	(b) On outer surface	

4.21	Finite element models for a three-pass welded plate .....	118
	(a) Conventional model (without interface elements)	
	(b) Model with interface elements	
	(c) Entire view of the model and boundary conditions	
4.22	Temperature changes at two locations during welding (a three-pass welded plate)	
	Node 5: weld centerline on bottom surface	
	Node 157 : 0.25" from the weld centerline on top surface .....	119
	(a) During first weld pass	
	(b) During entire weld pass	
4.23	Residual stress distributions with and without interface elements on top surface for a three-pass welded plate .....	121
	(a) Transverse stresses	
	(b) Longitudinal stresses	
4.24	Through-thickness residual stress distributions at 0.25" from the weld centerline for a three-pass welded plate .....	123
	(a) Transverse stresses	
	(b) Longitudinal stresses	
4.25	Distortion changes at 7.5" from the weld centerline on top surface for a three-pass welded plate .....	125
5.1	Idealized temperature dependent engineering stress-strain curves .....	149
5.2	Idealized temperature dependent engineering stress-plastic strain curves .....	150
5.3	Flow chart of the plastic strain relaxation effect algorithm .....	151
5.4	Schematic explanation of the plastic strain relaxation effect .....	152
	(a) One-dimensional bar model	
	(b) Stress-strain curves at different temperatures	
	(c) Temperature, thermal strain & elastic strain histories	
	(d) Plastic strain histories	
5.5	Examples of a one-dimensional model with the plastic strain relaxation effect .....	154
	(a) Temperature history	
	(b) Stress-strain curves at different temperatures under elastic-perfect plasticity assumption	
	(c) Elastic, thermal strain histories under (b) condition	
	(d) Plastic strain histories under (b) condition	

(e)	Stress histories under (b) condition	
(f)	Stress-strain curves at different temperature under isotropic hardening plasticity assumption	
(g)	Stress histories under (f) condition	
5.6	Schematic representation of a one-dimensional spring model	158
5.7	Material behavior of ASTM A36 mild steel for a one-dimensional model	160
(a)	Thermal and elastic strain histories	
(b)	Plastic strain histories	
(c)	Stress histories	
5.8	Relationship between $k$ (degree of constraint), $\Delta\epsilon^{pl}$ , and $\Delta\sigma_{res}$	161
6.1	Bilinear strain hardening effect assumed for ASTM A36 mild steel	180
6.2	Finite element model for a one-pass bead-on-plate weld on a 1/2" thick plate	181
6.3	Temperature profiles at 1/2" from the weld centerline on top surface (a one-pass bead-on-plate weld on a 1/2" thick plate)	182
6.4	Comparison of the numerical and experimental residual stress distributions on top surface (a one-pass bead-on-plate weld on a 1/2" thick plate)	183
(a)	Transverse stresses	
(b)	Longitudinal stresses	
6.5	Through-thickness residual stress distributions at weld centerline (a one-pass bead-on-plate weld on a 1/2" thick plate)	185
(a)	Transverse stresses	
(b)	Longitudinal stresses	
6.6	Comparison of the residual plastic strains with and without considering plastic strain relaxation effect on top surface (a one-pass bead-on-plate weld on a 1/2" thick plate)	187
(a)	Transverse plastic strains	
(b)	Longitudinal plastic strains	
(c)	Equivalent plastic strains	
6.7	Distortion changes at 2" from the weld centerline on bottom surface (a one-pass bead-on-plate weld on a 1/2" thick plate)	190

6.8	Finite element model for a one-pass partial penetration butt welded plate	191
	(a) View of weld area	
	(b) Entire model	
6.9	Comparison of residual stress distributions with and without considering plastic strain relaxation effect on top surface	
	(a one-pass partial penetration butt welded plate)	192
	(a) Transverse stresses	
	(b) Longitudinal stresses	
6.10	Through-thickness residual stress distributions at weld centerline	
	(a one-pass partial penetration butt welded plate)	194
	(a) Transverse stresses	
	(b) Longitudinal stresses	
6.11	Distortion changes at 10" from the weld centerline on bottom surface	
	(a one-pass partial penetration butt welded plate)	196
6.12	Finite element model for a one-pass butt welded plate with a single V groove	197
	(a) View of weld area	
	(b) Entire model	
6.13	Comparison of residual stress distributions with and without considering plastic strain relaxation effect on top surface	
	(a one-pass butt welded plate with a single V groove)	198
	(a) Transverse stresses	
	(b) Longitudinal stresses	
6.14	Through-thickness residual stress distributions at weld centerline	
	(a one-pass butt welded plate with a single V groove)	200
	(a) Transverse stresses	
	(b) Longitudinal stresses	
6.15	Distortion changes at 10" from the weld centerline on bottom surface	
	(a one-pass butt welded plate with a single V groove)	202
6.16	Finite element model for a three-pass butt welded plate with a single V groove	203
	(a) View of weld area	
	(b) Entire model	
6.17	Comparison of residual stress distributions with and without considering plastic strain relaxation effect on top surface	
	(a three-pass butt welded plate with a single V groove)	204

	(a) Transverse stresses	
	(b) Longitudinal stresses	
6.18	Through-thickness residual stress distributions at weld centerline (a one-pass butt welded plate with a single V groove) .....	206
	(a) Transverse stresses	
	(b) Longitudinal stresses	
6.19	Distortion changes at 10" from the weld centerline on bottom surface (a three-pass butt welded plate with a single V groove) .....	208
6.20	Finite element model for a tee-joint with fillet welds .....	209
	(a) View of weld area	
	(b) Entire model	
6.21	Comparison of residual stress distributions with and without considering plastic strain relaxation effect on top surface of the flange (a tee-joint with fillet welds) .....	211
	(a) Transverse stresses	
	(b) Longitudinal stresses	
6.22	Distortion changes at 4.0625" from the centerline on bottom surface of the flange .....	212

## CHAPTER 1

### INTRODUCTION

#### 1.1 Background

Welding of metal structures provides a method of joining together a number of components without significantly impairing the properties of those components. Fusion welding processes are generally used to join structural members. These welding processes generally employ a moving heat source that attains a sufficiently high temperature to melt the material at the joint. The resulting temperature distributions are highly nonlinear and cause non-uniform expansion and contraction in the welded joint. This non-uniform expansion and contraction creates non-linear distribution of plastic strains. As a result, residual stresses are retained in the weldments after welding, whereas welded joints deform, a process usually referred to as 'distortion'.

The presence of residual stresses and distortion is of primary concern in both designing and evaluating welded structures. Residual stresses increase crack driving force and largely affect the strength and resistance to brittle fracture. They can play a

major role in cracking and fracture problems in the structure. Tensile residual stresses can promote premature weldment cracking and fracture problems in heavy structures with welded thick plates, while compressive residual stresses tend to reduce the buckling strength of compressive members. Through-thickness residual stresses may cause lamellar tearing in thick-section weldments.

Distortion can make it difficult to maintain dimensional tolerances and cause misalignment of welded joints. This may result in reaction stresses that are not usually considered in the design.

Moreover, multi-pass welding of thick sections subjects the components to multiple thermal cycles and inelastic strain patterns, creating a more severe and complex residual stress distribution through the plate thickness and distortion.

There is limited amount of data available pertaining to the magnitude and distribution of the residual stresses occurring in multi-pass welding and even less pertaining to the distribution of the residual stresses through the thickness of the plate. Although various measuring techniques for residual stresses are available, they are destructive, time consuming, and equipment dependent. Therefore, analytical techniques for the prediction of residual stresses in multi-pass welded joints are alternatives to those experimental methods.

There have been attempted by researchers to establish empirical approaches for understanding the behavior of materials due to welding processes. To date, due to complexity of the welding process, thermal and mechanical behaviors of weldment are not completely understood. Considerable effort has been made to develop analytical

solutions to predict the thermal and mechanical responses of weldments. Although some solutions have been useful, they are difficult to implement in realistic welded structures. This is due to severe limitations in the geometry of the weldments and the inherent assumptions made to derive the equations. Therefore, more effort has been expended to develop numerical models to predict the transient thermal response and the transient and residual stress responses. This became possible after the progress of computer technology. Subsequently, some numerical modeling technologies have been developed. One of the powerful and widely used numerical analyses is the finite element method (FEM). The FEM can handle non-linear material behavior, such as complicated geometries, complex boundary conditions, as well as temperature dependent material properties.

There are many publications on weld modeling using FEM [1 - 17]. Recently, some effort [16, 17] has been made to develop simplified finite element analysis (FEA) procedures so that realistic temperature/stress histories in a weldment can be simulated with commonly available FEA packages. The Ohio State University (OSU) researchers have developed these FEA techniques for the multi-pass welds on a thick plate [1 - 6]. Representative examples are two-dimensional (2-D) models with ramp heat input functions, lumped models for multi-pass welds, and three-dimensional (3-D) shrinkage models.

The thermal and mechanical response of a weldment is a 3-D problem that requires a considerable amount of computational time. The computational time required to simulate a multi-pass weld increases in proportion to the number of weld passes.

Therefore, it is necessary to develop a simulation model to reduce the computational time while preserving the accuracy of the solution. However, the final state of stresses and distortion has been proceeded to be dependent of the quasi-steady conditions during welding. Therefore, a 2-D analysis can be used with appropriate simplifications without the expenses of the numerical accuracy [1, 2, 6].

To include the filler metal effect, the element rebirth technique has been recognized as one of the few reasonable methods that can be readily incorporated in the existing commercial FEA packages. In this technique, the element simulation of filler metal deposits is generated along with the FEA meshes for the workpiece. These elements are kept inactive until a designated 'rebirth' time, which is associated with the welding process, is approached in the simulation [1, 2, 6]. In order to consider the thermal mismatch effect in numerical modeling, the interface element technique has recently been developed. The element rebirth technique cannot consistently represent the model because the weld deposit elements are activated with nodes having the temperature assigned by the activated neighbor elements. One variation of the element rebirth technique is to introduce special interface elements between the deposit and the workpiece meshes so that the reactivated elements interact with the workpiece through the interface elements [7, 8]. Also, in order to consider the mechanical mismatch effect in numerical multi-pass welding modeling, reactivated elements are required to reset to a state with zero stresses and strains [18]. Some researchers [7] reported that the interface element approach shows physical consistency with the actual heat transfer process in welding.

In the welding process, the state of the weld metal changes from solid to liquid during heating, and from liquid to solid during cooling. When the temperature reaches the liquidus, the plastic strain is relieved, and when the metal solidifies, the plastic strain is accumulated again. The non-zero material properties above melting temperature, however, would cause the plastic strains to continue accumulating as well as to reach artificially high values owing to the very low magnitude of the material properties. In fact, the effect of the melting and resolidification of the fusion material during welding is ignored in most numerical analyses. Therefore, it is necessary to modify the numerical analysis program and, if possible, to impose the relaxation of the accumulated plastic strain when the material melts.

When these techniques are applied to the numerical analysis of the welding problem, one obvious limitation is that it can only be implemented by an experienced analyst on a case-by-case basis. Considerable care needs to be exercised during the whole process. The procedure can become extremely complicated when a multi-pass weld is simulated.

## 1.2 Research issues

Some researchers have proposed modeling techniques that incorporate more comprehensive welding phenomena in the model such as phase transformation effects [9 - 15], and others have tried to get stress values from simplified numerical procedures [16, 17]. Even though many modeling techniques have been developed, it is difficult to tell

which one is most efficient in predicting residual stresses and distortion within economic feasibility. Moreover, in the case of multi-pass welding, the simulation becomes more complicated because the multi-pass welding effect is not a simple accumulation of single-pass welds.

In this dissertation, the welding modeling method is used simplified numerical procedures that predict weld residual stresses and distortion with reasonable accuracy. The thermal and mechanical mismatch effects [7, 8, 18] is included in this study to simulate the realistic welding conditions. The appropriate modeling procedures are established, through evaluating and modifying current procedures, to get reasonable residual stresses in the multi-pass weld models.

In this study, the plastic strain relaxation effect is also considered in the FEA numerical simulation. In nature, the accumulated plastic strain is relieved when the weld reaches the melting point. The plastic strain may resume its accumulation process when the weld temperature falls below the melting temperature. However, in the numerical analysis, the plastic strain accumulation continues even if the weld exceeds the melting temperature. Consequently, the accumulated plastic strains are large where the plastic strains are actually non-existence, especially in the weld area. The overestimated plastic strains may affect the predicted results of residual stresses and/or distortion. The effect of plastic strain may be the cause for numerical errors associated with the modeling analysis. This modeling issue would be important, however, it has never been reported in the literature. In this dissertation, the plastic strain relaxation effect is studied using FEM.

### 1.3 Objectives

This dissertation has two objectives: the first is to develop an effective FEA procedure for residual stress and distortion calculation in multi-pass weld model, and the second is to study the plastic strain relaxation effect in numerical calculation when material state is changed. Details are as follows.

In the first object, the study of appropriate FEA procedure addresses the element rebirth technique to predict the residual stresses and/or distortion for multi-pass welding. The FEA procedure, from mesh generation for the weld deposits to the element 'rebirth' between weld passes, is integrated with the commercial code ABAQUS [19]. In order to establish the appropriate FEA procedure by conducting bench test analyses on typical case problems, the study of the characteristics of thermal and mechanical analyses for welding simulation is investigated. This investigation include the thermal heat input modeling technique, ramp heat input function effect, and lumping (grouping) modeling technique. Three different multi-pass welding cases are conducted. Through the first two cases, the effective heat input conditions, the effective lumping techniques, and the residual stresses/distortion effects according to the heat inputs are discussed. In the third case, the interface element technique is employed. In order to include thermal and mechanical mismatch conditions, the modeling technique must be different from the conventional method (without using interface elements) [1 - 6]. The interface element technique should be introduced to satisfy the mismatch conditions [7, 8, 18]. By

comparing the results of the conventional method with those of the method using interface elements, the advantages and disadvantages are discussed on the basis of the effective FEA procedure.

The second objective of this study is to consider the plastic strain relaxation effect on welding numerical simulation results . During the welding process, plastic strain accumulates. Finally, when the temperature reaches to the melting point, material properties are lost because the material loses its characteristics as a solid state. Therefore, the accumulated plastic strains are relaxed and the stress values are zero. After the temperature goes below the melting point, the material properties return and stress distribution and plastic strain are calculated from the state with zero plastic strain. In this dissertation, the effect mentioned above is studied for numerical welding simulation. First of all, a definition of the plastic strain relaxation effect is required. Then, it is necessary to modify the process of the UMAT user subroutine, which is to represent material behavior [19]. To do this, the study of the thermo-elastic-plastic material behavior is essential.

First, the plastic strain relaxation effect is studied theoretically and compared with one-dimensional (1-D) simple examples. After then, the plastic strain relaxation effect is applied to the 2-D welding models: bead-on-plate welding, partial penetration butt welding, multi-pass welding, and tee-joint welding. It is anticipated that the plastic strain relaxation effect changes the residual stresses and distortion after welding. The numerical results, with and without the plastic strain relaxation effect, are compared. Based on the

differences of the numerical results. the effect of the plastic strain relaxation is discussed. Finally, the results of residual stresses and distortion using the plastic strain relaxation effect is compared with experimental data.

## CHAPTER 2

### LITERATURE REVIEW

This review investigates the progress of the state-of-the-art on welding heat flow, residual stresses and distortion analyses. This chapter concentrates on numerical analyses of welding heat flow, residual stresses, and distortion.

#### 2.1 Welding heat flow analysis

Analysis of welding heat flow includes heat generation by the welding arc, heat loss, and heat conduction. Many researchers have studied welding heat flow problems analytically and numerically. Early attempts were performed using analytical methods to solve welding heat flow problems with simplified assumptions. Since 1980s, the numerical analysis using computers has been performed with more realistic welding conditions.

### 2.1.1 Analytical studies

The basic theory of heat flow developed by Fourier, and applied to moving heat sources by Rosenthal [20] is still widely used for calculating the thermal history of welds. By using the conventional heat transfer differential equation for a quasi-stationary state, Rosenthal developed 2-D and 3-D equations for point, linear and plane sources of heat. Myers *et al.* [21] has discussed the effect of limitations and assumptions on the accuracy of temperature distributions. The assumptions are as follows:

1. The material is solid at all times and at all temperatures, undergoes no phase changes, and is isotropic and homogeneous.
2. The thermal conductivity, density, and specific heat are constant with temperature.
3. There are no heat losses at the boundaries.
4. The piece is infinite, except in the directions specifically noted.
5. Conditions are steady with time, i.e., while in the middle of a long weld, during heat input, etc.
6. The source of heat is concentrated in a zero-volume point, line or area.
7. There is no Joule heating.

Near the heat source, the simplified assumptions 1, 2 and 6 cause errors in the predicted temperature distribution. Assumption 3 means that solutions are most accurate when the heat source is far away from the weldment boundaries. Solutions can be achieved for three geometric assumptions (see Figure 2.1). All of these geometries are

assumed to have an infinite size in two directions. Simple solutions can be achieved if the thickness is assumed to be infinite or very small. The solution is more complicated for a moderately thick plate.

To overcome most of these limitations, some researchers have studied the treatment of the heat flow at regions near the weld pool. Nippes *et al.* [22] found large differences between the results from Rosenthal's equation, and tests for cooling rates in the heat affected zone (HAZ). Wells [23] developed another equation to relate the average size of the fusion zone (FZ) to the amount of heat input in a single-pass butt-weld using Rosenthal's 2-D line heat source solution. Adams [24] derived the simplified equations of 2-D and 3-D heat flow analyses using mathematical approximations to predict centerline cooling rates and peak temperature distribution in fusion welding. Jhaveri *et al.* [25] investigated the effects of plate thickness, thermal properties, and welding process variables on important thermal phenomena. Reference 25 shows the dependence of cooling rate on plate thickness, energy input, initial plate temperature, and surface heat loss. Christensen *et al.* [26] performed theoretical and experimental analyses using the point heat source model for predicting the dimensions and shape of the weld pool, the temperature distribution in and outside the weld pool, and the cooling rate. The research conducted by these individuals used temperature independent thermal properties. Grosh *et al.* [27] tried to refine the analytical solutions by implementing temperature dependent parameters into the existing equations. Most nonlinear problems, however, require numerical analysis due to the limitations of employing temperature dependent parameters into the analytical solutions.

### 2.1.2 Numerical studies

Analytical studies have limited accuracy due to assumptions that simplify the physical model. As computer technologies are developed, computational numerical techniques such as FEM or finite difference method (FDM) are developed. The development of numerical techniques allows more exact welding thermal models with nonlinear thermal properties, distributed heat source, joining geometry, etc. Accordingly, many investigators have used various numerical methods to analyze heat flow in welds. Since Rosenthal's point or line models assume that the flux and temperature are infinite at the source, the temperature distribution has many similarities to the stress distribution around the crack tip in linear elastic fracture mechanics. However, since it would not account for the actual distribution of heat in the arc, and hence would not accurately predict temperatures near the arc, this approach is not pursued in this study.

Pavelic *et al.* [28] first suggested that the heat source should be distributed. A Gaussian distribution of flux deposited on the surface of the workpiece for Gas Tungsten Arc Welding (GTAW) (see Figure 2.2) was proposed. The FDM technique was applied for predicting temperatures for a 2-D plate. When parameters were correlated as a function of maximum molten width and length, peak temperature predictions in the HAZ were in agreement with the measured values. Stoeckinger *et al.* [29, 30] developed a 3-D heat transfer analysis for simulating a moving square wave heat source. Contact conductance was developed by using a FDM. The subsequent works of Krauts *et al.*

[31], and Friedman [32] are particularly notable. In their work, Pavelic's disc model was combined with a FEA to achieve improved temperature distributions in the FZ and HAZ. Paley *et al.* [33] used a constant power density distribution in the FZ with a finite difference analysis. Friedman *et al.* [34] employed a FEM for temperature distribution in thick NiCrFe 600 plates subjected to a stationary GTAW heat source. A double ellipsoidal welding heat source model based on a Gaussian distribution of power density in space was proposed by Goldak *et al.* [35, 36]. Goldak's model can easily change the size and shape of the heat source for both shallow and deep penetration welding processes (see Figure 2.3). In addition, this model has the versatility and flexibility to handle non-axisymmetric 3-D heat source cases. The disc model by Pavelic *et al.* [28] and the volume source model by Paley *et al.* [33] are more specific applications of Goldak's model. Fan *et al.* [37] used a skew Gaussian flux distribution as the heat source for 2-D FEM modeling. Latent heat was treated as a change in specific heat during melting and solidification. Temperature dependent thermal properties, and surface heat loss were also used. Kraus [38] treated the steady state and transient state heat transport problems associated with thin plate welding by using the FEM. The phase change was accounted for through element phase property averaging and quadratic/integral capacitance fitting techniques. A comparison of experimental results exhibited similar weld pool sizes. In numerical analysis of temperatures, and associated cooling rates, Kannatey-Asibu *et al.* [39] developed a moving FEA grid with an adaptive scheme that permits mesh refinement in required regions, thereby achieving a more efficient computation for

desired accuracy. The numerical results for a 2-D analysis correlate with temperature measurements.

Many investigators have employed commercial numerical analysis codes for calculating the history of temperature distributions. The aim of calculating temperature distribution is to do residual stress or distortion analysis. Therefore, the following literature reviews for thermal analysis are subsequential processes for residual stress or distortion analysis. Tekriwal *et al.* [40, 41] developed a 3-D FEA model to simulate the thermal history of a weld joint produced by both GTAW and Gas Metal Arc Welding (GMAW) processes using ABAQUS. Karlsson *et al.* [42, 43] employed ADINAT, another FEA code, for the thermal analysis in a single-pass butt-welded pipe. A rotationally symmetric FEA model was employed in Reference 42, and a full 3-D FEA model was used in Reference 43. The procedure for thermal analysis of a thick plate with a multi-pass welding process was developed by Tsai *et al.* [2] and Shim *et al.* [1, 6]. ABAQUS FEA codes were used for transient thermal analysis. Heat input from the welding arc was modeled using a ramp function. A comparison between numerical results and experimental data using thermocouples determined ramp time.

## 2.2 Residual stress analysis

Analysis of welding residual stresses have been studied since the early 1900s. These early studies were completed by developing analytical solutions and experiments. One of the earliest studies on residual stresses in a welded plate was achieved by Boulton

*et al.*[44]. They calculated the longitudinal stress for an edge welded plate using 1-D strip model. The alternation in length of longitudinal lines of a welded plate was experimentally determined by reading the length gages. The authors calculated the residual stresses in the elastic and plastic region of the plate by using equilibrium conditions of a welded plate and the strain measurements. They developed the approximate theory for calculating the residual stresses and strains.

By developing the computer technologies, many researchers have calculated the residual welding stress numerically with more realistic welding conditions. The residual stress analysis is reviewed by concentrating on the numerical analysis aspect.

#### 2.2.1 Causes of residual stresses

During welding residual stresses develop due to an uneven distribution of non-elastic strains, as well as uneven heating and cooling. There are three sources which cause welding induced residual stresses. One source is the difference in shrinkage between the hot and cool areas of a welded joint. As it cools, the weld metal, originally subjected to the highest temperature, tends to contract more than the metal in all other areas. This contraction is hindered by other parts of the welded joint, resulting in the formation of high longitudinal stresses in the direction of the weld. The second source is uneven cooling in the thickness direction of the weld. Surface layers cool more rapidly than interior layers, especially in thick plates. This gives rise to thermal stresses which can lead to non-uniform plastic deformation and residual stresses. Finally, the third

source consists of residual stresses arising from phase transformations that occur during cooling. These transformations are accompanied by an increase in the specific volume of the metallurgical phase being transformed. This expansion is halted by cooler material and causes residual stress. Residual stress may also be generated by inelastic strains from external structural loads or elastic reaction stresses caused by external restraints, such as jigs, fixtures, or other clamping devices.

The primary factors influencing residual stresses in weldments are the physical and mechanical properties of the materials. These are yield stress, Young's modulus, Poisson's ratio, and thermal expansion. These properties are usually temperature dependent. Other factors are plate thickness, joint geometry, and clamping fixtures used during welding. These factors alter the degree of constraint imposed on the weldment.

### 2.2.2 Numerical studies

Many techniques have been developed for determining residual welding stresses. Studies of thermal stress analysis were made by Masubuchi [45] to develop an analytical method of evaluating residual welding stress and distortion. Tall [46] developed a method to calculate the longitudinal thermal stress in a weld using temperature dependent material properties. Based on a knowledge of the temperature distribution, Tall's method is a step-by-step computation of residual stresses arising in welded plates. The accuracy is limited due to insufficient information about material properties with high temperatures and boundary heat losses during welding. Stresses were calculated for both center-

welded and edge-welded structural steel plates and were compared with experimental results for the same plates.

On the basis of Tall [46]'s model, a 1-D computer code was developed by Masubuchi [45]. Muraki *et al.* [47, 48] developed a 2-D computational code for analyzing stress during butt-welding and bead-on-plate welding. Powerful computers and numerical techniques were used to analyze complicated welding problems and welding processes. One of the first numerical thermal and mechanical models for welding was developed by Hibbitt *et al.* [16]. They analyzed GMAW with a 2-D thermal model and a plane strain state assumption using the uncoupled FEM. They observed that creep was useful in modeling the stress relief process and the time-dependent plasticity theory with temperature dependent properties was appropriate for weld analysis. Friedman [32] employed the incremental plasticity with small strain and modeled the reduction of plastic strain due to annealing. Residual stresses were greatest in the weld metal and HAZ, while the accumulated plastic strain was greatest at the interface of these zones on the underside of the weldment. The material was assumed to be an isotropic elastic-plastic continuum having temperature dependent mechanical properties. To calculate the magnitude and distribution of residual stresses for multi-pass girth-butt welded pipes, a computational model was developed by Rybicki *et al.* [49]. Elastic-plastic temperature dependent mechanical properties and unloading due to stress reversals were included in the model. Residual stresses obtained with models of seven-pass welds and thirty-pass welds were compared with the experimental data. Argyris *et al.* [17] studied thermo-mechanical response of bead on steel plate using the FEM. The 2-D heat flow analysis was

conducted with the transient diffusion package, SMART II. The mechanical response of a welded plate was calculated by thermo-elastic-visco-plastic analysis with a plane strain state assumption. Volumetric changes and latent heat effect during recrystallization were included in the analysis. Josefson [50] conducted a numerical study of stress redistribution during local post weld heat treatments for a multi-pass butt-welded pipe with mechanically unrestrained ends. The pipe material was micro-alloyed C-Mn steel. Temperature and stress analyses were performed by the FEM where rotational symmetry was assumed. Free *et al.* [51] analyzed residual stress in multi-pass weldments with PAFEC, a FEA package. A typical cross section was modeled assuming an axisymmetric or plane strain condition. Room temperature material properties were used for both the thermal and mechanical analyses. Each weld pass was modeled individually rather than grouped together in layers. Experimental verification was performed using high temperature strain gages, the blind hole drilling method, and the extensometer. Through-thickness residual stresses were measured by the sectioning method. A coupled thermal-mechanical analysis was performed by Mahin *et al.* [52] for GTAW of a circular 304L stainless steel specimen. FEA package PASTA2D was employed for the numerical analysis. A 2-D analysis was conducted with an axisymmetric assumption. Karlsson *et al.* [42, 43] studied residual stresses in a single-pass girth butt-welded pipe of carbon-manganese using the FEA codes ADINAT/ADINA. Karlsson [42] employed a rotationally symmetric FEA model in both thermal and mechanical analyses. This model was used to investigate the influence on the residual stress state of pipe geometry, mesh density and material modeling. Karlsson *et al.* [43] employed two different FEAs with

full 3-D solid elements and shell elements. Anderson *et al.* [53] also studied the reduction of residual stresses in a single-pass butt-welded pipe with mechanical and thermal loading using ADINAT/ADINA. Josefson *et al.* have calculated the residual stresses in single-pass butt-welded pipe with rotational symmetry condition [9] , and in multi-pass butt-welded pipes with rotational symmetry and symmetry conditions [10, 54] by SOLVIA, a FEA code. Lindgren *et al.* [55] employed shell element modeling by using NIKE3D, a FEA package, for calculating deformations and residual stresses in butt-welded plate and butt-welded thin wall pipe. They used shell elements in the FEA models. Simulation of automatic butt-welding of large plates was investigated by Jonsson *et al.* [56]. The plates were tack-welded before the butt-welding. The investigator reported that the most important welding parameters were the arc energy per unit length of the weld and the welding speed. Farong *et al.* [57] calculated the weld residual stresses by using boundary element method. Then they compared the results with that from FEM. Tekriwal *et al.* [40, 41, 58, 59] developed a 3-D FEA model to simulate the mechanical analysis of a welded joint produced by both GTAW and GMAW processes using ABAQUS [19].

As the plate thickness in a structure increases, the number of weld passes required to complete a welded joint also increases that requires extensive computation time for numerical analysis. Computation time can be saved by grouping the actual weld passes into several lumped passes. This lumped pass model for multi-pass welds was investigated by Ueda *et al.* [60], Leung *et al.* [18], and Rybicki *et al.* [49]. Ueda *et al.* [60] performed theoretical and experimental investigations on an idealized research

model for multi-pass girth butt-welds on a pressure vessel to determine the residual stress distribution in the through-thickness direction. Two layers of actual weld passes were regarded as one grouped pass. They reported between the predicted and measured stresses. Leung *et al.* [18] developed a modeling technique for thermal and mechanical analysis of a welded plate using ABAQUS. AISI 316L stainless steel models were used for the analysis of submerged arc welding. An uncoupled analysis was employed and a Gaussian heat flux distribution was introduced in the weld pool. A 2-D cross section perpendicular to the welding direction was used for both analyses. Several lumping techniques were attempted. Rybicki *et al.* [49] studied lumped pass modeling in case of pipes. They investigated multi-pass girth pipe welds by combing all passes in a layer into a single stress analysis sequence.

The procedure for thermal and stress analyses of a thick plate with a multi-pass welding process was developed by the OSU researchers. Tsai *et al.* [5], Shim *et al.* [6] and Lee [62] have employed ABAQUS FEA code for the simulation. They employed the element rebirth technique in which bead elements were initially removed and activated as actual weld beads accumulated. A lumped model technique was studied by Lee [62]. He proposed two alternative ramp models for lumped pass models.

The lumped modeling investigators[18, 49, 60, 62] commonly suggested that the residual stress distribution is affected mainly by the first few passes and subsequently by the final pass. Intermediate passes are less important to determine the residual stresses.

In many cases of welding stress analysis, thermo-elastic-plastic material behavior was considered [1 - 10]. The effects of final phase transformations in the weld metal and the HAZ in many analyses were neglected [1 - 6]. However, if the structure is made of high strength steel, phase transformation effect were considered for strong local effects [10]. The final phase transformation effect has been studied by Josefson *et al.* [9, 10, 63]. According to Reference 63, the authors performed FEA calculations of transient and residual stresses in single-pass butt-welding of a C-Mn steel pipe. The FEA calculations were compared with the experimental result for the same pipe [42]. Even though the agreement between FEA results and experimental measurements were reasonably good, large stress differences in circumferential direction were found in the welded region. It was believed that information about the material behavior during welding was still insufficient, and therefore, the difference was due to the exclusion of the transformation plasticity effect. An attempt to model effects of how the transformation plasticity reduces the yield stress in the time interval during the phase transformation, associated with the volume changes resulted in only slightly reduced differences [42]. In Reference 42, Karlsson emphasized that the changes in thermal strain during phase transformations have a great influence for determining residual stresses. In Reference 9, transformation plasticity effects were considered in pipe model. The total strain increment is decomposed into one elastic part, one thermal part, and two plastic parts. One of the plastic parts is the plastic strain caused by the phase transformation. This strain is obtained by evaluating the plastic strain rate at the end of each time, or load step. The FEA-code SOLVIA was used. It was possible to get a reasonably accurate solution for residual stresses in the HAZ and

weld metal. However, the stress differences appeared between FEA results and experiments. In Reference 43, Karlsson *et al.* reported that low-temperature solid-state phase transformation is significant and important to the residual stress field.

Similarly, in some references [11 - 13] the final phase transformations are considered in the weld metal and the HAZ in the FEA model, the resulting effects can be represented. In Josefson's study [14], the stress changes induced in the pipe during final phase transformation remains partly at room temperature because of the low circumferential restraint during the final cooling. In the plate case, however, the residual stress field was governed mainly by the large stress increase that occurred after final phase transformation. Stress changes induced in the plate before final phase transformation were hardly noticeable in the residual stress field. Andersson [15] researched thermal stresses in a 2-D butt-welded plate of IIT36 steel considering phase transformation. The author concluded that the differences in residual stress distribution between FEA and experimental results are due to not considering Baushinger effects.

However, it seems that few investigators have studied the plastic strain relaxation effect. According to Friedman [32], the plastic strain relaxation effect was mentioned. During the welding process, material near the weld center experiences loading to a plastic state of stress prior to melting. The plastic deformation accumulated during heating process is completely relieved when melting takes place. The transient and residual stress and distortion patterns that are generated during welding depend on the state of plastic strains. Consequently, the plastic strain relaxation effect can be important. Instead of

incorporating the plastic strain relaxation effect in the FEA model, the empirical relation was used to approximate the reduction of the previously accumulated plastic strain at high temperature. The amount of plastic strain reduction was based upon the peak temperature, being between 5 % at 150 °K below the melting temperature and 100 % at the melting temperature. Also, Papazoglu [64] mentioned the significance of the plastic strain relaxation effect. The accumulation of plastic strains in the regions that become molten during welding cycle. The presence of non-zero material properties above melting temperature would cause the plastic strains to continue accumulating as well as to reach artificially high values owing to the very low mechanical material properties. Therefore, it is necessary to modify ADINA by imposing the total plastic strain relief when the material melts.

### 2.3 Distortion analysis

The following are the fundamental reasons for changing the dimensions during the welding process: (1) transverse shrinkage of weldment perpendicular to the welding direction, and (2) longitudinal shrinkage of weldment parallel to the welding direction. Typical welding distortion types include transverse shrinkage, angular change, rotational distortion, longitudinal shrinkage, longitudinal bending and buckling distortion (Figure 2.4) [65]. These phenomena result from the fact that the concentrated moving heat source during the welding process causes localized mechanical deformation consisting of

contraction after solidification in the FZ, and of plastic straining induced by thermal expansion in the HAZ.

### 2.3.1 Experimental studies

Kumose *et al.* [66] performed experimental studies to define the effect of plastic and elastic restraint upon angular distortion. They developed formulas and curves to calculate angular distortion caused by one-pass fillet welding. Guyot [67] developed transverse shrinkage curves and formulas that can be used to predict distortion and applied them to practical locomotive parts. Watanabe *et al.* [68] carried out the extensive studies regarding welding distortion. They studied the effect of welding conditions on the shrinkage distortion in welded structures. They also developed several empirical equations based on experimental data to predict angular distortion in fillet welded T-joints, as well as several other geometric types using shielding metal arc welding. You *et al.* [69] used the same equations developed by Watanabe *et al.* [68], but they calculated the coefficients to adapt the equations to the flux core arc welding.

### 2.3.2 Numerical studies

For a long time, welding distortion predictions have been primarily empirical based upon experimental data. However, because of the development of computational technology, the numerical studies have become more active. Very early studies on

numerical distortion simulation were performed by Masubuchi [65]. He developed the programs for 1-D long beams, 2-D bead-on-plate, and butt joints. Recently, Brown *et al.* [70] calculated residual stresses and distortions of a six-inch long fillet welding in a ring-stiffened cylinder with three dimensional geometry and moving heat source using ABAQUS. However, the computational time for the simulation was terribly long. In order to reduce the computational time for distortion controls, some simplified methods have been introduced by the OSU researchers[71, 72]. This research has developed an inherent strain model which predicts weld distortion by prescribing an initial shrinkage strain condition along the welds. In particular, the spring-shrinkage model was developed using linear-elastic structural FEA procedures for a more direct engineering approach to prediction of weld distortion [72].

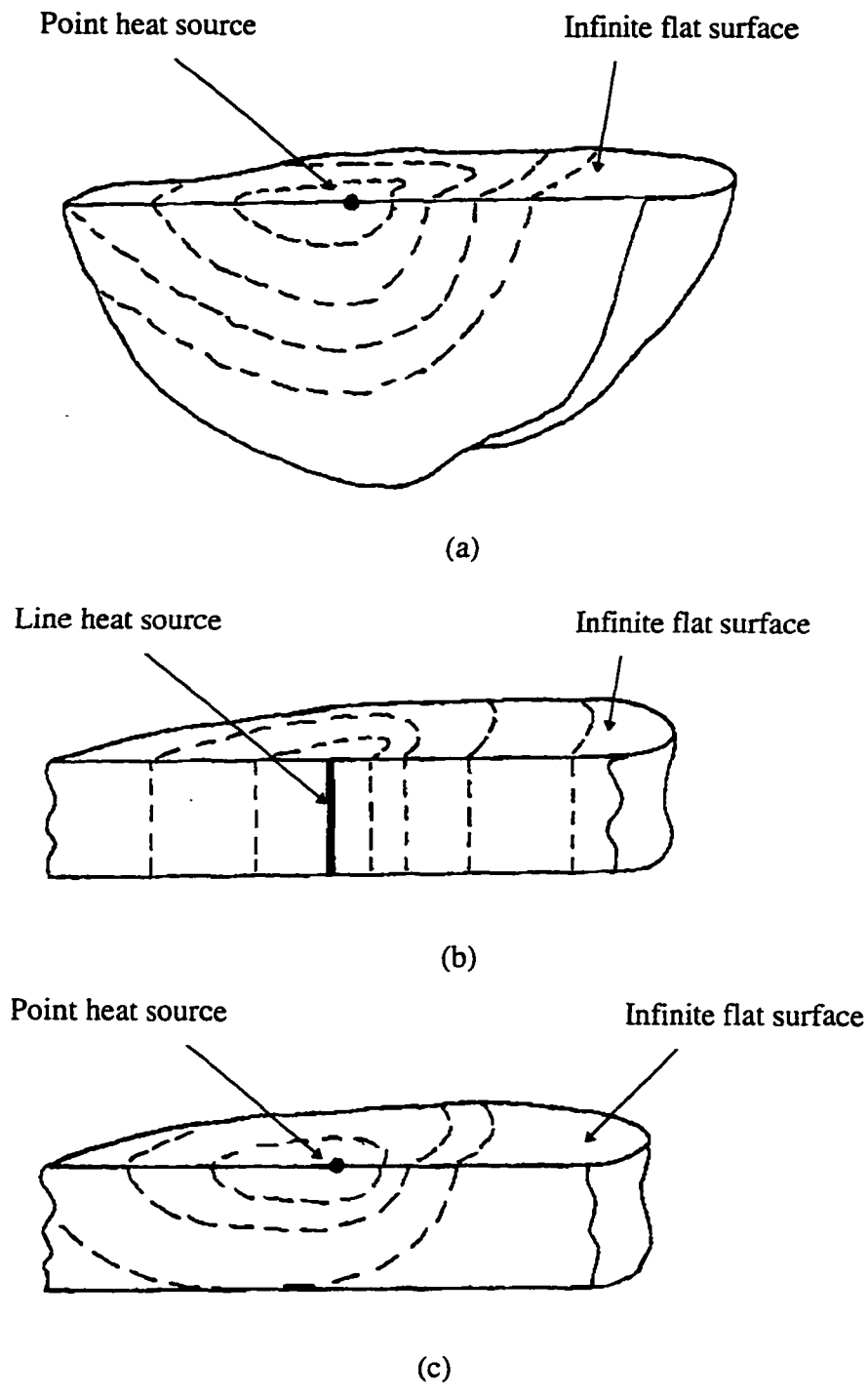


Figure 2.1 Some assumed geometries for solutions of heat flow during welding  
 (a) Semi-infinite body  
 (b) Two-dimensional infinite body  
 (c) Finite thickness plate with point heat source

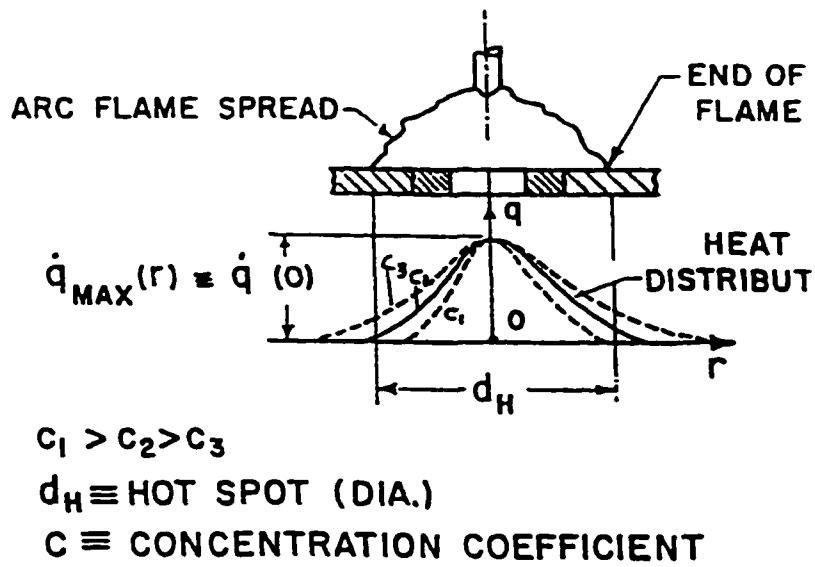


Figure 2.2 Gaussian circular heat input model [28]

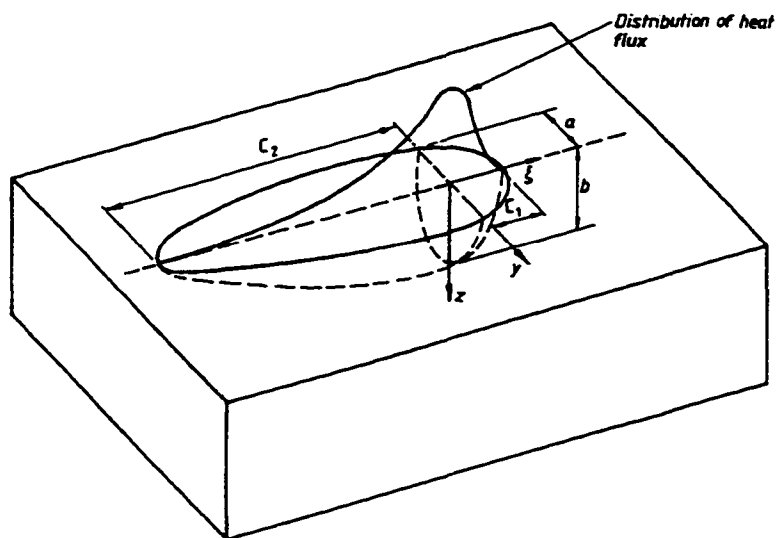


Figure 2.3 Double ellipsoidal heat source configuration together with the power distribution function along the  $\xi$  axis [35]

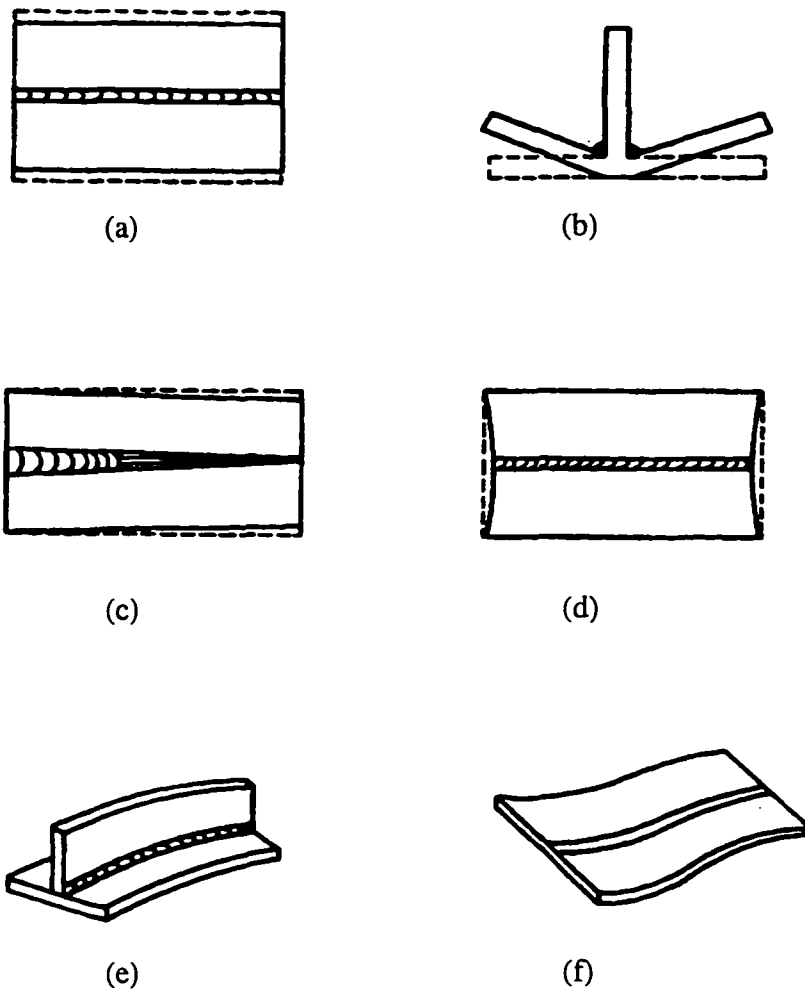


Figure 2.4 Various types of weld distortion [65]

- (a) Transverse shrinkage
- (b) Angular change
- (c) Rotational distortion
- (d) Longitudinal shrinkage
- (e) Longitudinal bending distortion
- (f) Buckling distortion

## CHAPTER 3

### FINITE ELEMENT MODELING TECHNIQUES FOR THERMAL AND MECHANICAL WELDING ANALYSES

An uncoupled (subsequentially coupled) thermo-mechanical analysis is performed (see Chapter 3.1). The thermal analysis is performed to determine the entire temperature history according to the specified welding procedure. The temperature data file is retrieved as a thermal loading input for the subsequent mechanical analysis. Both thermal and mechanical analyses are nonlinear, time dependent, and require a large amount of computational time (Chapter 3.5). The thermal and mechanical responses of a thick plate is a 3-D problem in nature that requires a considerable amount of computation. The computational time is required to simulate a multi-pass weld increases in proportion to the number of passes. Therefore, simplification in the simulation models according to the physical weld behaviors are investigated to develop procedures for less computational time with acceptable accuracy. A 2-D analysis is sought to replace the 3-D analysis with appropriate assumptions depending on the nature of the problem (Chapter 3.2).

A modified Gaussian heat input is developed and the ramp heat input function is adopted here to study the moving arc effect (Chapter 3.3).

Also, to model the multi-pass welding process, the element rebirth technique is employed (Chapter 3.6). Interface element technique is studied to consider the thermal and mechanical mismatch effects between weld metal and base metal (Chapter 3.7).

Adequate results with the plane strain assumption have been reported by some investigators [17, 50]. According to the studies by Shim *et al.* [1, 6], the plane strain analysis showed an unrealistically large tensile stress zone which increased with the plate thickness and the number of weld passes. Therefore, the generalized plane strain assumption is implemented to incorporate the lateral constrain effect in the 2-D models (Chapter 3.8).

To further reduce the computational time, the lumping (grouping) technique is employed (Chapter 3.9). Multiple weld layers are lumped into fewer number of larger passes in the 2-D model.

The size and number of the elements affects the accuracy and computational time of the analysis. Where rapid change of temperature distribution occurs, smaller meshes are required in the weld area for accurate stress distribution (Chapter 3.10).

### 3.1 Uncoupled thermo-mechanical analysis

In a general thermo-mechanical analysis the temperature field and the mechanical field should be taken as thermodynamically coupled. For most thermal stress problems in welding the influence of the coupling terms between the temperature field and the mechanical field is very small. Therefore, the analysis can be divided into two main

parts, the determination of the temperature field and the determination of the stress fields. In such cases temperature is calculated in a heat transfer analysis or prescribed directly by the user, and is read into the mechanical analysis as a predefined field. In the mechanical analysis, temperature is a field variable in the sense that it varies with position. It is also time dependent.

This is valid as long as plastic work rates do not significantly heat the metal, and local deformation does not change the geometry of any element to the point where the heat conduction equation for the undeformed body is invalidated. Hence, in welding simulation, the temperature and stress fields can be solved separately. [1, 2, 6, 7, 16, 60, 62].

Also, it was shown by Argyris *et al.* [17] that the coupling between the temperature and stress field during welding is insignificant. In Karlsson *et al.*'s [73] study, the authors employed the coupling terms in the heat equation. These terms were calculated as products between the actual stress-strain and plastic strain rates. They concluded that the thermodynamical coupling in the heat equation can be neglected because the effects are very small.

The uncoupled (subsequentially coupled) thermo-mechanical analysis is employed in this study. The heat transfer analysis is performed and the temperature history is stored for uses as a thermal loading input in the subsequent mechanical analysis. The FEA mesh and time steps for both heat transfer and stress analyses are identical. Figure 3.1 shows the numerical analysis procedures developed for the uncoupled analysis.

### 3.2 Numerical model types

Welding problem is 3-D by nature. This kind of numerical simulation takes lots of computational time. To reduce the computational cost, simplified assumptions, without loss of the solution accuracy, have been proposed [1, 2]. One method entails using 2-D assumptions.

Both heat transfer and thermal stress analyses can be either 2-D or 3-D. Two-dimensional analyses are economic and less CPU time, but less accurate than those carried out in 3-D analyses. The 2-D model types, the cross-sectional and the in-plane analyses, are shown in Figure 3.2. Figure 3.2 schematically illustrates how the 2-D FEA model is applied to the actual weldment.

In heat transfer analysis, an in-plane analysis is most accurate where through-thickness variations in the temperature are small. However, an in-plane analysis is not accurate for weldments of reasonable thickness where weld penetration is small. Also, this analysis takes more computational time than that of cross-sectional analysis, because the weld length considered in cross-sectional model is only unit length, while the weld length in in-plane analysis depends on the model.

For large thickness weldments, a cross-sectional model can be used. The welding speed is sufficiently high to allow the amount of heat conducted ahead of the welding source to be small relative to the total heat input. Therefore, for a thick plate, a fast welding speed is assumed in order to neglect the heat flow effect in the welding direction. Utilizing the concept of quasi-stationary state heat flow, it is assumed that every cross

section along the welding direction experiences an identical temperature profile.

Modeling of the heat flow is limited to each cross section perpendicular to the welding direction. Consequently, it is assumed that the same residual stress distribution exists in every cross section perpendicular to the welding direction.

With these assumptions in mind, a simplified 2-D FEA model is developed. This simplified model represents a single cross section of the weldment which is perpendicular to the weld direction.

### 3.3 Thermal model

The thermal models developed and modified in this study are explained by specific modeling techniques, i.e., the new heat input model and the ramp heat input model.

#### 3.3.1 Heat source model

In the heat input model, the arc directly influences the temperature profile, cooling rate, fusion zone size, heat affected zone, and weld metal strength. Net heat input from the arc for the weldment is expressed by the following equation:

$$Q = \eta E I \tag{3.3.1}$$

where  $\dot{Q}$  is the net heat input from the arc (thermal power),  $\eta$  is the arc efficiency.  $E$  is the voltage, and  $I$  is the current.

The arc efficiency is effected by the welding process, metal transfer mode, shielding gas, and other factors making it very difficult to predict. Christensen *et al.* [26] measured the arc efficiency of various welding processes using the calorimetry method. Tsai [74] estimated that the arc efficiency of the GMAW process ranges from 80 to 90 percent. Thus, an arc efficiency of 85 percent was used for the net heat input to the plate for the GMAW process [1, 6, 62].

The heat distribution is as important as total heat input. The heat distribution plays a very significant role in determining the temperature profile and the related cooling rates in the weld vicinity. There are several different types of heat input models that were mentioned in the literature review of heat flow analyses. For example, the literature mentions Rosenthal's point and line heat source [20], Goldak's double hemispherical heat source [35], Tsai's skew Gaussian heat source [37], and Pavelic's [28] 'disc' type Gaussian heat source.

In the 'disc' model proposed by Pavelic *et al.* [28], the thermal flux has a Gaussian or normal distribution in the plane (see Figure 2.2):

$$\dot{q}(r) = \dot{q}(0)e^{-Cr^2} \quad (3.3.2)$$

where  $\dot{q}(0)$  is the maximum heat flux at the center of the heat spot,  $C$  the heat flux concentration coefficient, and  $r$  the radial distance from the center of the heat spot. This equation is valid for a stationary arc.

Tsai *et al.* [37] proposed a skewed Gaussian distribution in which the arc column is distorted backwards in order to consider the effect of weld speed. They modified the Equation (3.3.2) of Pavelic's model. The modified equation is as follows:

$$\dot{q}(r, w) = \dot{q}(0) e^{-cr^2 \frac{\beta V}{2\kappa}} \quad (3.3.3)$$

where  $\beta$  represents a weight function,  $V$  the arc speed,  $\kappa$  thermal diffusivity, and  $w$  the moving arc direction coordinate. They developed an analytical solution, called the 'finite source theory', and incorporated this heat source model with a finite plate thickness. This heat input model is considered realistic and accurate for welding processes.

A new heat input model is developed, which is based on Pavelic's 'disc' model [28]. This modified heat flux is as follows:

$$\dot{q}(x) = \dot{q}(0) e^{-cx^2} \quad (3.3.4)$$

The conservation of energy becomes

$$\dot{Q} = \dot{q}(0) \sqrt{\frac{\pi}{C}} L \quad (3.3.5)$$

where  $L$  is the weld length of consideration in welding direction (unit: inch). Unit length of weld is assumed in 2-D analysis. The total width of deposited weld bead,  $b$ , (unit: inch) is substituted into Equation (3.3.4), and  $\dot{q}(x)$  is assumed to be equal to 5 % of the maximum value of the thermal flux. Then, the heat flux on weld bead boundary can be written as

$$\dot{q}(b) = \dot{q}(0)e^{-Ab^2} = 0.05\dot{q}(0). \quad (3.3.6)$$

From Equation (3.3.6),

$$\begin{aligned} -Ab^2 &= \ln 0.05 \\ A &\equiv \frac{3}{b^2}. \end{aligned} \quad (3.3.7)$$

Equations (3.3.5) and (3.3.7) are substituted into Equation (3.3.4),

$$\dot{q}(x) = \frac{\dot{Q}}{bL} \sqrt{\frac{3}{\pi}} e^{-3\left(\frac{x}{b}\right)^2}. \quad (3.3.8)$$

The schematic explanation is shown in Figure 3.3.

When constant heat fluxes were used in the previous works [1, 6, 62], either surface heat flux or body heat flux was applied for thermal analysis. However, the combination of both surface and body heat flux can be applied for thermal analysis. The total heat input applied into the model is equal to the surface heat input plus the body heat input

$$\dot{Q} = \dot{Q}_s + \dot{Q}_B \quad (3.3.9)$$

where  $\dot{Q}_s$  and  $\dot{Q}_B$  indicate surface heat input and body heat input, respectively. In other words, when the heat input is applied to filler metal, the sum of the fractional surface flux and the body flux should be one.

Heat input energy per unit length and heat flux are calculated by the following equations for the heat flux:

Heat Input Energy:

$$H = \frac{\dot{Q}}{1055} \cdot \frac{v}{60} \quad (3.3.10)$$

Body Heat Flux:

$$\dot{q}_B = \frac{\dot{Q}_B}{1055 V_e} \quad (3.3.11)$$

Surface Heat Flux:

$$\dot{q}_s = \frac{\dot{Q}_s}{1055 b L} \sqrt{\frac{3}{\pi}} e^{-u \frac{x}{b}} \quad (3.3.12)$$

where  $H$  is heat input energy per unit length (unit: Btu/inch),  $\dot{Q}$  is net heat input from the arc,  $v$  is welding speed (unit: inches per minute),  $\dot{q}_B$  is body heat flux (unit: Btu/in<sup>3</sup>)

sec),  $\dot{q}_s$  is surface heat flux (unit: Btu/in<sup>2</sup> sec),  $V_c$  is the volume of bead elements in which heat flux is in (unit: in<sup>3</sup>).

The technique for the calculation of heat flux in this study is developed so that the heat input can be calculated by using the DFLUX user subroutine [19].

### 3.3.2 Ramp heat input model

A ramp heat input function was developed by the OSU researchers [1, 6] to gradually apply the heat flux with variable amplitude to the model. This model is used to avoid numerical divergence problems due to an instantaneous increase in temperature near the fusion zone. In addition, it enables the model to include the effect of a moving arc in a 2-D plane. The ramp function takes the out-of-plane energy flow into the 2-D model as the arc approaches, travels across, and departs from each plane under investigation. The general amplitude versus time curve shape for the ramp input model is shown in Figure 3.4. The actual welding time for the arc to travel across the unit thickness of the model is  $t_1 + t_2$ . The magnitude of  $\frac{1}{V}$  represents this heat scanning time. The temperature profiles are affected by the ramp time percentage, which is defined to be  $\frac{t_1}{t_1 + t_2} \times 100$ . According to the previous work [6], it was observed that a ramp time  $t_1$  of 20 % of the actual weld time  $t_1 + t_2$  gave the best correlation with the GTA

experimental data. The total area under the ramp heat input curve (Figure 3.4) is kept constant to insure that the same total heat input to the model is maintained.

In Reference 6, the ramp heat effect was controlled by using the `AMPLITUDE` command in ABAQUS [19]. However in this study, if the total time and the percentage of ramp heat time are determined, the ramp heat effects can be calculated by the `DFLUX` user subroutine [19].

### 3.3.3 Initial temperature conditions for welding model

In a 2-D cross-sectional model, the initial temperature condition can be issued. Most investigators have used room temperature as the initial temperature distribution in the base metal. However, two extreme cases have been considered for the initial temperature conditions in weld metal: one, room temperature, the other, the melting temperature.

Many investigators, including the OSU researchers [1, 2, 6, 62], have used room temperature in weld metal as the initial temperature condition.

However, in Karlsson *et al.*'s [43] study, the authors considered the temperature at the reborn elements (weld elements) as the solidification temperature. This temperature was used as the reference temperature for the weld elements for calculating thermal strains. In Reference 42, the authors used the melting temperature as the reference temperature for the weld metal, and they used the room temperature as the reference temperature for the base metal. Also, in Josefson's [75] work, the author used the

temperature above the melting point as the initial temperature of the weld metal, and a constant heat source was applied on the weld metal.

In this study, initial temperature distributions of both the weld metal and the base metal are assumed as room temperature for a five-pass welded plate model in Chapter 4.1.1. For a six-pass girth welded pipe model used in Chapter 4.1.2, two different initial conditions are employed for the weld metal: one is the same as the condition in Chapter 4.1.1, and the other is the melting temperature for the weld metal.

### 3.4 Temperature insensitivity for residual stress analysis

According to Lindgren *et al.*'s [76] study, if the residual stresses are of interest, the temperatures could be calculated from analytical solutions. The thermal material properties are assumed to be independent of the temperature in the analytical solutions. Also, Landau *et al.* [77] discussed that the residual stress is not very sensitive to the details of the temperature distribution.

In this study, the temperature insensitivity is evaluated in Chapter 4.1.2. Four different heat inputs are given for the stress analysis of a six-pass girth welded pipe model. It is found that heat input magnitudes have little effect on residual stress distributions.

### 3.5 Non-linear thermo-mechanical modeling

The essential material properties required to predict welding residual stresses, are the thermal expansion and yielding characteristics of the weldment. Temperature dependent mechanical behavior can be incorporated in thermal stress analyses.

The FEM is capable of incorporating the material and geometrical nonlinearities due to temperature-dependent thermo-mechanical properties, various boundary conditions, and pass-dependent plasticity. ABAQUS [19] is used to develop the complete thermo-elastic-plastic model for an arc welding process. ABAQUS was employed by Leung *et al.* [18, 78] and Shim *et al.* [1, 6] for thermo-mechanical analysis in 2-D single-pass and multi-pass welded plate, and by Tekriwal *et al.* [40, 41, 58, 59] for the analysis in 3-D welded plate.

For thermo-elastic-plastic welding problems, the temperature history is obtained from a numerical heat transfer analysis. The temperature distributions of the model produce the thermal strains, which are equated to nodal forces by differentiating the equation of total strain energy. The material is assumed to respond elastically up to yielding, and then additional plastic strain occurs. Yielding is based on the Von Mises yield criteria. Strain hardening is a function of plastic work only, and must be positive or zero for any deformation. The plastic stress-strain relationship is typically defined according to the Prandtl-Reuss equations associated with the Von Mises yield condition.

For multi-pass welds, both thermal and stress analyses are performed in several steps corresponding to the total number of passes being deposited. In thermal analysis,

each weld pass is considered as one step. The initial temperature distributions of the model are assumed as prescribed temperatures. During each weld pass, the temperatures of the weld elements of the model rises from the room to the melting temperatures and then cools down to the room temperature before the next weld pass is applied. The element rebirth technique is employed for multi-pass welding simulation (see Chapter 3.6. for details). Therefore, the elements for representing each weld pass is deactivated initially and the reactivated according to the weld pass sequence. Because the temperatures of the elements are not specified in the analysis when the elements are activated, the intermediate steps for specifying the temperature of the currently activated weld pass is required. The intermediate steps are necessary to preserve consistent conditions for each weld pass. Therefore, the number of total steps becomes  $(2N-1)$ , which is equal to the number of total weld passes ( $N$ ) plus the number of intermediate steps ( $N-1$ ).

Because of the need of  $(2N-1)$  steps in the  $N$ -pass weld heat transfer analysis, the mechanical analysis also needs the  $(2N-1)$  steps for consistency. The thermal load of the first weld pass is used to solve for the strains, displacements and stresses. The plastic strain and total displacement at the end of the analysis are saved. Elements modeling the next pass in the mesh are then activated, thereby retaining their initially zero plastic strain state. The plastic strain and displacement for the elements in the previous pass are restored, thus prescribing the old displacements on the new mesh. The prescribed displacements are applied gradually in steps, and the new elements are strained and displaced with respect to the old mesh. Continuity of plastic strain is maintained. The

thermal load from the next pass can be used to solve for final strains, displacements, and stresses similar to the original weld pass. This process is repeated for each weld pass in the weldment. The final residual stress field is obtained after all passes have been modeled. In heat transfer analysis, intermediate steps are required between each weld pass simulation.

The mechanical model requires more computing time than the thermal model even when using an identical mesh configuration, because severe nonlinearities and increased degrees of freedom are involved in mechanical analysis.

### 3.6 Element rebirth technique

The element rebirth technique is performed to include the multi-pass welding effect. Using this technique, the element or elements simulating the filler metal deposit (weld elements) are generated with the FEA mesh for the weldment. Weld elements are divided into groups to numerically represent layers of weld beads. These weld elements are initially removed and activated for each corresponding weld pass to simulate the deposit of weld beads. In the heat transfer analysis of multi-pass welds, using the `MODEL CHANGE` command in ABAQUS [19], the filler metal of each pass is modeled by depositing it instantaneously just before the welding of each pass. When weld elements are activated, the node temperatures in weld elements have prescribed temperature distributions.

The element rebirth techniques are employed in all cases in Chapter 4.

### 3.7 Mismatch effects

#### 3.7.1 Thermal mismatch

When the initial prescribed temperatures of both the base metal and the weld metal are considered as room and melting temperatures, respectively, it is reasonable to consider thermal mismatch along the interface between the weld metal and the base metal in heat transfer analysis [7, 8]. Using interface elements between the base metal and the weld metal so that it can be made fully consistent as mesh size is refined to zero [7], an alternate method of the element rebirth technique is constructed. Therefore, the element rebirth technique with interface element is proposed for multi-pass welding.

The discretization methods for treating this technique available in ABAQUS are indicated in Figure 3.5. Figures 3.5 (a) and (b) show the difference of modeling with and without interface elements. Figure 3.5(a) indicates that the finite elements of the deposit (weld metal) are meshed with the elements of the workpiece (base metal), but one kept inactive until a special birth time (element birth). Figure 3.5(b) shows the finite elements of the weld are meshed as completely detached elements that interact with neighbors through the interface elements which behave as defined by the GAPCON user subroutine [19]. GAPCON subroutine is used to define conductance between contact surfaces or nodes in a purely heat transfer analysis. In the heat transfer analysis, using the GAPCON user subroutine, the weld metal of each weld pass is introduced into the weld preparation of the model prior to each pass. The element rebirth scheme cannot be consistent because

the weld element is born (activated) with nodes having the temperature assigned by the active neighbor element. To avoid the inconsistencies of the element birth procedure, the interface element technique provides an alternative. Elements with all nodes at the weld temperature can be defined at the beginning of the calculation. These nodes are thermally connected to their twins by a heat flux  $\dot{q}_{IFE}$  given by

$$\dot{q}_{IFE} = \chi (T_5 - T_3) \quad (3.7.1)$$

in terms of the gap conductance  $\chi$ . The gap conductance  $\chi$  is defined as a function of the clearance between bodies and the surface temperatures. The units of  $\chi$  are energy per time per area per temperature. As time elapses, this flux causes the twinned nodes to come to nearly the same temperature over a time scale of  $\frac{\rho C_p \Delta l}{\chi}$ . Here  $C_p$  is the specific heat of the metal and  $\Delta l$  is the mesh size of the elements. Large  $\chi$  shortens the transient time for the interface element temperature difference.

### 3.7.2. Mechanical mismatch

As Leung *et al.* [18] mentioned, in mechanical analysis, problems are created whenever one introduces the undeformed weld metal into the deformed weld preparation after the first weld pass. Reactivated elements are anticipated to reset to a virgin state (zero stress, strain, etc.) in their original geometry before they are activated. Ideally the weld metal shape, specified by the nodal coordinates, should reflect the change in weld

preparation geometry resulting from the accumulated displacements of the previous weld passes. To overcome this difficulty the weld preparation nodal displacements after each weld pass are applied to the weld metal of the next pass as a boundary condition prior to introducing the material. After the weld metal is inserted into the weld preparation, intermediate steps are used to remove these boundary constraints from the model and return the material properties to normal before further analysis. This technique necessitates that the stress analysis is stopped after each weld pass so that the weld preparation nodal displacements can be retrieved and applied to the boundary constraint for the weld metal of the next weld pass. The strain in reactivated elements corresponds to the total displacements of their nodes, not just the displacements since they are reactivated. To add unstrained elements to a strained model without requiring the same strain on both sides of the interface between the new and old elements, one must use separate nodes on the both sides of the interface between the new elements and the old elements, and the EQUATION and BOUNDARY, FIXED commands in order to couple the displacements of these nodes correctly, to give[19]

$$u_i^N = u_i^O - u_i^O|_0 \quad (3.7.2)$$

where  $u_i^N$  is the displacement in direction  $i$  on the new side of the interface;  $u_i^O$  is the displacement in direction  $i$  on the old side of the interface; and  $u_i^O|_0$  is the displacement in direction  $i$  on the old side of the interface at the time when the new elements are added. If the displacement of the extra degree of freedom is set to zero with the BOUNDARY

option, the displacements of the new elements conform to the displacements of the rest on the mesh.

Fortunately, the mechanical mismatch is solved. When the elements are activated by using the MODEL CHANGE, ADD, the reactivated elements are reset to an annealing state (zero stress, strain, plastic strain, etc.) in the configuration in which they lie at the start of the activation step [19].

The interface element technique, including the consideration of the mismatch effect, is discussed in Chapter 4.2. A three-pass welded plate is assumed. Two different models with the same geometries are generated. One is the model without interface elements, and the other is the model with interface elements between the base metal and the weld metal.

### 3.8 Generalized plane strain assumption

The plane strain assumption was founded to be unrealistically large tensile zone which increased as the plate thickness and weld passes were increased [6]. Therefore, the generalized plane strain assumption is implemented in this study to consider the strain of the cross section in welding direction.

A generalized plane strain theory is used in the stress analysis for the purpose of considering the strain to the cross section in the direction of the weld [1, 6, 62]. The generalized plane strain theory assumes that the model lies between two initially parallel

planes in the thickness direction. These planes may move as rigid bodies with respect to each other, so that the axial strains vary linearly throughout the cross section. The generalized plane strain concept is explained in Figure 3.6 [19]. The ABAQUS ten-node generalized plane strain elements are used in the stress analysis for the cases in Chapters 4.1.1 and 4.2. A generalized plane strain element has two extra nodes in addition to the original eight nodes. The first of these extra nodes has one degree of freedom, which is the change in length of the axial material fiber connecting this node and its image in the other bounding plane. The second of these extra nodes has two degrees of freedom, which are the components of the relative rotation of one bounding plane with respect to the other. These extra nodes define the motions of translation along the axial direction and rotation of the two bounding planes in the generalized plane strain model.

### 3.9 Lumping (Grouping) techniques

Several attempts have been made to develop numerically for welding residual stresses in multi-pass welded structures [18, 49, 50, 60, 62]. However, due to the complexity of the problem, the computations are very time consuming. Therefore, several simplifications have been made. In some references [49, 79], only some of the weld passes are considered. They reported that the last few weld passes govern the welding residual stress fields.

Some investigators have studied lumped pass modeling techniques. To reduce the computing cost, the idea of grouping one or two layers of weld passes into one lumped

pass was used. Rybicki *et al.*[49] studied multi-pass girth pipe welds by combining all passes in a layer into a single stress analysis sequence. They simulated two welded pipe models, a seven-pass and a thirty-pass. In the seven-pass welded pipe, four-layer welds up to two passes per layer were combined. Also, in the thirty-pass model, nine-layer welds up to a maximum of four passes per layer, were combined. Symmetry was assumed about the weld centerline so that only half of a pipe section was simulated in the analysis model. The computed residual stress results for both models agreed with the experimental data. Leung *et al.*[18] proposed an approach similar to that in Rybicki *et al.*'s investigation [49]. However, Leung *et al.* discussed the difficulty to predict the stress distribution about the weld centerline because the real weld is not symmetric about the weld centerline. To overcome this deficiency, Leung proposed a two-step procedure. This work was limited to an analysis of a small number of weld passes. Ueda *et al.*[60] also investigated the lumping technique with a narrow-gap welding analysis. They concluded that the number of welding passes for multi-layer welding of thick plates can be reduced. Lee [62] proposed a lumped pass model technique for improving efficiency. He used two models. The first model was referred to as 'RAMP 1'. In this model, the heat scanning times for each pass were summed, and the individual passes were averaged according to the magnitudes of heat flux. In the second model, heat flux magnitudes were accumulated, and heat scanning times were averaged. This model was referred to as 'RAMP 2'. Both models were analyzed to evaluate their efficiency and compared with the non-lumped model, and with experiment (see Figure 3.7).

Lumped pass models reduce computational cost with reasonable residual stress field, especially for a thick plate.

In Chapter 4.1, two lumping concepts are employed. 'RAMP 2' and 'RAMP 1' concepts are used in the cases in Chapters 4.1.1 and 4.1.2, respectively. In Chapter 4.1, the stress results using a 'RAMP 1' model, show better consistency than that of a 'RAMP 2' model whenever the results are compared with the results of the non-lumped pass model or the results of experiment.

### 3.10 Meshing

The mesh for the model is selected in accordance with recommended FEA practice. The elements are chosen and the mesh is developed to approximate the temperature and stress fields with acceptable accuracy, and to utilize the fewest number of elements. Since a butt-welded plate is symmetric about the weld centerline, only one half of the plate is modeled using symmetric boundary conditions. This reduces the number of elements by half and the computational time by more than one half. This symmetric model allows errors in the analysis of multi-pass welds, especially in weld areas where the sequence and position of weld passes are not exactly symmetric about the weld centerline.

In most analyses the model is set up with refinement of the mesh in the region of the heat source. This allows the large variation in temperatures, which occurs in this region, which is to be modeled accurately. However, a fine mesh increases the matrix

size. As a result, meshes are graded, so that larger elements are used in positions where the temperature gradient is small.

Small elements are used in the weld and HAZ where the temperature gradients would be expected to be the highest. The mesh size is increased away from the weld area because the temperature and stress fields tend to change slowly and linearly. From the previous experiences [1, 6, 62], the element size at the weld area should be smaller than, or equal to, the depth of the weld bead.

It is common to utilize the same FEA mesh for both the thermal and stress analyses. This eliminates the need for interpolating the temperature results from the thermal analysis to provide nodal input to the stress analysis. However, it is not necessary to use the same mesh for both analyses. It is prudent to develop a thermal mesh that provide also accurate results for the mechanical analysis. From Lee's [62] study, it is shown that the computational time required to perform a thermal analysis is considerably less than the time required for a mechanical analysis, when the same mesh is used for both analyses. This is due to the difference in degree of freedom and model nonlinearity. If the same mesh is utilized for both analyses, the thermal analysis mesh may be over refined.

On the basis of the transient analysis in ABAQUS [19], the user may choose either to specify the time increment or to use an automatic time increment. The automatic time increment scheme is based on the maximum temperature change allowed at any node during an increment. The relationship between the minimum usable time increment and the element size is

$$\Delta t > \frac{\rho C_p \Delta l^2}{6\kappa} \quad (3.10.1)$$

where  $\Delta t$  is the time increment, and  $\kappa$  is the thermal conductivity. If smaller time increments are required, a finer mesh should be used in regions where the temperature changes first occur. There is no upper limit on the time increment unless nonlinearities cause numerical problems.

THERMAL ANALYSIS

STRESS ANALYSIS

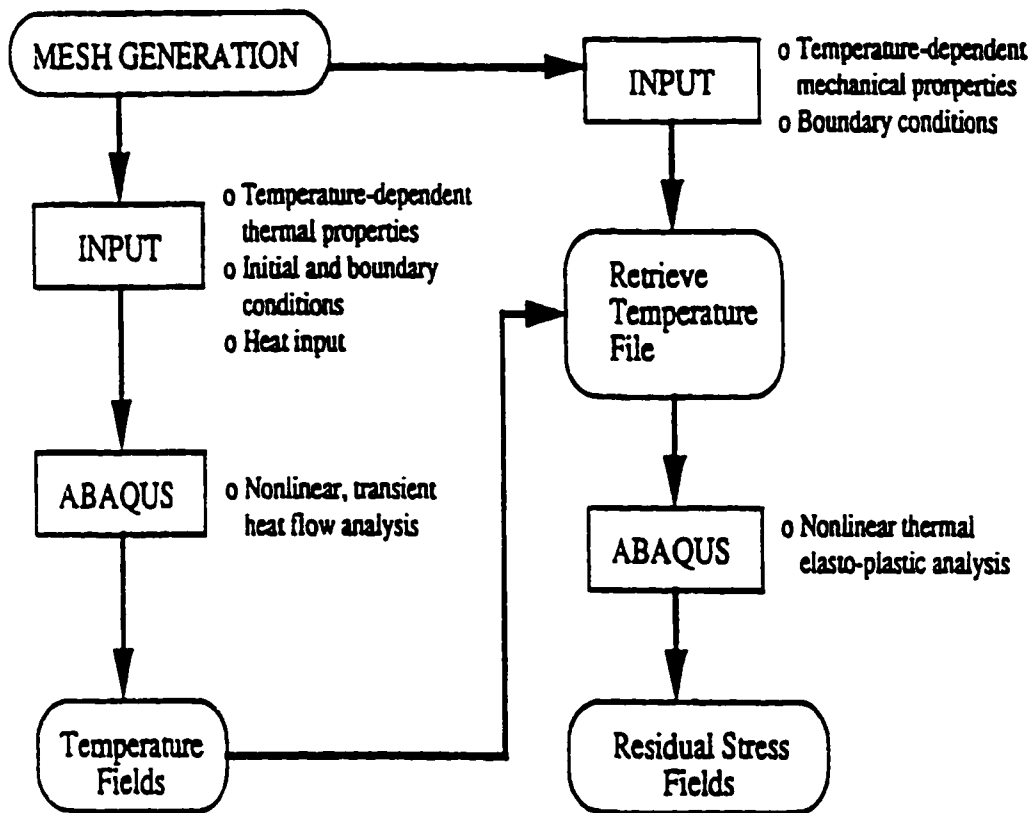


Figure 3.1 Numerical procedures for an uncoupled thermo-mechanical analysis [62]

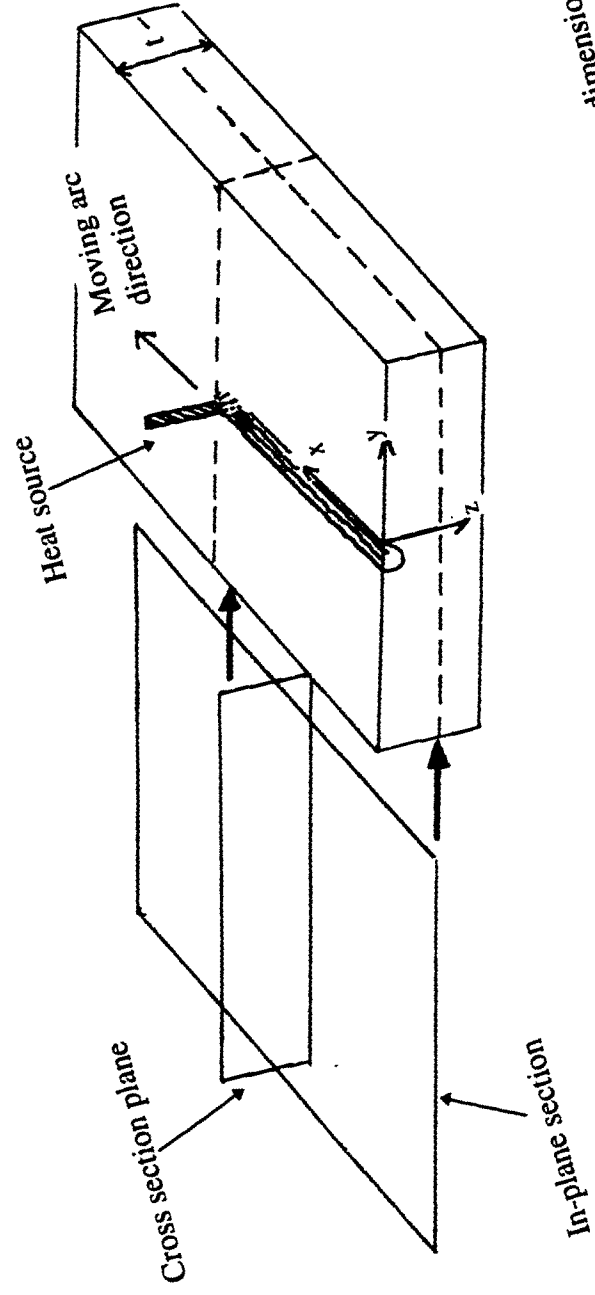


Figure 3.2 Definitions of Cross-sectional plane model and In-plane section model in two-dimensional analysis

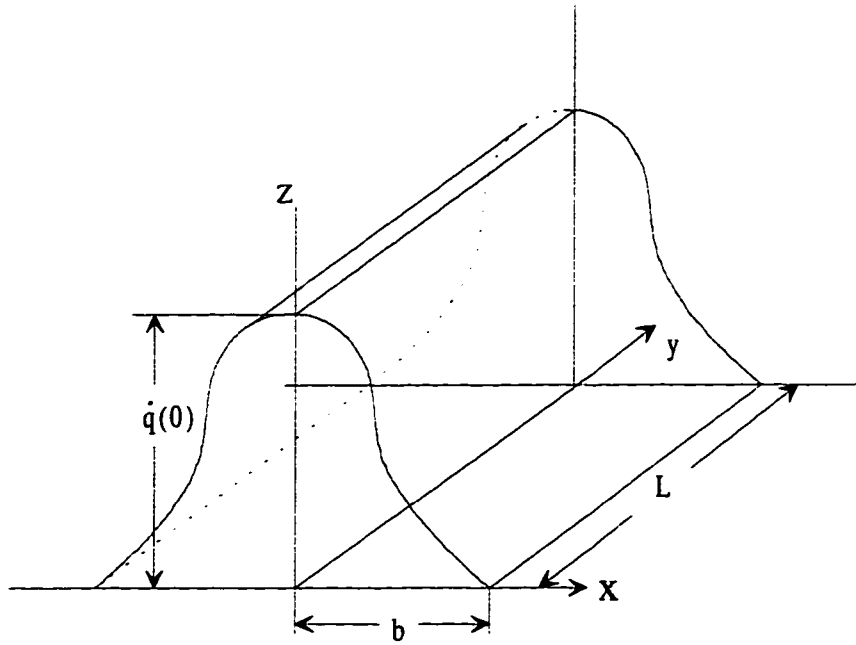
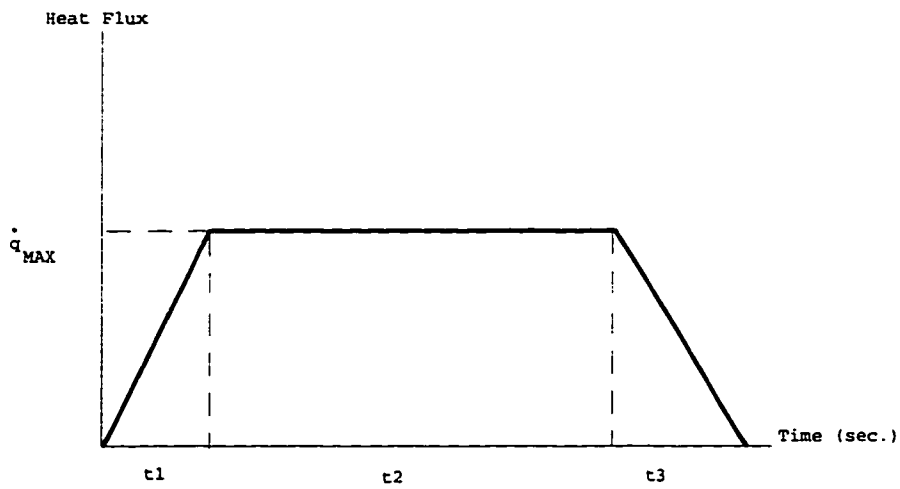


Figure 3.3 Modified Gaussian heat input scheme



t1: Initial Ramp Time  
t2: Maximum Ramp Time  
t3: Decaying Ramp Time

t1+t2: Actual Heat Scanning Time during Welding  
% Ramp Time =  $t1/(t1+t2) \times 100$

Figure 3.4 Shape of ramp heat input function

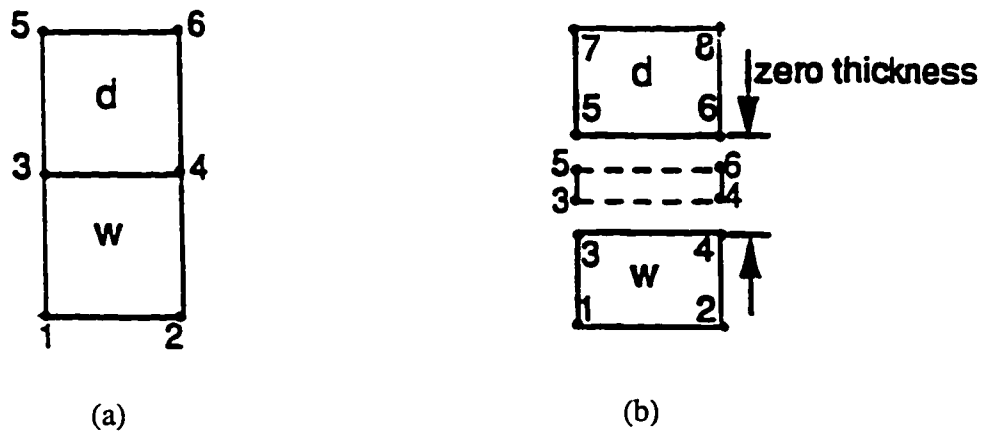


Figure 3.5 Two schemes of discretization for weld deposit(d) and workpiece(w) materials [7]  
 (a) Element rebirth (use \*MODEL CHANGE)  
 (b) Interface element shown schematically with broken line (use \*GAPCON user subroutine)

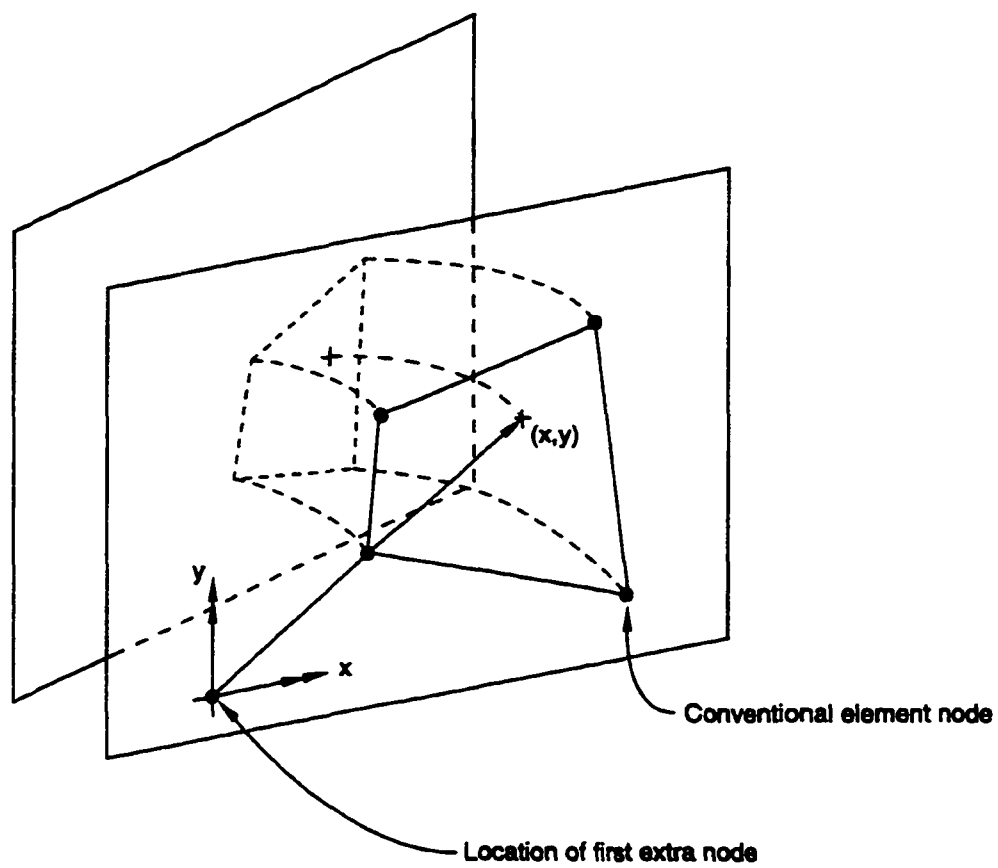
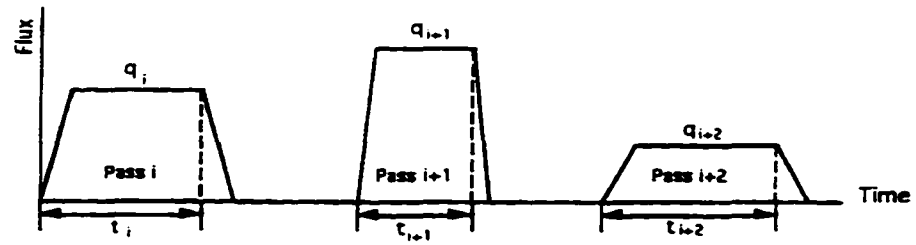
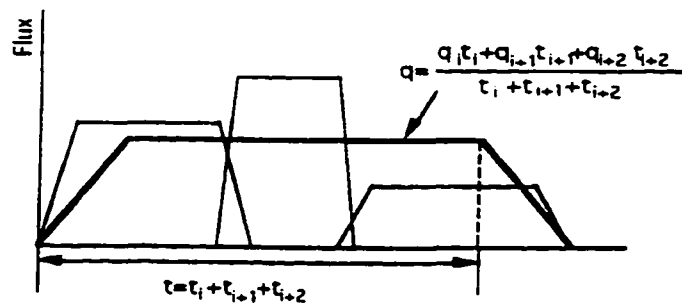


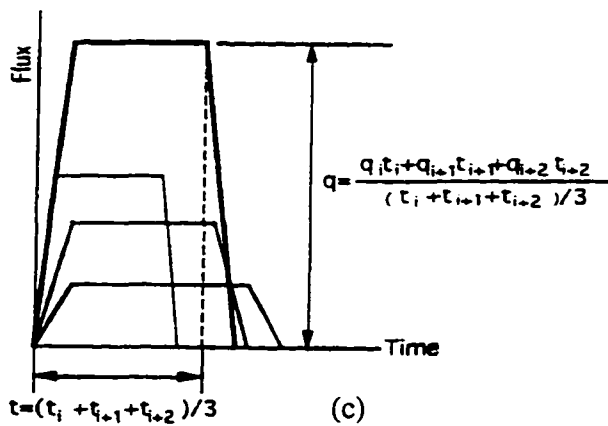
Figure 3.6 Concept of the generalized plane strain theory [19]



(a)



(b)



(c)

Figure 3.7 Definition of ramp functions of heat input before and after lumping [62]

- (a) Ramp functions of welding passes before lumping
- (b) Ramp function after lumping (RAMP 1)
- (c) Ramp function after lumping (RAMP 2)

## CHAPTER 4

### ASSESSMENTS OF NUMERICAL PROCEDURES

In this chapter, three different models are investigated. In Chapter 4.1, the first two models are used for studying the lumping technique. In Chapter 4.2, the third model is used for studying the interface element technique. The models of each cases are considered as multiple weld pass structures. Therefore, the element rebirth technique is employed for the numerical simulation of the models. As mentioned in Chapter 3, all cases employ the new modified Gaussian heat input for heat transfer analysis. Also, the generalized plane strain condition is considered for mechanical analysis in 2-D plate cases.

In Chapter 4.1.1, a five-pass welded plate is considered. The 'RAMP 2' lumping technique is introduced to reduce computational time. Therefore, the model is reduced to a three-weld pass model. The results by using the lumping technique are compared with those by using the non-lumping modeling technique. In Chapter 4.1.2, a six-pass girth welded pipe model is studied. The 'RAMP 1' lumping technique is tried. The results using the lumping technique are compared with experimental data. The effective lumping

technique is determined by comparing the results of the lumping techniques to the results of the non-lumping technique. In addition, these results are compared with the experimental results. Also, the thermal input insensitivity for stress analysis is observed. Four different heat inputs are given and the results are compared with each other and with the experiment.

In Chapter 4.2, a three-pass welded plate is considered for studying the interface element technique. Two welded plate model with the same geometries are considered for investigating the interface element technique. One model includes interface elements between base metal and weld metal. The other model does not include interface elements between base metal and weld metal. The advantages and disadvantages of the interface element technique are discussed by comparing the results with and without the use of the interface element technique.

#### 4.1 Lumping modeling techniques

Two different lumping techniques are studied. 'Ramp 1' and 'Ramp 2' lumped modeling techniques are employed the models in Chapters 4.1.1 and 4.1.2.

#### 4.1.1 Five-pass welded plate (Non-lumping and lumping modeling techniques)

##### 4.1.1.1 Model definition

A five-pass model is considered. This model is the same as one of the FEA models by Shim *et al.* [6]. Also, the lumped pass theory is applied to the model, and thus the five-pass model is reduced to a three-pass model. The model is considered as a full model because the geometry of the weld is not symmetric around its centerline. The material properties used are for ASTM A36 mild steel. Temperature dependent thermal and mechanical properties are shown in Figure 4.1 [6]. The initial temperature distributions of both the base and weld material for each weld pass are a uniform 70° F, i.e., at room temperature. The maximum allowable temperature change between time increments employed is 300° F.

The modeling of thermal and residual stress analyses is as follows:

- 1) Thermal model : Heat flow in the welding direction is neglected to reduce the problem to a 2-D analysis. Therefore, heat flow is limited to a cross section perpendicular to the welding direction.
- 2) Lumped model: A lumped pass model is used to reduce the total number of weld passes to be simulated.
- 3) Mechanical model: The cross section in the welding direction is used for a 2-D analysis. According to CHAPTER 3, the generalized plane strain assumption is implemented.

The 2-D full model is used for both the thermal and stress analyses. Identical FEA meshes and time steps are employed. ABAQUS is used for both the transient temperature distribution and the corresponding residual stress analysis. I-DEAS, a commercial pre- and post-processor, is used for mesh generation. Quadratic rectangular elements are used for both thermal and mechanical models.

The experimental data for the transient temperature distribution and stress are drawn from Shim *et al.* [6] and Tsai *et al.* [2], respectively.

#### 4.1.1.2 Finite element modeling

The model used is a one half inch thick plate with a single bevel preparation. The size of the model is 15 inches x 8 inches. GMAW is simulated. Pass sequence and welding parameters are shown in Table 4.1.

The heat transfer and stress analyses of weldments are nonlinear and time dependent. An uncoupled thermo-mechanical analysis is performed in which the thermal analysis is performed first, and the temperature history from that analysis is stored and used as a thermal loading input for the subsequent stress analysis. The FEA mesh, and time steps are identical for both the heat transfer analysis and the stress analysis. The material properties used are for ASTM A36 mild steel. The temperature dependent thermal properties are shown in Figure 4.1(a). The thermal conductivity decreases almost linearly from room temperature to 1500° F. Beyond this temperature, it increases slightly. The specific heat increases almost linearly in the whole temperature range from

room temperature to the melting point. The change of the conductivity and specific heat in the molten pool is not considered. In most metal, melting and solidification occur within a known temperature range between the solidus temperature and the liquidus temperature. The effect of latent heat on fusion, which is defined to be the internal energy change during melting or solidification, is considered. Table 4.2 shows the temperature dependent thermal properties used, the constants for the convection heat loss coefficient, and the arc efficiency.

Free convection boundary conditions are assumed for all exposed plate surfaces. A constant value for the heat loss coefficient is assumed for all surfaces (see Table 4.2). Other heat loss mechanisms such as radiation and forced convection due to shielding gas are neglected. These terms become significant when studying the behavior of a molten pool where high temperatures exist beyond melting, but are not significant for residual stress and distortion simulation. Similarly, radiation and convection influences on the microstructures and cooling rates of weld metal, as well as heat losses or gains from phase transformation are neglected.

The mechanical and physical properties of yield stress, elastic and plastic modulus, and the thermal expansion coefficient are considered temperature-dependent in the stress analysis. Figure 4.1(b) shows the mechanical properties of ASTM A36 steel. Both the elastic modulus and yield stress decrease with increasing temperature. Figure 4.1(b) shows how mild steel loses strength at an accelerated rate above 1000° F and, therefore, the contribution to residual stress due to temperatures above 1000°F is

expected to be small. Mechanical properties are assumed constant above 1400°F. The thermal expansion coefficient is also temperature-dependent. As shown in Figure 4.1(b), the thermal expansion coefficient increases almost linearly from room temperature to 1200°F.

An isotropic hardening plasticity model in ABAQUS [19] is used. This allows the process to involve large plastic strain. Plastic modulus is the slope of the linearized stress-strain curve in the plastic zone and is temperature-dependent. The data is plotted in Figure 4.2. Two slopes for plastic modulus are applied in the plastic zone. Figure 4.2 shows strain hardening at room temperature. The plastic modulus at high temperature is calculated using yield stress at corresponding temperature and strain hardening values. The temperature-dependency of Poisson's ratio is neglected. Therefore, a constant value of 0.3 is used for ASTM A36 steel.

Free boundary conditions are assumed for all free surfaces. Volume changes due to phase transformations are neglected during stress analysis. Initial stresses and strains used are zero.

The 2-D FEA meshes used for both heat transfer and stress analyses are shown in Figure 4.3. The area with oblique lines represents the layers of weld bead as determined by the actual weld beads shown in Figure 4.3. The number of elements for the model is about 300.

To include the filler metal effect, the element rebirth technique is performed. In using this technique, the elements simulating the weld metal with the FEA mesh are generated for the base metal.

The simulation is done in 3 parts: thermal model, lumped model and mechanical model.

### Thermal model

Because heat flow is limited to the cross section perpendicular to the welding direction, the problem is reduced to a 2-D model. The elements representing each weld layer are initially removed and activated for each corresponding weld pass to simulate the deposit of the weld beads. A heat flux is applied to the top surface of these newly activated elements. Initial temperature distributions of base and weld metal are assumed as room temperature. For accuracy of analysis, small time increments are used. The eight-node rectangular elements are used for thermal analysis. The temperature data for each time increment is saved as input to the stress analysis. An arc efficiency of 85% is used for the net heat input to the plate. Two different heat fluxes are considered. One heat flux is uniformly distributed over the length of each weld layer. The other one is followed by the modified Gaussian distributed heat flux (Equation (3.3.8)) over the length of each weld. Only surface heat fluxes are applied in both models. The general amplitude-time curve shape for the ramp input mode is shown in Figure 3.4. A ramp time consisting of 20% of total heat input time is used. The total area under the ramp heat curve is kept constant to insure that the same total heat input to the model is maintained. Elapsed time between weld passes is assumed to be 1,000 to 10,000 seconds, which is long enough time to return the temperature of the weldment and the base plate to room temperature.

### Lumped model

A lumped pass model is effectively used to reduce computational time. In this study, a five-pass welded model is considered. The first model assumed that the heat flux of each weld pass is distributed over the top surface of one layer of weld bead (see Figure 4.3(a)). The result of this temperature analysis is repeated for each pass to complete one layer. A lumped pass model is used for the second model. Each layer of weld bead is considered as one lumped pass. Heat fluxes for each pass in that layer are added and distributed over the top surface of the layer. The 'RAMP 2' model by Lee [62] is employed. A total of five-weld passes are lumped into three passes in this model (see Figure 4.3(b)).

### Mechanical model

Residual stresses are the final internal stresses accumulated during welding. Therefore, a complete history of the temperature distribution throughout the plate is required for the calculation of residual stresses. A generalized plane strain state theory is used for the stress analysis to consider the strain of the cross section in the direction of welding. ABAQUS ten-node generalized plane strain elements are used in the stress analysis. Volume changes due to phase transformation are neglected. Initial stresses and strains are assumed to be zero. On the basis of the study by Lee [62], mechanical boundary conditions are determined. The boundary conditions are shown in Figure 4.4.

#### 4.1.1.3 Results

##### Thermal analysis

The transient temperature distributions for the first pass at a 1/4 inch and a 1/2 inch from the centerline on the top surface are shown in Figures 4.5 (a) and (b). The experimental results [6] are compared with numerically calculated values of two types of heat flux models, i.e.; the constant heat flux model and the modified Gaussian heat flux model. The predicted temperature distributions agree with the measured ones. This is particularly true if a modified Gaussian distribution of surface heat flux is used.

##### Stress analysis

The schematic illustration for the definitions of transverse and longitudinal directions, with respect to the weld direction, is shown in Figure 4.6. Figure 4.7(a) shows the transverse (perpendicular to welding direction) stresses on the top surface of the plate after finishing the final weld pass. A total of five passes are lumped into three passes. The results of the five-pass model (non-lumped) and the three-pass model (lumped) are compared. Also, the numerical results are compared with the measured one [2]. The stress is measured much higher than those of numerical ones. The discrepancies between three-pass and five-pass models appear to be significant near the weld toe. The three-pass model predicts lower stresses than the five-pass model and has larger tensile stress zone than that of the five-pass model since it introduces much higher heat content to the

weldment. The discrepancies become less significant away from the weld toe. Figure 4.7(b) shows the same results for the bottom surface.

Figure 4.8(a) shows the longitudinal (welding direction) stresses on the top surface of the plate after finishing the final weld pass. The three-pass model shows higher compressive stresses outside the weld, lower tensile stresses inside the weld, and larger tensile stress zone around the weldment when compared with the five-pass model. The stresses are compared with the experimental one [2]. The measured stress shows good agreement with the numerical results. Figure 4.8(b) shows the same results for the bottom surface.

Figures 4.9 (a) and (b) show the through-thickness transverse and longitudinal stress variation at 2/5 inches from the centerline, respectively. In transverse stress, general trends are similar for both models, but the stress variation of the five-pass (non-lumped) model is larger than the three-pass model. The tensile transverse stresses at both surface areas are balanced by the compressive stress in the middle of the plate. The sizes and locations of the compressive stress zone for both cases are identical. For longitudinal stress, the general trends are similar for both models, whereas the stress of the five-pass model in the middle of the plate is smaller than the three-pass model. In both transverse and longitudinal stress distributions, all stresses of models show positive values. Both transverse and longitudinal stress distributions show that maximum tensile stress exists near the surface of the plate and gradually decreases to the middle of the plate.

Figures 4.10 to 4.13 show the transverse and longitudinal stress distribution on the top surface after each pass. These figures show trends for both stress distributions to be

similar for each pass. After the second pass, the stress distribution becomes almost the same as the fifth pass. This means that the residual stress distribution is determined during initial passes.

#### 4.1.2 Six-pass girth welded pipe (Lumping technique)

##### 4.1.2.1 Model Definition

A six-pass girth welded pipe model is selected. This model is the same as one of the FEA models by Brust *et al.* [80] (Figure 4.14). The lumped pass theory is applied to the model, and then the six-pass weld is reduced to three-weld layers. The model is considered as a half model because of symmetry along the weld centerline. 304 stainless steel is selected, and the temperature-dependent material properties are shown in Figure 4.15. The initial temperature distributions of the base and weld material for each weld pass are 70° F, i.e., at room temperature, and 2500° F, i.e., at melting temperature. The maximum allowable temperature change between the time increments employed is 300° F.

The 2-D axisymmetric half model is used for both the thermal and stress analyses. Identical FEA meshes and time steps are employed. ABAQUS is used for both the heat transfer and the corresponding residual stress analyses. I-DEAS, a commercial pre- and post-processor is used for mesh generation. Quadratic rectangular axisymmetric elements are used for both thermal and mechanical models.

The experimental and reference data for stress distribution are drawn from Brust *et al.* [80].

#### 4.1.2.2 Finite element modeling

The pipe geometry is 6.0" inner radius, 0.375" wall thickness, and 10.0" long. The weld-pass sequence and welding parameters are indicated in Table 4.3.

The heat transfer and stress analyses of weldments are nonlinear and time dependent. An uncoupled thermo-mechanical analysis is performed. The FEA mesh, and time steps are identical for both the heat transfer analysis and the stress analysis.

From Figure 4.15, the mechanical and physical properties of yield stress, elastic and plastic modulus, Poisson's ratio, and the thermal expansion coefficient are considered temperature-dependent in the stress analysis. Both the elastic modulus and yield stress decrease with increasing temperature. The elastic modulus decreases almost linearly in range from room temperature to about 1400° F and then drops to almost zero value rapidly at about 2000° F. The yield stress decreases almost linearly from 34 ksi to near-zero value. The plastic modulus for isotropic hardening also decreases according to temperature increase. The thermal expansion coefficient increases from room temperature to 2000° F. Poisson's ratio increases and decreases with temperature increase. The range of Poisson's ratio is 0.23 to 0.32.

Symmetric boundary conditions are used along the weld centerline and free boundary conditions are assumed for other free surfaces. Volume changes due to phase transformations are neglected during stress analysis. Initial stresses and strains used are zero.

The 2-D axisymmetric FEA meshes used for both heat transfer and stress analyses are shown in Figure 4.14. The number of elements for the model was about 290.

The simulation is done in two parts: thermal model and mechanical model. Lumping techniques are assumed in both analyses.

### Thermal model

The elements representing each weld layer are initially removed and activated for each corresponding weld pass to simulate the deposit of the weld beads. A heat flux is applied to both the top surface and the volume of these newly activated elements. The surface heat input is followed by the modified Gaussian distributed heat flux (Equation 3.3.8)) over the length of each weld and, the body heat input through the element volume is a constant heat flux. The four node axisymmetric elements are used for thermal analysis. The analysis is accomplished for three-layer lumping passes. The 'RAMP 1' model [62] is employed for using the lumping technique.

As mentioned in Chapter 3, the residual stress is not very sensitive to the details of the temperature distribution. The temperature insensitivity is evaluated in this chapter. Four different heat inputs and two different initial temperature conditions are assumed for the cases of the pipe model. Two different initial conditions are used for the weld metal:

one is room temperature, and the other is melting temperature. The combinations of heat inputs and initial temperature conditions are shown in Table 4.4.

### Mechanical model

Four-node axisymmetric elements are used in the stress analysis. Volume changes due to phase transformation are neglected. Initial stresses and strains are assumed to be zero. The boundary conditions are used for a symmetric model.

#### 4.1.2.3 Results

Figures 4.16 to 4.17 show the stress distributions along inner and outer surfaces with different heat inputs indicated in Table 4.4. The stress distributions in Cases 1, 2 and 4 show similar trends along inner and outer surfaces. However, Case 3 shows the deviation of the stress distributions along the surfaces. This deviation seems to be caused by the magnitude of the heat inputs. In these four Cases, the heat inputs consist of the surface flux and the body flux. The body flux used is dominant, compared with the surface flux. The body heat input, given properly, plays an important role in making the size and the shape of the fusion zone in the model identical to the size and the shape of the fusion zone during the welding numerical analysis. Therefore, the change of the fusion zone size and the shape affect the residual stress distributions. If the fusion zone size and shape are not changed much with respect to the heat input magnitudes, the residual stress distributions are almost identical. However, in excessive amounts, the

body heat input widens the size of the fusion zone and changes the shape of the fusion zone. This results in a change in the residual stress distributions. As seen in Figures 4.16 and 4.17, even though the applied heat inputs are not the same, similar trends of the stress distributions are observed in Cases 1, 2, and 4. This means that the fusion zone sizes are almost the same as the given weld size. In Case 3, however, the fusion zone size is bigger than the given weld size due to excessive (very high) heat input when the weld elements are activated.

As mentioned in Chapter 3, the residual stress distributions are not sensitive to the heat input magnitudes. However, if the heat input magnitude becomes too high and exceeds a certain range, the size and shape of the fusion zone changes and, consequently, the residual stress distribution also changes.

The distortion results of two points are shown in Figure 4.18. These results are same for the heat inputs in the stress analysis. The selected Nodes 1 and 5 are indicated in Figure 4.14. The location of Node 1 is 0.375 inch from the weld on the inner surface of the pipe and the location of Node 5 is 5 inches from the weld on the top surface of the pipe. The distortion histories of these points, during the welding process, show the differences. As the residual stress distributions for Cases 1, 2, and 4 show similar trends, the corresponding distortion histories are similar to each other for Cases 1, 2 and 4, respectively. However, the distortion history for Case 3 deviates from the other cases. This is caused by the heat input magnitude. The heat input magnitude becomes too high and exceeds a certain range, the size and shape of the fusion zone changes and, consequently, the distortion history changes.

The distortion is also insensitive to the heat input magnitude, if the fusion zone size and shape are given properly. However, the distortion is a little bit more sensitive than the residual stresses with respect to the heat input magnitude.

Stress distributions from Case 1 are selected for comparison with experimental data [80]. Figures 4.19 to 4.20 show the stress results from the experiment and FEM. In these Figures, 'Battelle Code' means the results from using the in-house code provided by Battelle Memorial Institute [80]. The calculated stress distributions show reasonable agreement with experimental data. Figures 4.19 (a) and (b) show the residual axial stress distributions along the outer and inner surfaces, respectively. In Figure 4.19(a), the FEA results show distributions of stress with higher values than those obtained from experiment and from the Battelle code. In the fusion zone the FEA results show considerably lower values than those obtained from the experiment. The FEA results start at very low tensile values (below 5 ksi) and then jump up to around 48 ksi beyond the fusion boundary before they start to decrease. The stresses decrease rapidly beyond 0.8 inch from the weld centerline and changed to compressive around 1.25 inch from the weld centerline. Because there is very little experimental data, it is hard to tell whether the FEA results match the experimental results. In Figure 4.20(b), FEA results show values a little bit lower than those from the experimental values. The FEA results show good agreement with the experimental values on the inner surface. The FEA results show compressive values (-25 ksi) inside the fusion zone. The residual stresses change to tensile at 1.25 inch beyond the weld centerline.

Figures 4.20 (a) and (b) show the residual circumferential (hoop) stress distributions along the outer and inner surfaces, respectively. In Figure 4.20(a), FEA results follow the experimental results. The FEA results vary from compressive to tensile twice and finally become compressive. In Figure 4.20(b), the FEA results show reasonable agreement with the experimental ones. The FEA stresses show high tensile values (50 ksi) inside the fusion zone. Beyond the fusion boundary, the values stay around 40 ksi and decrease rapidly around 0.9 inch from the weld centerline. After that they become compressive around 1.1 inch from the weld centerline.

Finally, using 'RAMP 1' lumping technique, the FEA results show reasonably good agreement with the experiment.

## 4.2 Effect of interface mismatch

### 4.2.1. Model definition

The models provided here are three-pass welded plate. The objective is to show the effect of the interface element technique. Two models are provided; one model is generated by using the concept of the element rebirth technique that is employed in Chapters 4.1.1 and 4.1.2, and the other, is generated by using the concept of the element rebirth technique with the interface elements. The two models have the same geometries and the same mesh size. The only difference is whether or not in heat transfer analysis interface elements between the weld elements and the base metal elements exist.

#### 4.2.2 Finite element modeling

The FEA model is a three-pass welded plate (Figure 4.21). As with Chapter 4.1, the same material properties are used. Also, the modified Gaussian heat input model and generalized plane strain condition are considered. The full model is given. The geometry of the model is 15" wide x 0.5" high. The each weld size is 0.25" wide x 0.125" high. An eight-node quadrilateral element is used. The number of total elements is almost 550.

##### Thermal model

In order to consider the mismatch effect between base metal and weld metal, two different initial temperatures are considered. They are the melting and the room temperatures, respectively.

The heat transfer between weld metal and base metal occurs mainly by heat conduction. When the interface elements between base metal and weld metal are employed, the heat transfer is controlled by the gap conductance. The gap conductance is defined by the temperature differences between contact nodes and/or the clearance between the bodies. Therefore, because the gap has a vary small value (almost zero), the conductance becomes very large. When the value of the heat conductance is large enough, the heat transfer becomes very smooth. This means that the heat transfer histories, with a large gap conductance value, look similar to the heat transfer histories without interface elements. Therefore, the heat transfer of the model having the interface

elements with large heat conductance becomes identical to the heat transfer of the model without interface elements.

### Mechanical model

During the mechanical analysis, the model should be modified a little bit. The interface elements between the weld metal and the base metal are not useful anymore. Therefore, the interface elements should be removed. In order to represent the behavior between the weld metal and the base metal, the concept of the multiple point constraints (MPC) is employed [19]. This option allows constraints to be imposed between the different degrees of freedom of the model. One of the functions of MPC is to make all active degrees of freedom equal at two nodes. This function is very useful to establish a relationship between those adjacent nodes which have the same location on the interface between the weld metal and the base metal. Using the thermal analysis results, the mechanical stress analysis is completed.

### 4.2.3 Results

#### Thermal analysis

The transient temperature histories of Node 5 (located at the weld centerline on the bottom surface) and Node 157 (0.25 inch from the weld centerline on the top surface) are shown in Figure 4.22. A large value of thermal conductance is used. Therefore, the temperature histories are almost identical in each model during the first pass (Figure

4.22(a)). During the whole weld pass sequence, the temperature histories are identical in each model (Figure 4.22(b)). This means that the heat transfer histories look similar to the heat transfer histories without interface elements.

With regard to computer performance, the CPU time on an IBM work station is not much different in each model (Table 4.6). When the conventional modeling technique is used, the CPU is 212.8 sec., while the CPU is 209.7 sec. when the interface element technique is used.

### Residual stress analysis

Residual stress distributions are shown in Figures 4.23 and 4.24. The residual stresses distributions are obtained along the top surface and through the thickness direction.

Figure 4.23(a) indicates the residual transverse stresses along the top surface. Stress variation without interface elements is bigger than that with interface elements inside the fusion zone. At the boundary between fusion zone and base metal zone (0.125 inch from weld centerline), the case with the interface element shows less stress variation. After this boundary, the stress distribution with the interface element is a little bit higher than that without interface element.

Figure 4.23(b) indicates the residual longitudinal stresses along the top surface. As shown in Figure 4.23(a), a similar stress variation is observed inside the fusion zone and at the boundary between the fusion zone and the base metal. Beyond the boundary, the stresses with the interface element are a little bit higher than those without the

interface element. However, the stresses without the interface element are higher than those with the interface element beyond 1 inch from the weld centerline. The differences between stresses with and without interface element are about 5 ksi. The tensile stresses inside and near the fusion zone shows good agreement in each model.

Figure 4.24 (a) and (b) show the residual transverse and longitudinal stresses through-thickness direction (0.25 inch from the weld centerline). As shown in Figures, there is not much difference in the stress distributions with or without the interface element. The transverse and longitudinal stresses with the interface element are almost identical with those without the interface element. However, when the CPU times are compared, there is a big difference (Table 4.6). When the conventional modeling technique is used, the CPU time on an IBM work station is 708.5 sec., while the CPU time is 491.6 sec. when the interface element technique is used. When the interface element technique is used, the CPU time is reduced to 30.6 % of that for the mode without interface elements.

### Distortion

The pick-up point for checking the distortion is at the end of plate (7.5 inch from the weld centerline on the top surface). In Figure 4.25, the distortion in the y-direction without the interface element gives a value bigger than that with the interface element. The final distortion with conventional method was 0.4418 inch, while the value was 0.2319 inch with interface element technique (Table 4.6). The distortion value is reduced by around 50 % when the interface element technique is employed. In general, the

distortion is underestimated in most numerical analysis. In Chapter 4.1.2, the distortion histories are compared with different heat inputs and initial conditions. If the heat input magnitudes are reasonable, the final distortion values are not much different. Therefore, the distortion results with the interface element technique are not adequate for distortion modeling.

### 4.3 Discussion

FEA models are developed for analysis of residual stresses and distortion in multi-pass welding of plate and pipe. In all cases, the modified Gaussian distributed heat input model and lamp heat input model are implemented. Also, in plate model cases, the generalized plane strain state assumption is employed for mechanical analysis.

In Chapter 4.1.1, geometric unsymmetry around the weld centerline in the plate model is treated by constructing the full FEA model. The material properties of both base and filler metal are kept identical, and the initial temperature distributions of both base plate and filler metal correspond to room temperature. Temperature distributions from the numerical analysis agree closely with experimental results. The mechanical model shows reasonable stress distribution in both transverse and longitudinal directions. The lumped model (RAMP 2) is developed to reduce the computational time and cost for thermal and stress analyses. Each layer of weld bead is considered as one lumped pass. Therefore, a five-pass model is reduced to a three pass model. The results of the five-

pass model (non-lumped) are compared with the three-pass model (lumped). The results from the lumped pass model show reasonable stress trends. The lumped pass model shows higher compressive stresses outside the weld, lower tensile stresses inside the weld, and a larger tensile stress zone around the weld when compared with the non-lumped model.

In Chapter 4.1.2, the axisymmetric model is performed for the pipe model. Using geometric symmetry, a half model is used. The lumped technique 'RAMP 1' introduced by Lee [62] is employed. Therefore, a six-pass model is reduced to a three-pass model. The material properties of both base and filler metal are kept identical, and the initial temperature distributions of filler metal correspond to those of room and melting temperatures, respectively. Axisymmetric elements are used for both heat transfer and mechanical analyses. The residual stress distributions for axial and circumferential direction along inner and outer surfaces are calculated by using lumping techniques. Heat input Cases 1 to 4 show that the residual stress distributions are not sensitive to the heat input magnitudes. However, when the heat input magnitude becomes so high, as to change the size of the fusion zone, the residual stress distributions also change. Similar to the stress distributions, the distortion is also insensitive to the heat input magnitude, if the fusion zone size and shape are given properly. However, the distortion is a little bit more sensitive than the residual stresses with respect to the heat input magnitude. 'Ramp 1' lumping model, within residual stress distributions show reasonable agreement with experimental data.

According to Chapter 4.1, the 'Ramp 1' lumping technique shows better results than that of 'Ramp 2' compared with the results by the non-lumping technique or with the results by experiment. When the 'Ramp 2' technique is used, excessively high heat input during simulation easily make the anticipated fusion zone bigger, and as a result, this can cause a deviation away from the other residual stress distributions. It is important to make identical to the size and the shape of the fusion zone in the model, and the size and the shape of the fusion zone during the welding numerical analysis.

In Chapter 4.2, three-pass welded plates are considered. The models employ two different modeling techniques. One is the conventional element rebirth technique, the other is the interface element technique. The models have the same geometries and the same simulation conditions except that in one the interface elements are absent while in the other the interface elements are present between the weld metal and the base metal. More effort is needed to model the latter than the former. The stress distributions are not much different from each other and the anticipated distortion of the model with the interface elements are much smaller than those of the model without interface elements. Therefore, if the residual stress analysis is focused on , using the interface element technique, better computer performance is obtained. This means that using the interface element technique requires less CPU time than using the conventional method. However, the distortion histories show considerable differences. The distortion history using the conventional method is much bigger than that using the interface element technique. Because the distortion is underestimated in most numerical analysis compared with the

experimental one, the distortion results obtained with the interface element technique are not accurate enough for the prediction of distortion.

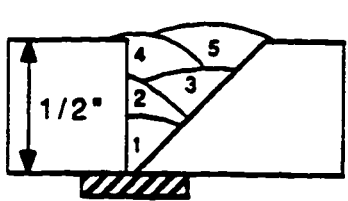
Pass sequence	Pass No.	Welding parameters		
		Current (Amp.)	Voltage (V)	Speed (IPM)
	1	215	24	14.4
	2	205	25	14.4
	3	215	26	14.4
	4	210	24	14.4
	5	210	24	14.4

Table 4.1 Pass sequences and welding parameter of each pass for a five-pass welded plate [1]

Properties	Data used for numerical analysis
Density (lb/in <sup>3</sup> )	.283
Latent heat (Btu/lb)	117.
Liquidus temperature (°F)	2770.
Solidus temperature (°F)	2700.
Film coefficient (Btu/in <sup>2</sup> °F)	0.00001
Initial temperatures for base metal and weld metal (°F)	70.
Percent heat input (%)	85.

Table 4.2 Temperature-independent material properties and initial conditions for a five-pass welded plate model

Pass No.	Layer No.	Welding parameters	
		Heat input (KJ/mm)	Speed (mm/s)
1	1	.88	1.57
2,3	2	.45	8.13
4,5,6	3	.45	8.13

Table 4.3 Pass sequences and welding parameters of each pass for a six-pass girth welded pipe model [80]

CASE	Percent heat input (%)	Fractions		Prescribed temperature conditions	
		Surface heat flux	Body heat flux	Weld metal	Base metal
Case 1	72	.11	.89	Melting temperature	Room temperature
Case 2	38	.05	.95	Melting temperature	Room temperature
Case 3	135	.11	.89	Room temperature	Room temperature
Case 4	100	.11	.89	Room temperature	Room temperature

Table 4.4 Combination of heat inputs for a six-pass girth welded pipe

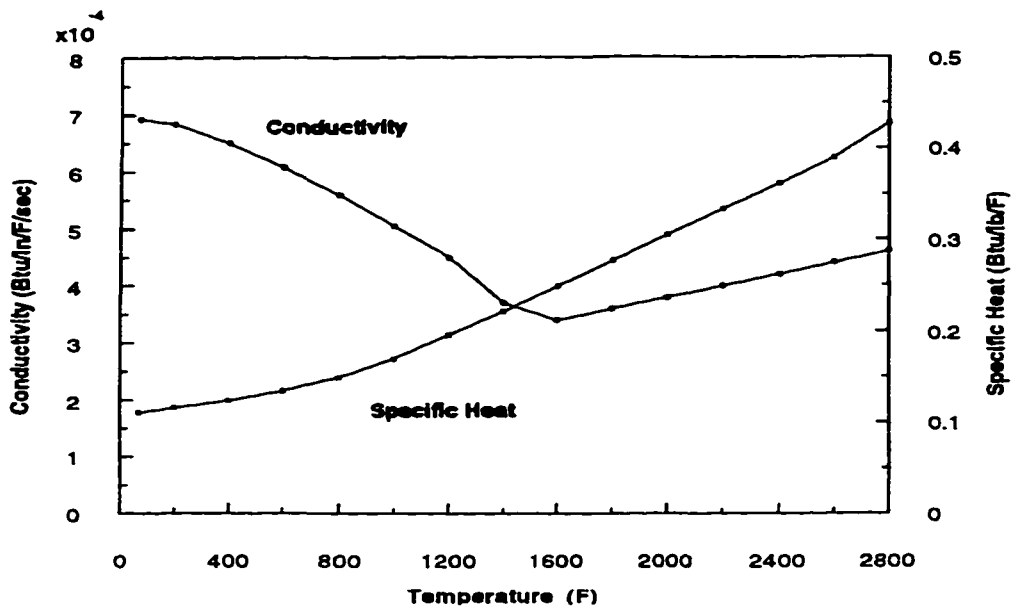
Pass sequence		1st pass	2nd pass	3rd pass
Current (Amp.)		215	215	215
Voltage (V)		24	24	24
Welding speed (IPM)		20	20	20
Percent heat input (%)		60	60	60
Initial temperature conditions (°F)	Base metal	70 (Room temperature)	70	70
	Weld metal	2700 (Melting temperature)	2700	2700
Fraction of heat fluxes	Surface flux	90	90	90
	Body flux	10	10	10

Table 4.5 Pass sequences and welding parameters of each pass for a three-pass welded plate

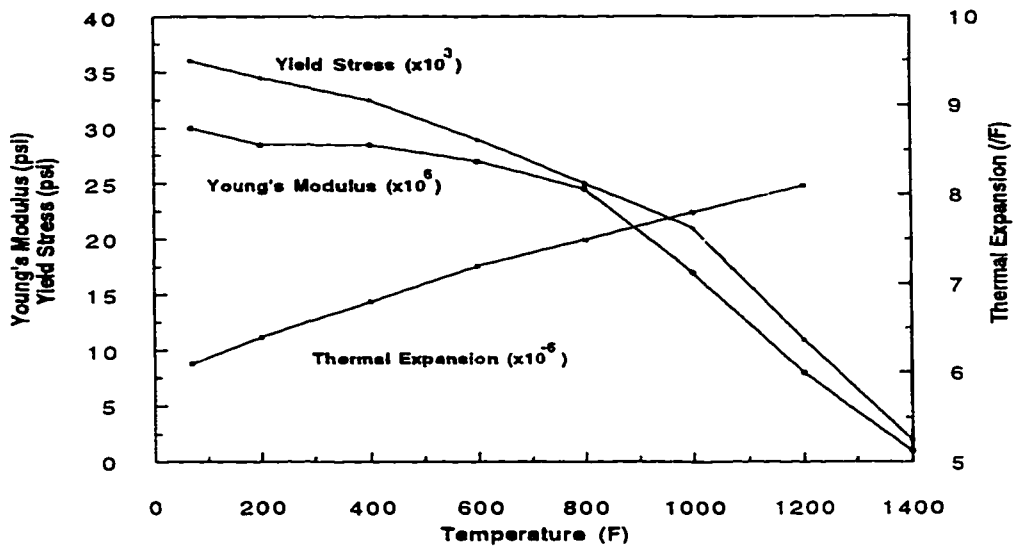
	Three-pass welding		
	Without interface element	With interface element	Difference * (%)
CPU (sec.) (thermal analysis)	212.8	209.7	-1.4
CPU (sec.) (mechanical analysis)	708.5	491.6	-30.6
Displacement (in.)	0.4418	0.2319	-47.5

\*  $\text{Difference (\%)} = \frac{(\text{With interface element} - \text{Without interface element})}{(\text{Without interface element})} \times 100$

Table 4.6 Comparison of CPU time and distortion for the a three-pass welded plate with and without the mismatch effects



(a)



(b)

Figure 4.1 Temperature-dependent material properties of ASTM A36 mild steel for finite element analysis [6]

- (a) Thermal material properties
- (b) Mechanical material properties

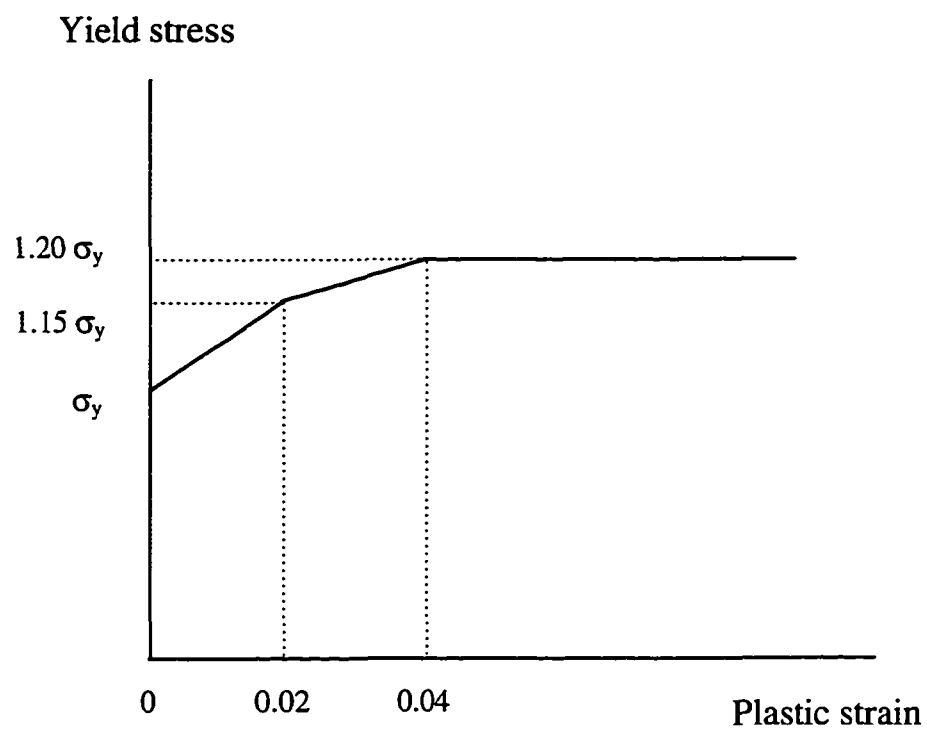
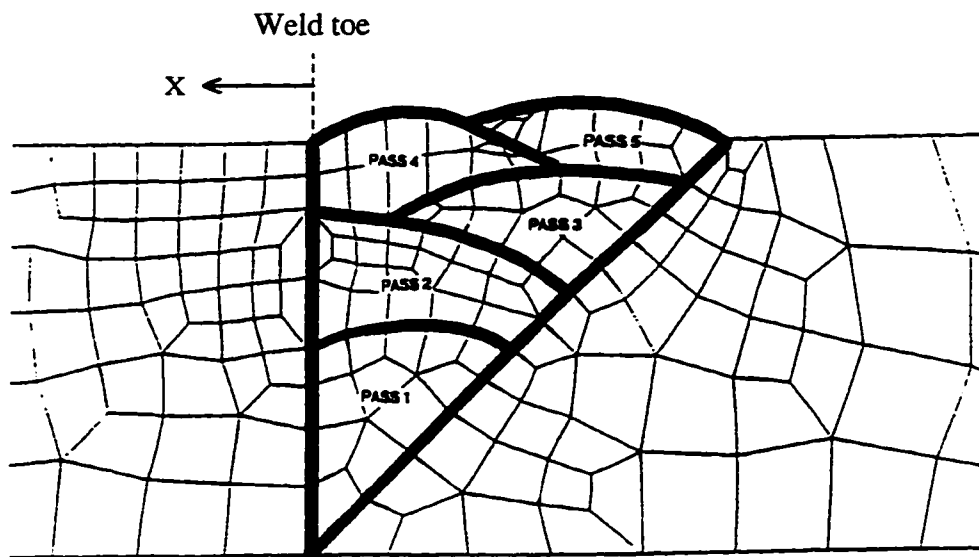
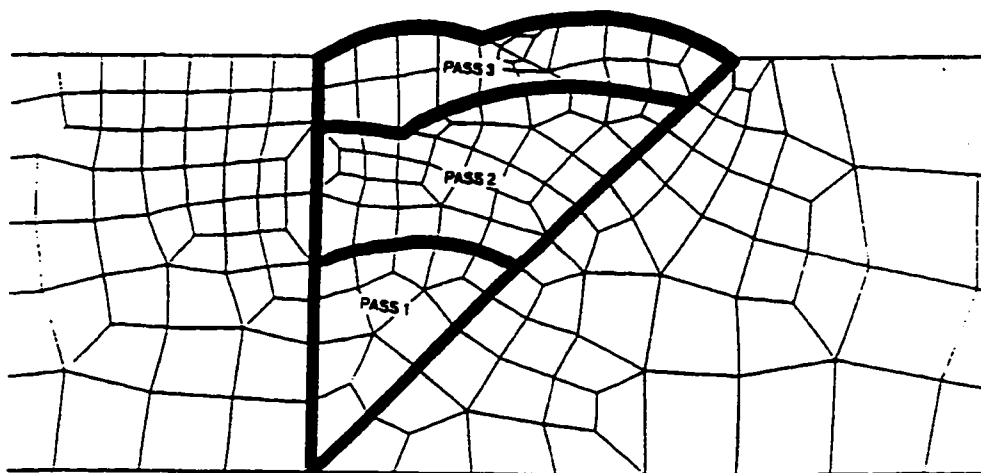


Figure 4.2 Strain hardening effect used for ASTM A36 steel



(a)

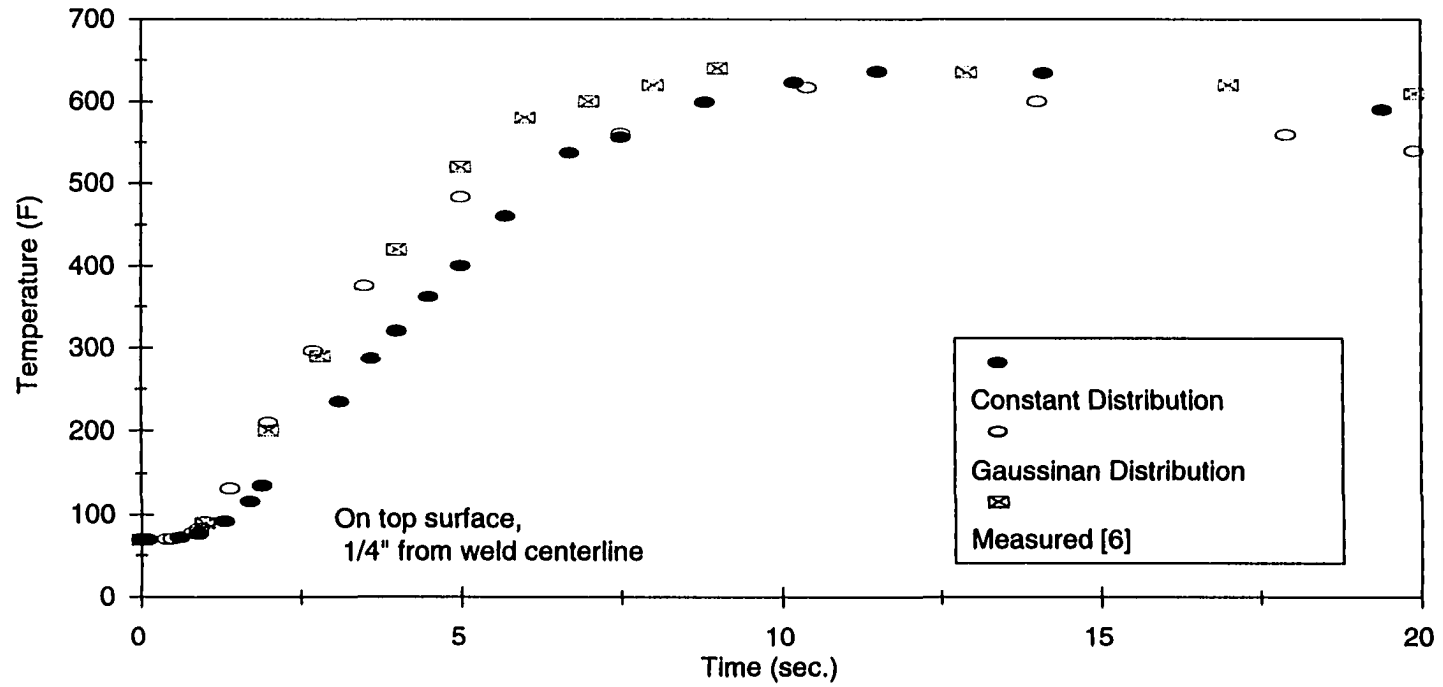


(b)

Figure 4.3 Finite element model for a five-pass welded plate  
 (a) Weld detail - 5 pass model (non-lumped model)  
 (b) Weld detail - 3 pass model (lumped model)



Figure 4.4 View of entire model and mechanical boundary conditions for a five-pass welded plate



(a)

Figure 4.5 (Continued)

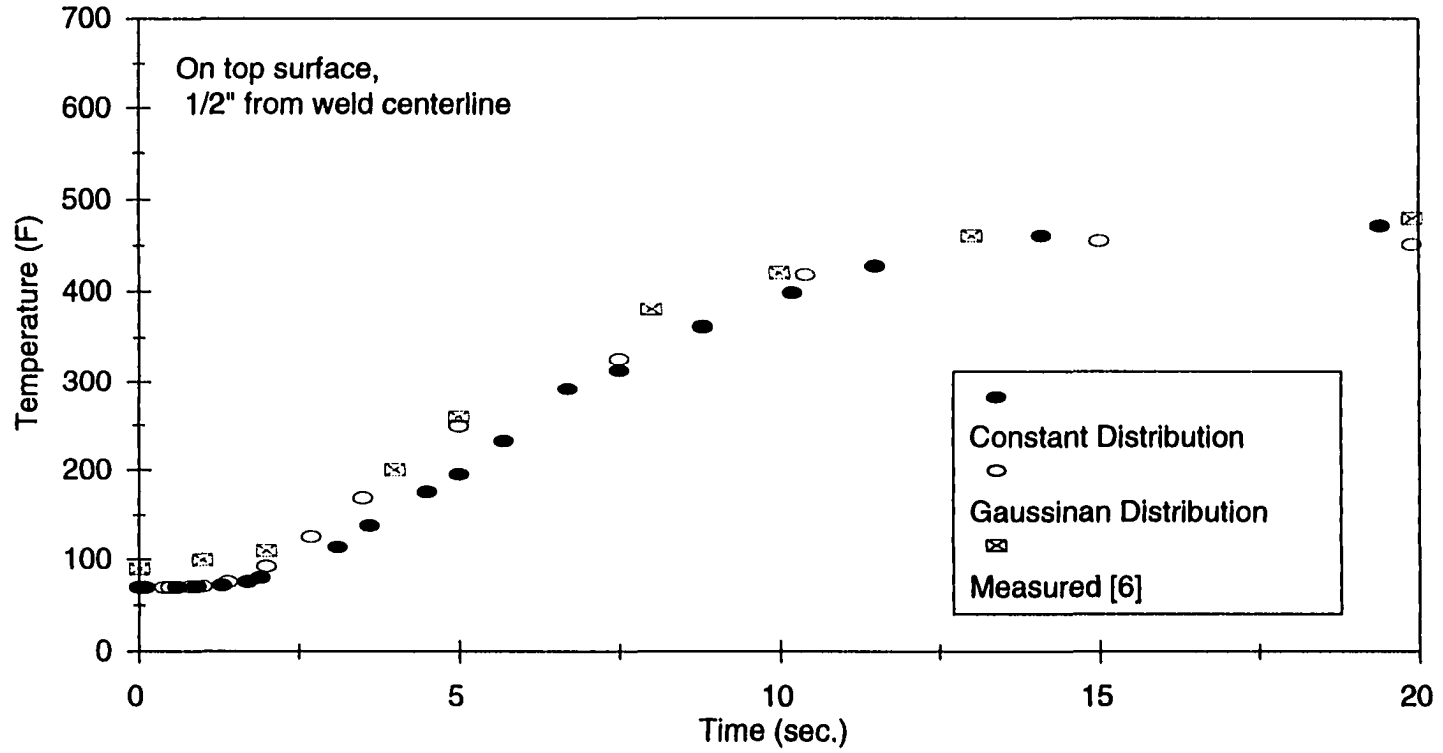
Figure 4.5 Comparison of the numerical and experimental temperature changes at two locations during welding

(first weld pass, a five-pass welded plate model)

(a) On top surface, 1/4" from the weld toe

(b) On top surface, 1/2" from the weld toe

Figure 4.5 (Continued)



(b)

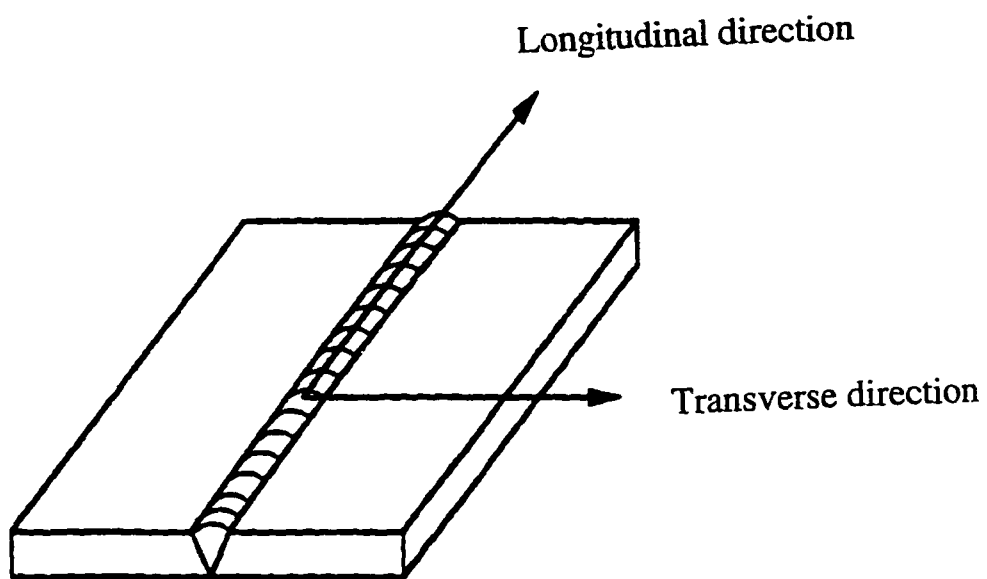
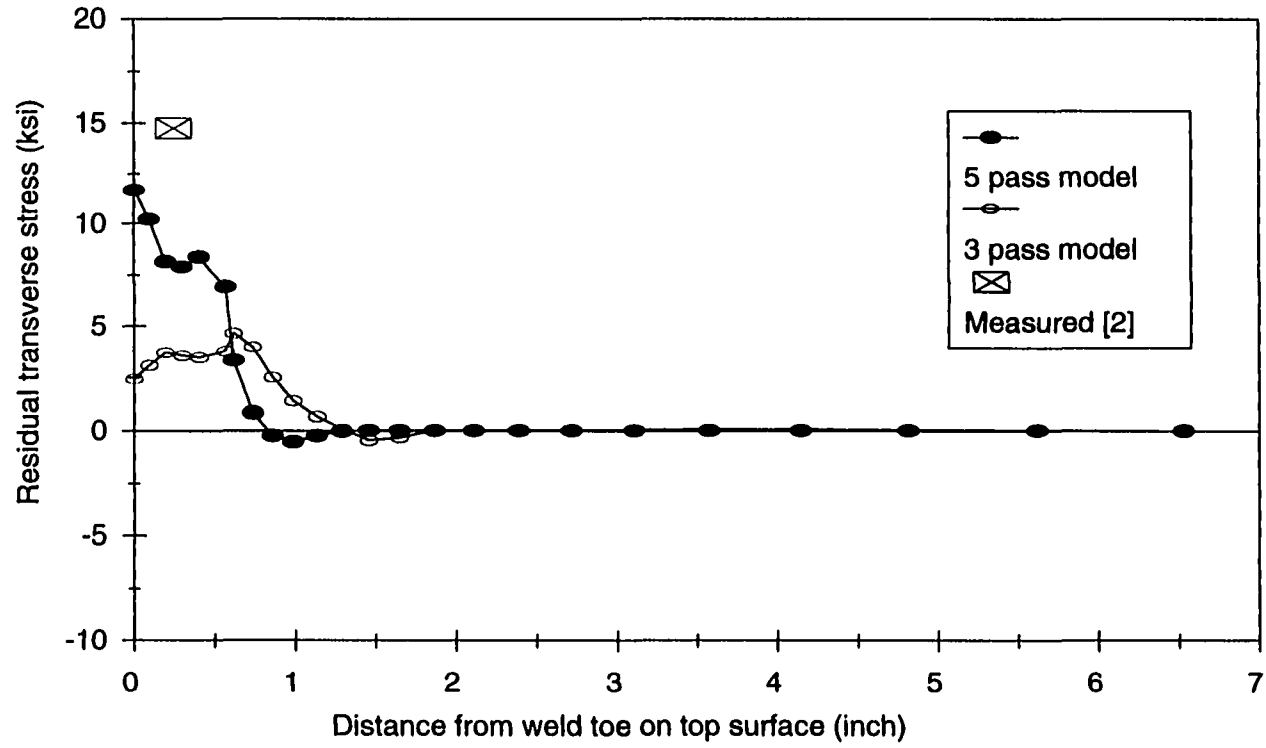


Figure 4.6 Definitions of stress directions



(a)

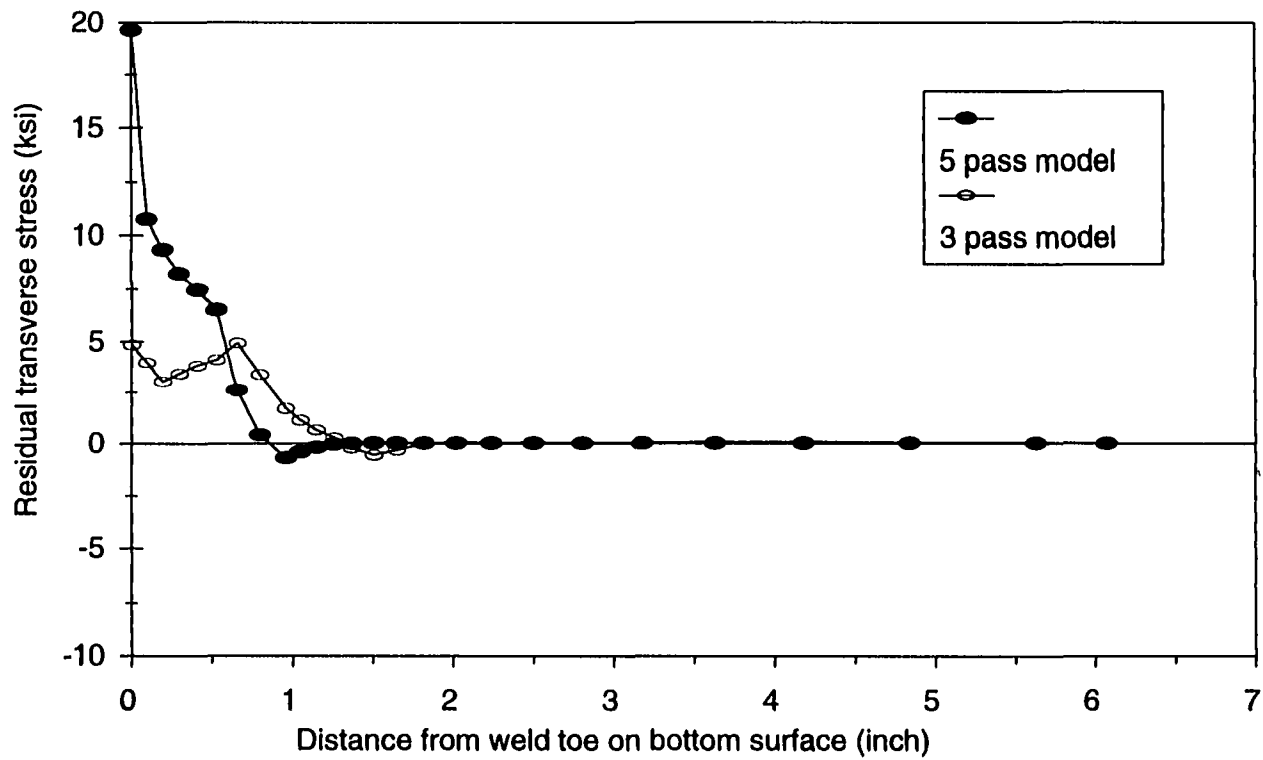
Figure 4.7 (Continued)

Figure 4.7 Residual transverse stress distributions after final weld pass for a five-pass welded plate model

(a) On top surface

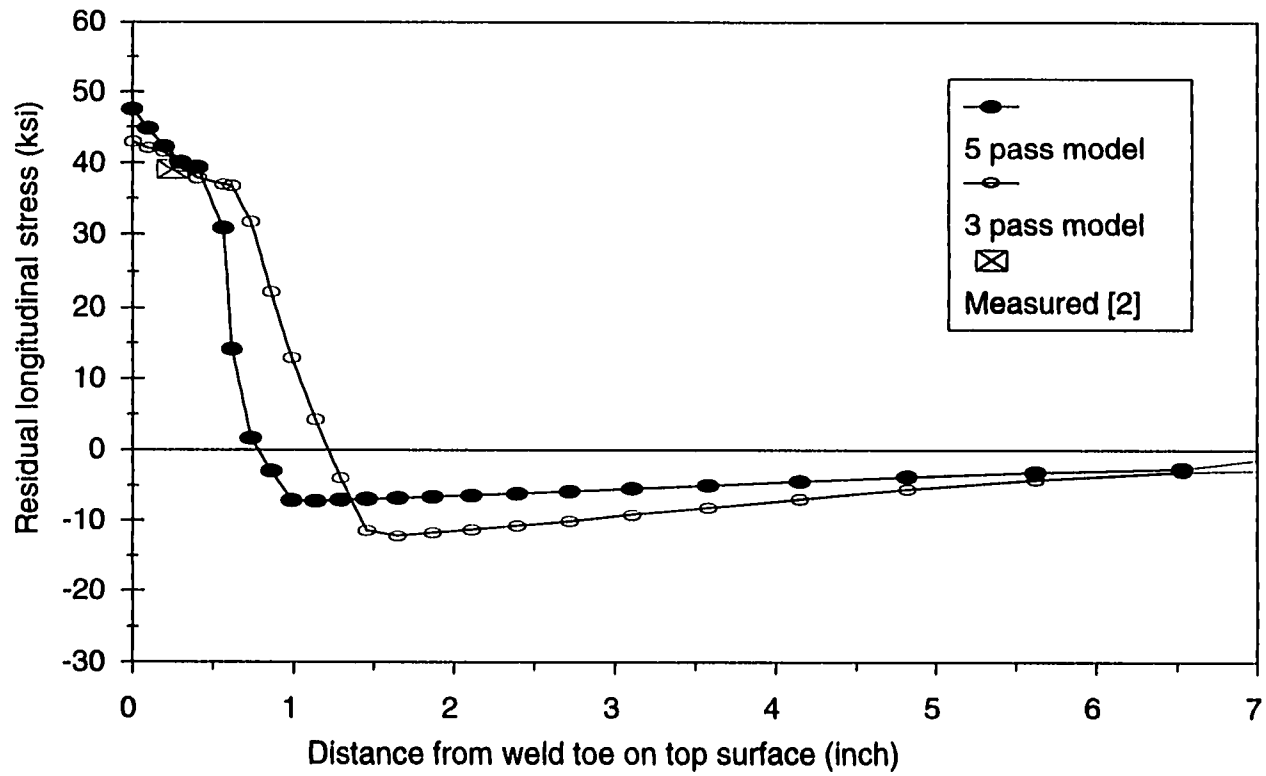
(b) On bottom surface

Figure 4.7 (Continued)



97

(b)



(a)

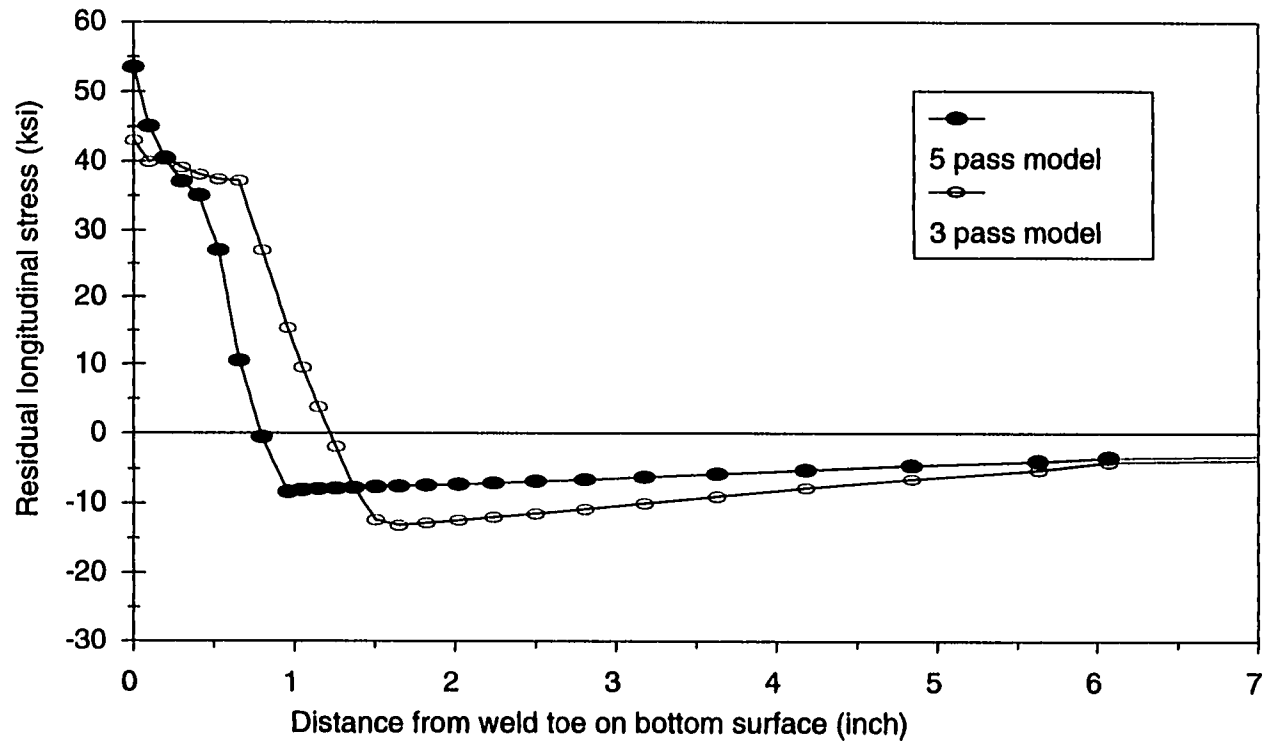
Figure 4.8 (Continued)

Figure 4.8 Residual longitudinal stress distributions after final weld pass for a five-pass welded plate model

(a) On top surface

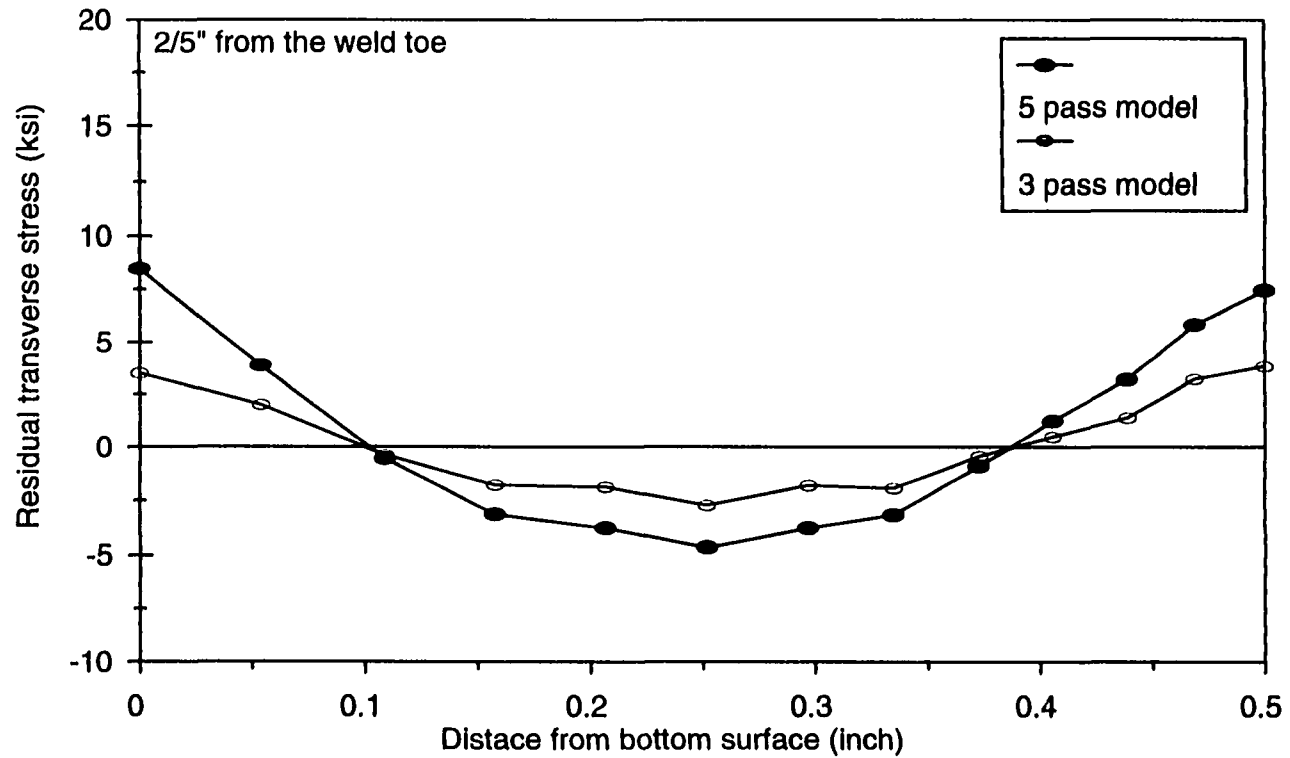
(b) On bottom surface

Figure 4.8 (Continued)



66

(b)



(a)

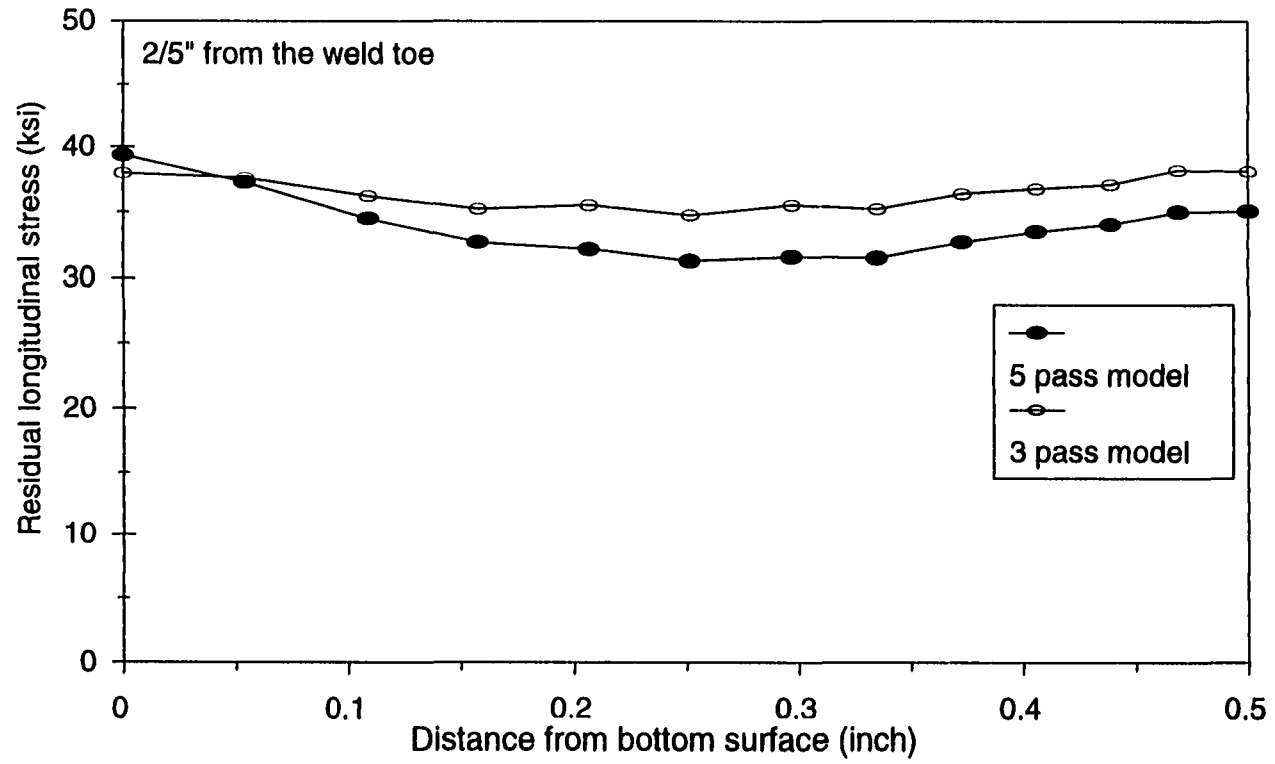
Figure 4.9 (Continued)

Figure 4.9 Through-thickness residual stress distributions after final weld pass at 2/5" from the weld toe for a five-pass welded plate model

(a) Transverse stress distributions

(b) Longitudinal stress distributions

Figure 4.9 (Continued)



101

(b)

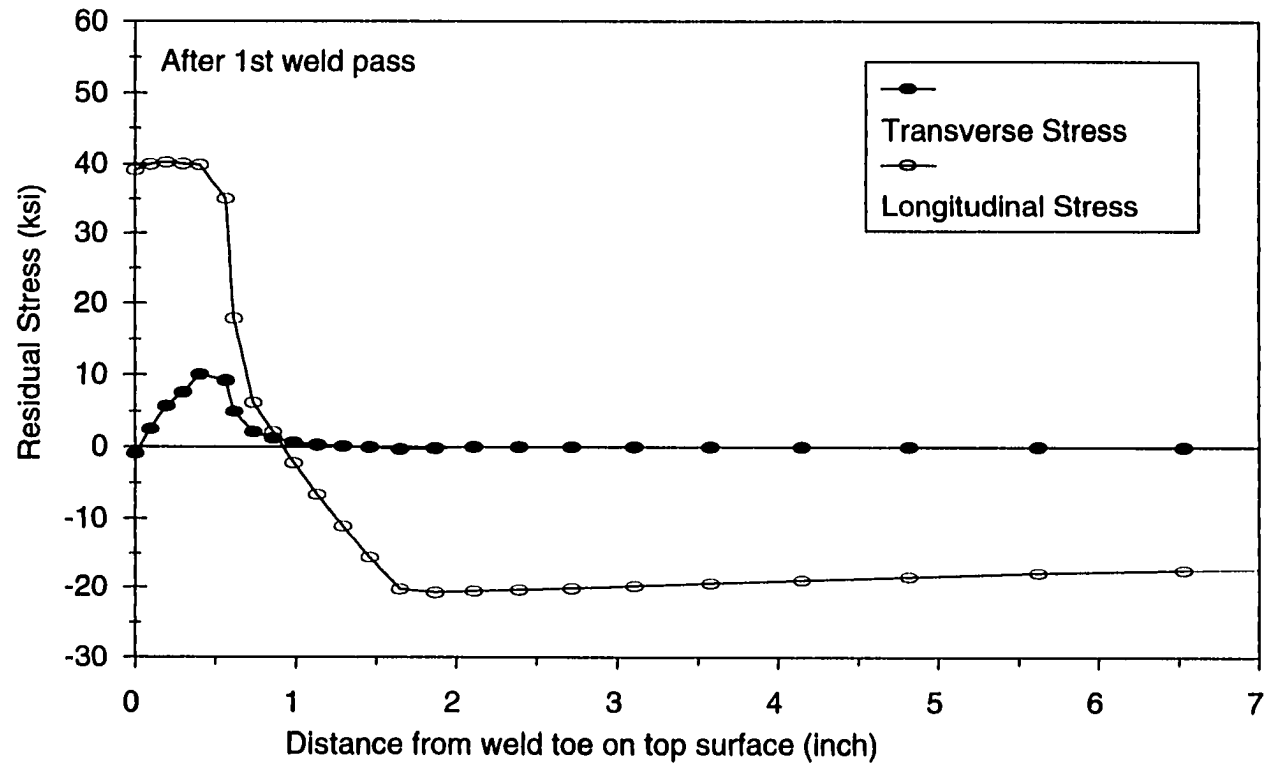


Figure 4.10 Stress distribution on top surface after 1st weld pass for a five-pass welded plate model

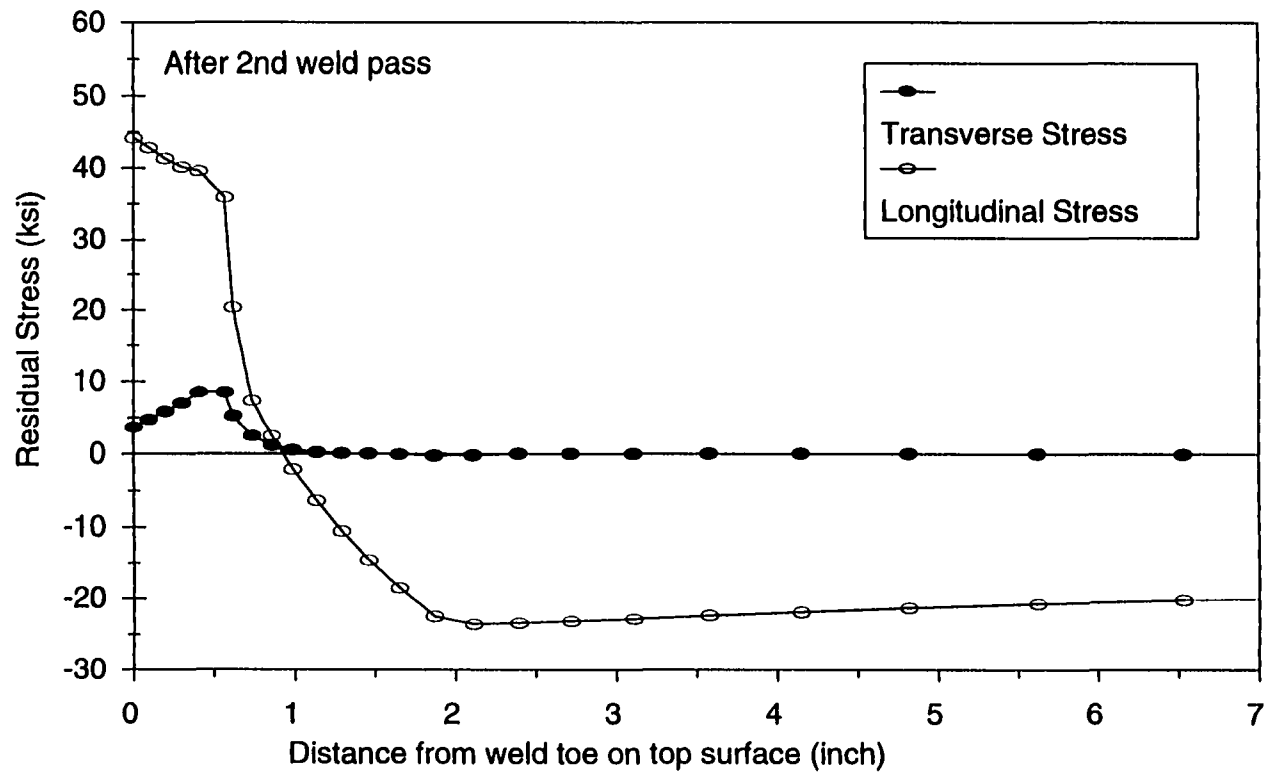


Figure 4.11 Stress distribution on top surface after 2nd weld pass for a five-pass welded plate model

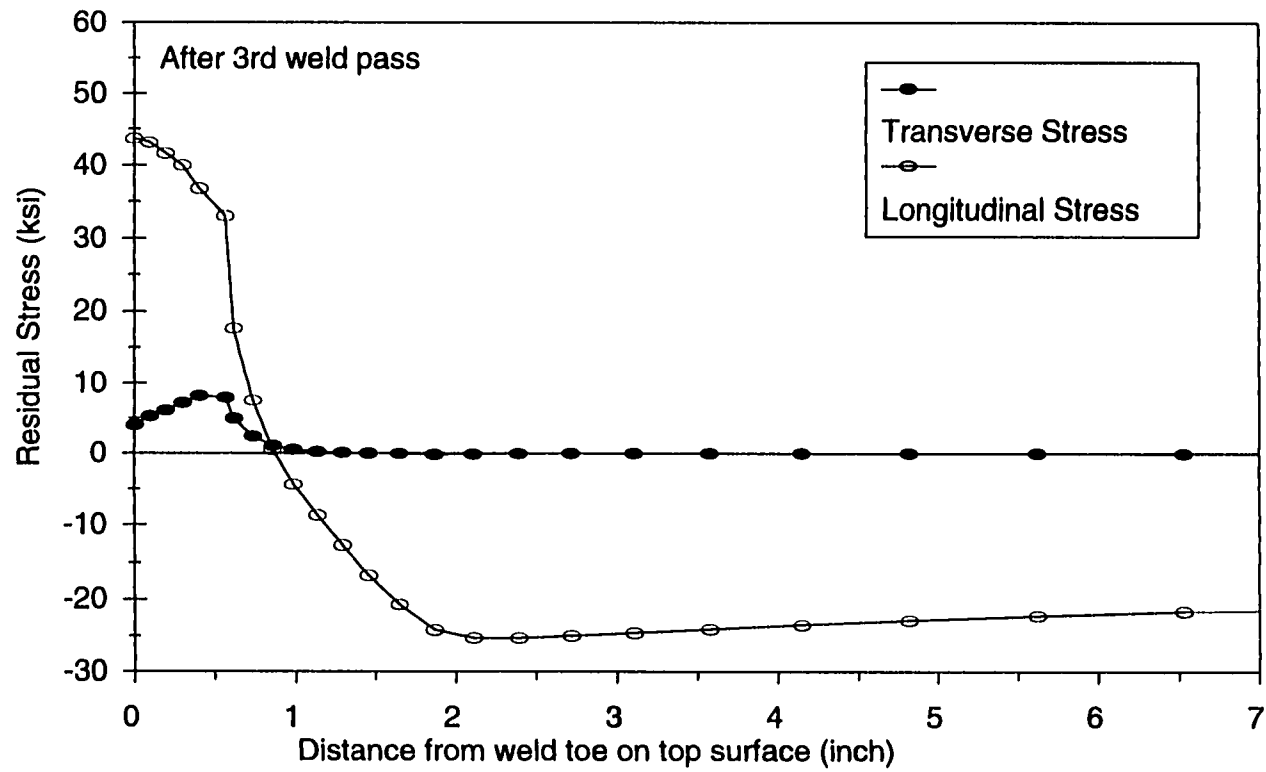


Figure 4.12 Stress distribution on top surface after 3rd weld pass for a five-pass welded plate model

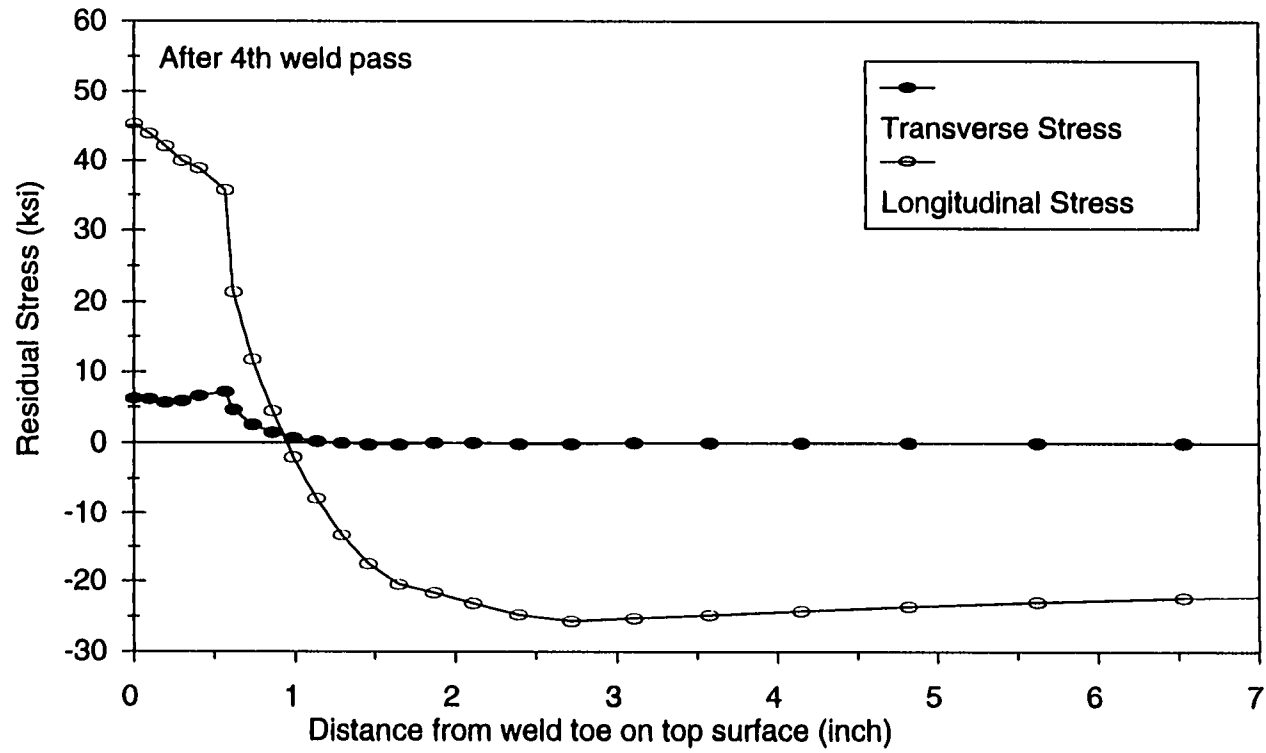


Figure 4.13 Stress distribution on top surface after 4th weld pass for a five-pass welded plate model

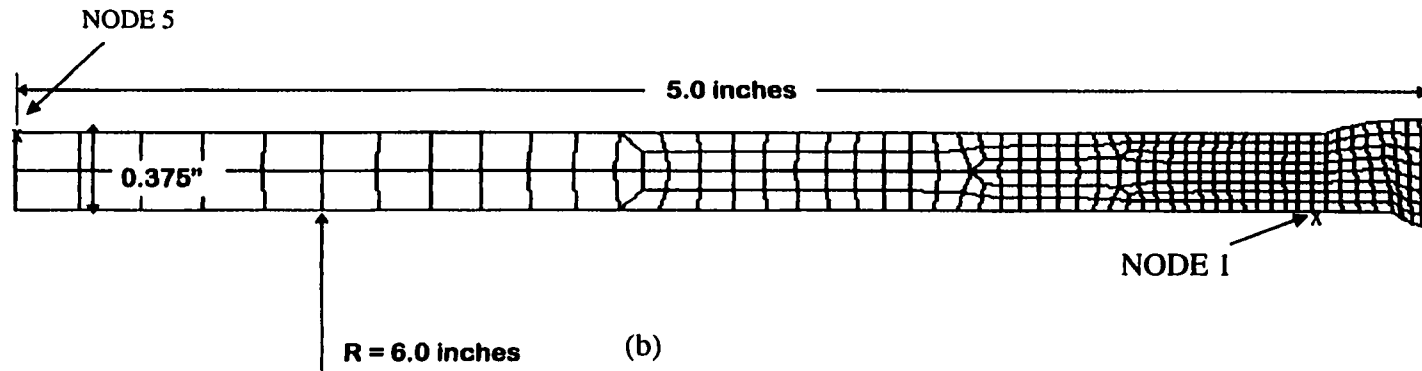
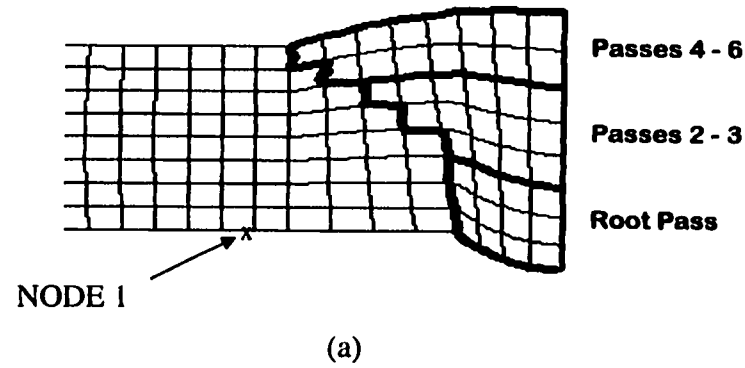


Figure 4.14 Finite element model for a six-pass girth welded pipe  
(a) View of weld area  
(b) Entire view of the axisymmetric pipe model

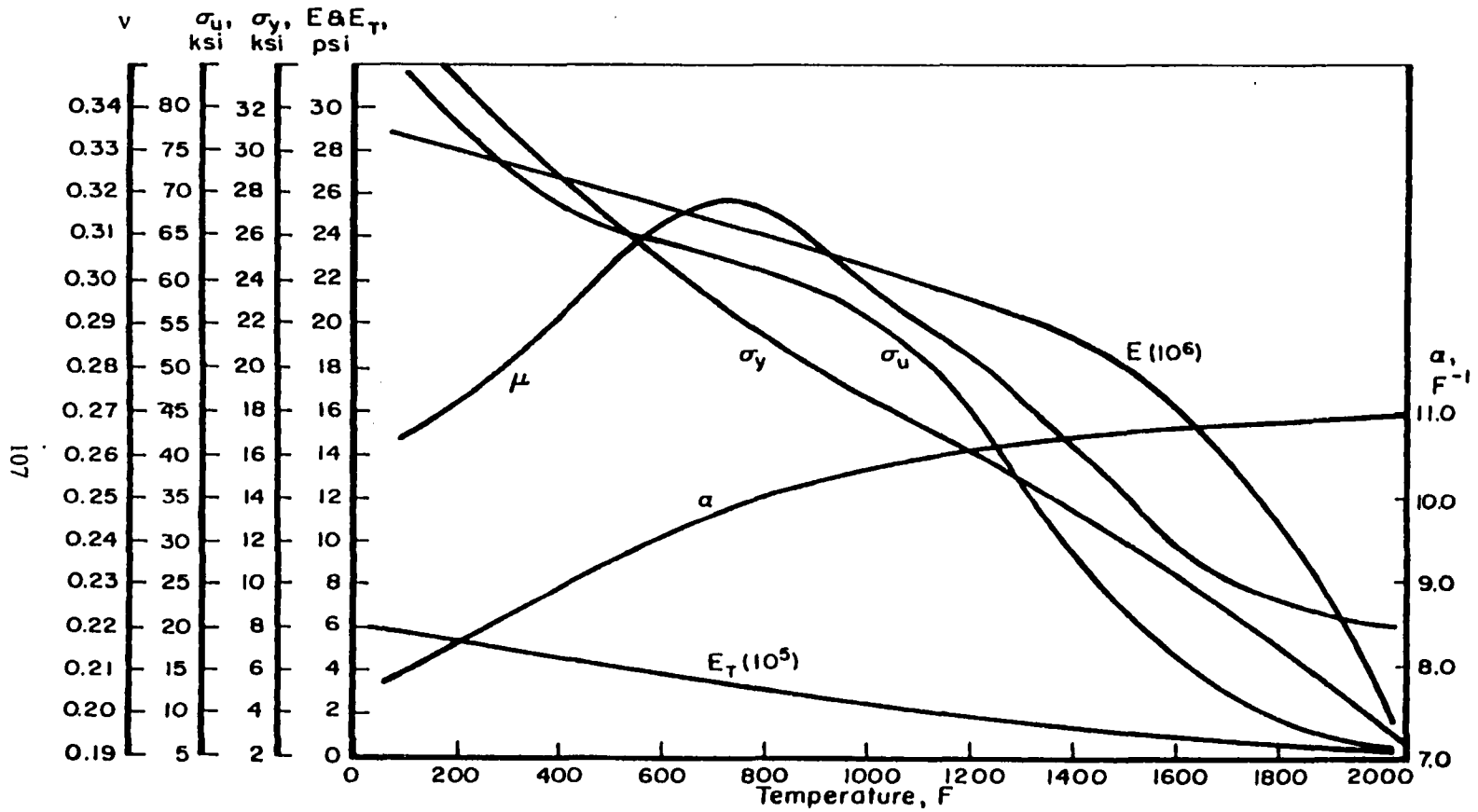
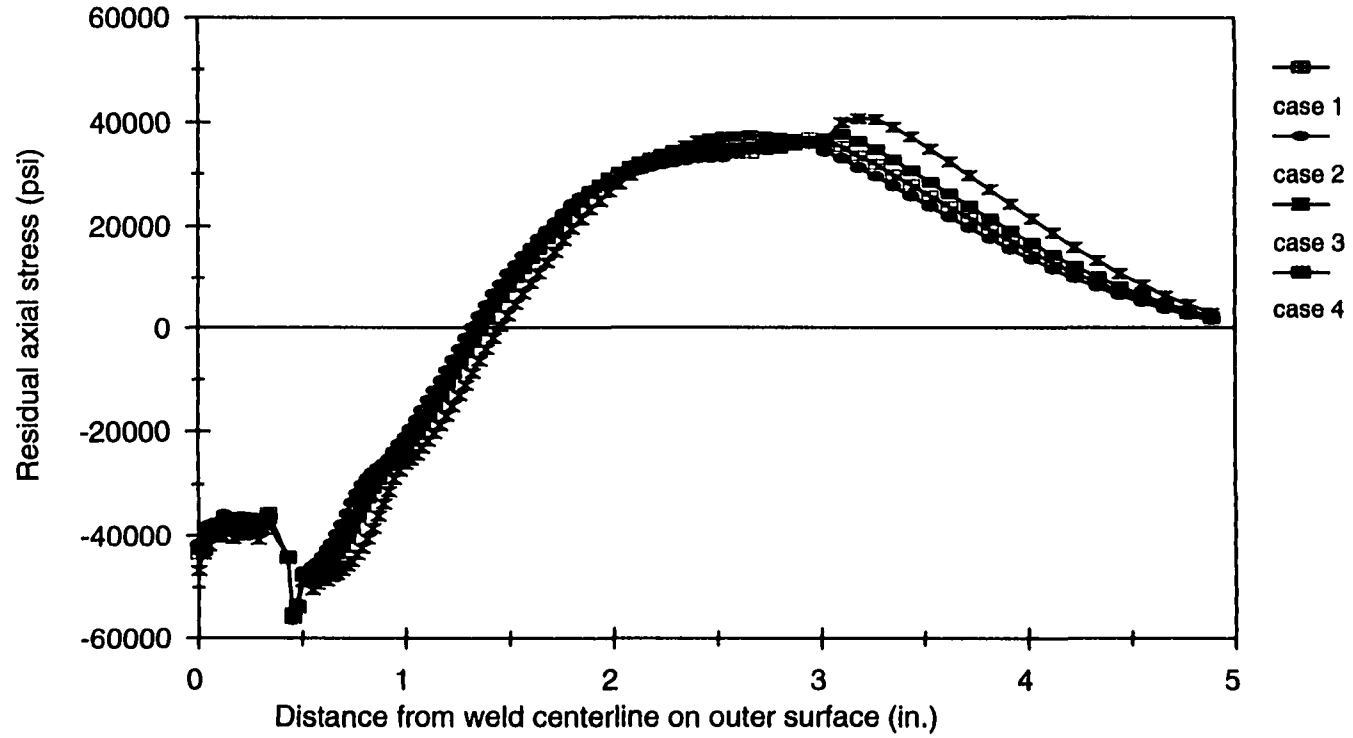


Figure 4.15 Temperature dependent material properties of 304 stainless steel for finite element stress analysis

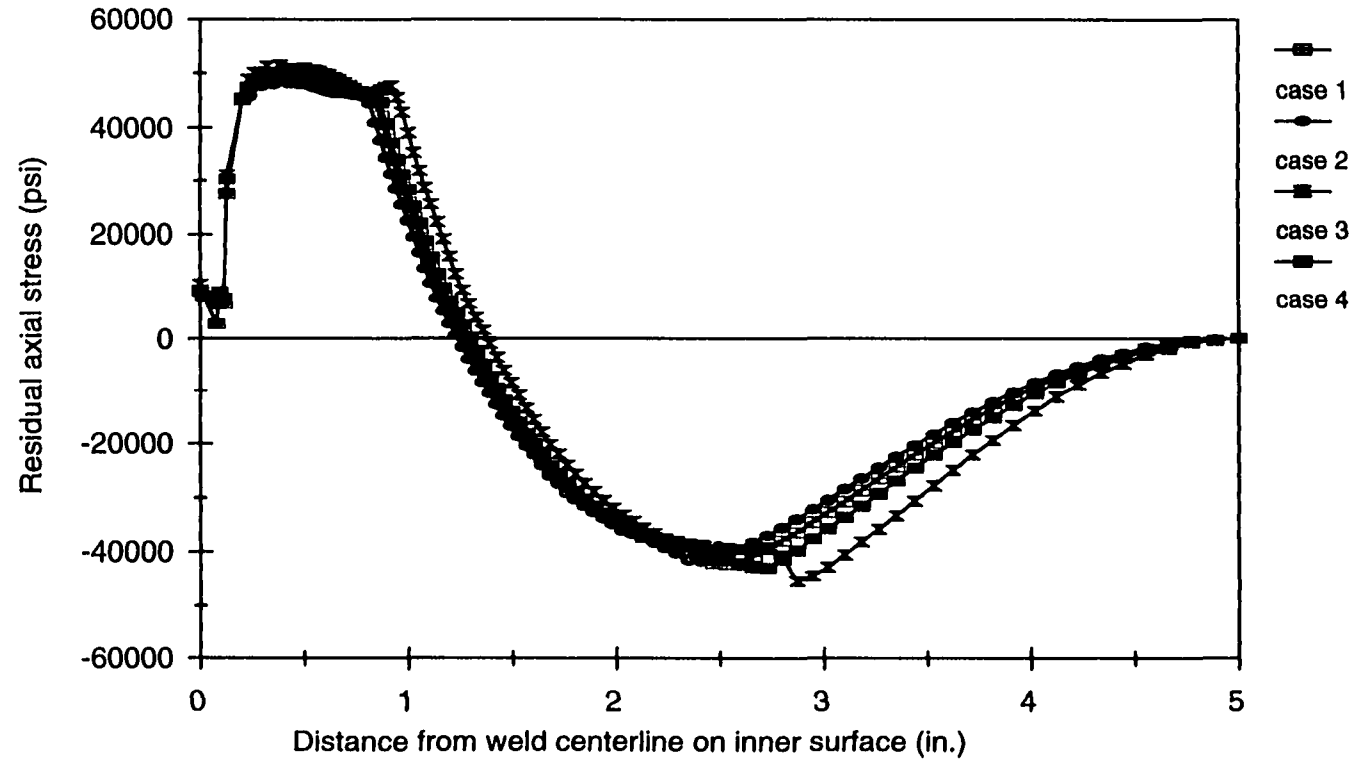


(a)

Figure 4.16 (Continued)

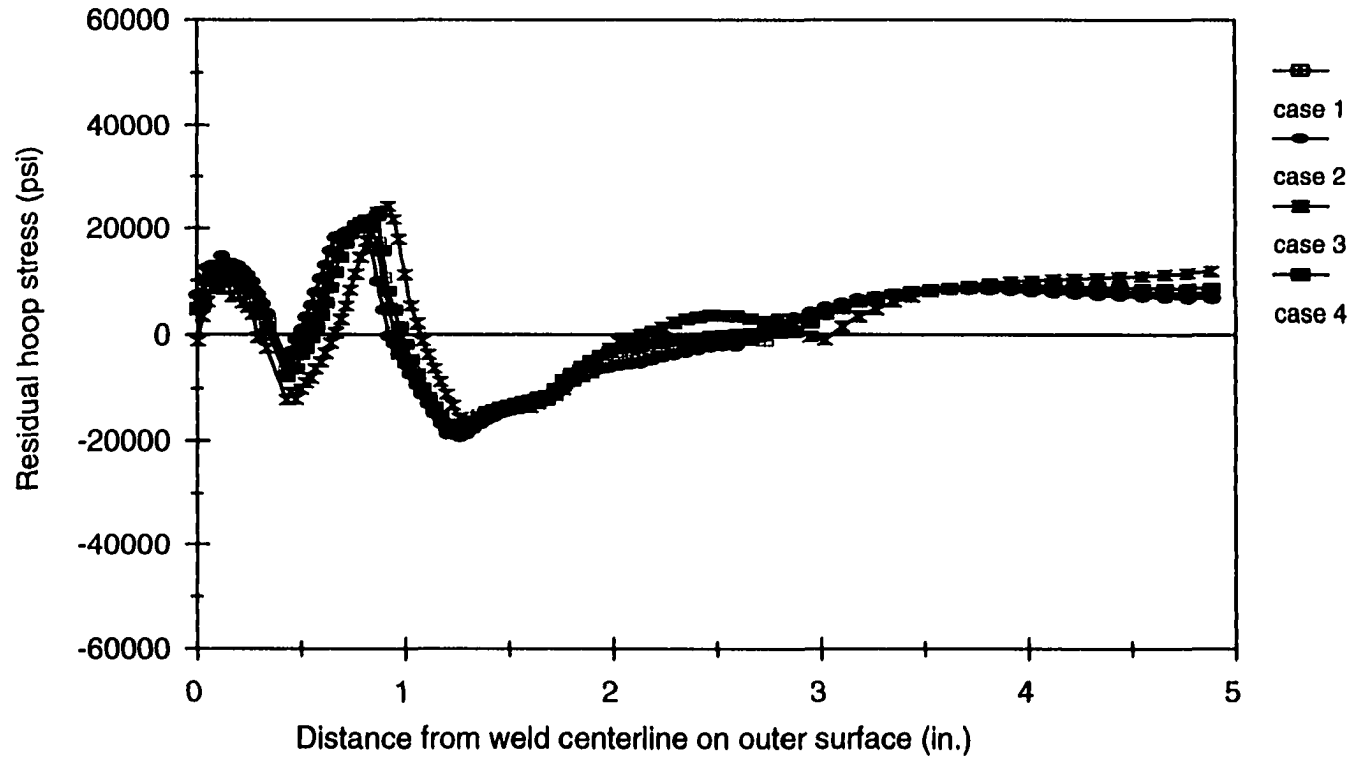
Figure 4.16 Residual axial stresses for different heat inputs (a six-pass girth welded pipe)  
(a) On outer surface  
(b) On inner surface

Figure 4.16 (Continued)



601

(b)



(a)

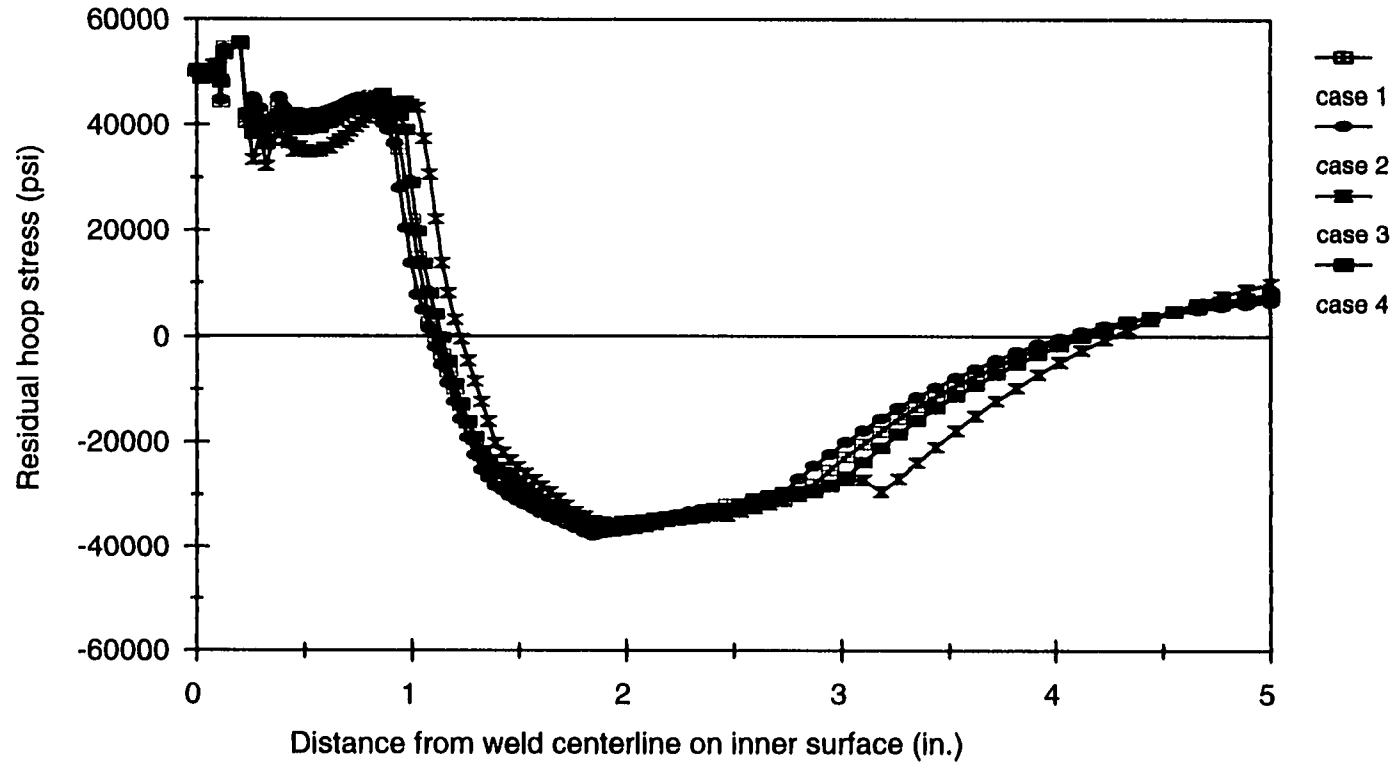
Figure 4.17 (Continued)

Figure 4.17 Residual circumferential (hoop) stresses for different heat inputs (a six-pass girth welded pipe)

(a) On outer surface

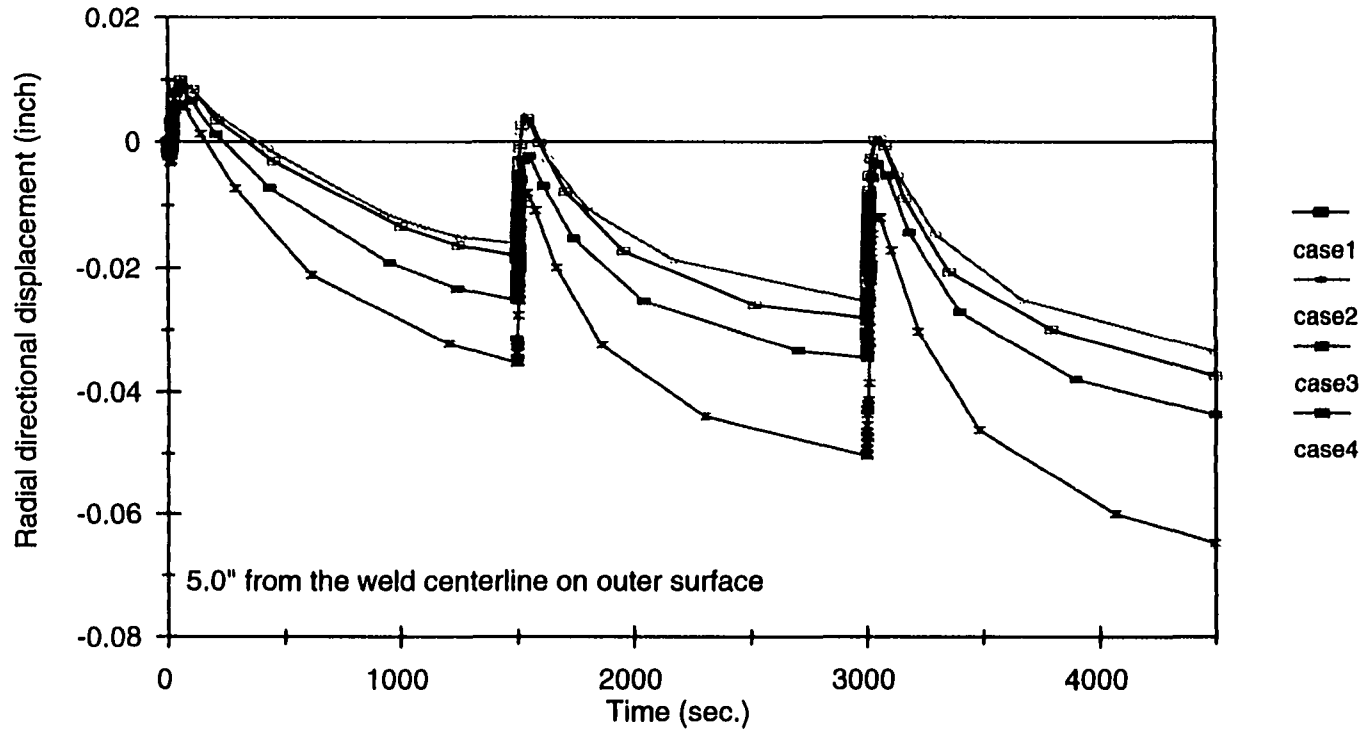
(b) On inner surface

Figure 4.17 (Continued)



111

(b)

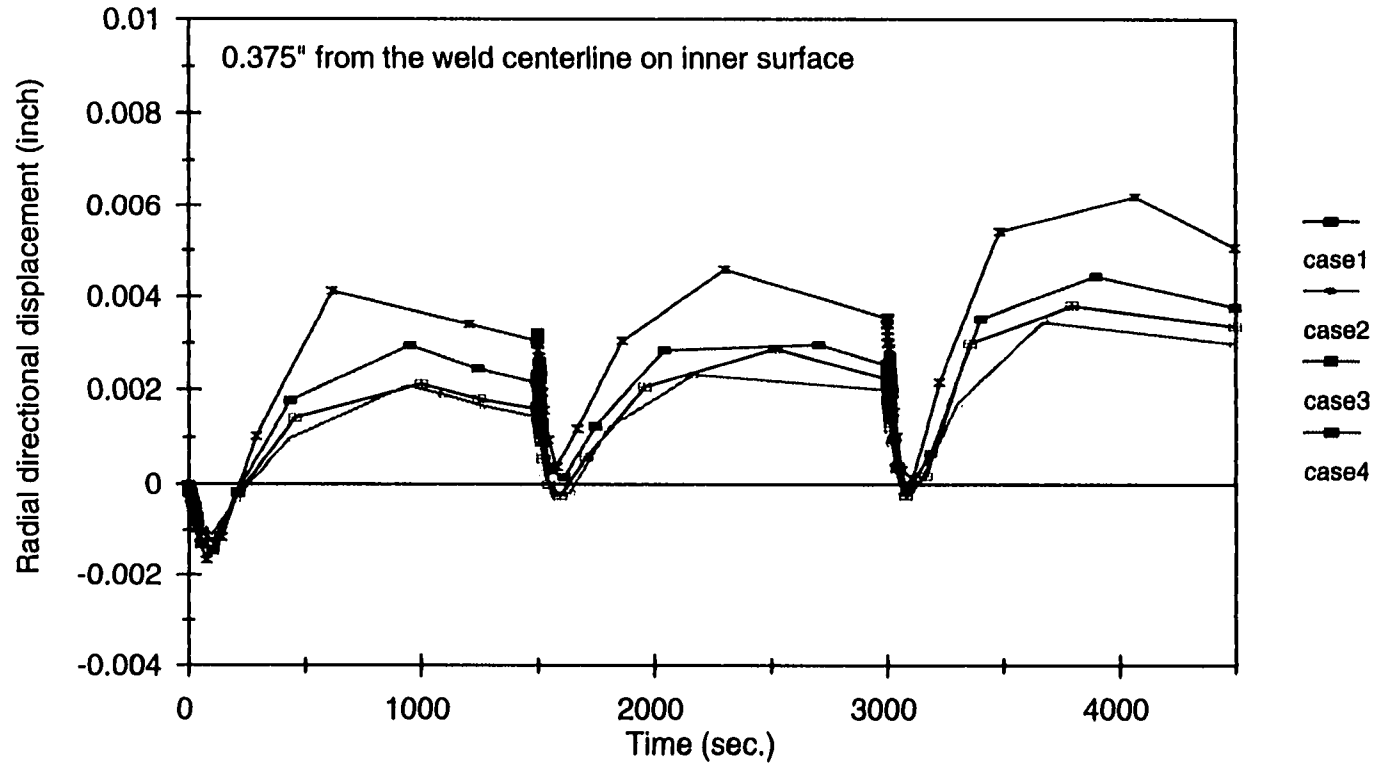


(a)

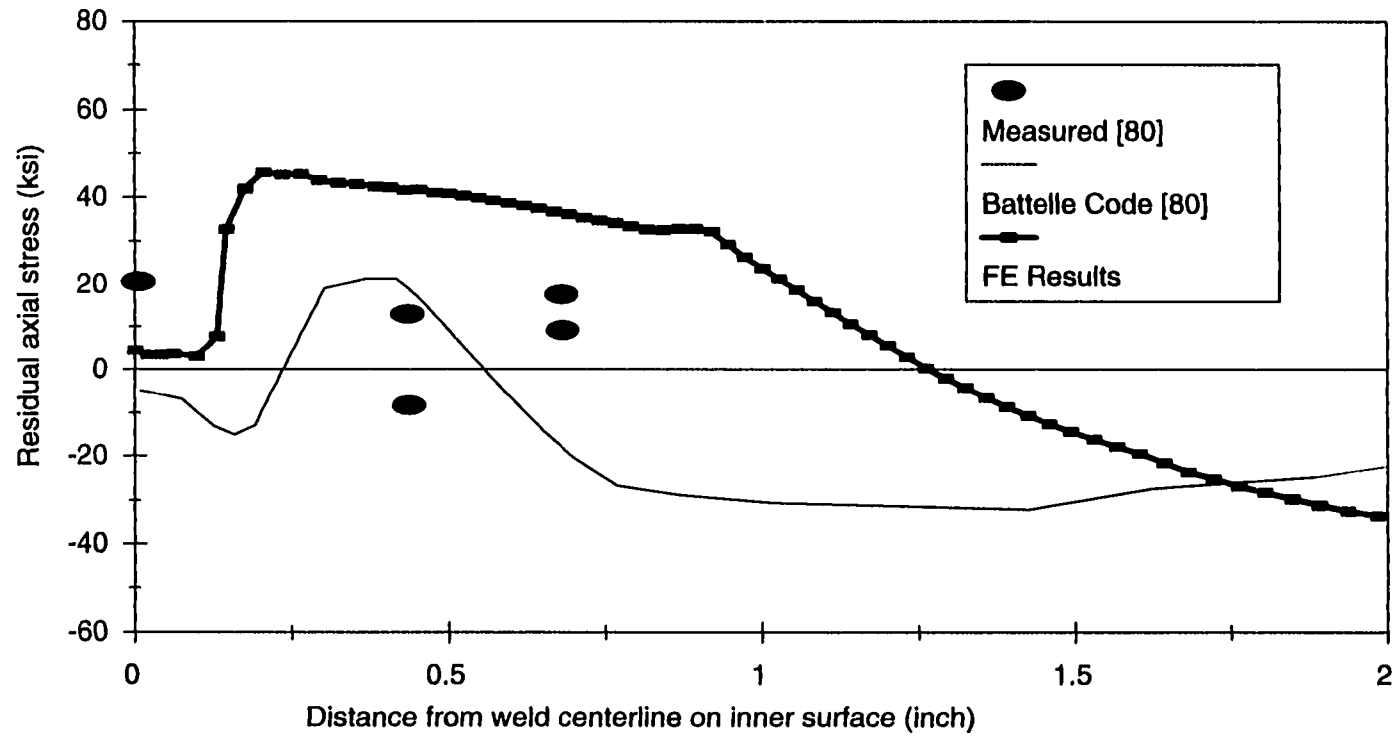
Figure 4.18 (Continued)

Figure 4.18 Distortion changes with different heat inputs at two locations during welding  
(a six-pass girth welded pipe)  
(a) 5.0 " from weld centerline on outer surface  
(b) 0.375" from weld centerline on inner surface

Figure 4.18 (Continued)



(b)

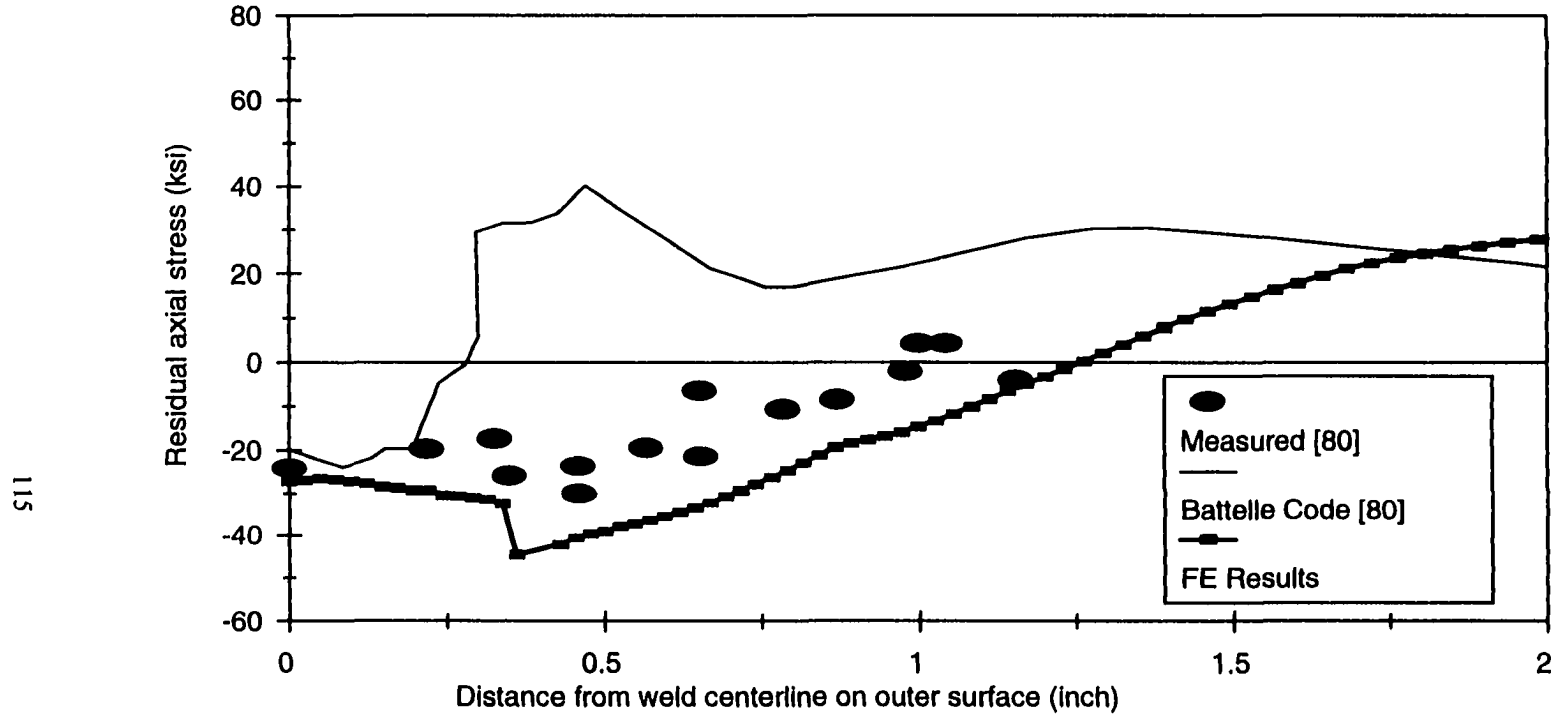


(a)

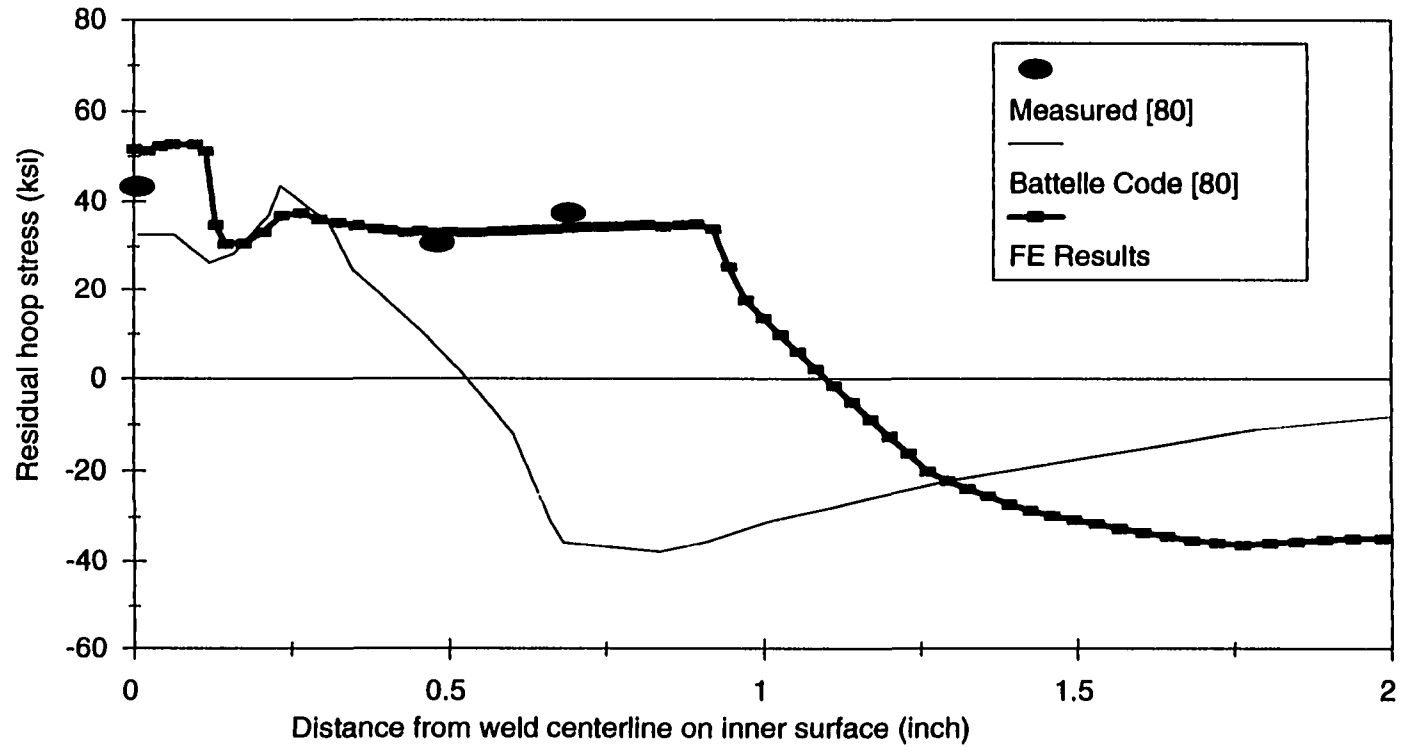
Figure 4.19 (Continued)

Figure 4.19 Comparison of the numerical (Case 1 heat input) and experimental residual axial stress distributions for a six-pass girth welded pipe  
 (a) On inner surface  
 (b) On outer surface

Figure 4.19 (Continued)



(b)



(a)

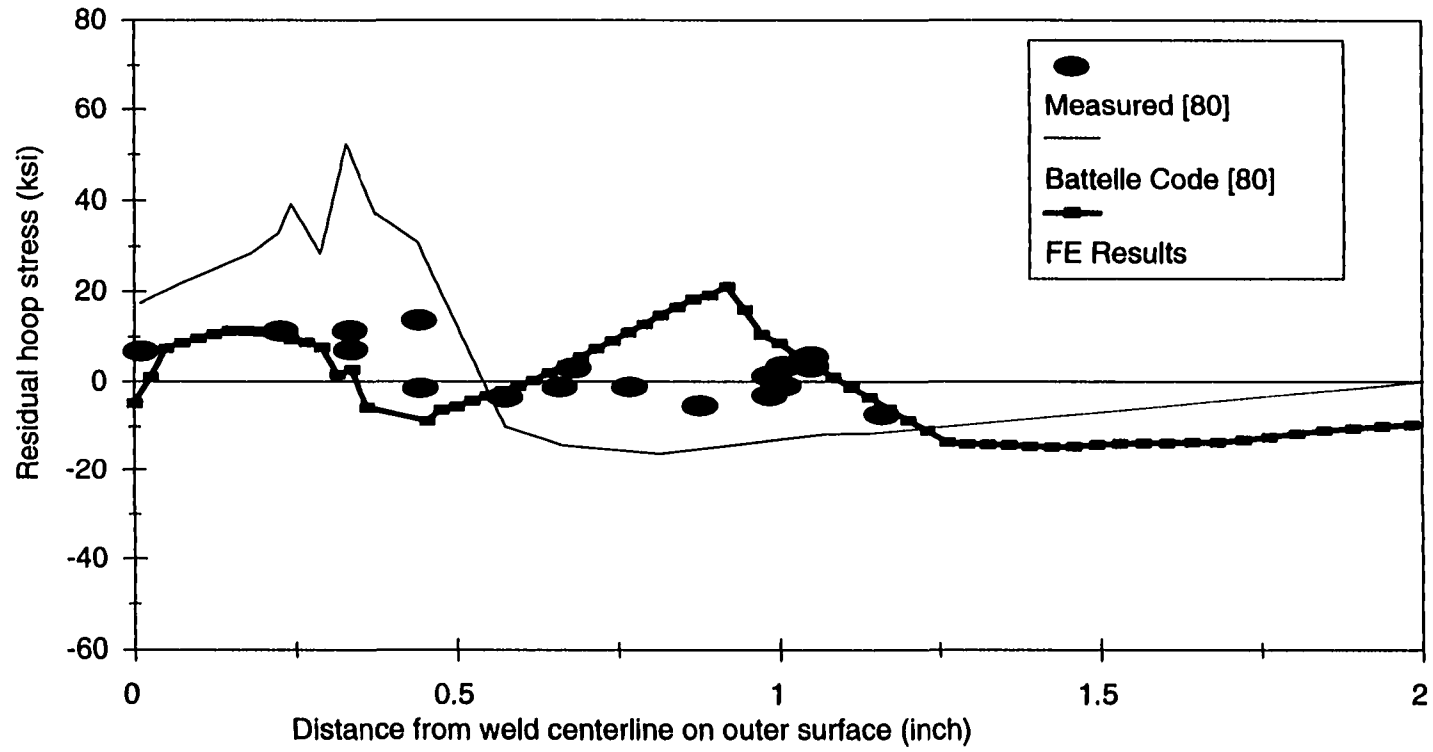
Figure 4.20 (Continued)

Figure 4.20 Comparison of the numerical (Case 1 heat input) and experimental residual circumferential (hoop) stress distributions for a six-pass girth welded pipe

(a) On inner surface

(b) On outer surface

Figure 4.20 (Continued)



117

(b)

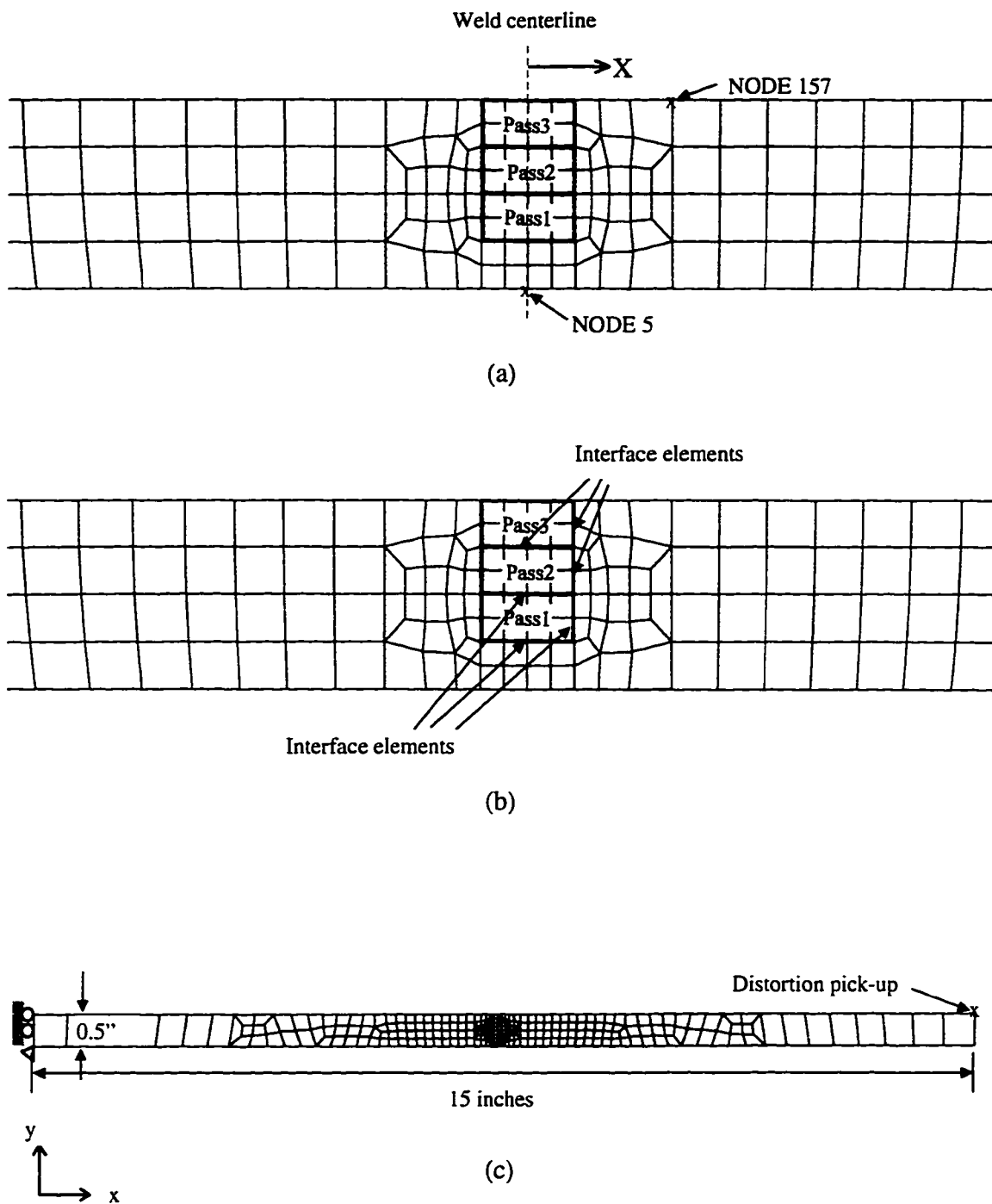
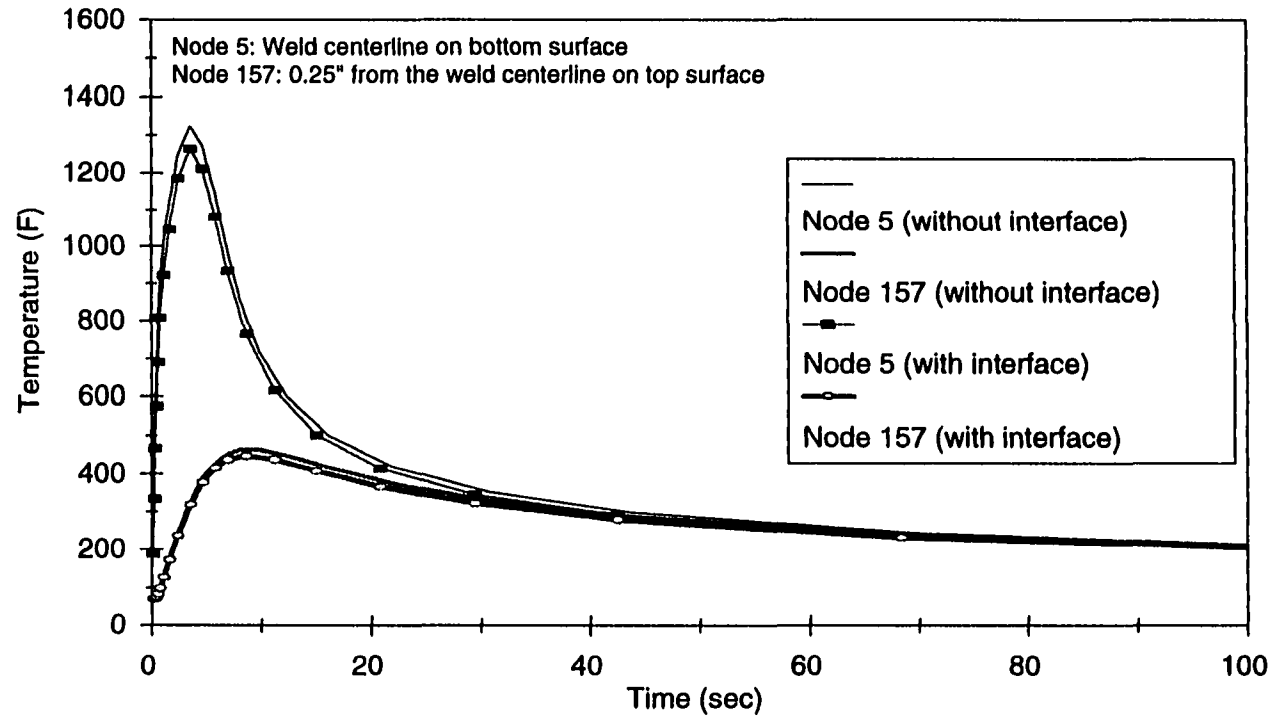


Figure 4.21 Finite element models for a three-pass welded plate  
 (a) Conventional model (without interface elements)  
 (b) Model with interface elements  
 (c) Entire view of the model and boundary conditions



(a)

Figure 4.22 (Continued)

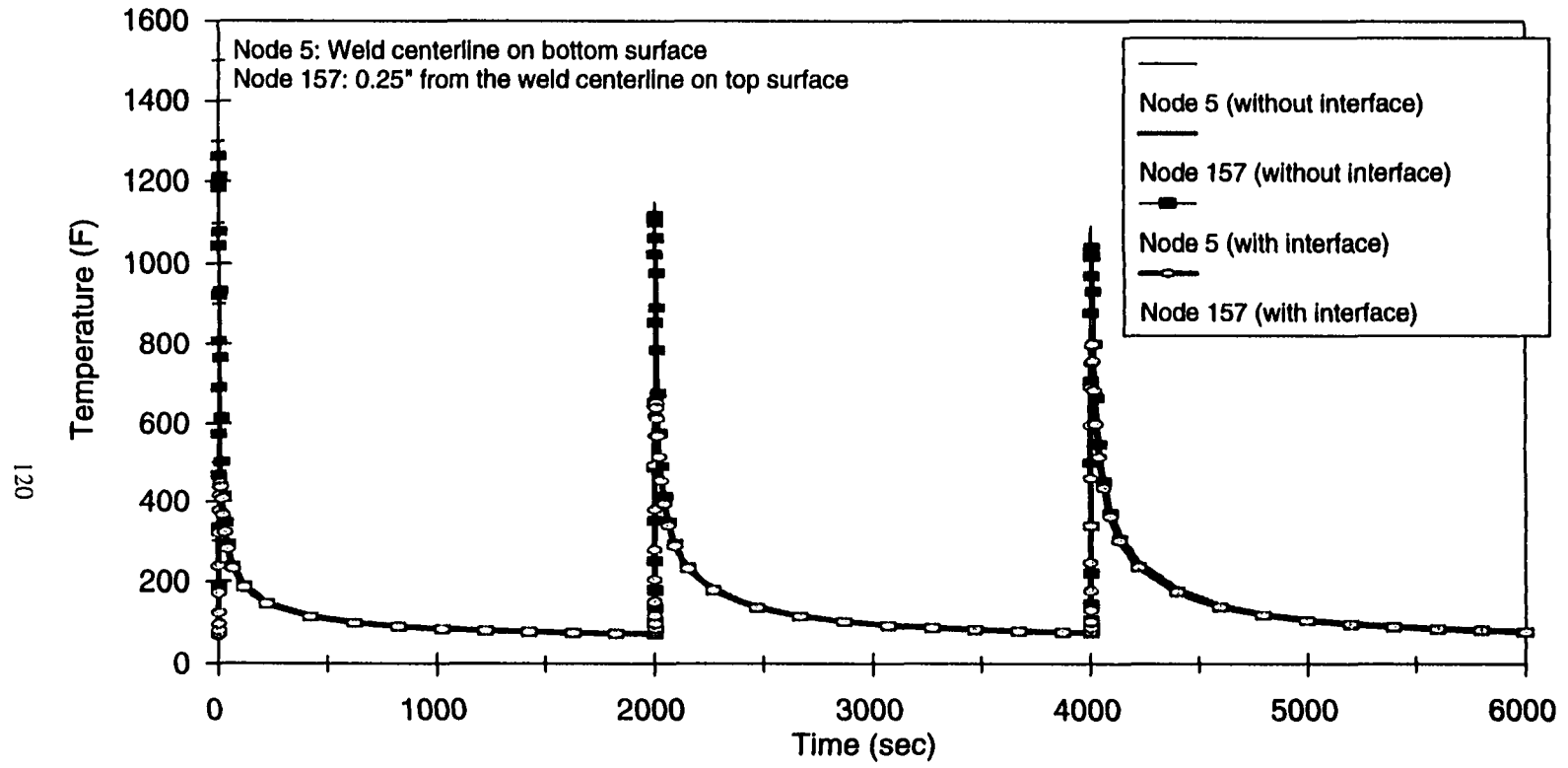
Figure 4.22 Temperature changes at two locations during welding (a three-pass welded plate)

Node 5: weld centerline on bottom surface, Node 157: 0.25" from the weld centerline on top surface

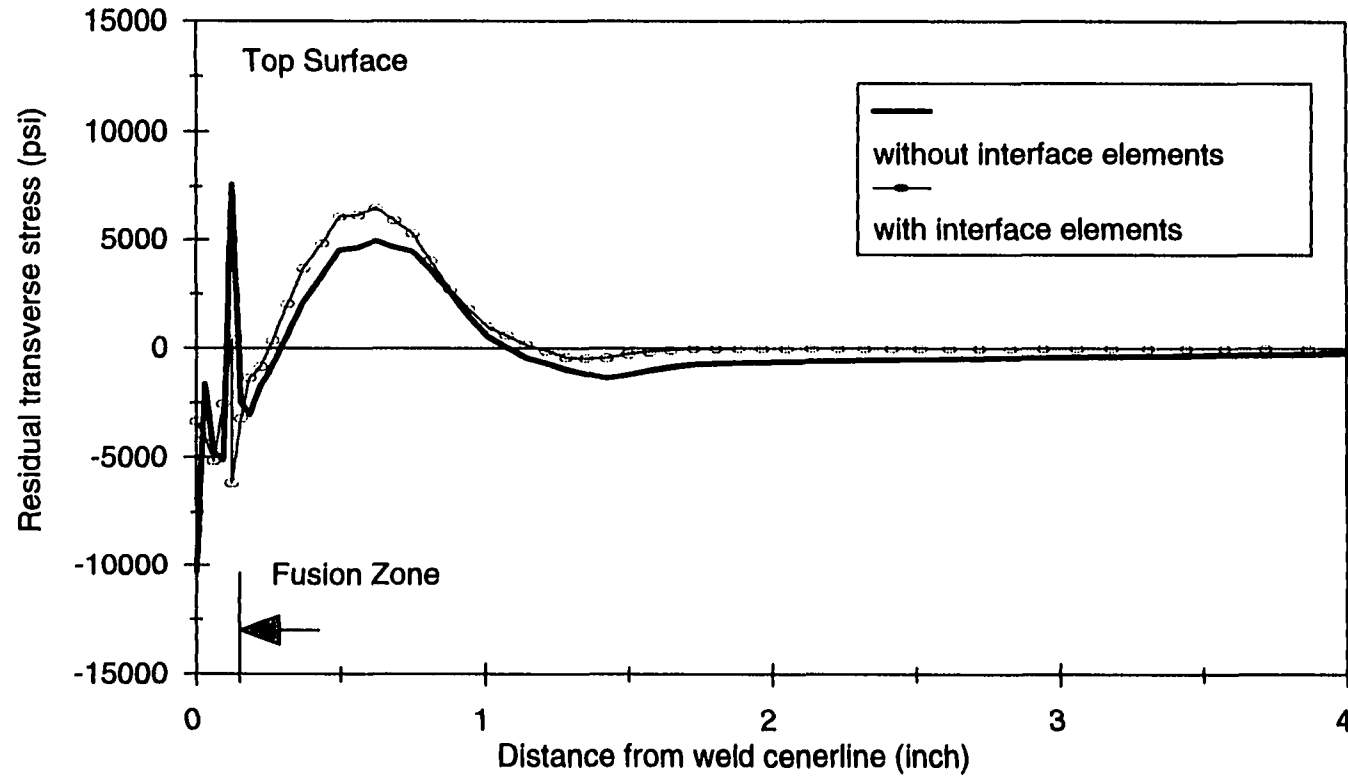
(a) During first weld pass

(b) During entire weld pass

Figure 4.22 (Continued)



(b)



(a)

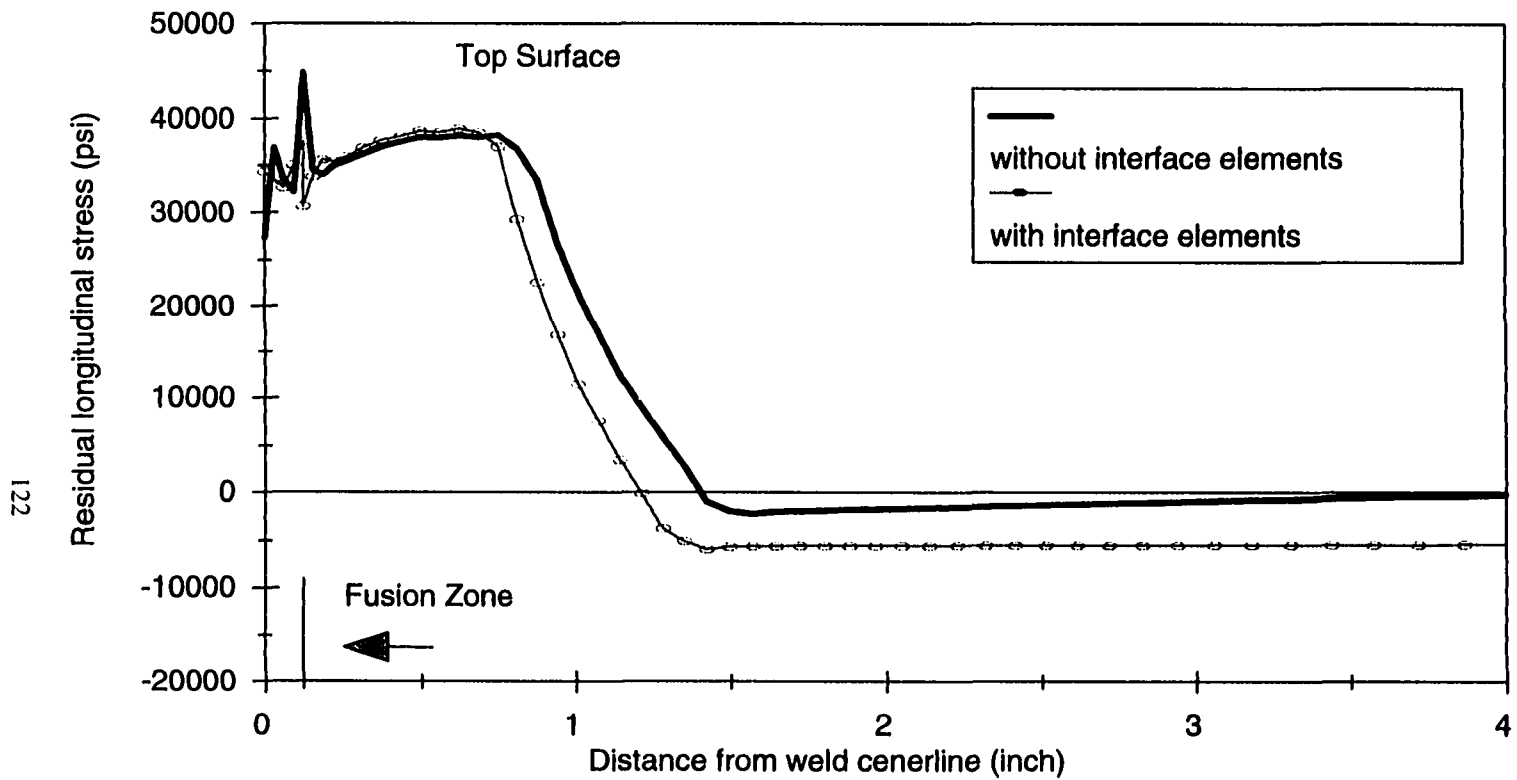
Figure 4.23 (Continued)

Figure 4.23 Residual stress distributions with and without interface elements on top surface for a three-pass welded plate

(a) Transverse stresses

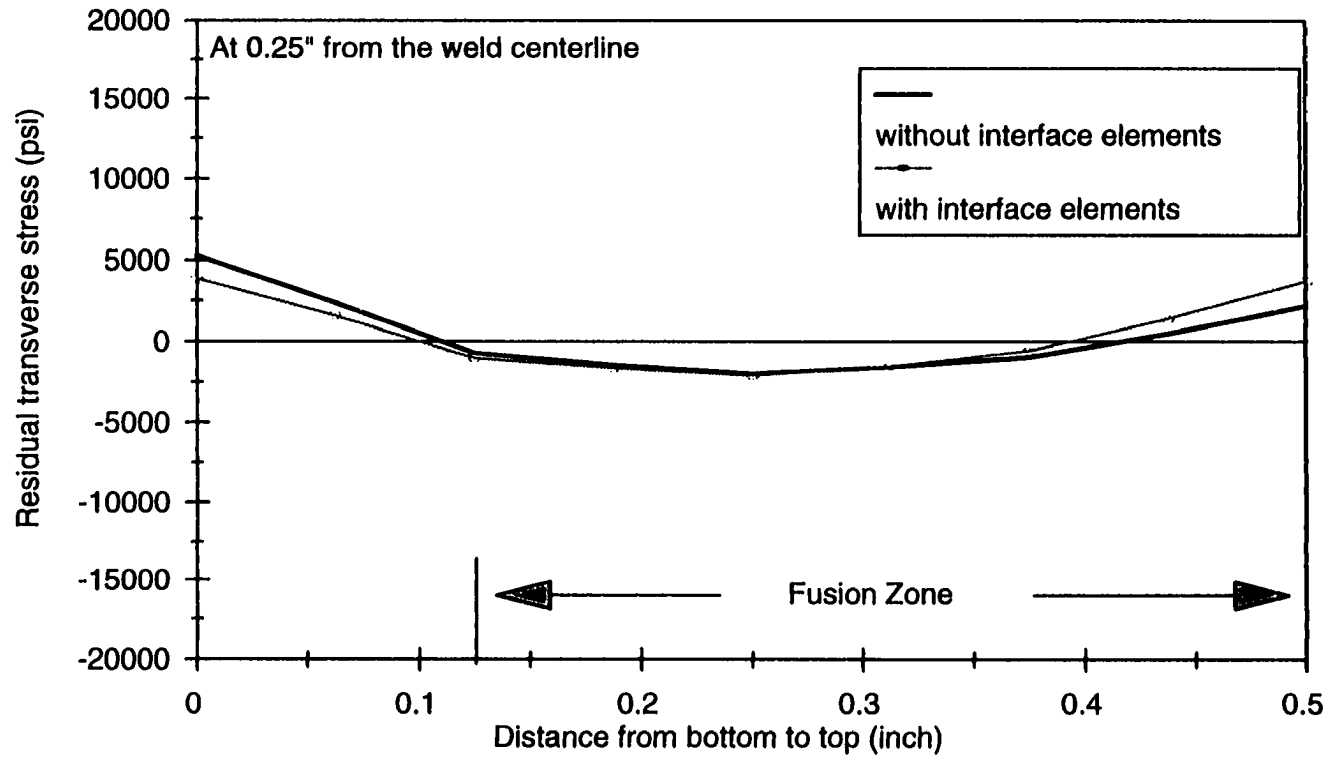
(b) Longitudinal stresses

Figure 4.23 (Continued)



122

(b)



(a)

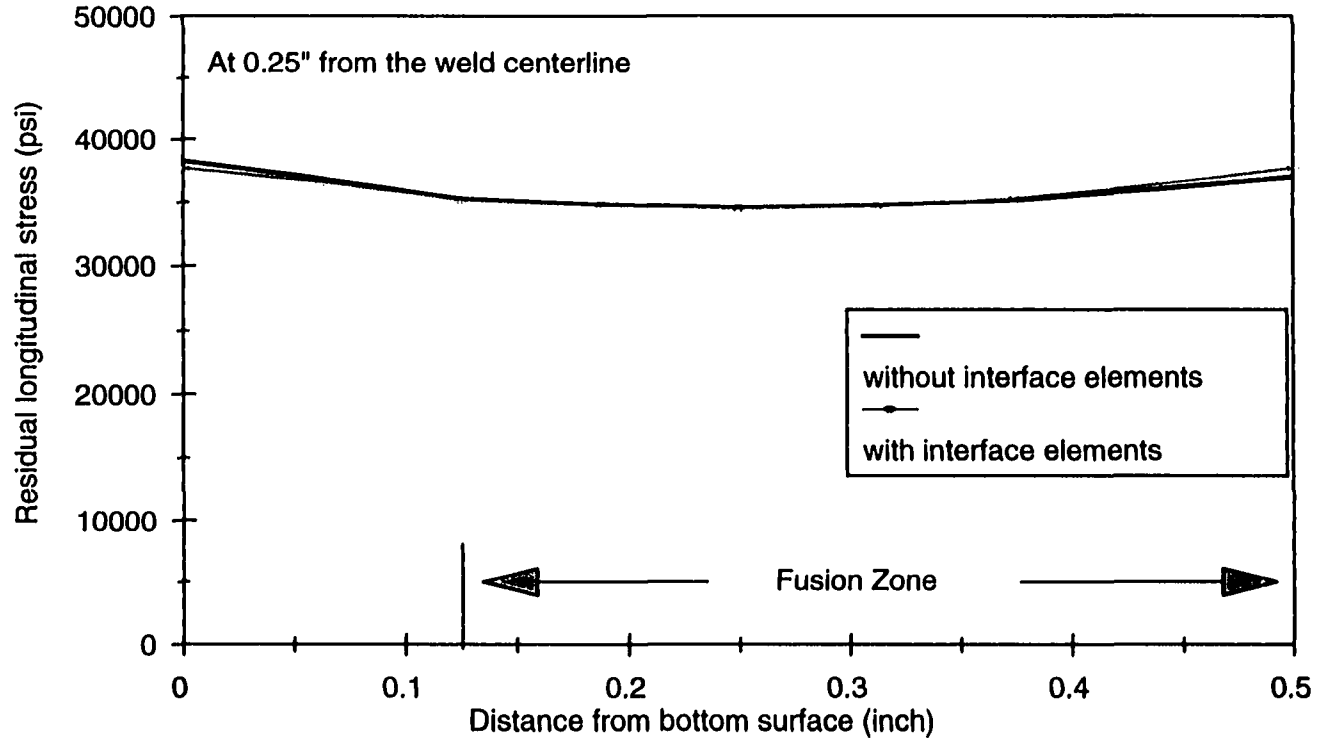
Figure 4.24 (Continued)

Figure 4.24 Through-thickness residual stress distributions at 0.25" from weld centerline for a three-pass welded plate

(a) Transverse stresses

(b) Longitudinal stresses

Figure 4.24 (Continued)



124

(b)

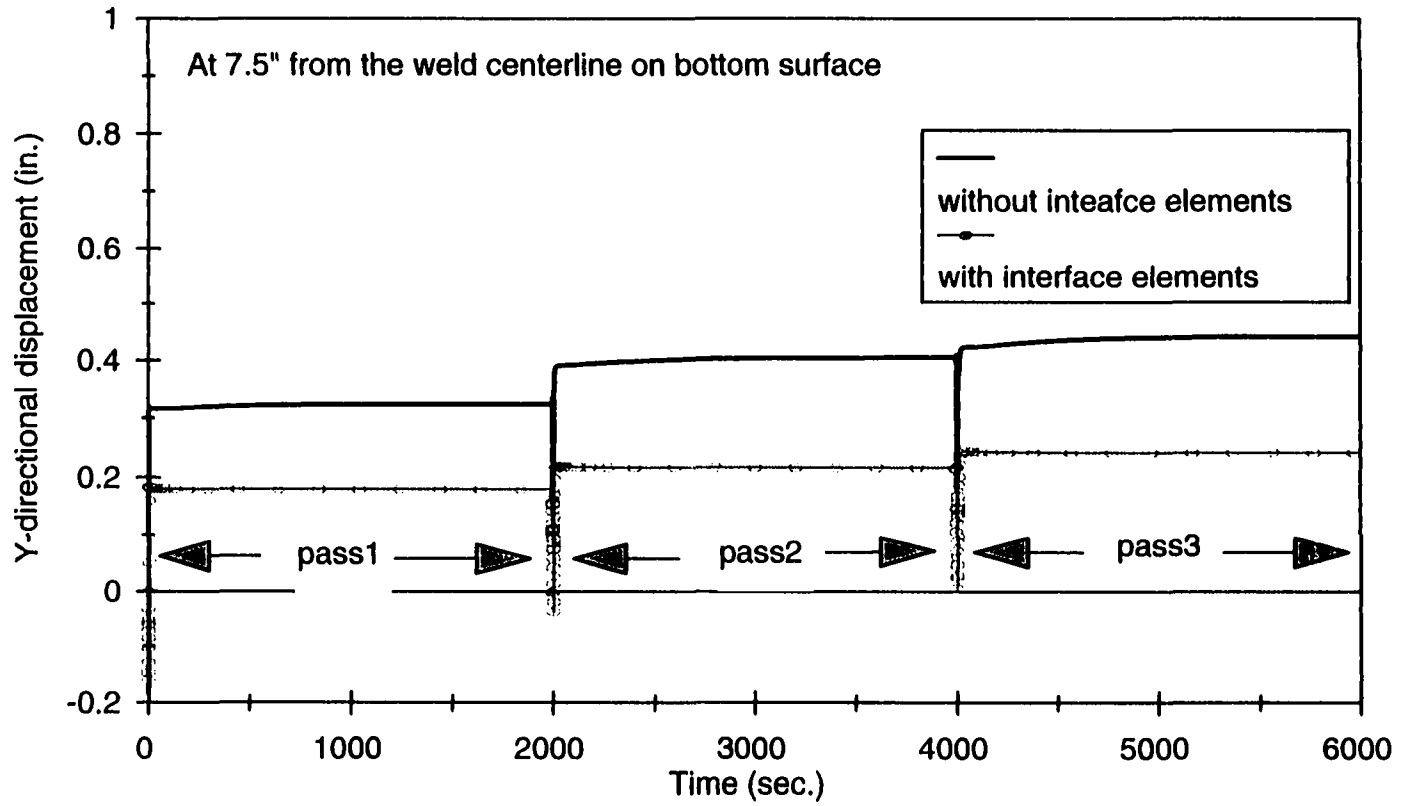


Figure 4.25 Distortion changes at 7.5" from the weld centerline on top surface for a three-pass welded plate

## CHAPTER 5

### PLASTIC STRAIN RELAXATION EFFECT

In the welding process, the weld material state is changed from solid to liquid during heating, and from liquid to solid during cooling. Therefore, it is reasonable that the thermo-mechanical characteristics of the temperature-dependent material are analyzed. However, most numerical welding analyses ignore the effect of the melting and resolidification of the fusion material during welding. In fact, numerical welding analysis does not consider the change of state from solid to liquid and back again. One of the most important problems in numerical welding analysis that should be solved is the accumulation of plastic strains in the regions that melt during the welding process. Once the temperature reaches the melting point, these plastic strains are relieved, but start to accumulate again when the material resolidifies. In most numerical analyses, the existence of non-zero material properties above the melting temperature causes the plastic strains to continue accumulating and to reach high values owing to the very low magnitude of the mechanical properties. Therefore, it is necessary to modify a numerical program so as to relieve the total plastic strain when the material melts. A general

theoretical treatment of such plastic strain accumulation effect was recently offered by Zhang *et al.* [82] within the context of materials thermo-plasticity constitutive behavior. However, it is very difficult to consider plastic strain relaxation and to determine the material properties at high temperature in thermo-mechanical analyses in commercial FEA codes. It is certain that the plastic strain relaxation affects the residual stresses and/or the distortions. However, it is not clear how much the plastic strain relaxation affects the residual stresses and/or the distortions. Even if the plastic strain relaxation effect is not much affected to the residual stresses and/or distortions, it is important to understanding the welding residual stresses and/or distortion with the plastic strain relaxation effect.

In order to perform the numerical simulations, a commercial numerical analysis package, ABAQUS [19], is used. Even though ABAQUS is a very useful tool, it is not specifically oriented toward welding simulation. In addition, ABAQUS also has the same problem mentioned above in the numerical welding analyses. Therefore, it is necessary to modify ABAQUS so as to relieve the accumulated plastic strains when the material melts, because ABAQUS does not have this feature. It can only be introduced by using the UMAT user subroutine, which represents the material behavior. Even if the development of the UMAT user subroutine is limited to modifying the material behavior artificially, its development is useful due to the high potential for applicability.

In order to incorporate the plastic strain relaxation effect, it is required to understand the constitutive equation of the thermo-elastic-plastic material, and then determine the proper method for representing the numerically material behavior. The

following chapters explain the constitutive equations, how to calculate the stress increments, and how to modify the stress increment calculation so as to incorporate the plastic strain relaxation effect. After that, the theoretical development and the verification of the plastic strain relaxation effect are explained.

## 5.1 Thermo-elastic-plastic materials behavior

### 5.1.1 Constitutive equations for thermo-elastic-plastic materials

When the material is assumed to be isotropic, one can drive the constitutive equations for thermo-elastic-plastic material behavior [12, 55, 82] in differential form. The total strain increment, valid for small deformation and small rotation, can be decomposed as follows:

$$d \varepsilon_{ij} = d \varepsilon_{ij}^e + d \varepsilon_{ij}^p + d \varepsilon_{ij}^T + d \varepsilon_{ij}^c. \quad (5.1.1)$$

Here  $d\varepsilon_{ij}^e$  is the elastic strain increment,  $d\varepsilon_{ij}^p$  is the plastic strain increment,  $d\varepsilon_{ij}^T$  is the thermal strain increment, and  $d\varepsilon_{ij}^c$  is the creep strain increment. In welding problems, the creep strain is negligible. Therefore, Eq.(5.1.1) can be rewritten as

$$d \varepsilon_{ij} = d \varepsilon_{ij}^e + d \varepsilon_{ij}^p + d \varepsilon_{ij}^T. \quad (5.1.2)$$

The sum of the first two terms in Eq.(5.1.2) is referred to as the mechanical strain.

The deviatoric stress is

$$S_{ij} = \sigma_{ij} - \frac{1}{3} \delta_{ij} \sigma_{kk} , \quad (5.1.3)$$

and deviatoric strain is

$$e_{ij} = \varepsilon_{ij} - \frac{1}{3} \delta_{ij} \varepsilon_{kk} , \quad (5.1.4)$$

where  $\delta_{ij}$  is Kronecker delta.

From Eqs. (5.1.2) and (5.1.4), one obtains the deviatoric strain increment (with

$$de_{ij}^T = 0)$$

$$de_{ij} = de_{ij}^e + de_{ij}^p . \quad (5.1.5)$$

The shear modulus is defined as

$$G = \frac{E}{2(1+\nu)} \quad (5.1.6)$$

where E is Young's modulus and  $\nu$  is Poisson's ratio. Therefore, Hook's law in deviatoric form is

$$e_{ij}^e = \frac{1}{2G} S_{ij} . \quad (5.1.7)$$

Differentiation of Eq.(5.1.7) gives

$$de_{ij}^e = \frac{1}{2G} dS_{ij} + \frac{1}{2} S_{ij} d\left(\frac{1}{G}\right) \quad (5.1.8)$$

and from Eqs.(5.1.5) and (5.1.8)

$$d S_{ij} = 2 G (d e_{ij} - d e_{ij}^p) - G S_{ij} d \left( \frac{1}{G} \right). \quad (5.1.9)$$

The change in stress is

$$d \sigma_{ij} = d S_{ij} + \frac{1}{3} \delta_{ij} d \sigma_{kk} \quad (5.1.10)$$

where  $d \sigma_{kk}$  is obtained from Hook's law, which gives

$$\varepsilon_{kk}^e = \frac{1-2\nu}{E} \sigma_{kk}. \quad (5.1.11)$$

Differentiation of Eq.(5.1.11) yields

$$d \varepsilon_{kk}^e = \frac{1-2\nu}{E} d \sigma_{kk} + \sigma_{kk} d \left( \frac{1}{3K} \right). \quad (5.1.12)$$

Here, K is the bulk modulus of the material and is defined as

$$K = \frac{E}{3(1-2\nu)}. \quad (5.1.13)$$

The volume change due to temperature change is

$$d \varepsilon_{kk}^T = \delta_{ii} d \varepsilon^T = 3 d \varepsilon^T \quad (5.1.14)$$

where  $\varepsilon^T$  is the uniaxial thermal dilatation for the material.

The total volume change with  $d \varepsilon_{kk}^p = 0$  is

$$d \varepsilon_{kk} = d \varepsilon_{kk}^e + d \varepsilon_{kk}^T. \quad (5.1.15)$$

Eqs.(5.1.12), (5.1.14), and (5.1.15) yield

$$d\sigma_{kk} = 3K[d\varepsilon_{kk} - \sigma_{kk} d(\frac{1}{3K}) - 3d\varepsilon^T] \quad (5.1.16)$$

and hence Eq.(5.1.10) with Eqs.(5.1.9) and (5.1.16) becomes

$$d\sigma_{ij} = 2G(d\varepsilon_{ij} - d\varepsilon_{ij}^p) - G S_{ij} d(\frac{1}{G}) + \delta_{ij} K[d\varepsilon_{kk} - \sigma_{kk} d(\frac{1}{3K}) - 3d\varepsilon^T]. \quad (5.1.17)$$

An associated flow rule is assumed as

$$d\varepsilon_{ij}^p = d\lambda S_{ij}. \quad (5.1.18)$$

Here the following Von Mises yield condition is adopted.

$$f = \frac{1}{2} S_{ij} S_{ij} - \frac{1}{3} \sigma_y^2 (\varepsilon^p, T) = 0 \quad (5.1.19)$$

where  $\sigma_y$  is the yield stress for the material.

For simplicity, isotropic hardening is assumed in this study.

The effective plastic strain is defined as

$$\sigma_e d\varepsilon^p = \sigma_{ij} d\varepsilon_{ij}^p = S_{ij} d\varepsilon_{ij}^p \quad (5.1.20)$$

and the effective Von Mises stress is

$$\sigma_e^2 = \frac{3}{2} S_{ij} S_{ij}. \quad (5.1.21)$$

Differentiation of Eq.(5.1.19) gives

$$d f = S_{ij} d S_{ij} - \frac{2}{3} \sigma_y \left( \frac{\partial \sigma_y}{\partial \epsilon^p} d \epsilon^p + \frac{\partial \sigma_y}{\partial T} d T \right) = 0. \quad (5.1.22)$$

Eqs.(5.1.18), (5.1.20), and (5.1.21) in Eq.(5.1.21) together with Eq.(5.1.9) for  $d S_{ij}$  gives

$$d \lambda = \frac{[S_{ij} d e_{ij} - \frac{1}{3} \sigma_e^2 d(\frac{1}{G}) - \frac{\sigma_y}{3G} (\frac{\partial \sigma_y}{\partial T}) d T]}{\frac{2}{3} \sigma_e^2 (1 + \frac{\partial \sigma_y / \partial \epsilon^p}{3G})}. \quad (5.1.23)$$

In order to further evaluate the above expression (5.1.23) for  $d \lambda$ , it is necessary to obtain  $\frac{\partial \sigma_y}{\partial \epsilon^p}$  and  $\frac{\partial \sigma_y}{\partial T}$ . It is assumed that a relationship between  $\sigma_y$ ,  $\epsilon^p$ , and  $T$  can be derived from the data obtained in a series of tensile tests at different temperatures using virgin material specimens. This data is used to develop the idealized, bilinear, engineering stress- strain curves shown in Figure 5.1.

In isotropic hardening, the size of the yield surface changes uniformly with the same shape as initially, while its center remains fixed in the stress space. The size of yield surface is based on the accumulated effective plastic strain and the temperature level. To convert the curves shown in Figure 5.1 to stress-plastic strain curves, we have for constant temperature  $T$  and  $\sigma \geq \sigma_{y0}$ ,

$$\sigma = \sigma_{y0} + E_T \left( e - \frac{\sigma_{y0}}{E} \right), \quad (5.1.24)$$

$$e^p = e - \frac{\sigma}{E} \quad (5.1.25)$$

where  $\sigma_{y0}$  is the initial (virgin) material yield stress, and  $E_T$  is the tangential modulus.

Combining the above equations and noting that the current stress is the current yield stress (i.e.,  $\sigma = \sigma_y$ ) results in

$$\sigma_y = \sigma_{y0} + \frac{E \cdot E_T}{E - E_T} e^n. \quad (5.1.26)$$

Thus, Eq.(5.1.26) gives the relationship between the yield stress and the plastic strain for monotonic uniaxial loading at constant temperature. The curves described by Eq.(5.1.26) are shown in Figure 5.2. It is assumed that Eq.(5.1.26) relates the yield stress and accumulated effective plastic strain for multiaxial loading conditions. Additionally, it is assumed that the relationship holds regardless of the history leading to  $\epsilon^p$ .

Then,

$$\frac{\partial \sigma_y}{\partial \epsilon^p} = \frac{E \cdot E_T}{E - E_T} = H', \quad (5.1.27)$$

$$\frac{\partial \sigma_y}{\partial T} = e^n \frac{\partial H'}{\partial T} + \frac{\partial \sigma_{y0}}{\partial T}. \quad (5.1.28)$$

Substitution of Eqs.(5.1.27) and (5.1.28) into Eq.(5.1.23) gives

$$d\lambda = \frac{[S_{ij} d e_{ij} - \frac{1}{3} \sigma_e^2 d(\frac{1}{G}) - \frac{\sigma_y}{3G} (e^n \frac{\partial H'}{\partial T} + \frac{\partial \sigma_{y0}}{\partial T}) dT]}{\frac{2}{3} \sigma_e^2 (1 + \frac{H'}{3G})}. \quad (5.1.29)$$

Eqs.(5.1.17), (5.1.23), and (5.1.9) lead to the following constitutive equation

$$dS_{ij} = 2G(d\epsilon_{ij} - \frac{3S_{ij}S_{kk}d\epsilon_{kk}}{2\sigma_c^2(1+H'/3G)}) + \frac{(e^p \frac{\partial H'}{\partial T} + \frac{\partial \sigma_{v0}}{\partial T})dT S_{ij}}{\sigma_c(1+H'/3G)} - \frac{d(\frac{1}{G})H' S_{ij}}{3(1+H'/3G)}. \quad (5.1.30)$$

With the help of Eqs.(5.1.4), (5.1.7), (5.1.12), (5.1.17), (5.1.18), and (5.1.30), the change in the stress,  $d\sigma_{ij}$ , is:

$$d\sigma_{ij} = 2G(d\epsilon_{ij} + \frac{\nu}{1-2\nu}\delta_{ij}d\epsilon_{kk}) - \frac{3GS_{kk}d\epsilon_{kk}S_{ij}}{\sigma_c^2(1+H'/3G)} + (\frac{1}{1+H'/3G} - 1)Gd(\frac{1}{G})S_{ij} + \frac{(e^p \frac{\partial H'}{\partial T} + \frac{\partial \sigma_{v0}}{\partial T})dT}{\sigma_c(1+H'/3G)}S_{ij} - \delta_{ij}K[d(\frac{1}{3K})\sigma_{kk} + 3d\epsilon^T]. \quad (5.1.31)$$

The variation of the material parameters  $G$  and  $K$  in Eq.(5.1.31) is due to temperature.

In the case of elastic conditions, the change in stress,  $d\sigma_{ij}$ , can be written as

$$d\sigma_{ij} = 2G(d\epsilon_{ij} + \frac{\nu}{1-2\nu}\delta_{ij}d\epsilon_{kk}) - Gd(\frac{1}{G})S_{ij} - \delta_{ij}K[d(\frac{1}{3K})\sigma_{kk} + 3d\epsilon^T]. \quad (5.1.32)$$

In matrix notation the thermo-elastic-plastic constitutive equation (5.1.31) becomes

$$\{d\sigma\} = [D]\{d\epsilon\} + C\{S\} - M\{d\epsilon^T\}. \quad (5.1.33)$$

In extended notation Eq.(5.1.33) can be expressed as

$$\begin{Bmatrix} d\sigma_{11} \\ d\sigma_{22} \\ d\sigma_{33} \\ d\sigma_{12} \end{Bmatrix} = 2G \begin{bmatrix} \frac{1-\nu}{1-2\nu} \frac{S_{11}^2}{L} & \frac{\nu}{1-2\nu} \frac{S_{11}S_{22}}{L} & \frac{\nu}{1-2\nu} \frac{S_{11}S_{33}}{L} & -\frac{S_{11}S_{12}}{L} \\ & \frac{1-\nu}{1-2\nu} \frac{S_{22}^2}{L} & \frac{\nu}{1-2\nu} \frac{S_{22}S_{33}}{L} & -\frac{S_{22}S_{12}}{L} \\ & & \frac{1-\nu}{1-2\nu} \frac{S_{33}^2}{L} & -\frac{S_{33}S_{12}}{L} \\ & & & \frac{1}{2} - \frac{S_{12}^2}{L} \end{bmatrix} \begin{Bmatrix} d\epsilon_{11} \\ d\epsilon_{22} \\ d\epsilon_{33} \\ d\epsilon_{12} \end{Bmatrix} \\
 + C \begin{Bmatrix} S_{11} \\ S_{22} \\ S_{33} \\ S_{12} \end{Bmatrix} - M \begin{Bmatrix} 1 \\ 1 \\ 1 \\ 0 \end{Bmatrix} \tag{5.1.34}$$

where

$$C = \left( \frac{2}{3} \frac{\sigma_c^2}{L} - 1 \right) G d \left( \frac{1}{G} \right) + \frac{2}{3} \frac{\sigma_c}{L} \left( e^{\nu} \frac{\partial H'}{\partial T} + \frac{\partial \sigma_{y0}}{\partial T} \right) dT, \tag{5.1.35}$$

$$M = K d \left( \frac{1}{3K} \right) \sigma_{kk} + 3 d \epsilon^T, \tag{5.1.36}$$

$$L = \frac{2}{3} \sigma_c^2 (1 + H'/3G). \tag{5.1.37}$$

Here, the strain rate and temperature rate are assumed to be constant during the increment. Then Eq.(5.1.34) can be written in incremental form

$$\{ \Delta \sigma \} = [D] \{ \Delta \epsilon \} + Cg \{ S \} + Mg \{ I \} \tag{5.1.38}$$

where

$$Cg = \frac{\Delta G}{G} + \left[ \frac{(\varepsilon^p \Delta H' + \Delta \sigma_{y0})}{\sigma_e} - \frac{\Delta G}{G} \right] \frac{1}{1 + H'/3G}, \quad (5.1.39)$$

$$Mg = \frac{\Delta K}{K} \frac{\sigma_{kk}}{3} - 3K \Delta \varepsilon^T. \quad (5.1.40)$$

### 5.1.2 Thermo-mechanical material properties

It is assumed that the constitutive relations can be described in terms of thermo-elastic-plasticity. In the mechanical analysis, the parameters required to describe the constitutive model are Young's modulus (elastic modulus),  $E$ ; Poisson's ratio,  $\nu$ ; initial yield stress,  $\sigma_0$ ; hardening modulus,  $H'$ ; and thermal expansion coefficient,  $\alpha$ .

#### Thermal expansion coefficient ( $\alpha$ )

In ABAQUS [19], the thermal expansion coefficients are defined on an average basis. They are interpreted as total expansion coefficients from a reference temperature, so that they generate thermal strains according to the following formula:

$$\varepsilon^T = \alpha(T)(T - T_0) - \alpha(T_1)(T_1 - T_0). \quad (5.1.41)$$

Here  $\varepsilon^T$  is the total thermal strain at a material point,  $T$  is the current temperature at the same material point,  $T_1$  is the initial temperature at the same material point,  $T_0$  is the

reference value for the thermal coefficient,  $\alpha ( T )$  is the mean coefficient of thermal expansion.

As mentioned in Feng's [83] dissertation, the effect of solidification shrinkage can be incorporated into the finite element models by modifying the thermal expansion coefficient in the solidification temperature range. Apparently, the thermal contraction of liquid metal does not cause any mechanical stress/strain in the solid portion of the model, i.e., the liquid metal can flow freely. Therefore, the solidification shrinkage can be effectively neglected in the upper portion of the solidification temperature range where a solid network has not formed. Based on this consideration, only the solidification shrinkage and thermal contraction due to temperature change below the coherent temperature ( the temperature at which solid network of dendrites is formed) are included in the thermal stress models.

For mathematical convenience, the liquidus temperature is chosen as the reference temperature for calculating the thermal expansion coefficient. The advantage is that the thermal expansion coefficient for temperatures above the coherent temperature is set to zero. As a result absolutely no thermal expansion or contraction get calculated in the FEA.

#### Poisson's ratio ( $\nu$ )

The Poisson's ratio has a weak dependence upon temperature.

### Elastic modulus (E)

The elastic modulus strongly depends on the temperature. The elastic modulus is assumed to decrease linearly to a very low value at the solidus temperature, to further decrease linearly to an even lower value at the coherent temperature, and to hold constant through the temperature to approximate the near zero strength of the molten weld pool.

### Hardening Modulus (H')

The hardening modulus also depends strongly on the temperature. The value of the hardening modulus at room temperature is greater than that at other temperatures. When the temperature increases, the value of the hardening modulus decreases to zero (see Figure 5.1). A zero value of the hardening modulus equals the elastic-perfectly plastic material behavior.

#### 5.1.3 Calculation of stress increments with the plastic strain relaxation effect

In the modification of material behavior for ABAQUS calculation, the radial return method is used for calculating the stress increments. The concept and procedure is taken from Hughes's work [84].

Lindgren *et al.*[55] applied the radial return method to shell structures in welding mechanical analysis. Also, Karlsson *et al.* [43] employed this method for a 3-D pipe

model. Karlsson *et al.* [73] used this method for calculations of FEA residual stresses in a butt-welded plate and a girth-welded pipe.

The radial return algorithm for thermo-elastic-plastic material with Von Mises yield condition, associated flow rule and linear, isotropic hardening is employed. The material properties are temperature dependent. The algorithm is suggested from Lindgren *et al.* [55] and Karlsson *et al.* [73] on the basis of the effort of Hughes *et al.* [84].

The algorithm is modified for the thermo-elastic-plastic material to incorporate the plastic strain relaxation effect. This modification results in the fact that the accumulated plastic strain vanishes when the temperature exceeds  $T_{\text{annealing}}$  ( the plastic strain relaxation temperature), so that the corresponding elastic constitutive matrix becomes small (non-zero to avoid numerical singularities) and the stresses also become very small. The following diagram (Figure 5.3) shows the schematic explanation of how to work the modified radial return algorithm inside the UMAT user subroutine [19].

The following steps are the modified stress increment calculation procedure for the thermo-elastic-plastic material to incorporate the plastic strain relaxation effect.

### Step 1. Initialization

1. Calculate elastic stress increment due to temperature dependent elastic constants:

$$\{ \Delta \sigma_T \} = \left( \frac{\Delta G}{G^n} \{ S \}^n + \frac{\Delta K}{K^n} \frac{\sigma_k^n}{3} I \right). \quad (5.1.42)$$

2. Set up elastic constitutive matrix  $[C]^{n+1}$ .

Step 2. Check plastic strain relaxation temperature ( $T_{annealing}$ )

1. If  $Temp + \Delta Temp \geq T_{annealing}$ , then the plastic strains and the stresses are assumed to be zero:

$$\begin{aligned} \{\varepsilon_p\}^{n+1} &= 0, \\ \{\sigma\}^{n+1} &= 0, \end{aligned} \quad (5.1.43)$$

and go to Step 1.

2. Else if  $Temp + \Delta Temp < T_{annealing}$ , then go to Step 3.

Step 3. Calculate the thermo-elastic trial stress

1. Calculate the thermo-elastic trial stress:

$$\{\sigma^{tr}\} = \{\sigma\}^n + [C]^{n+1} \{\Delta\varepsilon_M\} + \{\Delta\sigma_T\} \quad (5.1.44)$$

where  $\Delta\varepsilon_M = \Delta\varepsilon - \Delta\varepsilon^T I$ , the increment in total mechanical strains.

2. Calculate yield stress at the end of the time step assuming the elastic conditions:

$$\sigma_y = \sigma_{y0}(T^{n+1}) + H'(T^{n+1})\varepsilon_p^n. \quad (5.1.45)$$

3. Calculate deviatoric stress and effective stress:

$$\{S^{tr}\} = \{\sigma^{tr}\} - \frac{\sigma_{kk}^{tr}}{3} I, \quad (5.1.46)$$

$$\sigma_{e, tr} = \sqrt{\frac{3}{2} \{S^{tr}\}^T \{S^{tr}\}}. \quad (5.1.47)$$

#### Step 4. Check yielding

1. If  $\sigma_e^{rr} \leq \sigma_y$ , then the increment is assumed to be elastic:

$$\begin{aligned} \{\sigma\}^{n+1} &= \{\sigma^{rr}\}, \\ \sigma_y^{n+1} &= \sigma_y, \end{aligned} \quad (5.1.48)$$

go to Step 1.

2. Else if  $\sigma_e^{rr} > \sigma_y$ , then go to Step 5.

#### Step 5. Radial return of trial stresses onto yield surface

1. Calculate increment in effective plastic strain:

$$\Delta \varepsilon_p = \frac{\sigma_e^{rr} - \sigma_y}{3G^{n+1} + H'^{n+1}}. \quad (5.1.49)$$

2. Calculate radial return of stresses to the yield surface:

$$\{\sigma\}^{n+1} = \{\sigma_{rr}\} - 2G^{n+1} \Delta \varepsilon_p \frac{3}{2} \frac{\{S^{rr}\}}{\sigma_e^{rr}}. \quad (5.1.50)$$

#### Step 6. Update plastic strains and yield limit

1. Update effective plastic strain and yield limit:

$$\varepsilon_p^{n+1} = \varepsilon_p^n + \Delta \varepsilon_p, \quad (5.1.51)$$

$$\sigma_y^{n+1} = \sigma_{y0} + H'(T^{n+1}) \varepsilon_p^{n+1}. \quad (5.1.52)$$

2. Update plastic strains:

$$\{\varepsilon_p\}^{n+1} = \{\varepsilon_p\}^n + \Delta\varepsilon_p \frac{\frac{3}{2}\{S^{rr}\}}{\sigma_e^{rr}}. \quad (5.1.53)$$

## 5.2. Theoretical development

The explanation of the simple theoretical example for the plastic strain relaxation is shown in Figure 5.4.

Consider a simple 1-D bar with length  $l$  fixed between two walls (Figure 5.4(a)). Assume the elastic-perfectly-plastic material behavior for the bar. The governing equation of the bar model is as follows;

$$\varepsilon^{total} = \varepsilon^e + \varepsilon^p + \varepsilon^T \quad (5.2.1)$$

where  $\varepsilon^{total} = 0$ .

As illustrated in Figure 5.4(b), the temperature-dependent material properties are employed for the analysis. The values of the material properties are assumed to be relatively large when the temperature is lower than or equal to  $T_1$ . Once the temperature rises above  $T_2$ , small values are assumed. If the temperature is between  $T_1$  and  $T_2$ , the material properties are determined by linear interpolation. The temperature history is shown in Figure 5.4(c). The bar is heated up linearly from room temperature to the annealing temperature,  $T_{annealing}$ , where the plastic strain relaxation occurs. This

annealing temperature for the plastic strain relaxation is set artificially. After the temperature reaches to  $T_{\text{annealing}}$ , the bar is cooled down to room temperature linearly.

The following explanation shows the characteristics of strain behaviors under given temperature histories shown in Figure 5.4(c). Two methods are explained: (i) the method without the plastic strain relaxation effect, and (ii) the method with the plastic strain relaxation. Figures 5.4(c) and (d) show the strain histories using two different methods. The thermal strains and elastic strains are given in Figure 5.4(c) and the plastic strains are shown in Figure 5.4(d).

### 5.2.1 Model without the plastic strain relaxation effect

As shown in Figure 5.4(c), the thermal strain is proportional to the temperature. The region  $o$  to  $d$  and the region  $d$  to  $g$  represent heating and cooling processes, respectively. In region  $o$  to  $a$ , the compressive elastic strain increases to the compressive elastic strain limit ( $-\epsilon_y$ ) and the thermal strain increases. The plastic strain does not appear in this region because the magnitudes of the compressive elastic strain and thermal strain are the same. In region  $a$  to  $b$ , the compressive elastic strain is kept constant due to the perfect-plasticity assumption. However, the compressive plastic strain increases as the thermal strain increases. In region  $b$  to  $c$ , the temperature reaches  $T_2$ . The compressive elastic strain decreases steeply because the yield stress decreases with increasing temperature. The compressive elastic strain reaches a value near zero. Therefore, the compressive plastic strain increases very rapidly with increasing thermal

strain. In region *c* to *d*, the temperature changes from  $T_2$  to  $T_{\text{annealing}}$ . The compressive plastic strain increases, but the plastic strain increasing rate becomes the same as that in region *a* to *b* due to the constant elastic strain. When the temperature reaches  $T_{\text{annealing}}$ , the compressive strain and thermal strain have maximum values. In region *d* to *e*, the bar is cooled to  $T_2$ . The elastic strain becomes tensile, but it has a very small value. The compressive plastic strain decreases with decreasing the thermal strain. In region *e* to *f*, the temperature becomes  $T_1$ . The tensile elastic strain increases to the yield limit ( $\epsilon_y$ ), whereas the thermal strain decreases continuously. Therefore, the compressive plastic strain increases very gradually. In region *f* to *g*, the tensile elastic strain remains at the yield strain value. The compressive plastic strain decreases with decreasing thermal strain. Finally, the magnitude of the compressive plastic strain is the same as that of the final tensile elastic strain due to zero thermal strain.

### 5.2.2 Model with the plastic strain relaxation effect

As shown in Figures 5.4(c) and (d), the thermal, elastic and plastic histories are the same as those without the plastic strain relaxation effect during heating, whereas the thermal and plastic strain histories during cooling are totally different from those without the plastic strain relaxation effect. The elastic strain history during cooling is a little bit different from that without the plastic strain relaxation effect. However, the same elastic strain history without the plastic strain relaxation effect is still used since the difference between two elastic strains with and without the plastic strain relaxation effect is very

small. When the temperature reaches  $T_{\text{annealing}}$ , the accumulated plastic strain should be zero. Therefore, the elastic strains as well as the thermal strain should be zero in order to satisfy the governing equation (5.2.1). The thermal strain calculation is based on the reference temperature. The reference temperature is taken to be room temperature under the method without the plastic strain relaxation effect, whereas in the method with the plastic strain relaxation effect the reference temperature is set to room temperature during heating and is changed to  $T_{\text{annealing}}$  during cooling. Accordingly, the thermal strain at  $T_{\text{annealing}}$  can be zero. In region  $g$  to  $e$ , the tensile plastic strain increases from zero as the thermal strain decreases from zero. In region  $e$  to  $g$ , the tensile plastic strain increases as the thermal strain decreases. Finally, the tensile plastic strain becomes very large and the final thermal strain becomes compressive.

As depicted in Figure 5.4(d), the residual plastic strain difference between the two methods is observed. The residual plastic strains with the plastic strain relaxation effect become tensile, whereas the residual plastic strains without the plastic strain relaxation effect become compressive. Therefore, the residual stresses and distortion with the plastic strain relaxation effect might be different from those without the plastic strain relaxation effect. The differences between the residual stresses under both methods with and without the plastic strain relaxation effect are verified.

### 5.3 Verification

The same model is shown in Figure 5.4(a). All conditions follow the assumptions of Chapter 5.2. Figure 5.5(a) shows the temperature history. The bar is heated up from room temperature (20 °C) to 1520 °C uniformly and cooled down to room temperature.  $T_{\text{annealing}}$  is assumed to be 1520 °C.  $T_1$  and  $T_2$  are 1020 °C and 1320 °C, respectively.

As shown in Figure 5.5(b) and (f), two different stress-strain curves are assumed: one is for the assumption of elastic perfectly plastic behavior (Figure 5.5(b)), and the other is for the assumption of elastic plastic bilinear behavior with isotropic hardening effect (Figure 5.5(f)).

To include the plastic strain relaxation effect, the UMAT subroutine of ABAQUS is developed. The verification of the UMAT subroutine is required prior to the verification of the theory. The following steps indicate how to verify the UMAT subroutine. First, the results are calculated from a ABAQUS run. Next, the results under the method without the plastic strain relaxation effect are obtained from the ABAQUS run with UMAT. If the results from both ABAQUS runs agree, it can be determined that the UMAT works correctly. These results from the ABAQUS run are indicated as ‘without plastic strain relaxation’ in the figures. After then, the results from the ABAQUS run with the UMAT subroutine under the method with considering plastic strain relaxation effect are calculated. These results are labeled as ‘with plastic strain relaxation’ in the figures.

The results from both methods with and without the plastic strain relaxation effect with elastic-perfect plasticity assumption (Figure 5.5(b)) are shown in Figures 5.5(c) and (d). The results are similar to the those given in Figures 5.4(c) and (d). Therefore, the plastic strain relaxation concept is theoretically acceptable and numerically proven. Due to the elastic-perfect plasticity assumption, the stress histories corresponding to Figures 5.5(a) to (d) are almost identical to each other (Figure 5.5(e)).

Figure 5.5(g) gives the stress histories when the material is assumed to have elastic linear plasticity with isotropic hardening (Figure 5.5(f)). The stress values under the methods with and without the plastic strain relaxation effect deviate at  $T_{\text{annealing}}$ . However, the residual stress with considering plastic strain relaxation effect gives different value, but the difference is not much when compared with the value without the plastic strain relaxation effect. It is obvious that the plastic strain relaxation affects the final residual stress field a little bit.

#### 5.4 Application

In order to apply the plastic strain relaxation theory to a real material case, ASTM A316 mild steel is selected. As shown in Figure 5.6, the model is a 1-D bar with springs that have the same spring constant,  $k$ . Very rigid plates are attached to the bar and the springs at both top and bottom sides. If the spring constant is very large, this model can be considered the same as the model in Figure 5.4(a).

The temperature-dependent material properties used are given in Figures 4.1(a) and (b).  $T_{\text{annealing}}$  is assumed to be 1300 °F and an elastic linear plasticity with isotropic hardening effect is considered. It is assumed that the plastic strain relaxation occurs instantaneously at  $T_{\text{annealing}}$ . The spring constant,  $k$ , varies from a very large value to a very small one. The results of strains and stresses with  $k = 1 \times 10^8$  ksi-in are shown in Figures 5.7(a) to (c), respectively. The thermal and the elastic strains are given in Figure 5.7(a), and the plastic strains are shown in Figure 5.7(b). Also, the residual stresses are a little bit different due to the hardening effect (Figure 5.7(c)).

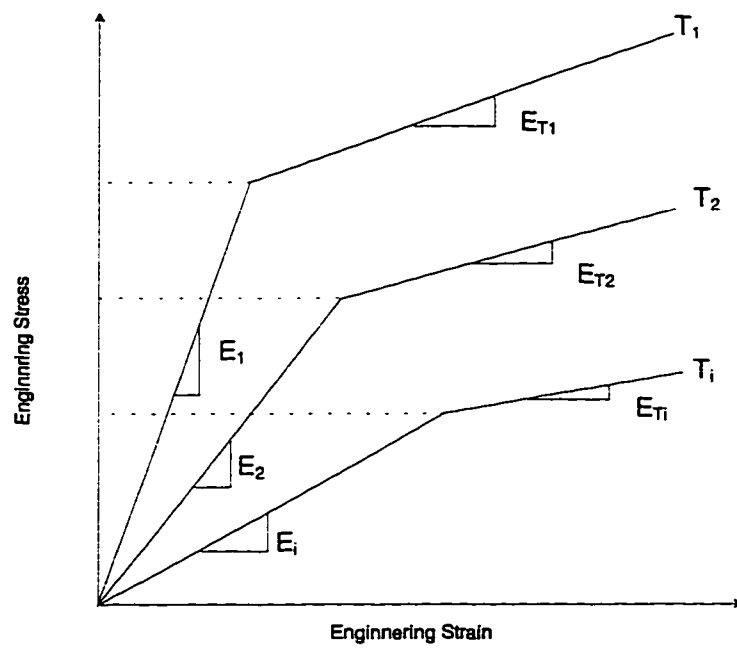
Figure 5.8 shows the effects of the differences in  $\Delta\varepsilon^{\text{pl}}$  and  $\Delta\sigma_{\text{res}}$  with varying spring constant when the methods with and without the plastic strain relaxation effect are compared each other.  $\Delta\varepsilon^{\text{pl}}$  and  $\Delta\sigma_{\text{res}}$  are defined as;

$$\Delta\varepsilon^{\text{pl}} = \varepsilon^{\text{pl}}(\text{with plastic strain relaxation}) - \varepsilon^{\text{pl}}(\text{without plastic strain relaxation}), \quad (5.4.1)$$

and

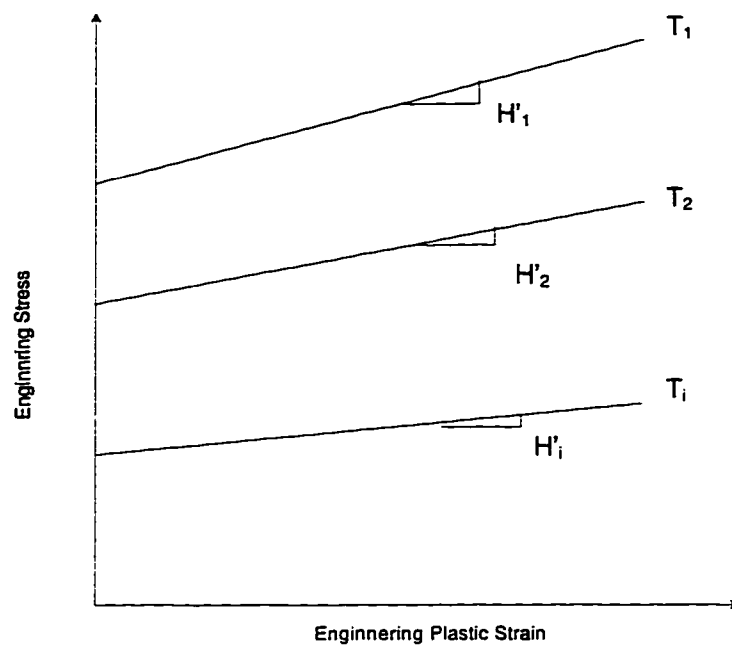
$$\Delta\sigma_{\text{res}} = \sigma_{\text{res}}(\text{with plastic strain relaxation}) - \sigma_{\text{res}}(\text{without plastic strain relaxation}). \quad (5.4.2)$$

The log scale is used for the axis of the spring constant (degree of restraint),  $k$ . The results show that  $\Delta\varepsilon^{\text{pl}}$  becomes bigger with increasing spring constant. Once  $k$  equals 10000 ksi-in, the  $\Delta\varepsilon^{\text{pl}}$  becomes constant with increasing  $k$ . However, the  $\Delta\sigma_{\text{res}}$  increases from  $k = 0.1$  ksi-in to  $k = 1000$  ksi-in and decreases steeply to  $k = 10000$  ksi-in. Once  $k$  exceeds 10000 ksi-in, the  $\Delta\sigma_{\text{res}}$  remains constant with increasing  $k$ . This means the spring is already stiffened enough and that therefore, the bar can not move along axial direction as the temperature.



$T_i$  = Temperature  
 $E_i$  = Young's Modulus at  $T_i$   
 $E_{Ti}$  = Tangential Modulus at  $T_i$   
 $\sigma_{yi}$  = Virgin Material Yield Stress at  $T_i$

Figure 5.1 Idealized engineering stress-strain curves



$T_i$  = Temperature  
 $E_i$  = Young's Modulus at  $T_i$   
 $H'_i$  = Hardening Modulus at  $T_i$   
 $\sigma_{yi}$  = Virgin Material Yield Stress at  $T_i$

Figure 5.2 Idealized engineering stress - plastic strain curves

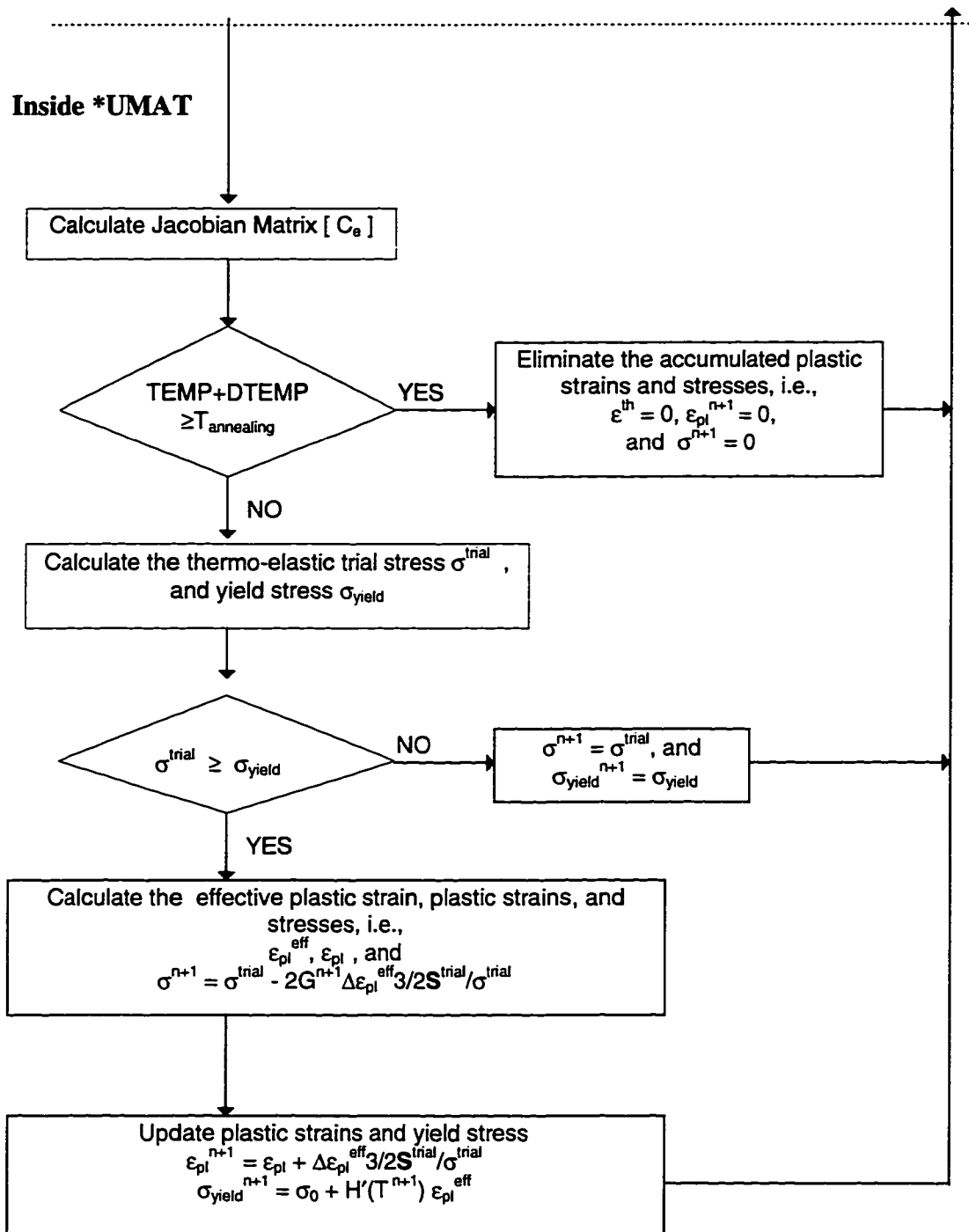
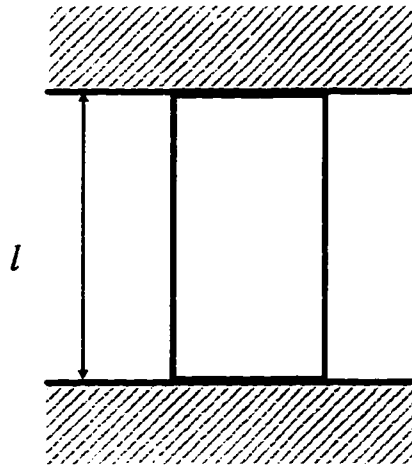
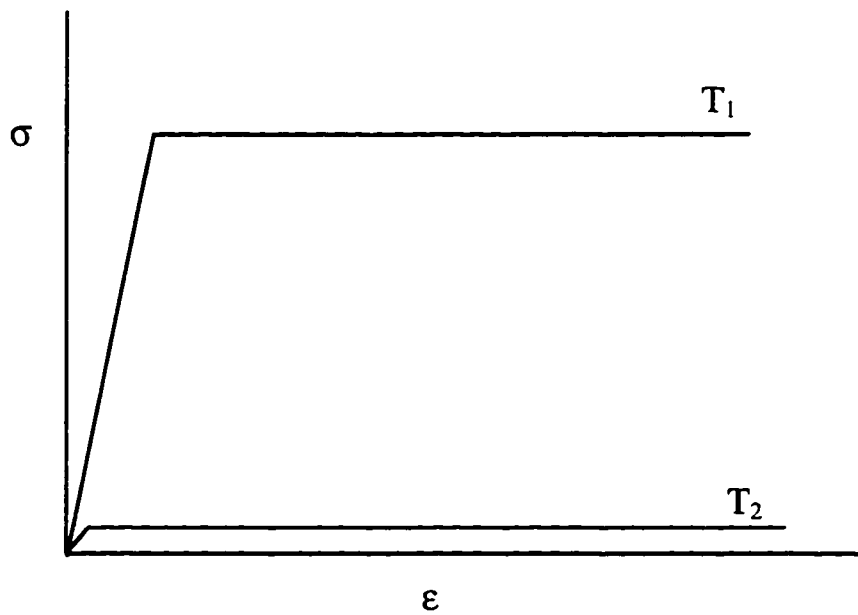


Figure 5.3 Flow chart of the plastic strain relaxation effect algorithm



(a)

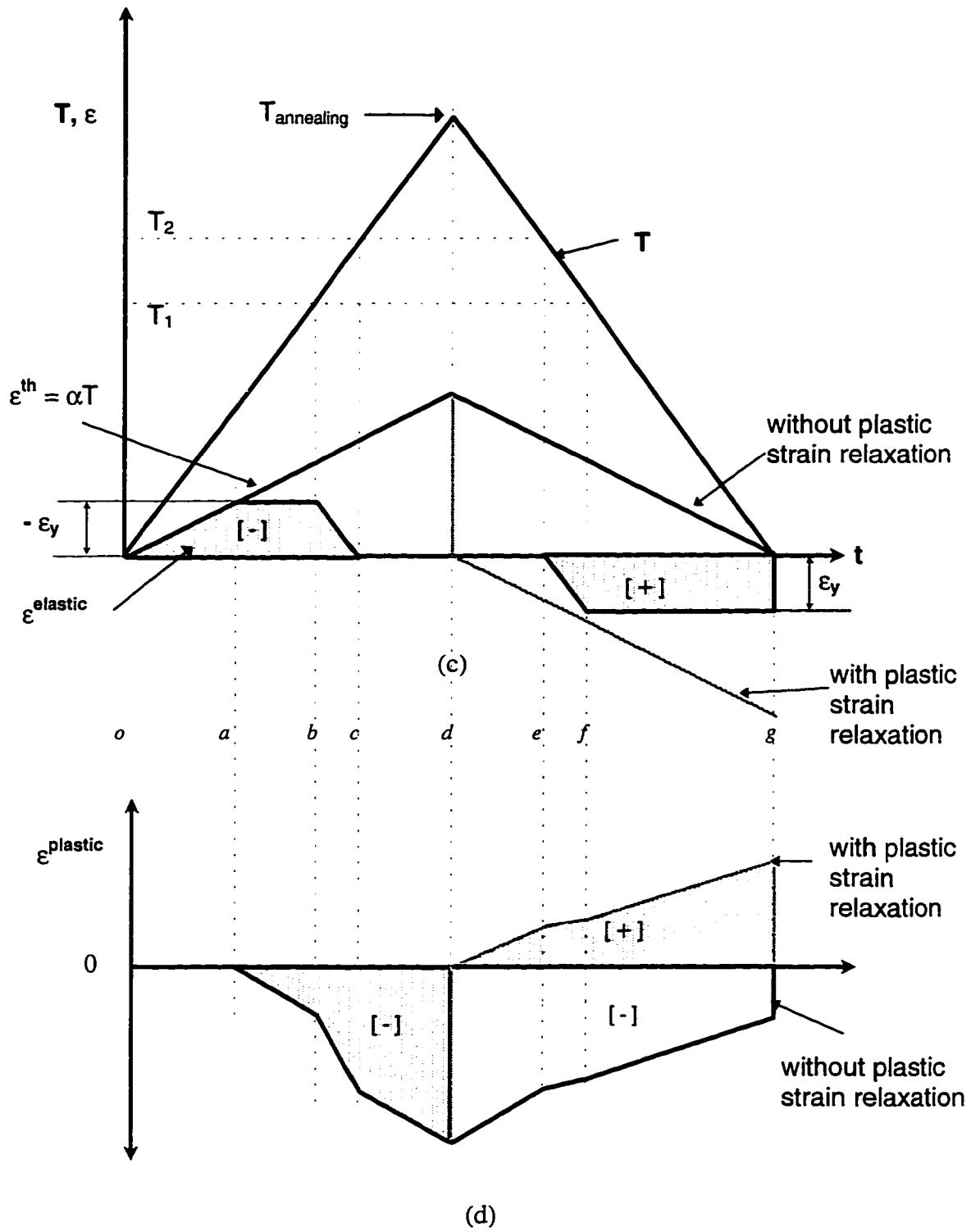


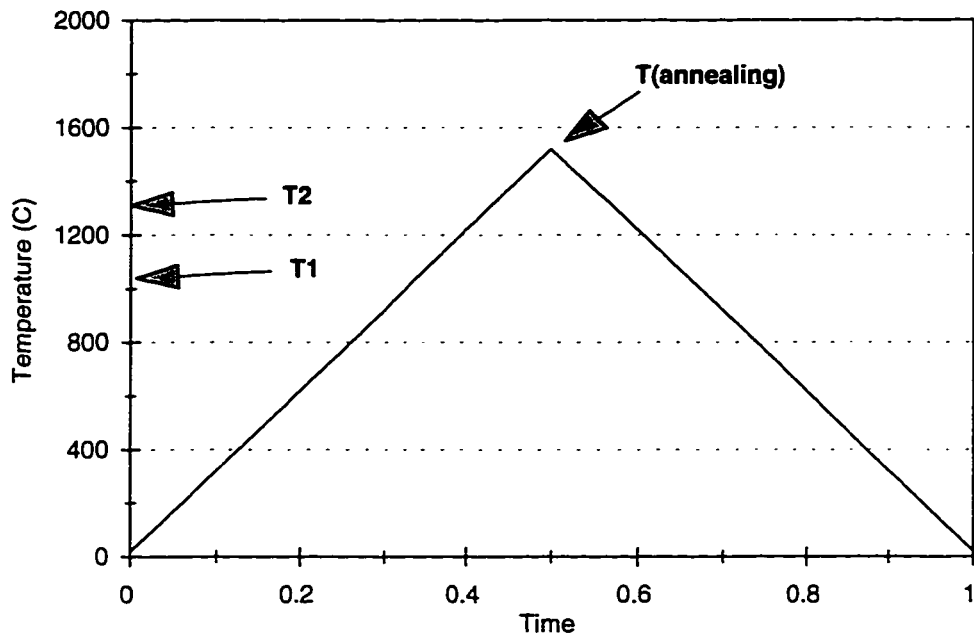
(b)

Figure 5.4 (Continued)

- Figure 5.4 Schematic explanation of the plastic strain relaxation effect
- (a) One dimensional bar model
  - (b) Stress-strain curves at different temperatures
  - (c) Temperature, thermal strain & elastic strain histories
  - (d) Plastic strain histories

Figure 5.4 (Continued)





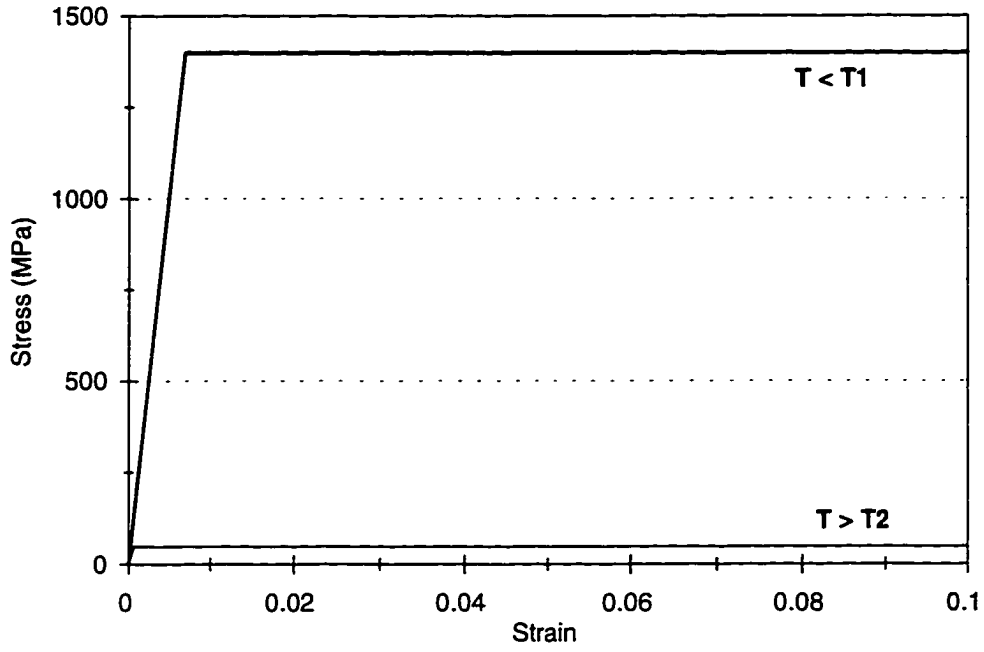
(a)

Figure 5.5 (Continued)

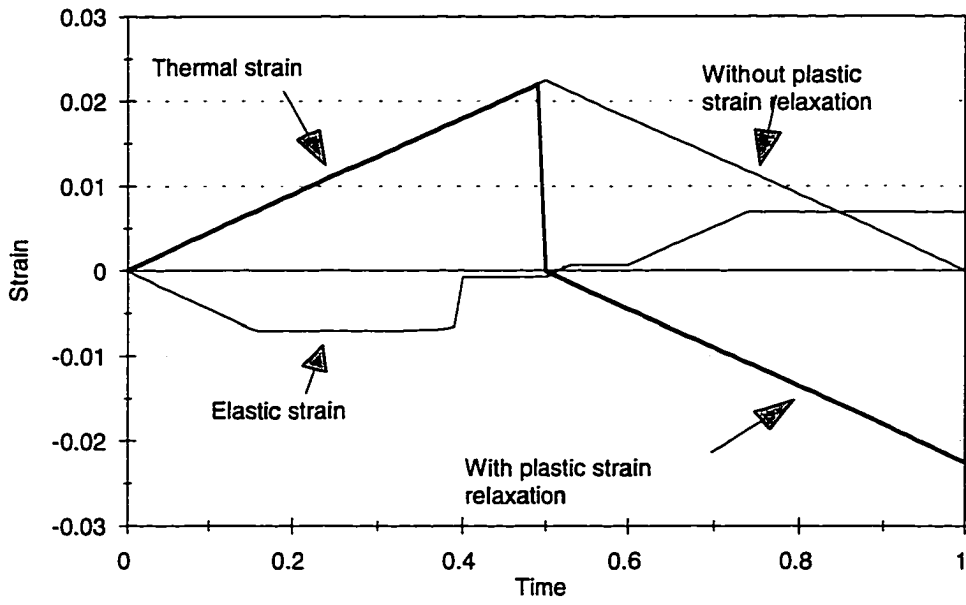
Figure 5.5 Examples of a one-dimensional model with the plastic strain relaxation effect

- (a) Temperature history
- (b) Stress-strain curves at different temperatures under elastic perfect plasticity assumption
- (c) Elastic, thermal strain histories under (b) condition
- (d) Plastic strain histories under (b) condition
- (e) Stress histories under (b) condition
- (f) Stress-strain curves at different temperatures under isotropic hardening plasticity assumption
- (g) Stress histories under (f) condition

Figure 5.5 (Continued)



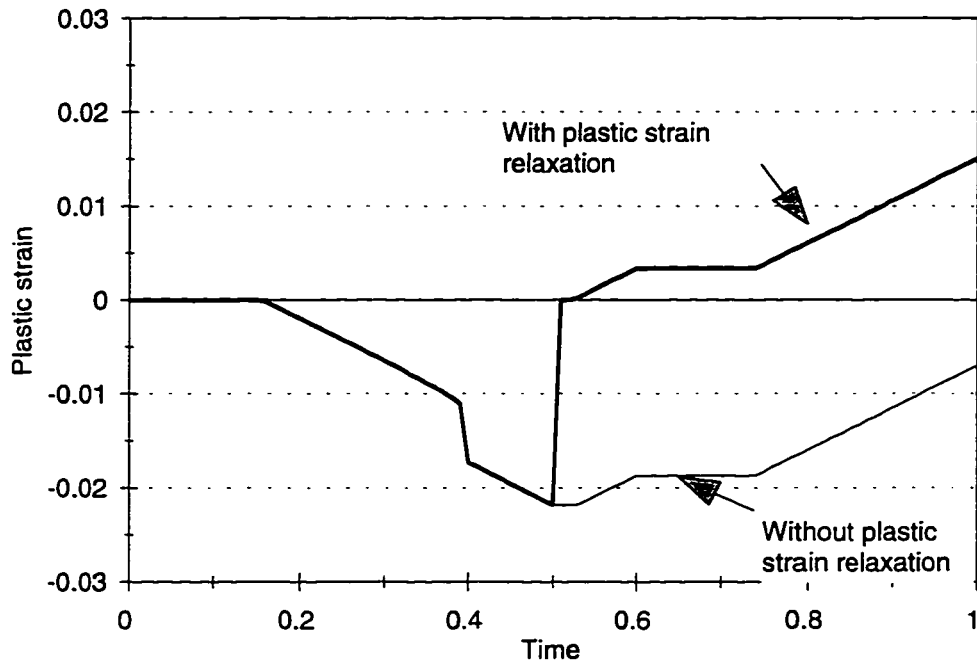
(b)



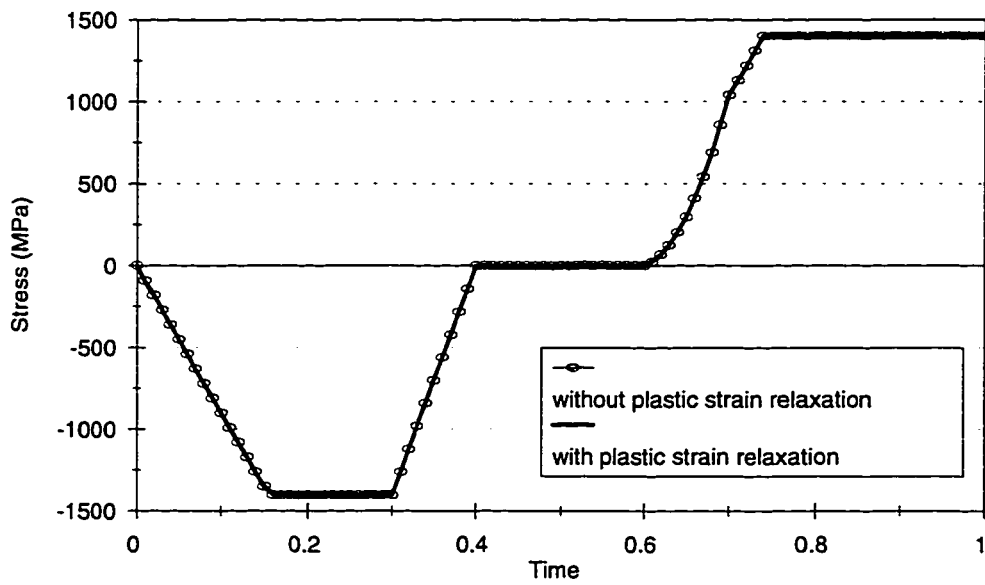
(c)

Figure 5.5 (Continued)

Figure 5.5 (Continued)



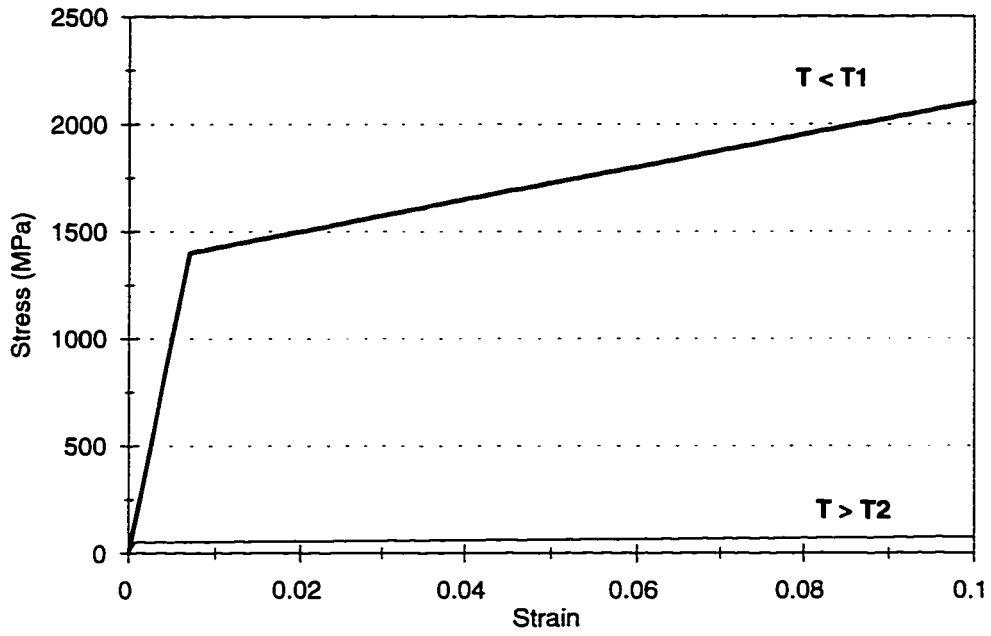
(d)



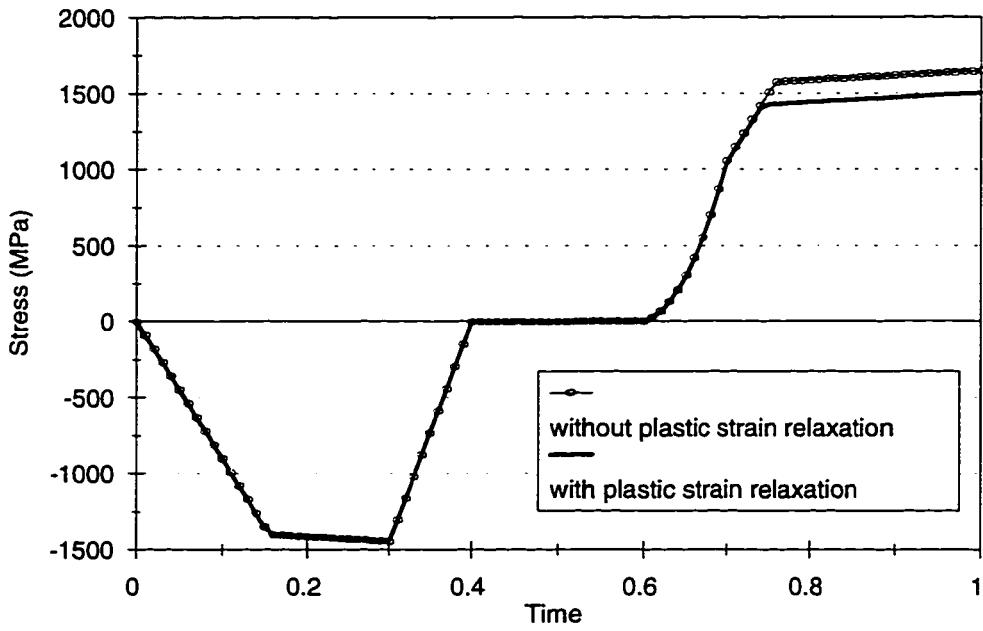
(e)

Figure 5.5 (Continued)

Figure 5.5 (Continued)



(f)



(g)

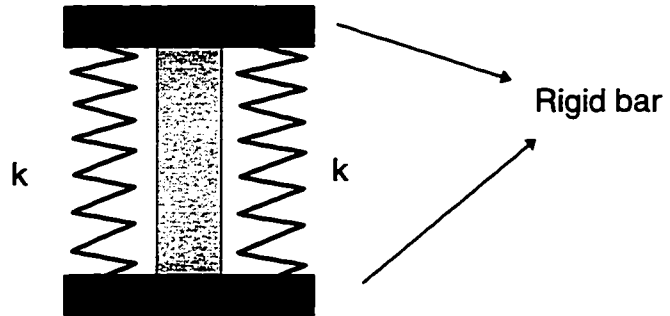
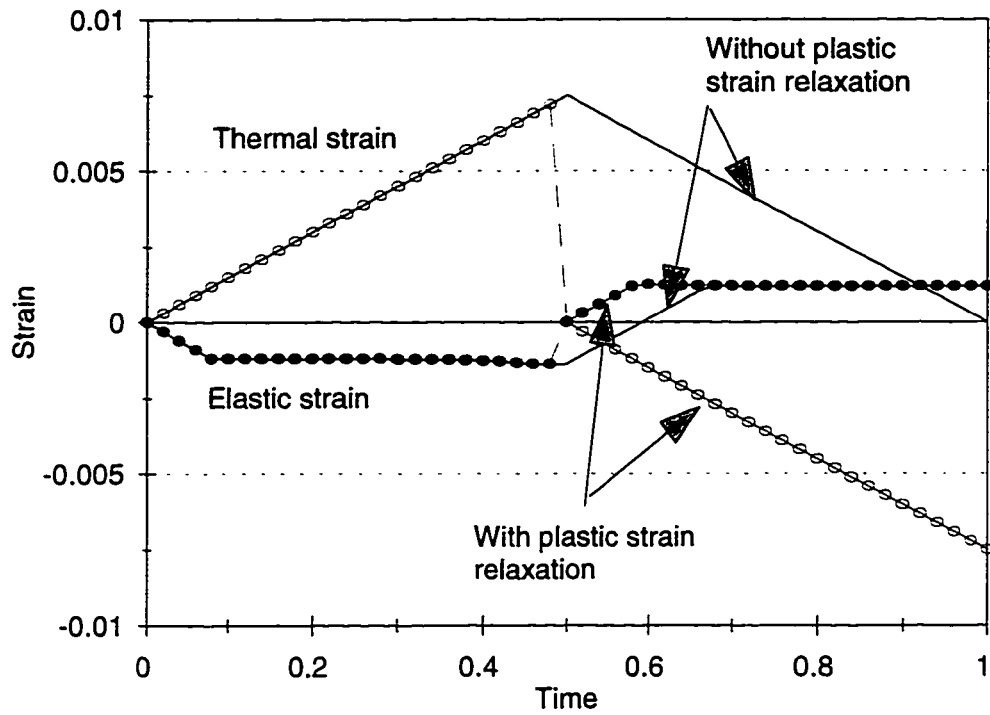


Figure 5.6 Schematic representation of a one-dimensional spring model

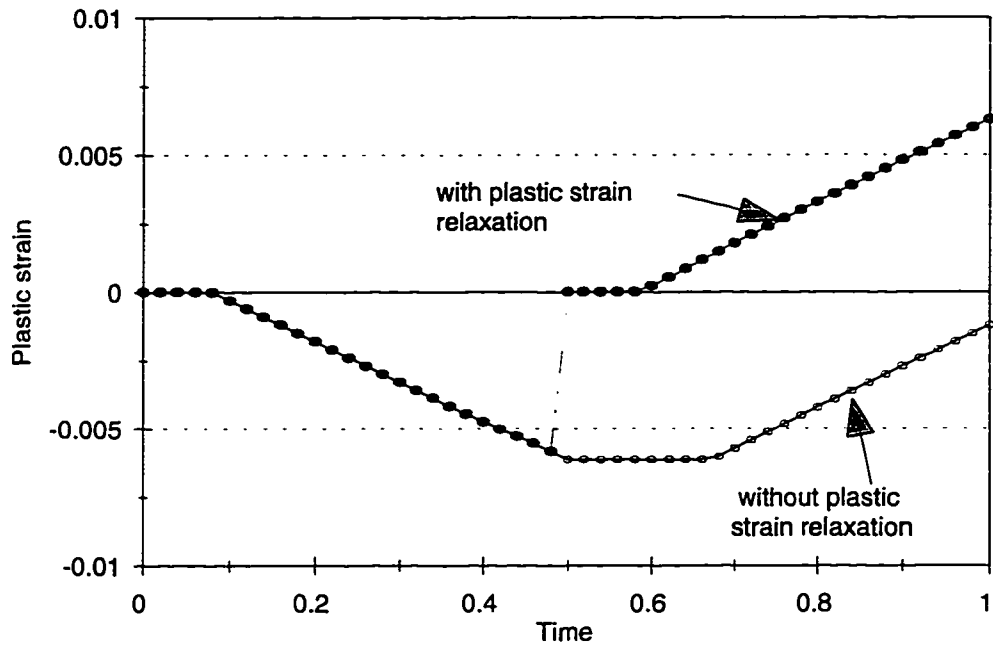


(a)

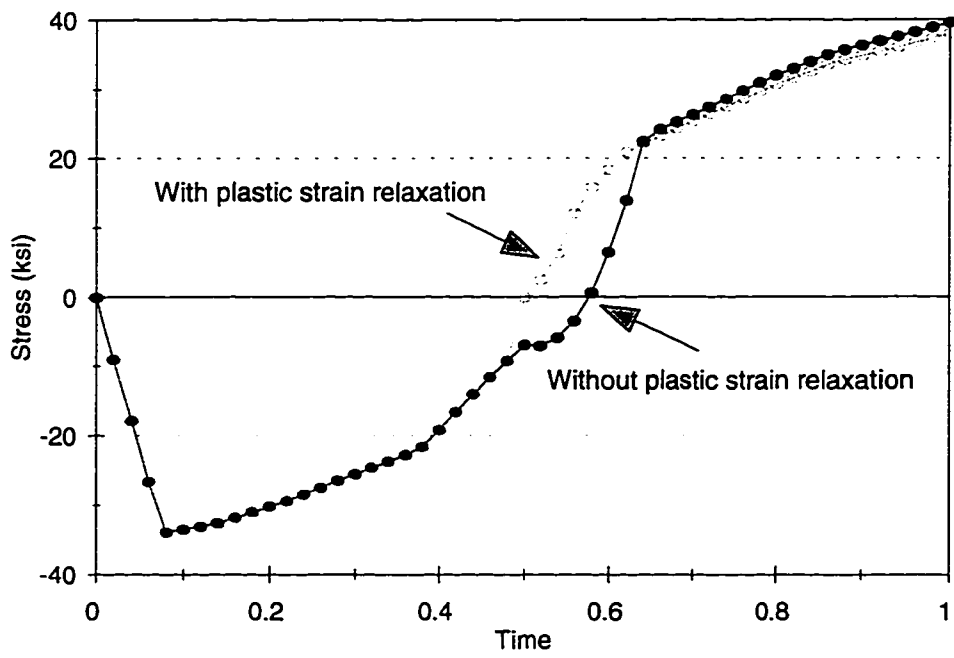
Figure 5.7 (Continued)

Figure 5.7 The material behavior of ASTM A36 mild steel for a one-dimensional model  
 (a) Thermal and elastic strain histories  
 (b) Plastic strain histories  
 (c) Stress histories

Figure 5.7 (Continued)



(b)



(c)

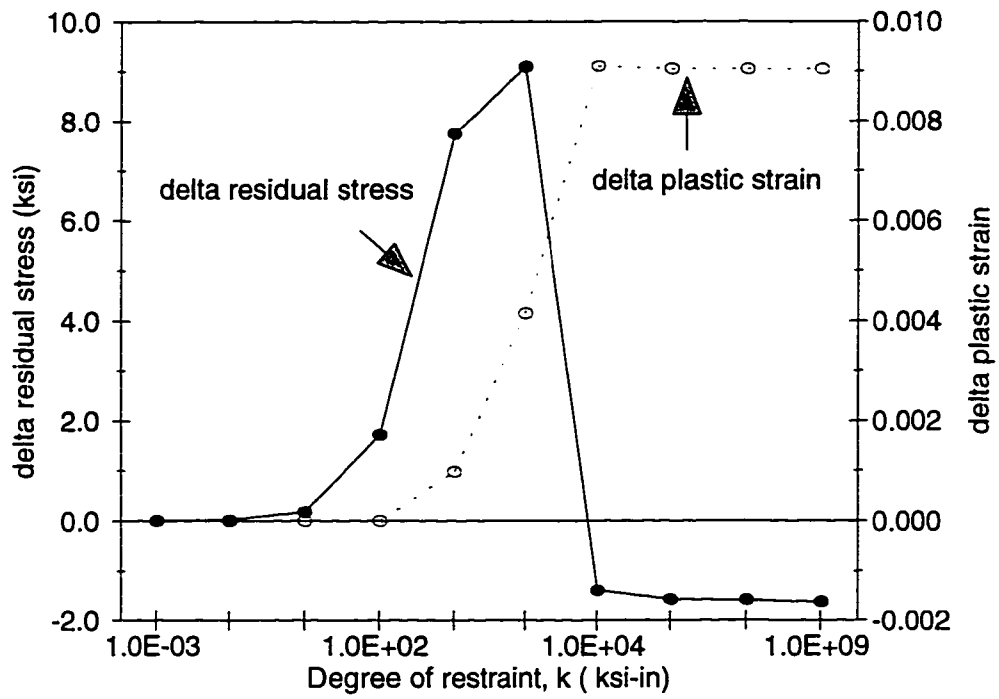


Figure 5.8 The relationship between  $k$  (degree of constraint),  $\Delta\epsilon^{pl}$ , and  $\Delta\sigma_{res}$

## CHAPTER 6

### EXAMPLES OF NUMERICAL ANALYSIS WITH THE PLASTIC STRAIN RELAXATION EFFECT

In this chapter, five examples are investigated to study the plastic strain relaxation effect. Some examples are selected from references [62, 71] and others are generated arbitrarily. By looking at various examples, the plastic strain relaxation effect in residual stresses and distortion is studied.

The given models are a one-pass bead-on-plate weld on 1/2" thick plate, a one-pass partial penetration butt welded plate, a one-pass butt welded plate with a single V groove, a three-pass butt welded plate with a single V groove, a tee-joint with fillet welds. The material properties used are assumed to be those of ASTM A 36 mild steel (Figure 4.1). The assumed hardening effect is indicated in Figure 6.1. The bilinear isotropic hardening is employed.

All numerical simulations are completed by using the ABAQUS FEA package [19]. ABAQUS four-node quadrilateral elements are used for heat transfer analysis and six-node generalized plane strain elements are adopted for mechanical analysis. Symmetry conditions are used to model the half structures. Initially, the base metal and

the weld metal are considered at room temperatures. The welding parameters and heat input data are indicated in Tables 6.1, 6.3, 6.5, and 6.7. The modified Gaussian heat inputs are employed. The other welding techniques discussed in Chapter 3 are employed.

In the material used it is assumed that the melting temperature is 2700 °F, and the temperature at which the plastic strain relaxation effect begins, is 2600 °F.

Two kinds of numerical results are obtained in each case. One is calculated by incorporating the plastic strain relaxation effect, and the other is obtained by omitting the plastic strain relaxation effect.

### 6.1 Bead-on-plate welding

The model simulated is the same as the model prepared by Lee [62]. The model plate is 4" long and 1/2" thick. The weld is located on the top at the center of the plate. The weld is 1/2" wide and a GMAW process is performed. Figure 6.2 shows the FEA model shape, including boundary conditions. Because of the symmetric boundary condition around the weld centerline, only one half of the plate is modeled. To prevent the plate from sagging at the free end under its own weight, interface elements are used to hold the plate. The interface elements play a role in allowing the plate to move into any direction except for preventing the plate from sagging below its original location. Leung *et al.* [78] also employed the interface elements for the same purpose.

Initially, the base metal and weld metal are considered at room temperatures. The welding parameters and the heat input data used are indicated in Table 6.1. The

temperature results of the numerical model are compared with the experimental data [62] in Figure 6.3. The temperature histories at 1/2" from the weld centerline on the top surface are measured with thermocouples. They show good agreement in the heating stage. Due to the difference of the response time of the peak temperatures, the results show discrepancies in the cooling stage. However, the differences between the numerically and the experimentally obtained temperatures are small. Therefore, the numerical temperature results can be considered good when compared with the experimental ones.

Figures 6.4 (a) and (b) compare the transverse and longitudinal residual stress distributions of the numerical models with the corresponding experimental results. The blind hole drilling method is implemented to measure the residual stresses at the surface of the plate. The plastic strain relaxation effect is occurred inside the fusion zone, because the plastic strain relaxation effect becomes activated when the temperature of the material reaches the melting point. The differences in the stress distributions are indicated inside and near the fusion zone. In Figure 6.4(a), the transverse stresses show good agreement with each other along the top surface. In particular, if the plastic strain relaxation effect is taken into account, numerical stress results match the experimental ones at peak stress. The numerical results with and without the plastic strain relaxation effect show similar trends. The transverse stresses are compressive inside the fusion zone, increase to become tensile, reach their peak values before they decrease to zero. The transverse residual stresses with the plastic strain relaxation effect taken into account show a higher peak value outside the fusion zone, while near the center of the weld area

they show a somewhat smaller value. In Figure 6.4(b), the stresses show good agreement along the top surface. Both numerical results with and without the plastic strain relaxation effect show similar trends. The longitudinal stresses are tensile in the weld zone, and reached to their peak value outside the fusion zone, before decreasing rapidly into the compressive zone, and then increasing gradually in the tensile zone. Like the transverse stresses, the longitudinal residual stresses with the plastic strain relaxation effect taken into account show a higher peak value outside the fusion zone, while the stresses with the plastic strain relaxation effect taken into account show a somewhat smaller value near the weld center area. Figures 6.5 (a) and (b) show the through-thickness residual transverse and longitudinal stresses at the weld centerline with and without the plastic strain relaxation effect taken into account. The stress distributions inside the fusion zone should show differences due to the plastic strain relaxation effect, but they turn out to be very small. In Figures 6.6 (a), (b), and (c), plastic transverse, longitudinal and equivalent strains are plotted, respectively. As expected, due to the plastic relaxation effect, the plastic strain distributions are changed inside and near the fusion zone. When the plastic strain relaxation effect is taken into account, the maximum plastic compressive transverse strain is observed near the weld center, while without the plastic strain relaxation effect the maximum plastic compressive transverse strain occurs at the fusion boundary. Further away from the weld centerline, the plastic strains do not develop because the maximum temperature is very low. In Figure 6.6(b), the plastic longitudinal strains show a large difference. Tensile residual plastic strains are indicated inside the fusion zone when the plastic strain relaxation effect is taken into account, while

without the plastic strain relaxation effect the plastic compressive strain is distributed inside the fusion. Because the longitudinal directional constraint is much larger than the transverse directional constraint, the longitudinal plastic strain behavior looks similar to the 1-D case of Chapter 5. In Figure 6.6(c), when the plastic strain relaxation effect is taken into account, the equivalent plastic strains inside and near the fusion zone are smaller than those for the case without the plastic strain relaxation effect. This means that the accumulated plastic strains are relieved when the weld reaches the melting point during welding.

In Figure 6.7, the distortion histories are compared. Figure 6.2 indicates the location where the distortion is picked up. The distortion is checked at 2" from the weld centerline on the bottom surface. As indicated in Table 6.2, the final distortion in the y-direction is 0.0127" when the method without the plastic strain relaxation effect is used, whereas 0.0146" is calculated when the plastic strain relaxation effect is considered. The final distortion is a 15% improvement of the distortion based on the method without the plastic strain relaxation effect. The plastic strain accumulation by conventional numerical analysis without the plastic strain relaxation effect shows less distortion due to over-accumulation of plastic strain after welding.

The CPU times on an IBM work station are compared (Table 6.2). Because both cases used identical temperature history data, only the CPU times for the mechanical analyses are compared. The CPU times with and without the plastic strain relaxation effect are 65.0 and 64.6 sec., respectively. The difference in the CPU times is very small (0.6%).

## 6.2 Partial penetration butt welded plate

The model plate is 20" long and 1/2" thick. The weld is located on the top and the center of the plate. The weld is 1/2" wide, is 60 % penetrated of the thickness. A GMAW process is performed. Figure 6.8 shows the FEA model shape, including boundary conditions. Because of the symmetric boundary condition around the weld centerline, only one half of the plate is modeled. The welding parameters and the heat input data used are indicated in Table 6.3.

Figures 6.9 (a) and (b) compare the transverse and longitudinal residual stress distributions of the numerical models, respectively. In Figure 6.9(a), both numerical results with and without the plastic strain relaxation effect show similar trends. The transverse stress trends are similar to those of the bead-on-plate welding case. The transverse residual stresses without the plastic strain relaxation effect vary rapidly inside the fusion zone, while with the plastic strain relaxation effect the stresses show smooth variations and somewhat lower values near the center of the weld area. When the plastic strain relaxation effect is considered, the longitudinal stresses became smoother inside the fusion zone in Figure 6.9(b). Figures 6.10 (a) and (b) show the through-thickness residual transverse and longitudinal stresses with and without the plastic strain relaxation effect at the weld centerline, respectively. Because of the fusion zone is larger than that of the bead-on-plate welding case, the stresses along the thickness direction vary noticeably.

In Figure 6.11, the distortion histories are compared. Figure 6.8(b) indicates the location where the distortion is picked up. The distortion is checked at 10" from the weld centerline on the bottom surface. As shown in Table 6.4, the final distortion in the y-direction is 0.0413" when the method without plastic strain relaxation effect is used, whereas when the plastic strain relaxation effect is used it is calculated to be 0.0931". The distortion with the plastic strain relaxation effect is improved by 125.4%. The distortion values for the butt welding case are larger than those for the bead-on-plate welding case. When the fusion zone size becomes large, the plastic strain relaxation effect becomes large. Consequently, the final distortion becomes large.

The CPU times on an IBM work station are compared (Table 6.4). The CPU times for mechanical analyses are compared. The CPU times with and without the plastic strain relaxation effect are 66.0 and 64.2 sec., respectively. The CPU difference is very small (2.8%).

### 6.3 One-pass single V groove butt welding

Except for the weld the geometries of the FEA model for a one-pass butt weld with a single V groove are the same as the geometries of the model for the partial penetration butt welding. The model plate is 20" long and 1/2" thick. The weld is located on the top at the center of the plate. The weld is 1/2" wide and fully penetrated from the top to the bottom surfaces. Figure 6.12 shows the FEA model shape including boundary conditions. Because of the symmetric boundary conditions around the weld

centerline, only one half of the plate is modeled. The welding parameters and the heat input data are indicated in Table 6.5.

Figures 6.13 (a) and (b) compare the transverse and longitudinal residual stress distributions of the numerical models, respectively. As discussed in Chapter 6.2, the transverse residual stresses with the plastic strain relaxation effect show smooth trends inside the fusion zone, while without the plastic strain relaxation effect the stresses vary rapidly inside fusion zone. When the plastic strain relaxation effect is taken into account, the longitudinal stresses become smoother inside fusion zone, but the variation is very small, as shown in Figure 6.13(b). These trends are very similar to Figure 6.9 (a) and (b). Figures 6.14 (a) and (b) show the through-thickness residual transverse and longitudinal stresses with and without the plastic strain relaxation effect along the weld centerline, respectively. When the fusion zone size increases, the stress variations along the thickness direction become noticeably larger.

In Figure 6.15, the distortion histories are compared. Figure 6.12(b) indicates the location where the distortion is picked up. The distortion is checked at 10" from the weld centerline on the bottom surface. As shown in Table 6.6, the final distortion in the y-direction is 0.0356" when the method without plastic strain relaxation effect is used, whereas when the plastic strain relaxation effect is used it is calculated to be 0.0798". The distortion is greatly improved (121.6%). When the plastic strain relaxation effect is considered, the distortion value becomes larger in comparison with the method without plastic strain relaxation effect.

The CPU times on an IBM work station are compared as shown in Table 6.6. The CPU times with and without the plastic strain relaxation effect are 79.9 and 88.9 sec., respectively. The CPU time is reduced (10.1%) when the plastic strain relaxation effect is considered.

#### 6.4 Three-pass single V groove butt weld

The geometries of the FEA model for a three-pass butt welded plate with a single V groove are the same as the model for a one-pass butt welded plate with a single V groove. Figure 6.16 shows the FEA model shape and weld pass sequences, including boundary conditions. Only one half of the plate is modeled because of symmetric boundary conditions around the weld centerline. The welding parameters, pass sequence, and heat input data are indicated in Table 6.7.

Figures 6.17 (a) and (b) compare the transverse and longitudinal residual stress distributions after the third weld pass along the top surface on the numerical models, respectively. In Figure 6.17(a), inside the fusion zone the transverse residual stresses with the plastic strain relaxation effect show lower trends than those without the plastic strain relaxation effect. In Figure 6.17(b), when the plastic strain relaxation effect is taken into account, the longitudinal stresses inside the fusion zone also show lower trends than those without the plastic strain relaxation effect. This is similar to Figure 6.17(a). Figures 6.18 (a) and (b) show the through-thickness residual transverse and longitudinal stresses with and without the plastic strain relaxation effect along the weld centerline,

respectively. The overall trends are similar in both cases. The transverse stress peaks just outside the fusion zone, in the vicinity of the fusion zone, and drops rapidly a short distance away from the fusion boundary. On the surface, the largest tensile stress is produced not on the weld centerline, but just outside of the fusion boundary. In addition, compressive residual stresses are produced on the top surface inside the weld. These tendencies of residual transverse stresses have been observed by some researchers [61, 79]. The reasons for these tendencies are as follows: In multi-pass welding, contraction of the new weld metal and HAZ of the newest pass is restrained by the region surrounding it. The restraint is progressively more severe toward the bottom, while the surface is much less constrained. Accordingly, the stresses on the surface of the finishing bead must be smaller than those just below the surface. In addition, during cooling, the contraction of these points in the direction of the thickness produces local bending, which induces compressive stresses on the surface of the finishing bead.

In Figure 6.19, the distortion histories are compared. Figure 6.16(b) indicates the location where the distortion is picked up. The distortion is checked at 10" from the weld centerline on bottom surface. As the weld passes accumulate, the distortion becomes successively larger. As indicated in Table 6.8, the final distortion after the third pass in the y-direction is 0.1220" using the method without plastic strain relaxation, whereas when the plastic strain relaxation effect is used it is calculated to be 0.1366". The difference in the distortion is 12%. In multi-pass welding case, the final distortion is much more severe than that in a single-pass welding case.

The CPU times on an IBM work station are compared (Table 6.8). The CPU times for the mechanical analyses are compared. The CPU times with and without the plastic strain relaxation effect are 200.1 and 266.3 sec., respectively. The CPU time is obviously reduced (- 24.9%) when the model with the plastic strain relaxation effect is used.

### 6.5 Tee joint with fillet welds

The model is the same as the model prepared by Penso [71]. The thickness of the flange and the web is 0.5". The width of the flange and the height of the web are 8.125" and 2.875", respectively. The weld size of the fillets is 3/8". Figure 6.20 shows the FEA model shape, including boundary conditions. Only one half of the plate is modeled because of symmetric boundary conditions around the centerline of the structure. In addition, the gap between the flange and the web is included. Also, the fillets are located at both sides and the welding sequences are actually different. However, with symmetry conditions, the welds of both fillets are made at the same time. The welding parameters, and the heat input data are indicated in Table 6.9.

Figures 6.21 (a) and (b) compare the transverse and the longitudinal residual stress distributions on the top surface of the flange of the numerical models, respectively. The only change in the stresses is found inside and near the fusion zone. Like the previous stress plots, the stress distributions obtained using the plastic strain relaxation effect

inside and near the fusion zone show less variation than those using the method without the plastic strain relaxation effect.

In Figure 6.22, the distortion histories are compared. Figure 6.20 indicates the location where the distortion is picked up. The distortion is checked at 4.0625" from the centerline on the bottom of the flange. When the web is located perpendicular to the reference plane, The final distortion is 0.0465" when the method without the plastic strain relaxation effect is used, whereas it is calculated to be 0.0535" when the plastic strain relaxation effect is used (Table 6.10). The distortion is improved by 15.0 %. The final distortion from the experiment is 0.0553" [71]. The experimental value shows good agreement with the distortion value obtained by using the method with the plastic strain relaxation effect. There is only a difference of 3.2% from the experimental value.

The CPU times for mechanical analyses are compared on an IBM work station (Table 6.10). The CPU times with and without the plastic strain relaxation effect are 138.5 and 130.0 sec., respectively. When the plastic strain relaxation effect is considered, the CPU time is increased by 6.5%.

## 6.6 Discussion

From Chapters 6.1 to 6.5, the models with the plastic strain relaxation effect are compared with those without the plastic strain relaxation effect. With regard to the stress distributions, the stress distributions with the plastic strain relaxation effect become

smoother (stress variations are smaller) inside and near the fusion zone than those without the plastic strain relaxation effect.

In the numerical analysis, when the plastic strain relaxation effect is considered, the final out-of-plane distortion is evidently bigger (12% ~ 125%) than that without the plastic strain relaxation effect. Generally, in numerical analyses the final distortion is underestimated in comparison with experimental analyses. In the case of the tee-joint with fillet welds, the final distortion with the plastic strain relaxation effect shows good agreement with the experimental data. This means that the plastic strain relaxation affects the improvement of the final distortion after welding because the accumulated plastic strains are reduced. These trends are more reasonable when compared with experimental ones.

From the view point of computational performance, the CPU time is obviously reduced in multi-pass welding cases with the plastic strain relaxation effect (24.5%), whereas the CPU time differences are not very significant in the other cases (-10% ~ 6.5%).

Bead-on plate weld on a 1/2" thick plate model(Lee's model [62])		Data used for numerical analysis
Current (Amp.)		245
Voltage (V)		27.8
Welding speed (IPM)		10
Percent heat input (%)		55
Initial temperature conditions (°F)	Base metal	70
	Weld metal	70
Fraction of heat fluxes	Surface flux	50
	Body flux	50

Table 6.1 Welding parameters for a one-pass bead-on-plate weld on a 1/2" thick plate model

	Bead-on-plate welding		
	Without plastic strain relaxation	With plastic strain relaxation	Difference** (%)
Displacement. (in.)	0.0127	0.0146	15.0
CPU (sec.)	64.6	65.0	0.6

\*\* Difference (%)= (With plastic strain relaxation - Without plastic strain relaxation) / (Without plastic strain relaxation) x 100

Table 6.2 Comparison of CPU time and distortion for a one-pass bead-on-plate weld on a 1/2" thick plate

One-pass partial penetration butt welded pipe model		Data used for numerical analysis
Current (Amp.)		250
Voltage (V)		25
Welding speed (IPM)		5
Percent heat input (%)		85
Initial temperature conditions (°F)	Base metal	70
	Weld metal	70
Fraction of heat fluxes	Surface flux	20
	Body flux	80

Table 6.3 Welding parameters for a one-pass partial penetration butt welded plate model

	One-pass partial penetration welding		
	Without plastic strain relaxation	With plastic strain relaxation	Difference** (%)
Displacement. (in.)	0.0413	0.0931	125.4
CPU (sec.)	64.2	66.0	2.8

Table 6.4 Comparison of CPU time and distortion for a one-pass partial penetration welded plate

One-pass butt welded plate model with a single V groove		Data used for numerical analysis
Current (Amp.)		250
Voltage (V)		25
Welding speed (IPM)		5
Percent heat input (%)		85
Initial temperature conditions (°F)	Base metal	70
	Weld metal	70
Fraction of heat fluxes	Surface flux	20
	Body flux	80

Table 6.5 Welding parameters for a one-pass butt welded plate model with a single V groove

	One-pass single V groove butt welding		
	Without plastic strain relaxation	With plastic strain relaxation	Difference** (%)
Displacement. (in.)	0.0356	0.0789	121.6
CPU (sec.)	88.9	79.9	-10.1

Table 6.6 Comparison of CPU time and distortion for a one-pass butt welded plate with a single V groove

Pass sequence		1st pass	2nd pass	3rd pass
Current (Amp.)		100	100	100
Voltage (V)		30	36	40
Welding speed (IPM)		8	5.5	5
Percent heat input (%)		70	70	70
Initial temperature condition (°F)	Base metal	70	70	70
	Weld metal	70	70	70
Fraction of heat fluxes	Surface flux	30	30	30
	Body flux	70	70	70

Table 6.7 Welding parameters for a three-pass butt welded plate model with a single V groove

	Three-pass single V groove butt welding		
	Without plastic strain relaxation	With plastic strain relaxation	Difference** (%)
Displacement. (in.)	0.1220	0.1366	12.0
CPU (sec.)	266.3	200.1	-24.9

Table 6.8 Comparison of CPU time and distortion for a three-pass butt welded plate with a single V groove

Tee-joint with fillet welds (Fenso's model [71])		Data used for numerical analysis
Current (Amp.)		290.
Voltage (V)		31.
Welding speed (IPM)		7.5
Percent heat input (%)		70.
Initial temperature conditions (°F)	Base metal	70.
	Weld metal	70.
Fraction of heat fluxes	Surface flux	30.
	Body flux	70.

Table 6.9 Welding parameters for a tee-joint with fillet welds

	Tee-joint with fillet welds		
	Without plastic strain relaxation	With plastic strain relaxation	Difference** (%)
Displacement. (in.)	0.0465	0.0535	15.0
CPU (sec.)	130.0	138.5	6.5

Table 6.10 Comparison of CPU time and distortion for a tee-joint with fillet welds

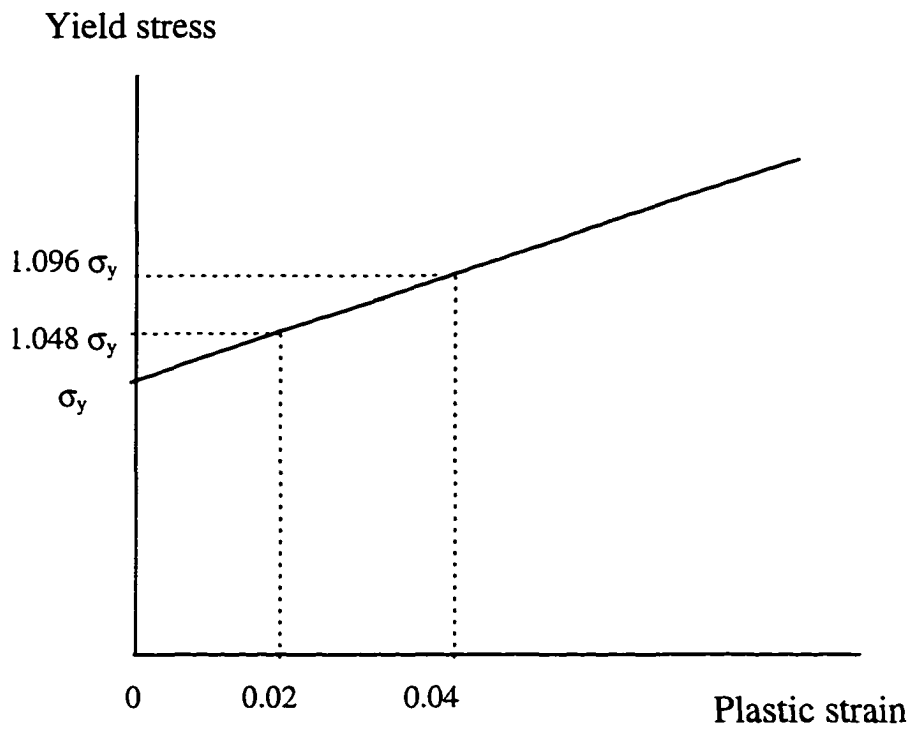


Figure 6.1 Bilinear strain hardening effect assumed for ASTM A36 steel

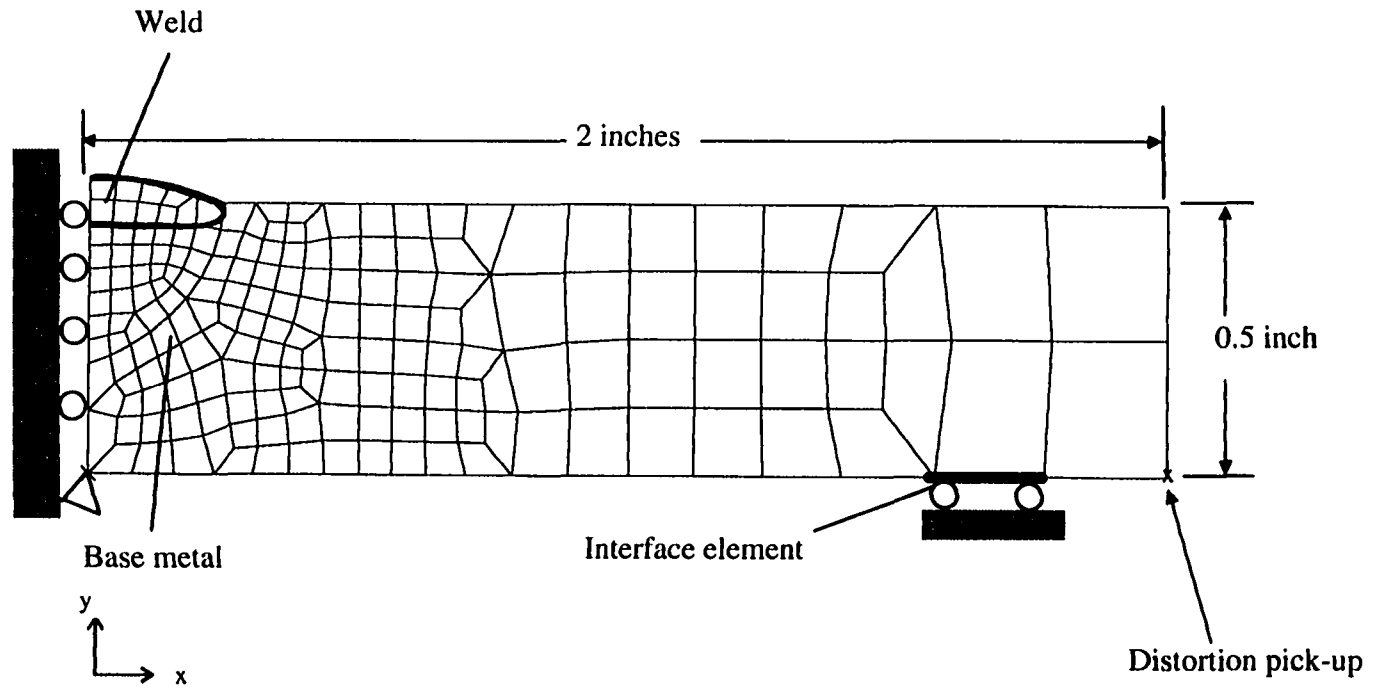


Figure 6.2 Finite element model for a one-pass bead-on-plate weld on a 1/2" thick plate

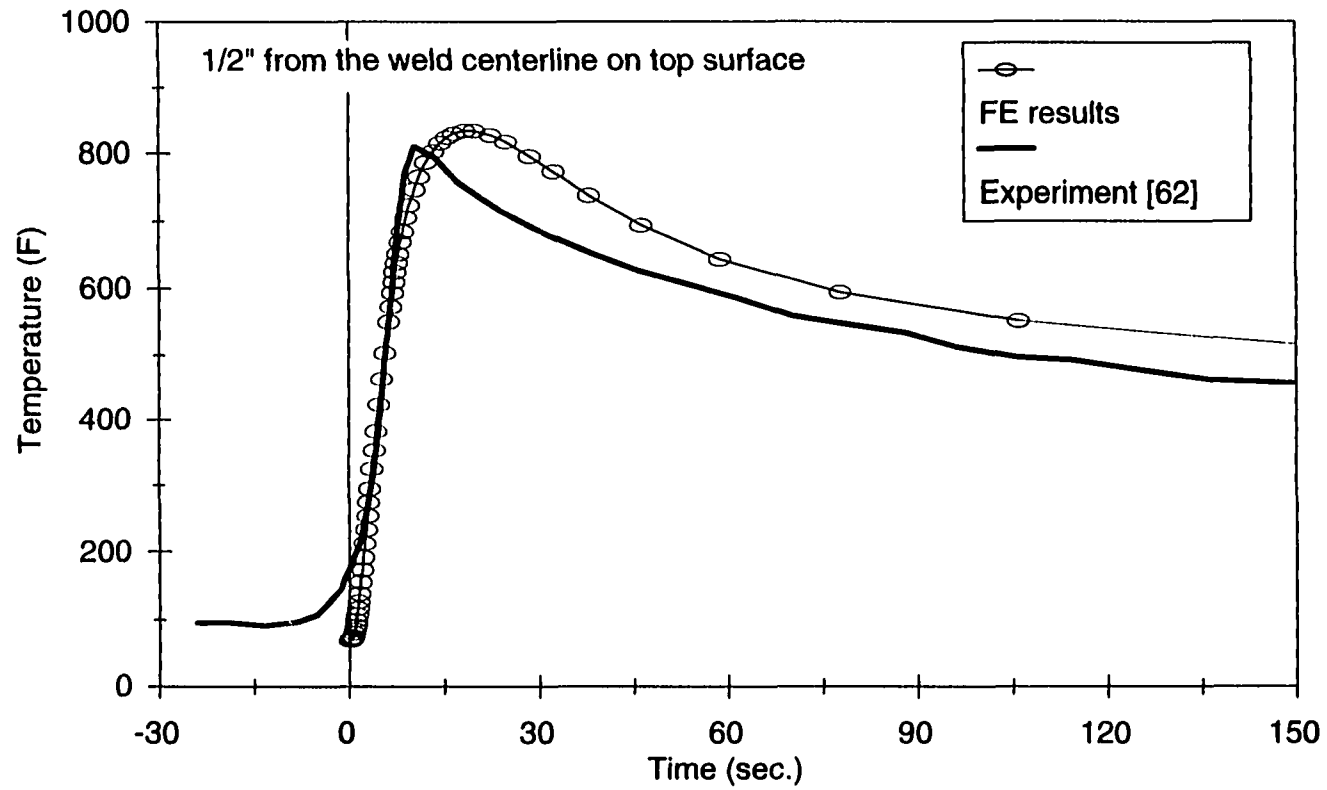
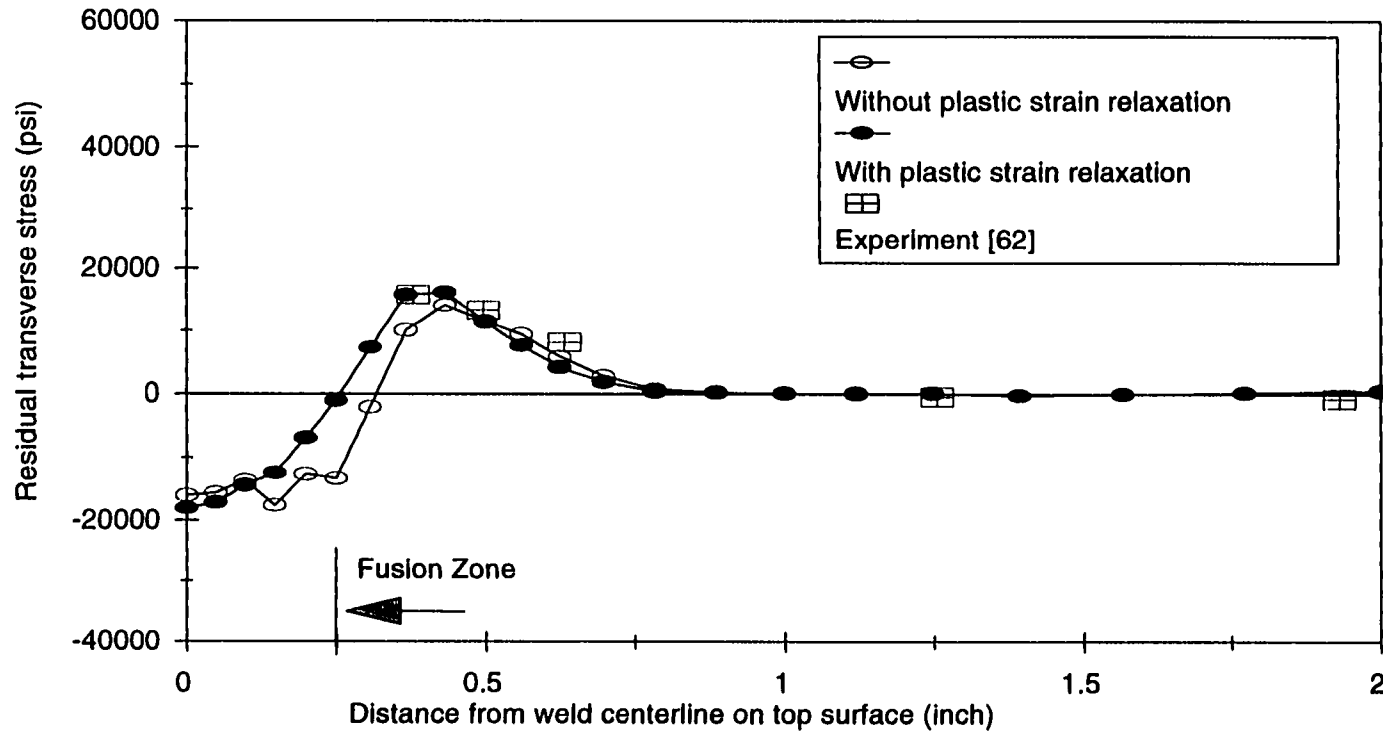


Figure 6.3 Temperature profiles at 1/2" from the weld centerline on top surface  
(a one-pass bead-on-plate weld on a 1/2" thick plate)



(a)

Figure 6.4 (Continued)

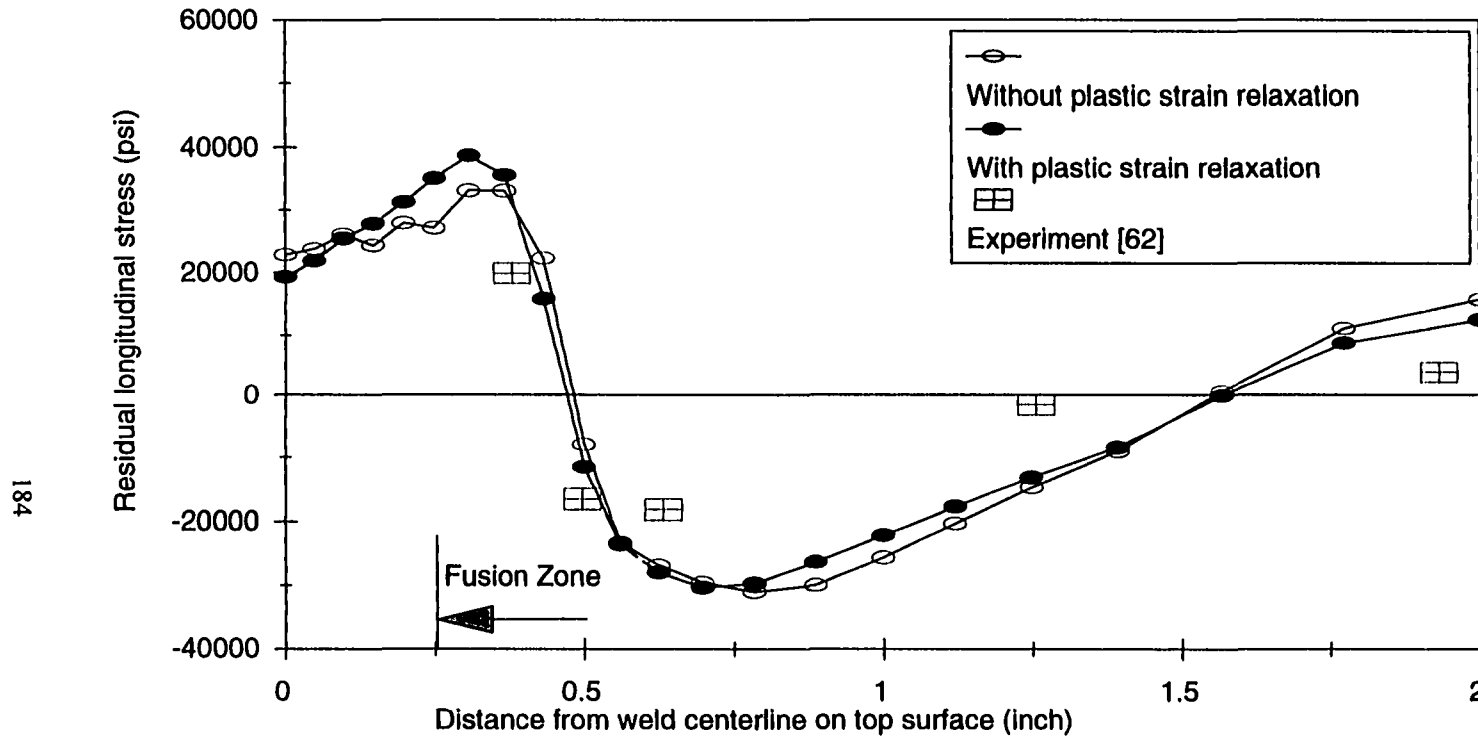
Figure 6.4 Comparison of the numerical and experimental residual stress distribution on top surface

(a one-pass bead-on-plate weld on a 1/2" thick plate)

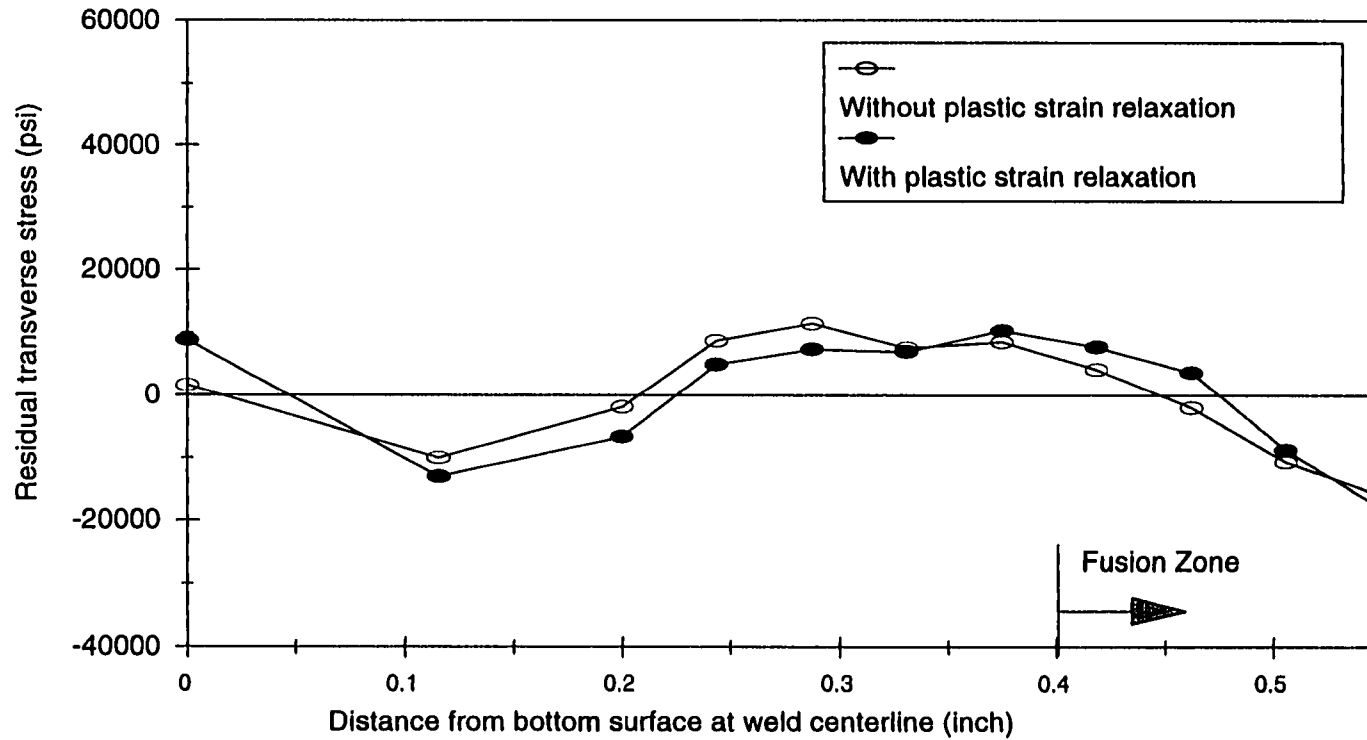
(a) Transverse stresses

(b) Longitudinal stresses

Figure 6.4 (Continued)



(b)

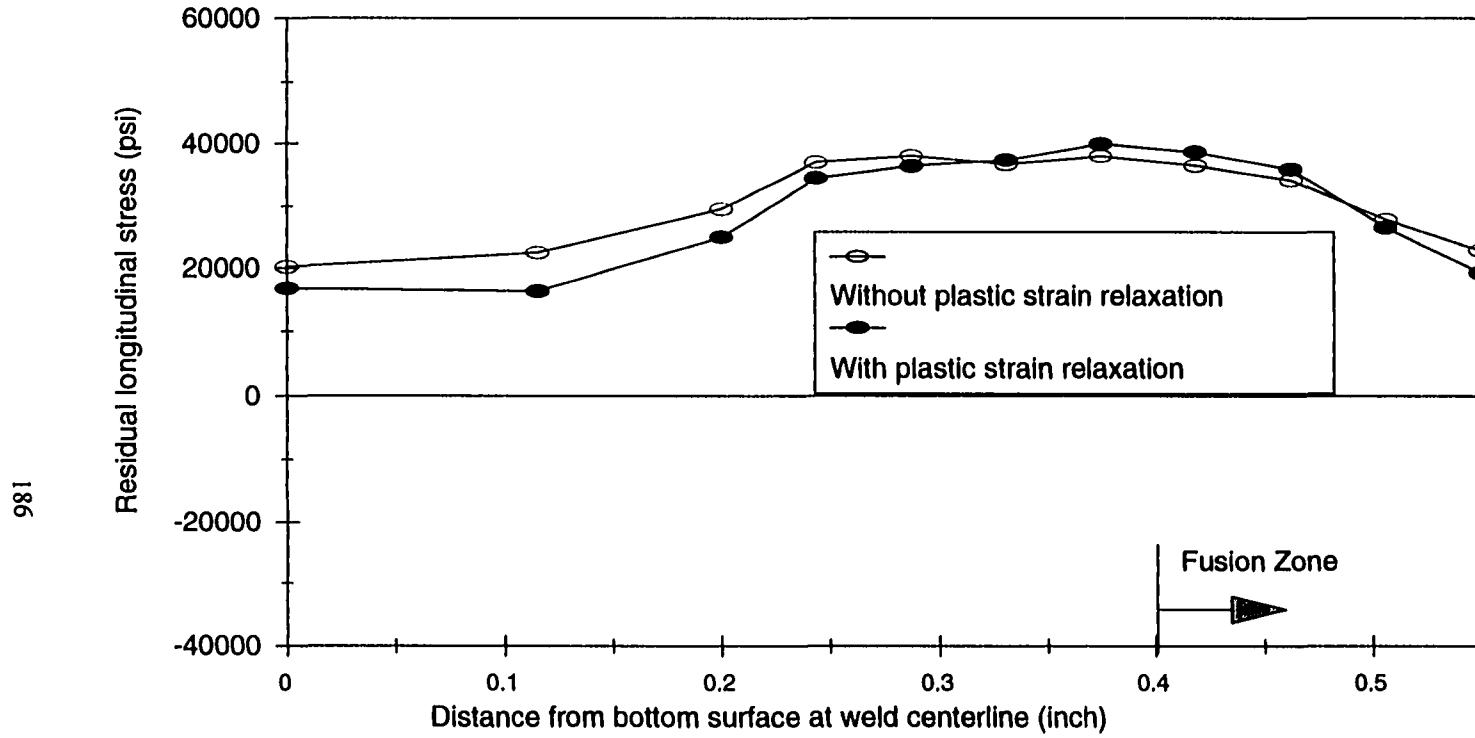


(a)

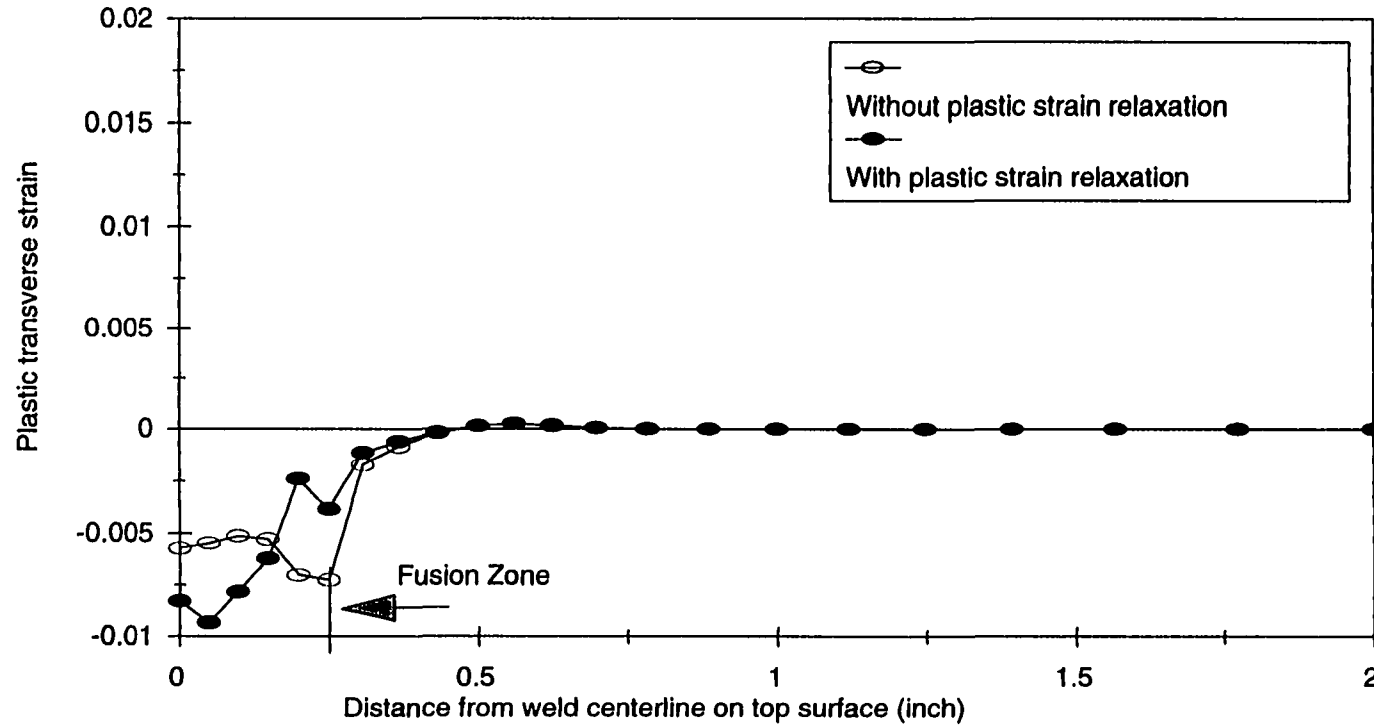
Figure 6.5 (Continued)

Figure 6.5 Through-thickness residual stress distributions at weld centerline  
(a one-pass bead-on-plate weld on a 1/2" thick plate)  
(a) Transverse stresses  
(b) Longitudinal stresses

Figure 6.5 (Continued)



(b)



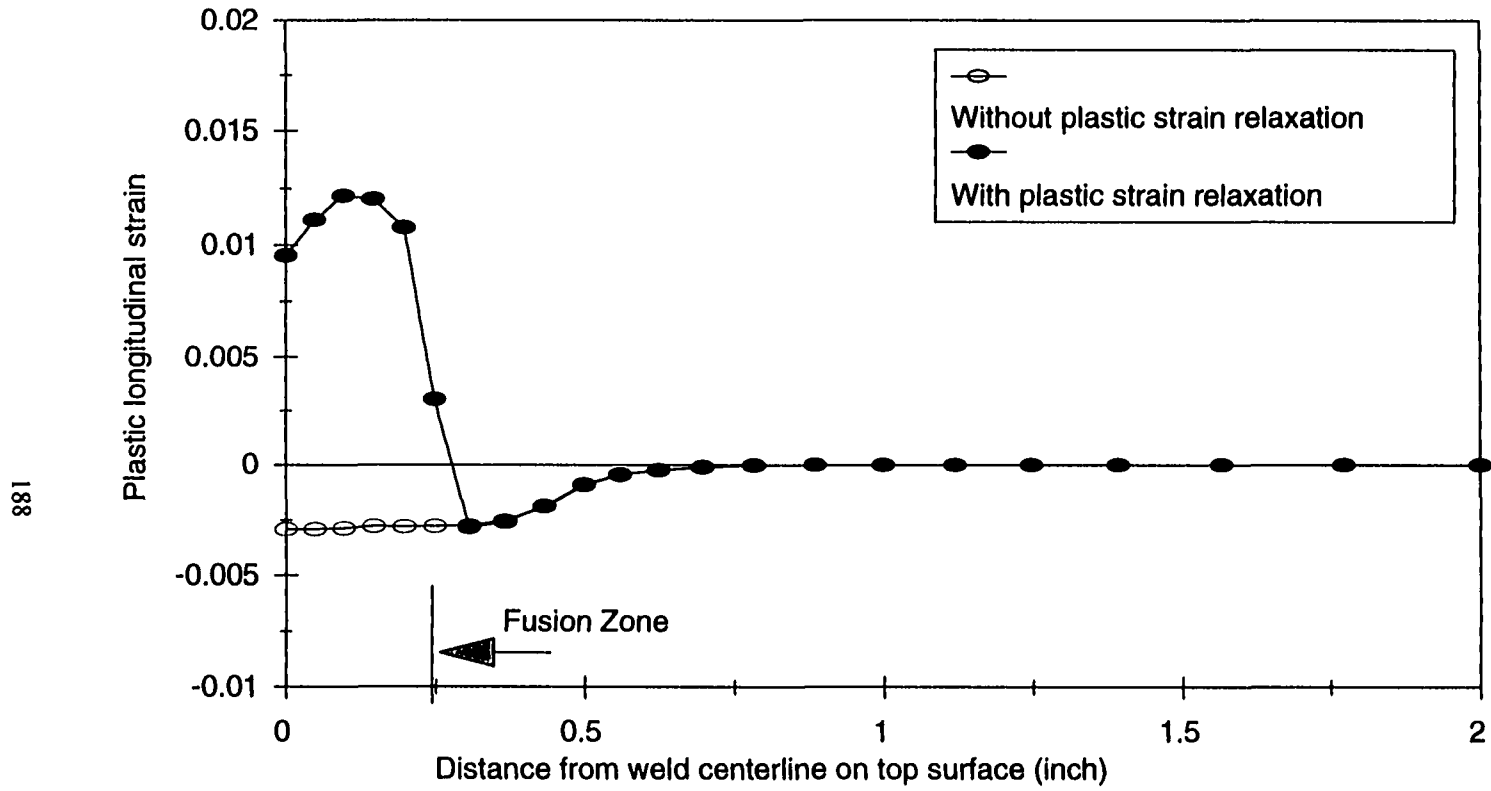
(a)

Figure 6.6 (Continued)

Figure 6.6 Comparisons of the plastic strains with and without considering plastic strain relaxation effect on top surface (a one-pass bead-on-plate weld on a 1/2" thick plate)

- (a) Transverse plastic strains
- (b) Longitudinal plastic strains
- (c) Equivalent plastic strains

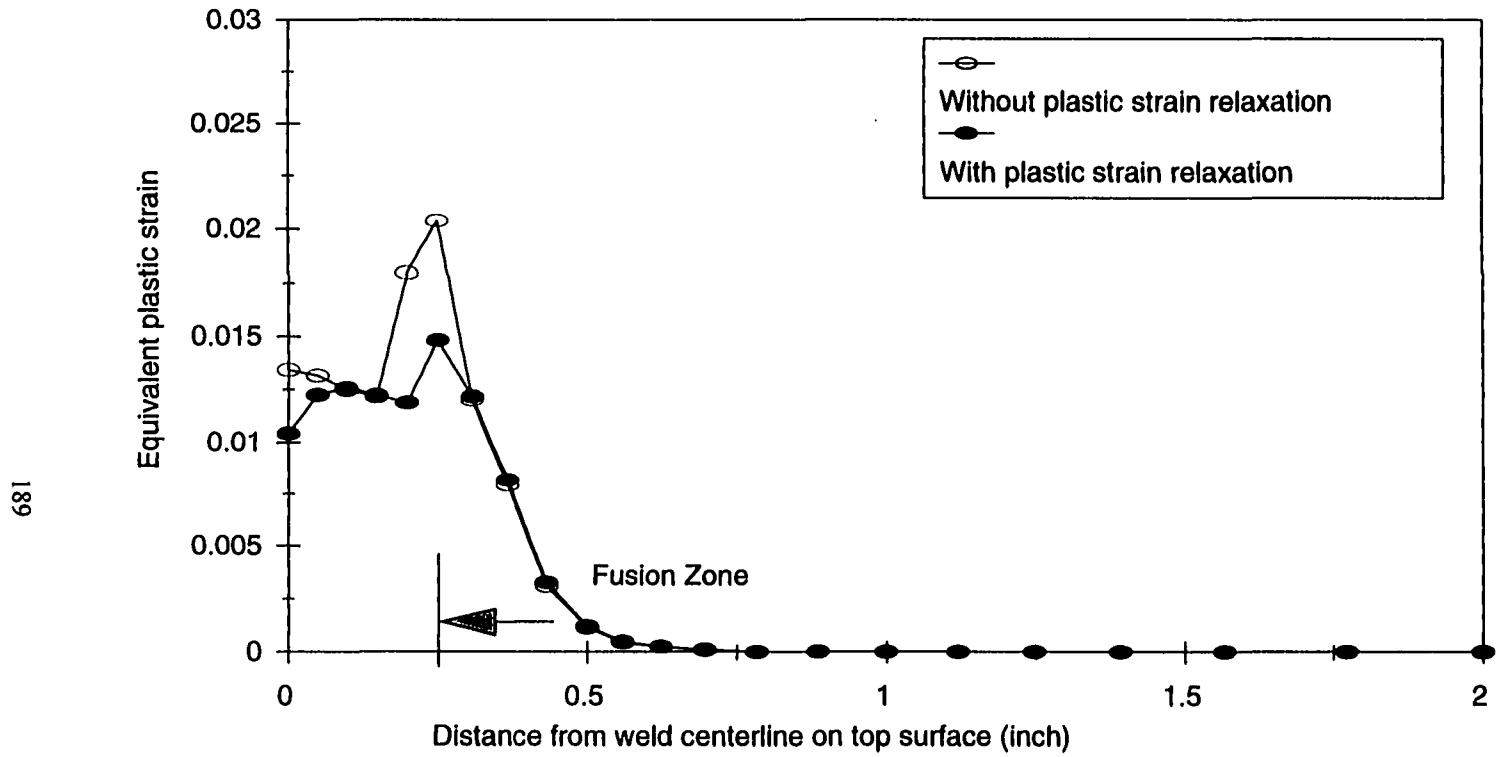
Figure 6.6 (Continued)



(b)

Figure 6.6 (Continued)

Figure 6.6 (Continued)



(c)

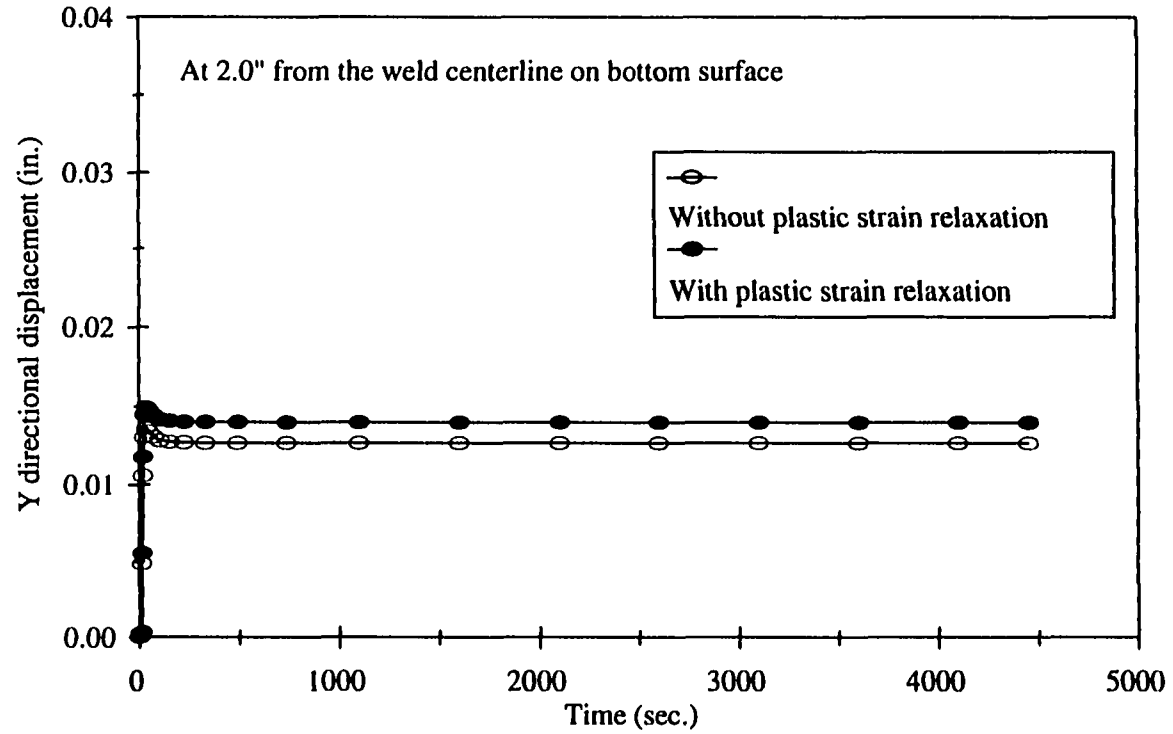
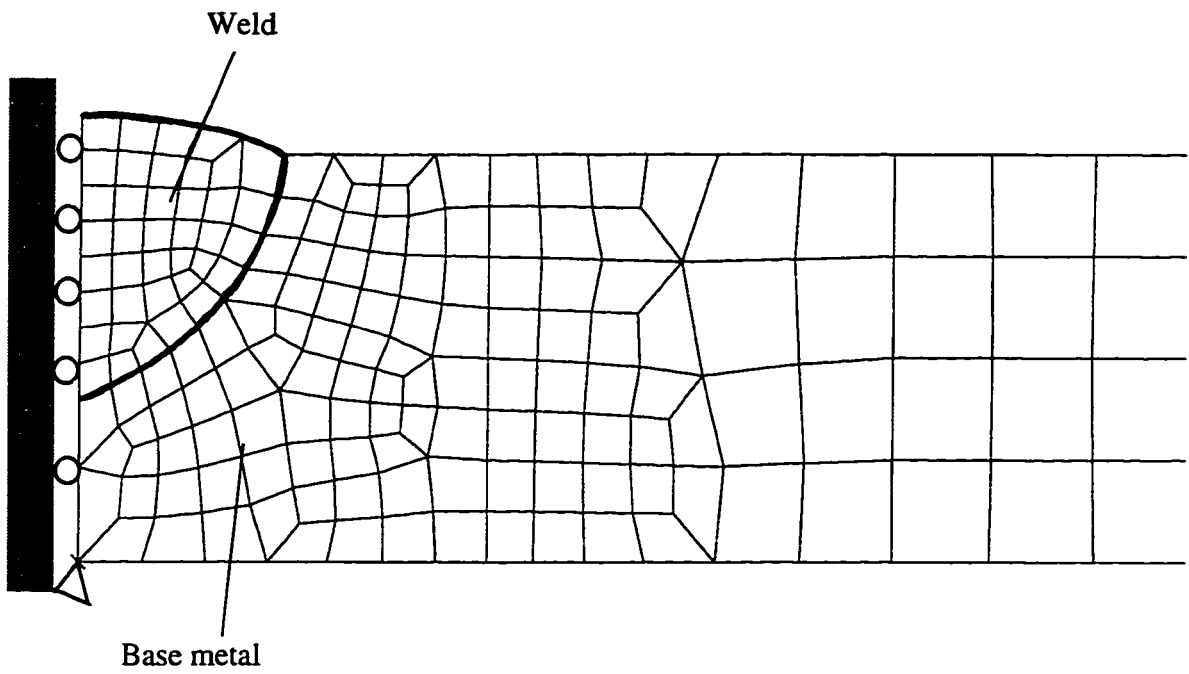
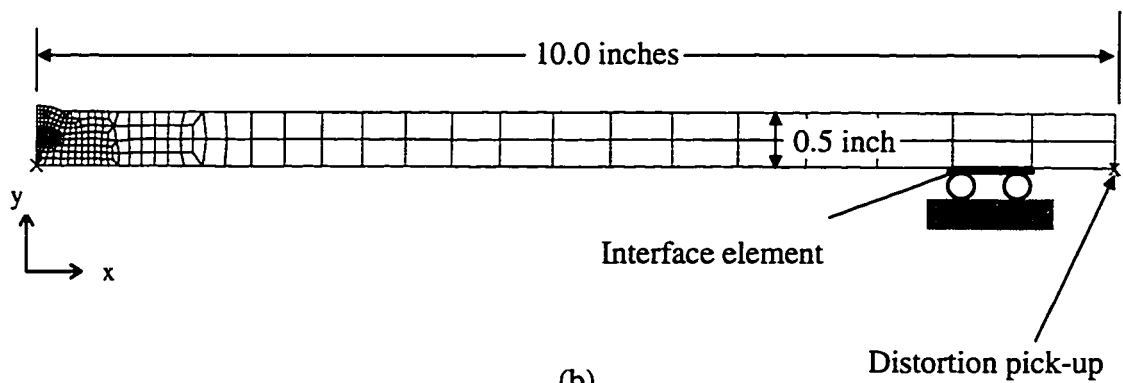


Figure 6.7 Distortion changes at 2" from the weld centerline on bottom surface (a one-pass bead-on-plate weld on a 1/2" thick plate)



(a)

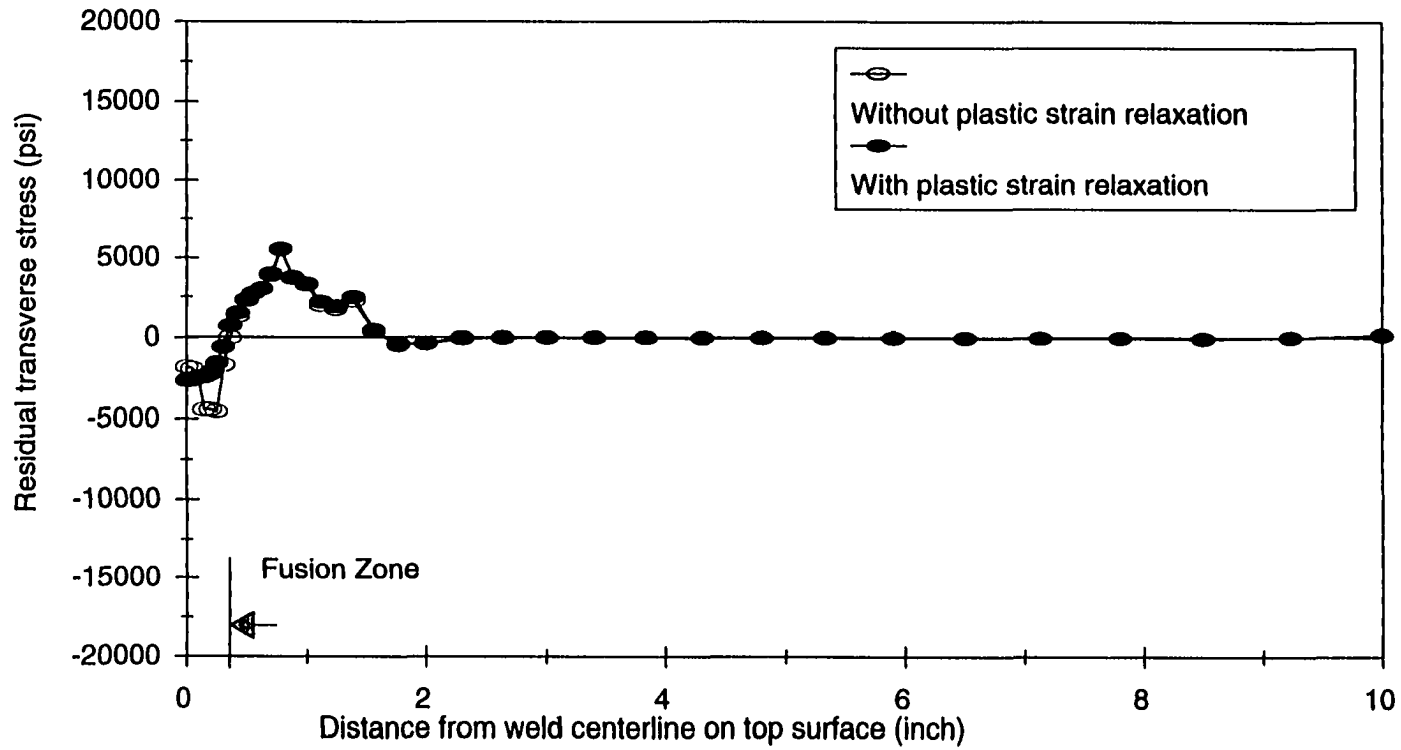


(b)

Figure 6.8 Finite element model for a one-pass partial penetration butt welded plate

(a) View of weld area

(b) Entire model



(a)

Figure 6.9 (Continued)

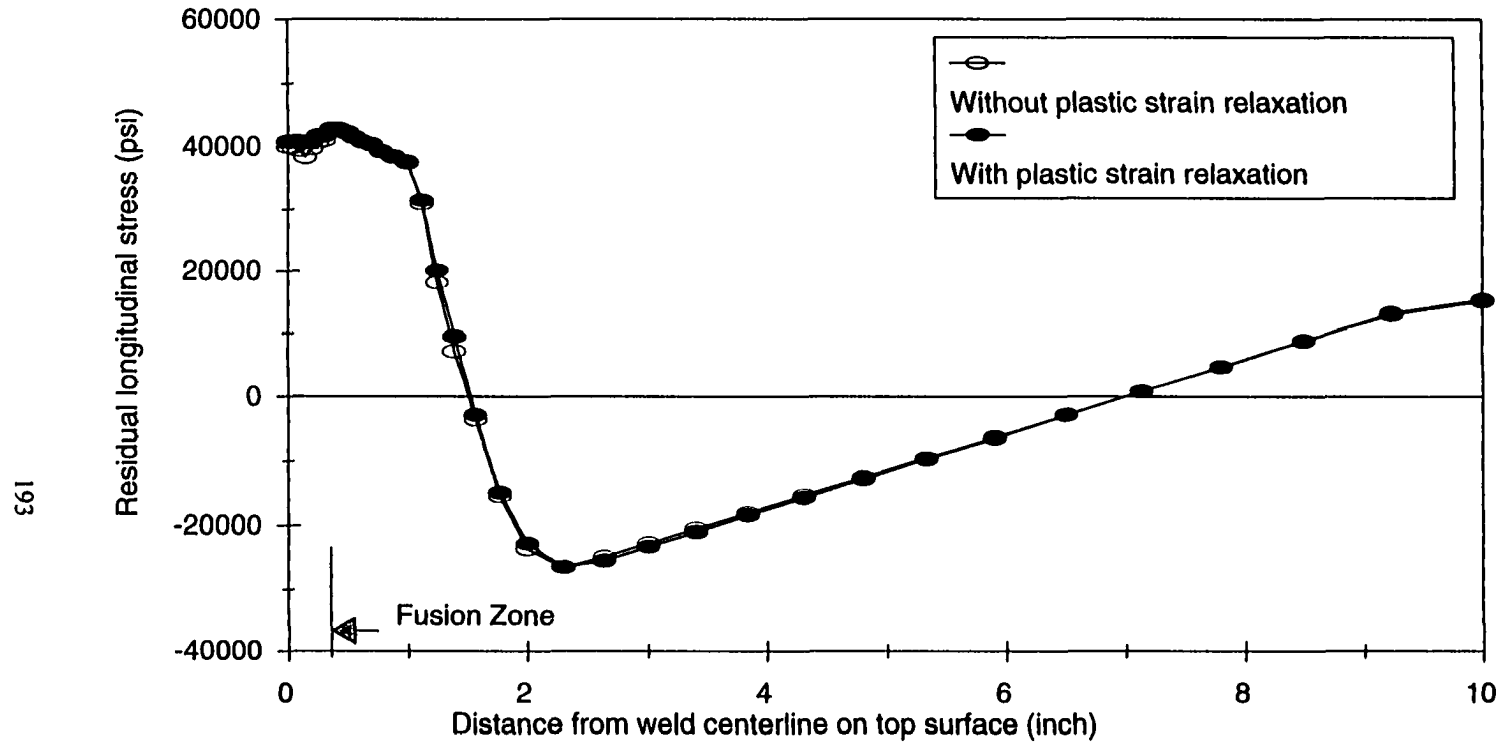
Figure 6.9 Comparison of residual stress distributions with and without plastic strain relaxation effect on top surface

(a one-pass partial penetration butt welded plate)

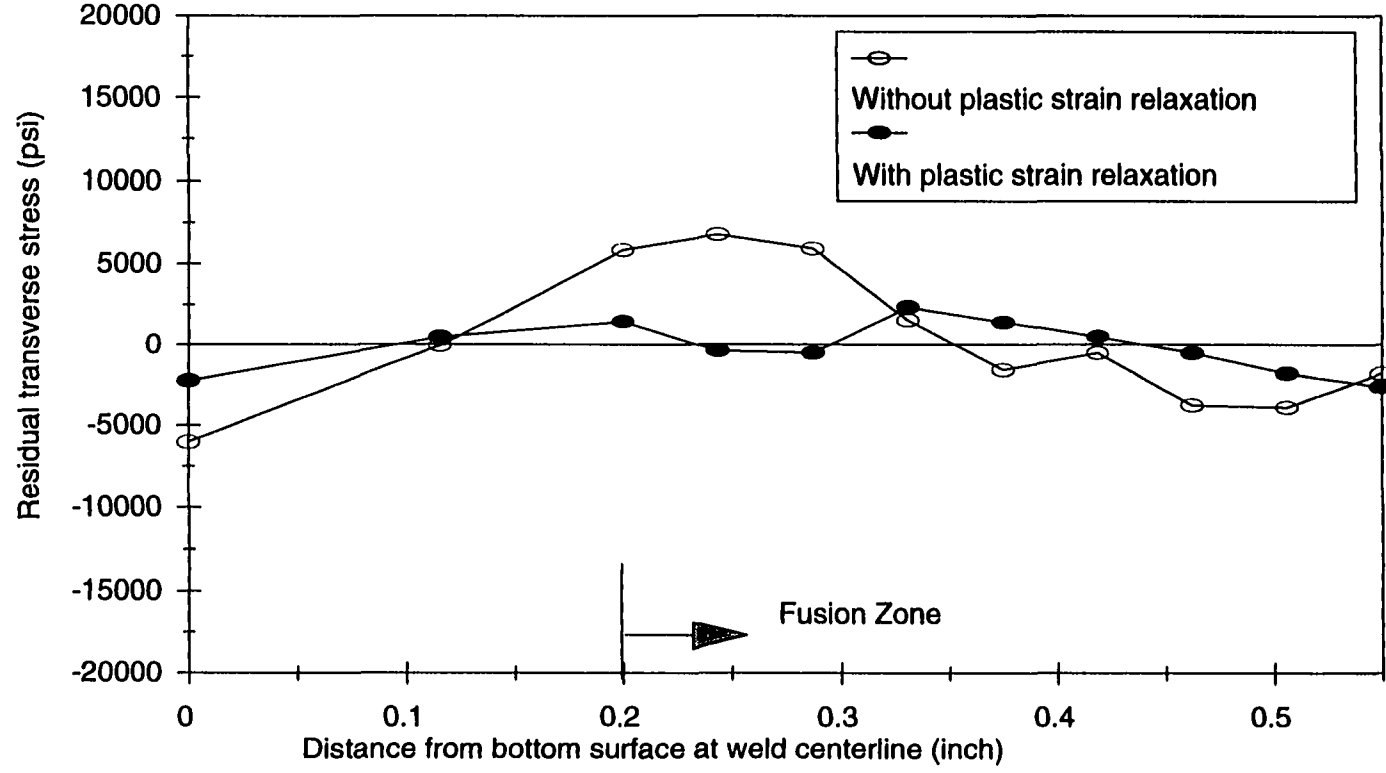
(a) Transverse stresses

(b) Longitudinal stresses

Figure 6.9 (Continued)



(b)

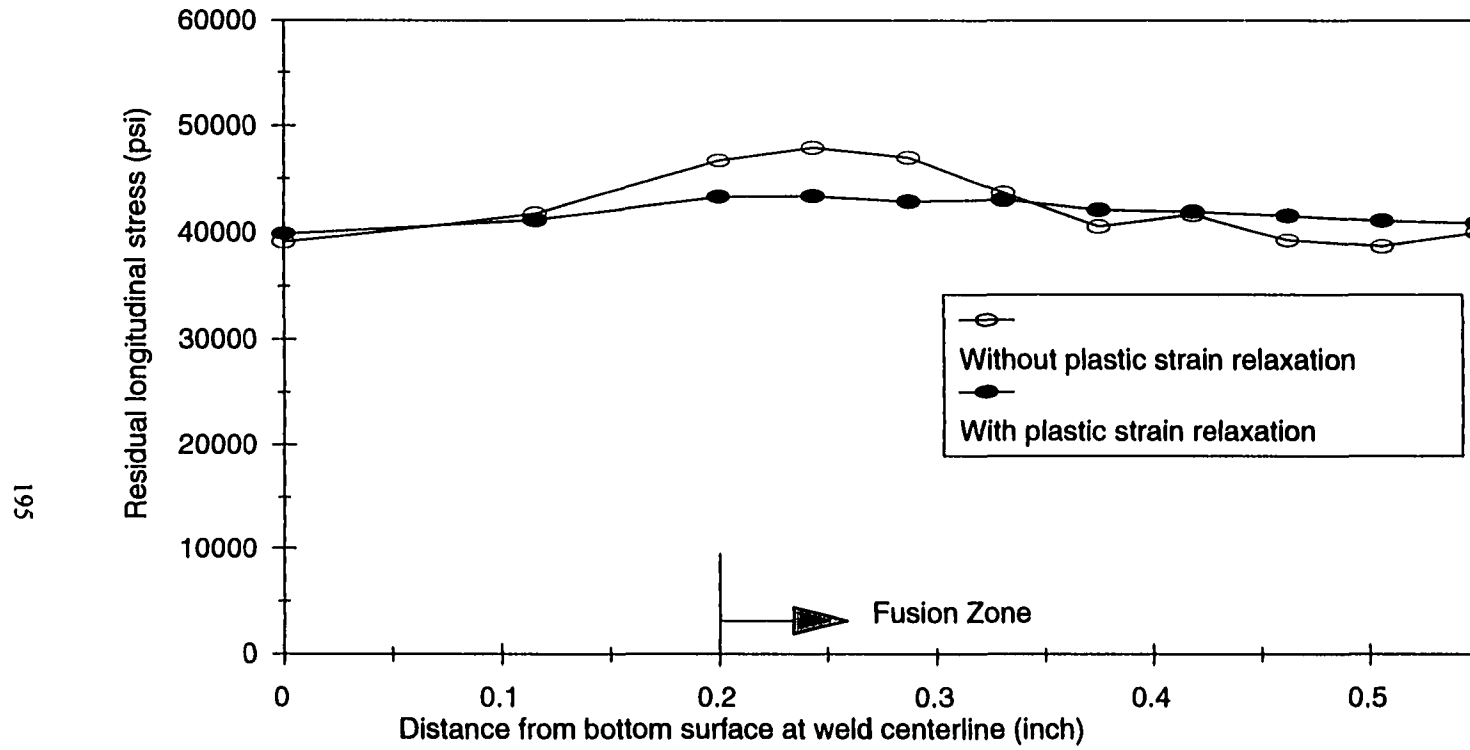


(a)

Figure 6.10 (Continued)

Figure 6.10 Through-thickness residual stress distributions at weld centerline (a one-pass partial penetration butt welded plate)  
(a) Transverse stresses  
(b) Longitudinal stresses

Figure 6.10 (Continued)



195

(b)

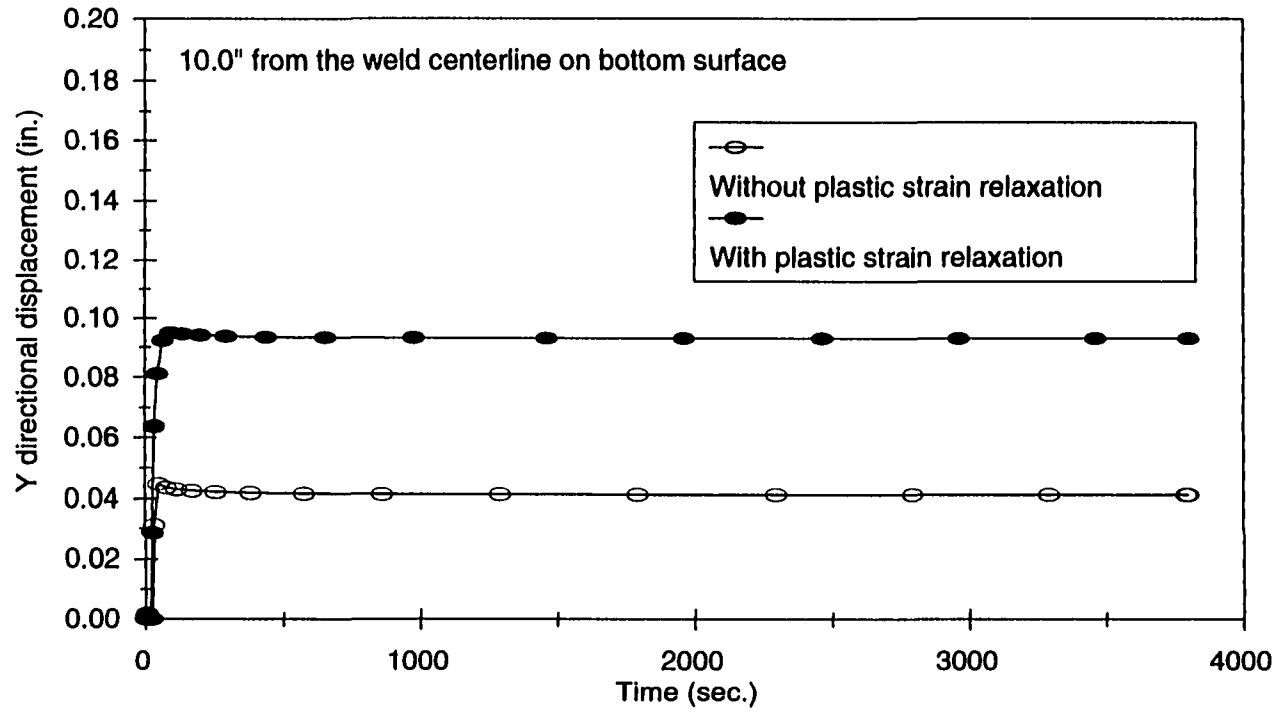
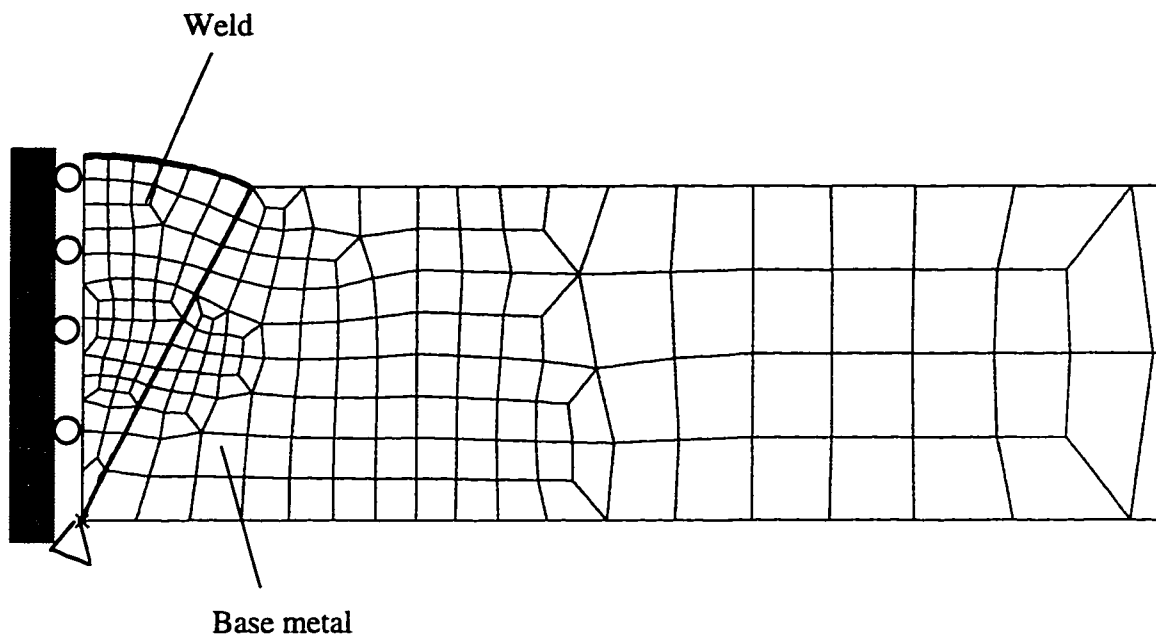
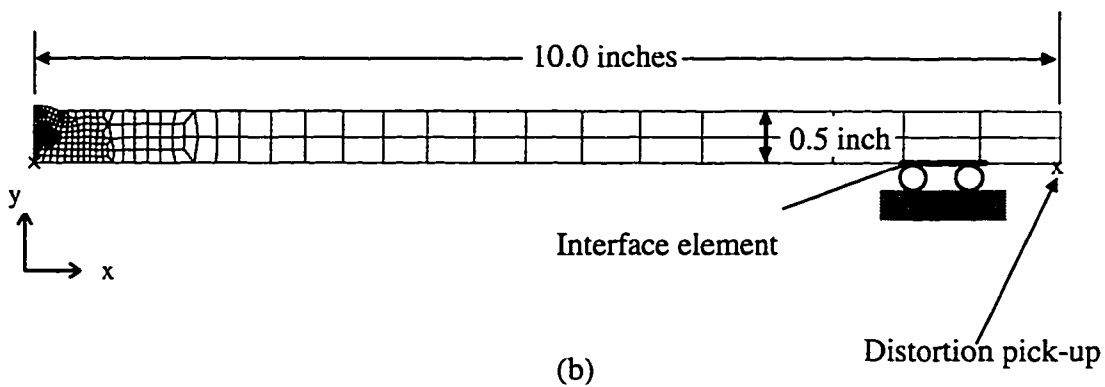


Figure 6.11 Distortion changes at 10" from the weld centerline on bottom surface (a one-pass partial penetration butt welded plate)

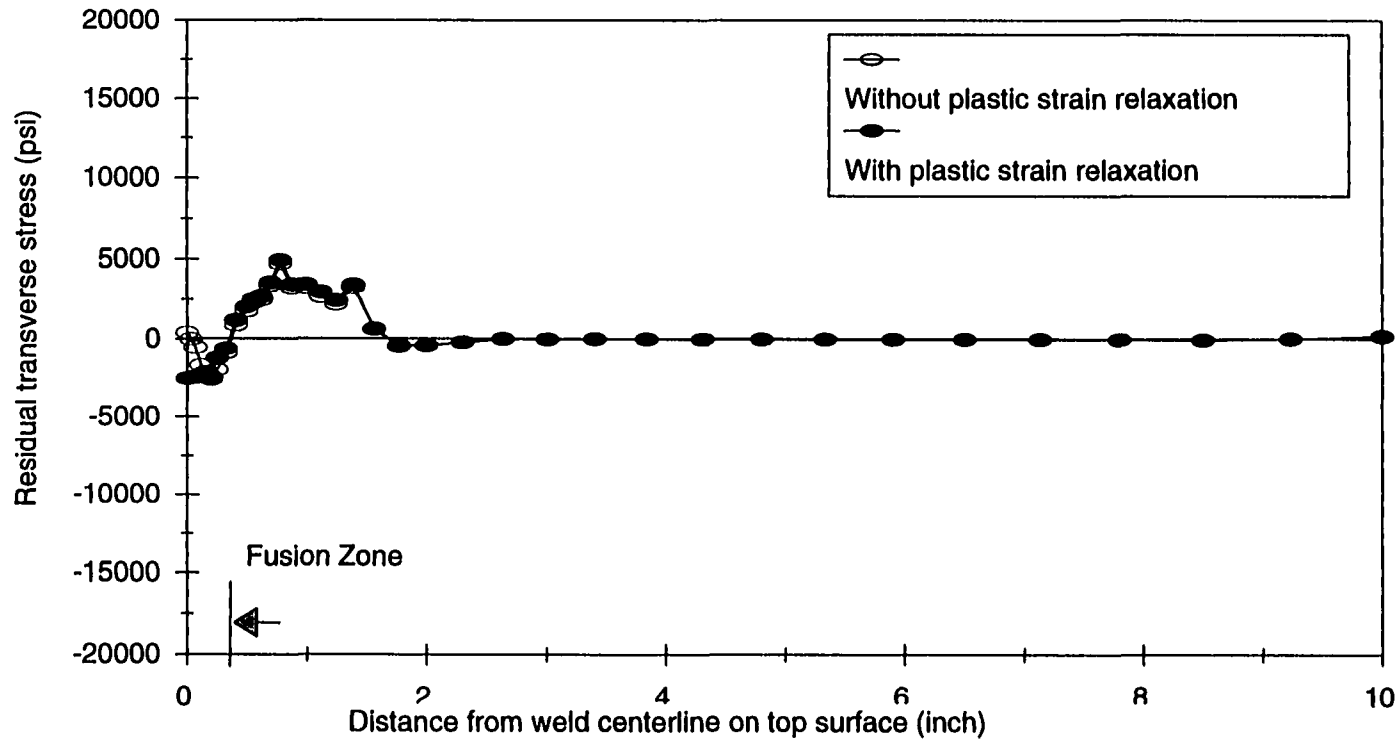


(a)



(b)

Figure 6.12 Finite element model for a one-pass butt welded plate with a single V groove  
 (a) View of weld area  
 (b) Entire model



(a)

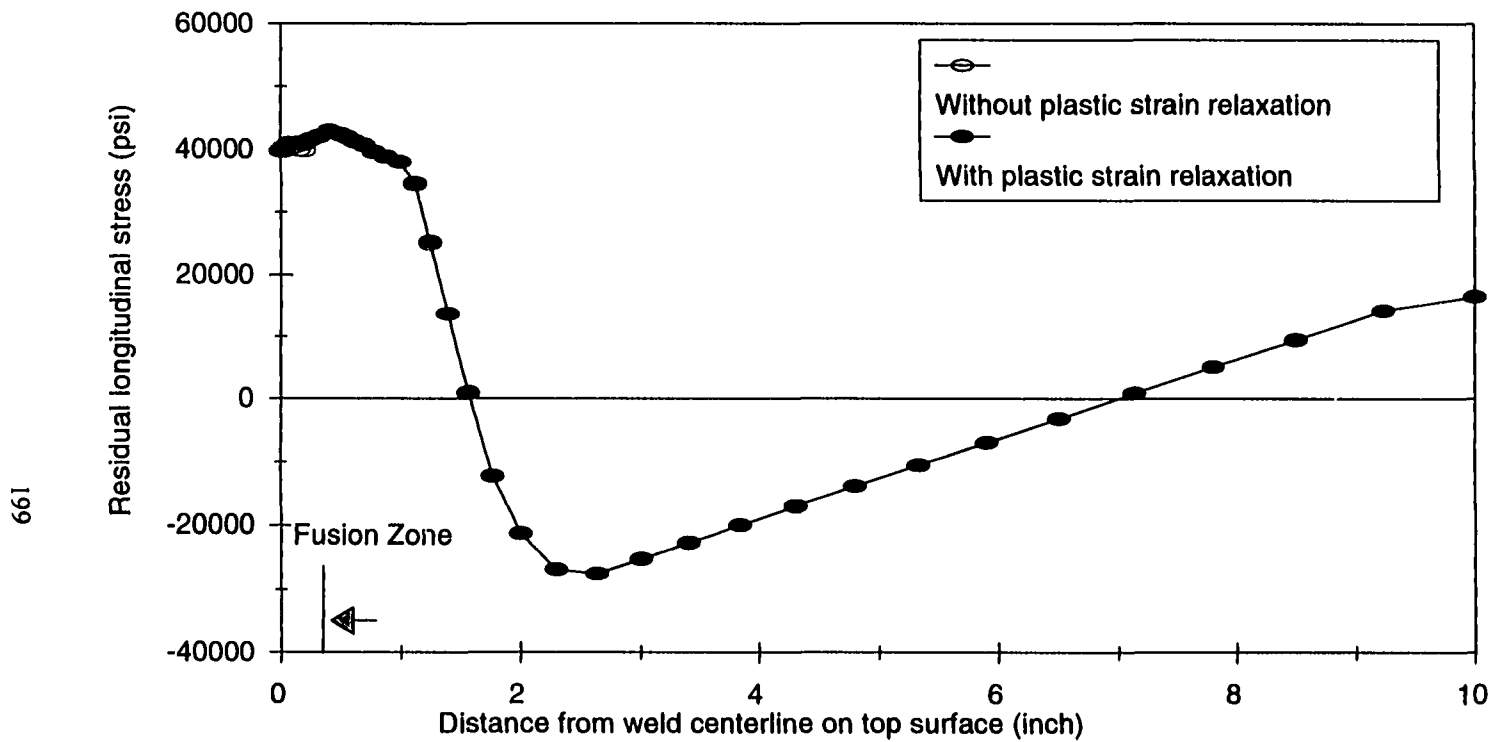
Figure 6.13 (Continued)

Figure 6.13 Comparison of residual stress distributions with and without considering plastic strain relaxation effect on top surface (a one-pass butt welded plate with a single V groove)

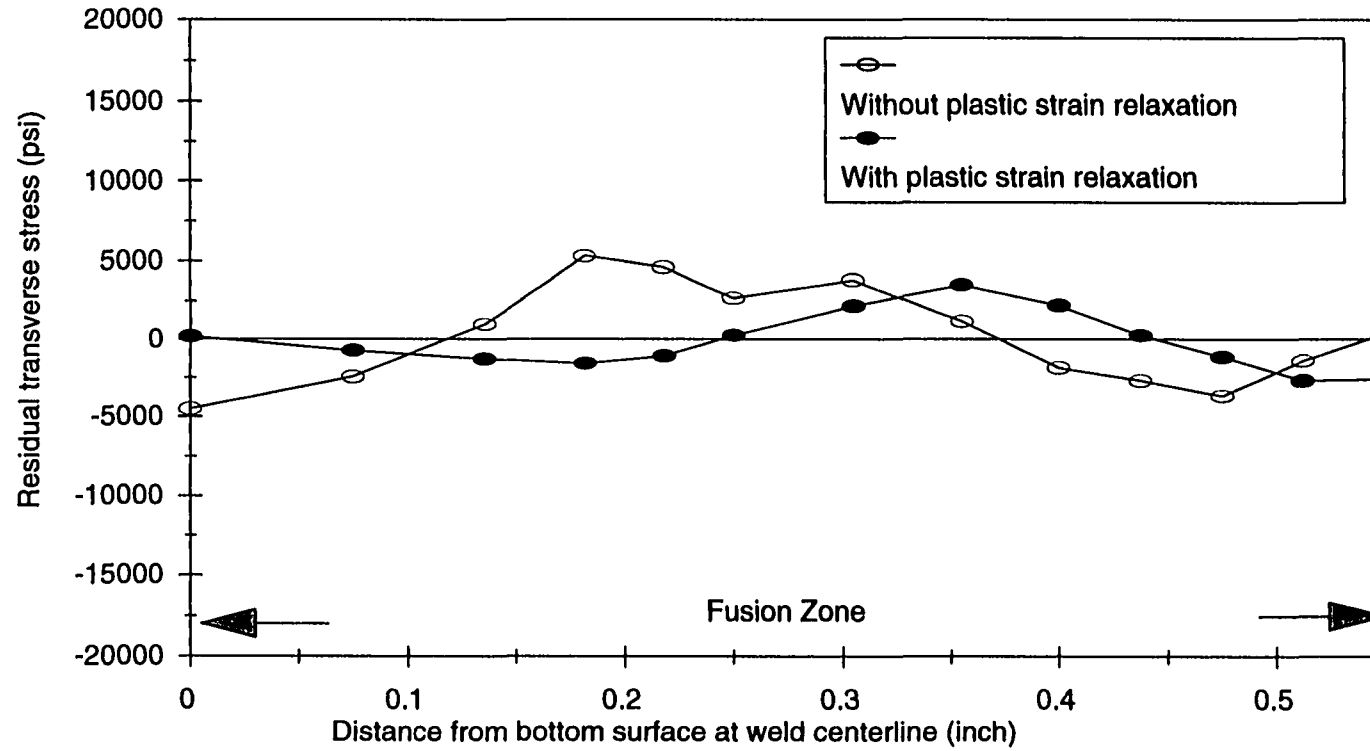
(a) Transverse stresses

(b) Longitudinal stresses

Figure 6.13 (Continued)



(b)

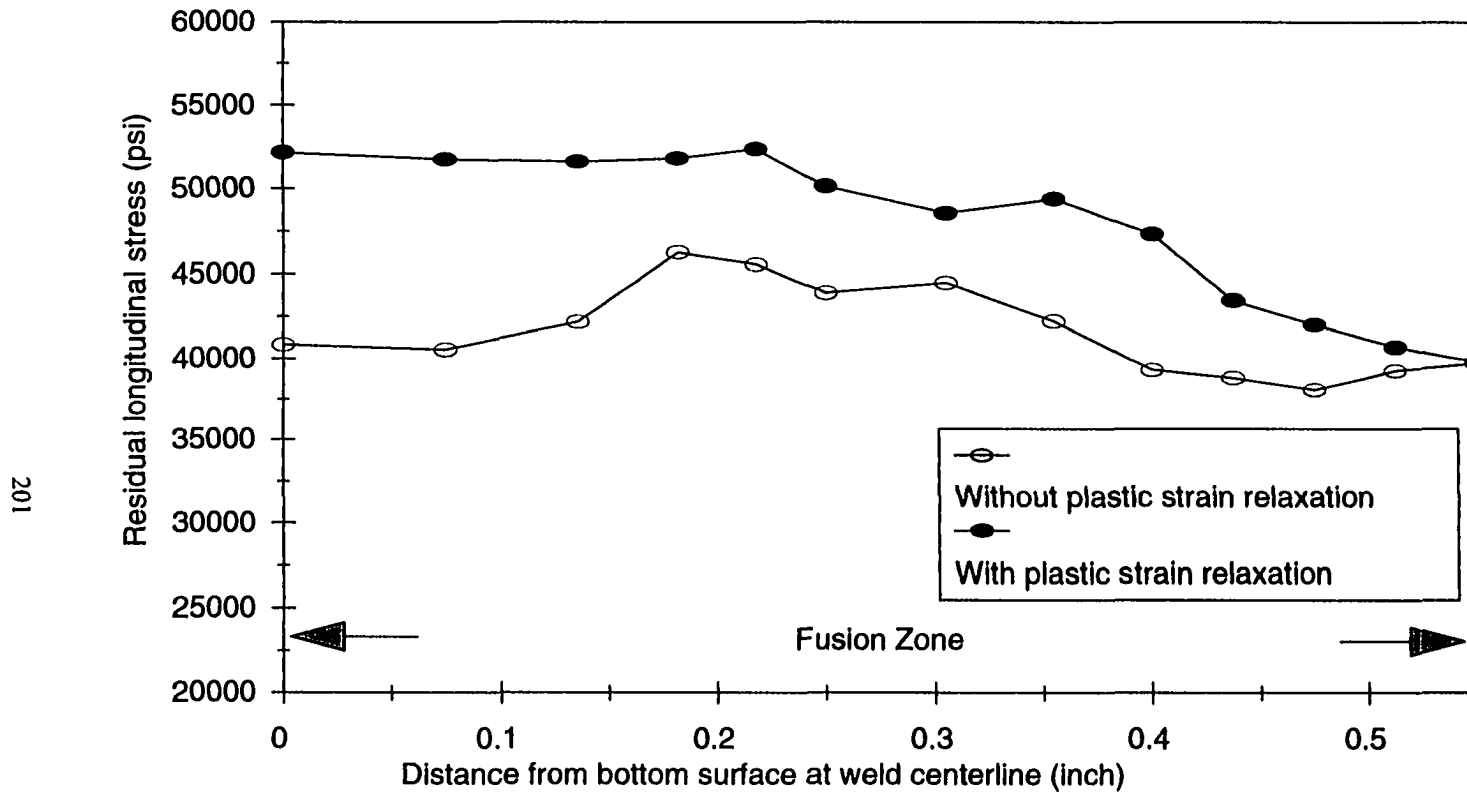


(a)

Figure 6.14 (Continued)

Figure 6.14 Through-thickness residual stress distributions at weld centerline  
 (a one-pass butt welded plate with a single V groove)  
 (a) Transverse stresses  
 (b) Longitudinal stresses

Figure 6.14 (Continued)



(b)

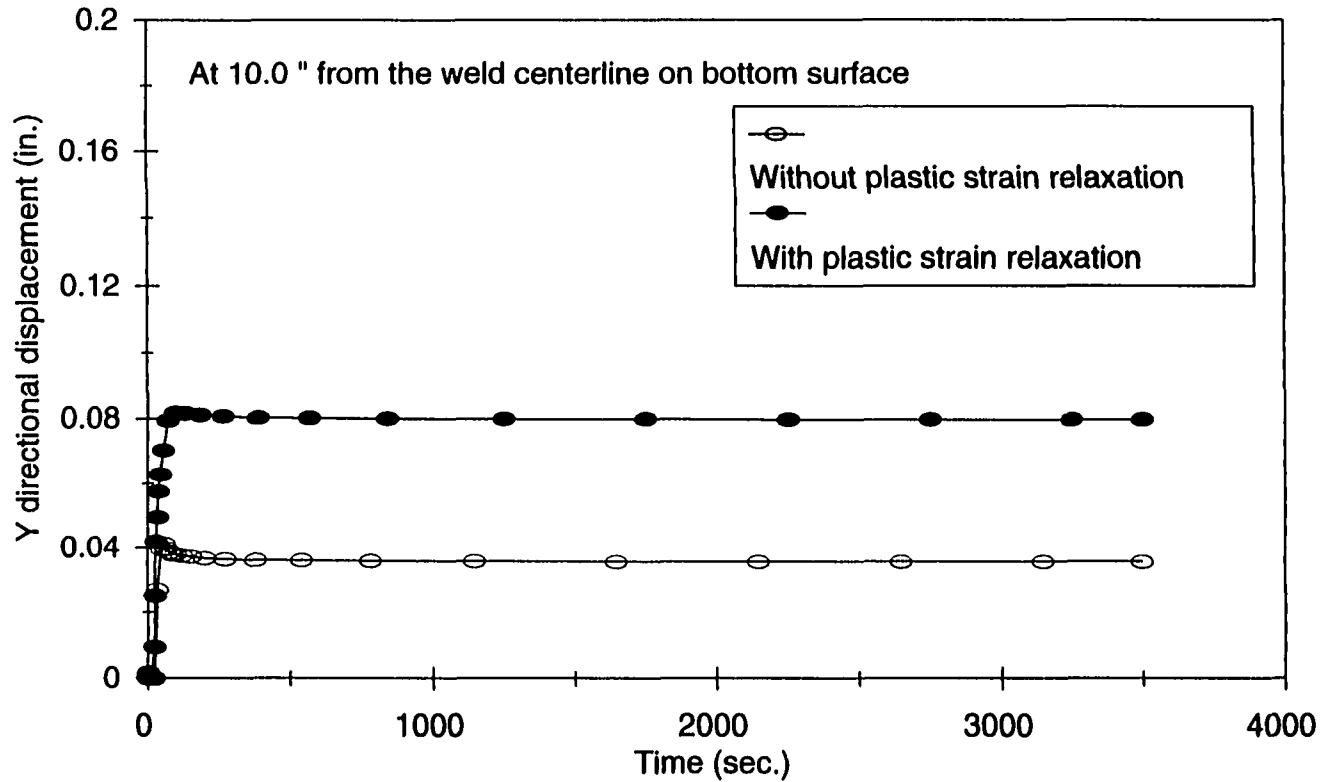
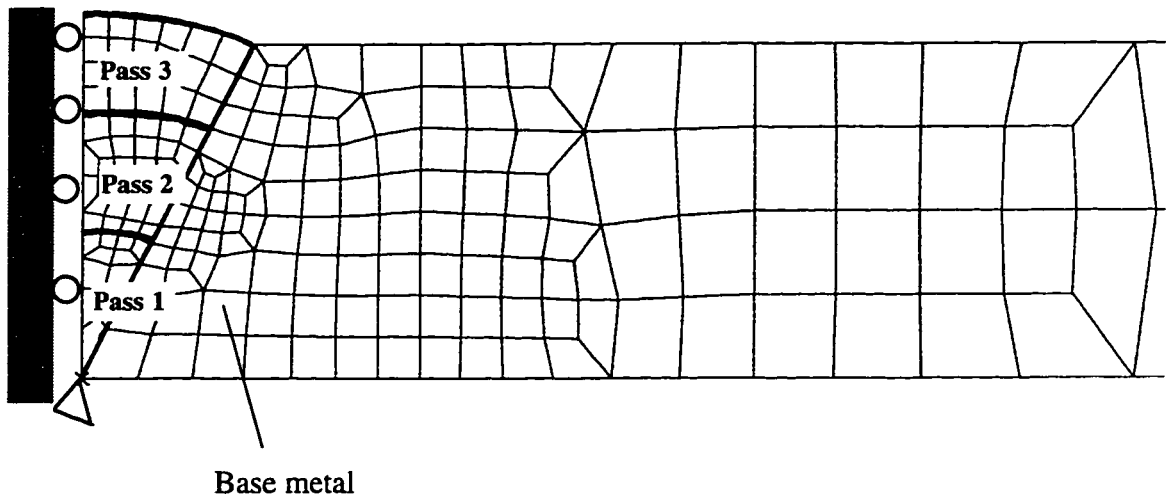
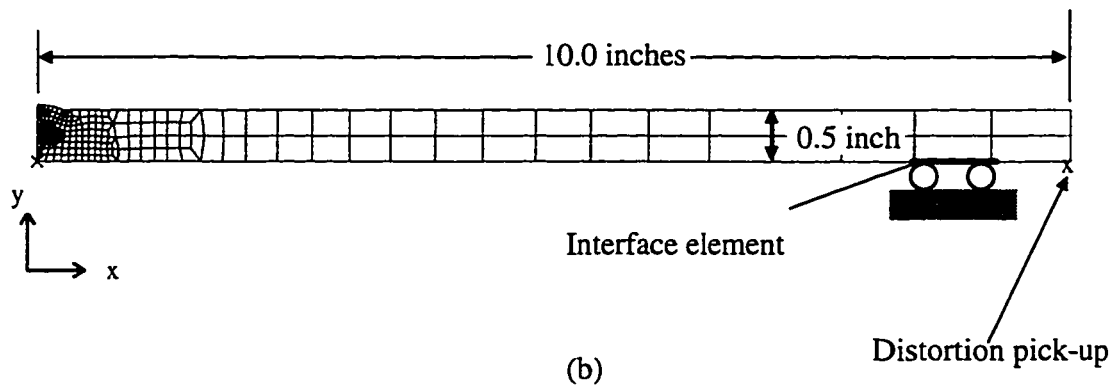


Figure 6.15 Distortion changes at 10" from the weld centerline on bottom surface (a one-pass butt welded plate with a single V groove)

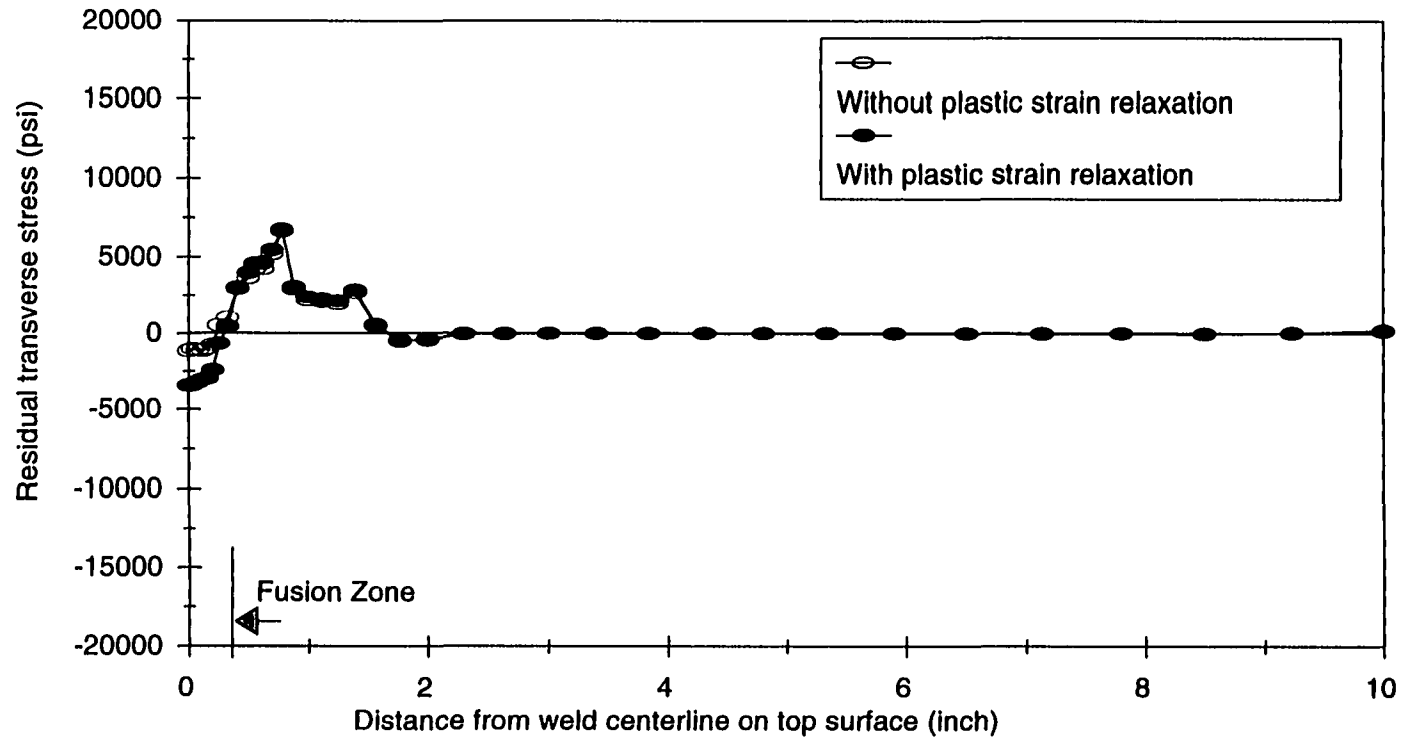


(a)



(b)

Figure 6.16 Finite element model for a three-pass butt welded plate with a single V groove  
 (a) View of weld area  
 (b) Entire model



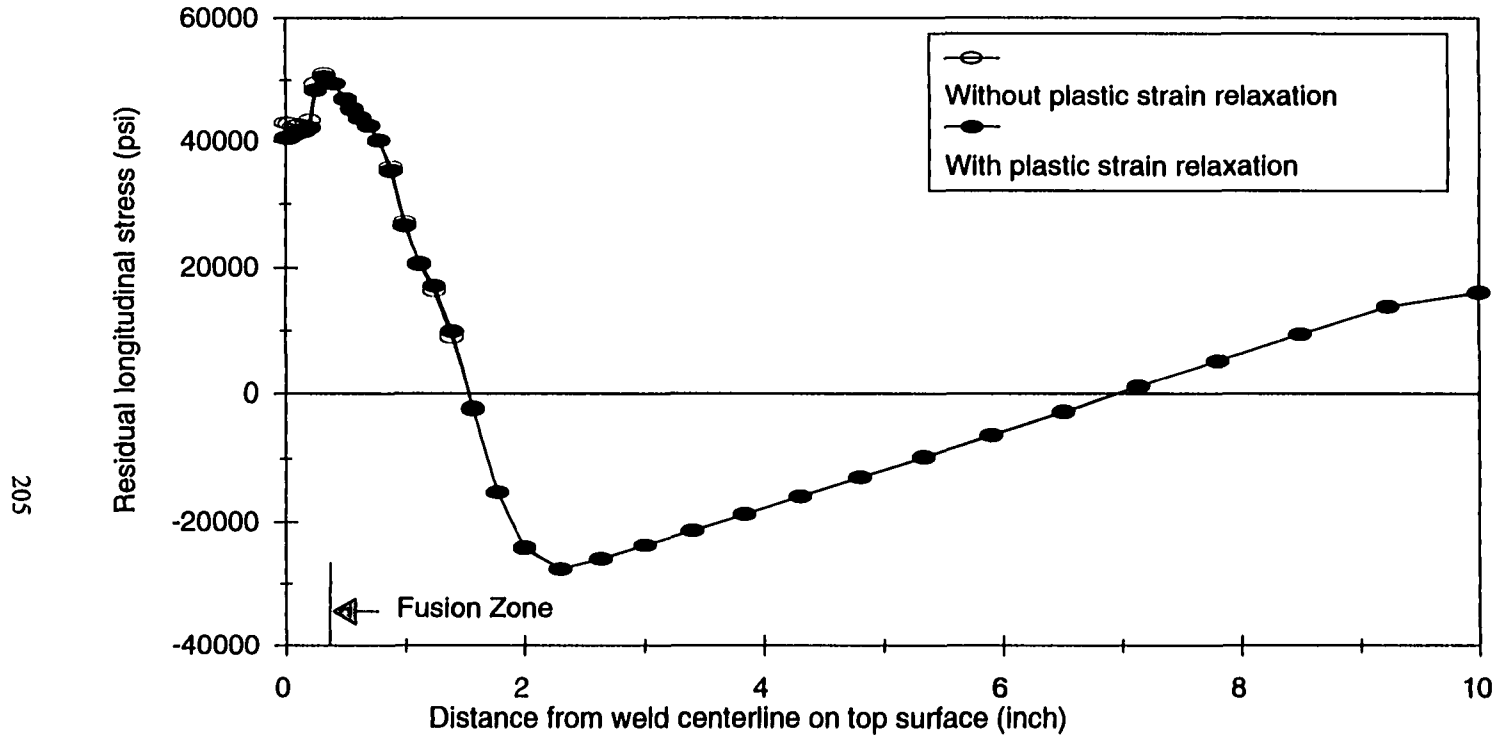
(a)

Figure 6.17 (Continued)

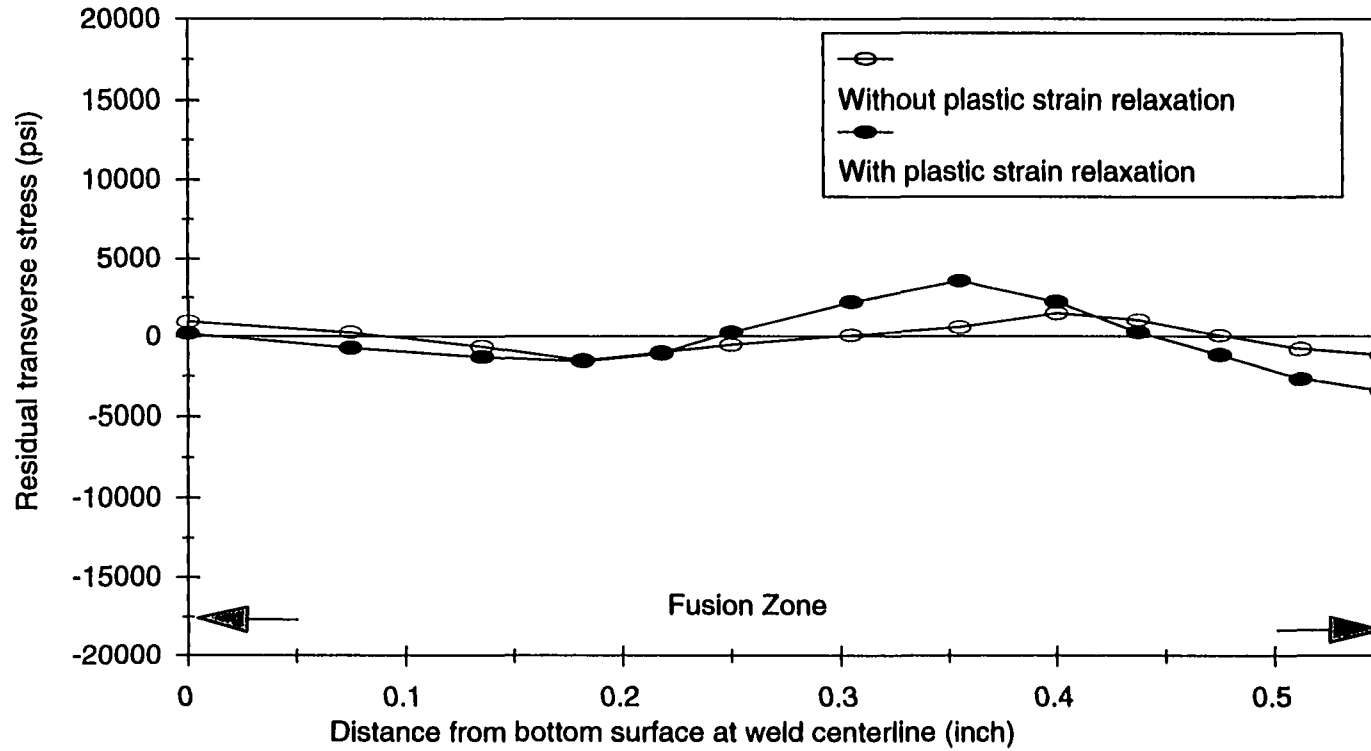
Figure 6.17 Comparison of residual stress distribution with and without considering plastic strain relaxation effect on top surface (a three-pass butt welded plate with a single V groove)

- (a) Transverse stresses
- (b) Longitudinal stresses

Figure 6.17 (Continued)



(b)

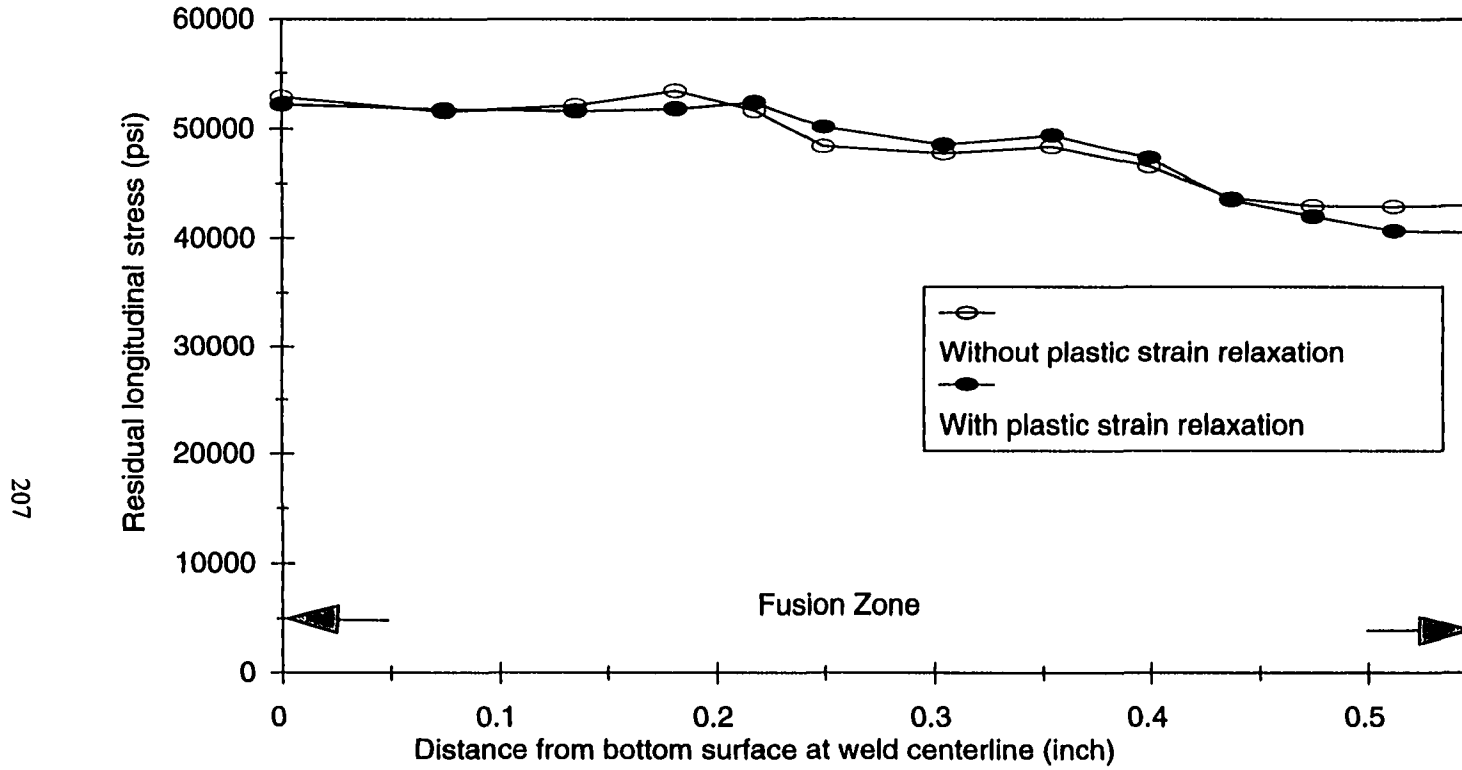


(a)

Figure 6.18 (Continued)

Figure 6.18 Through-thickness residual stress distributions at weld centerline  
 (a three-pass butt welded plate with a single V groove)  
 (a) Transverse stresses  
 (b) Longitudinal stresses

Figure 6.18 (Continued)



207

(b)

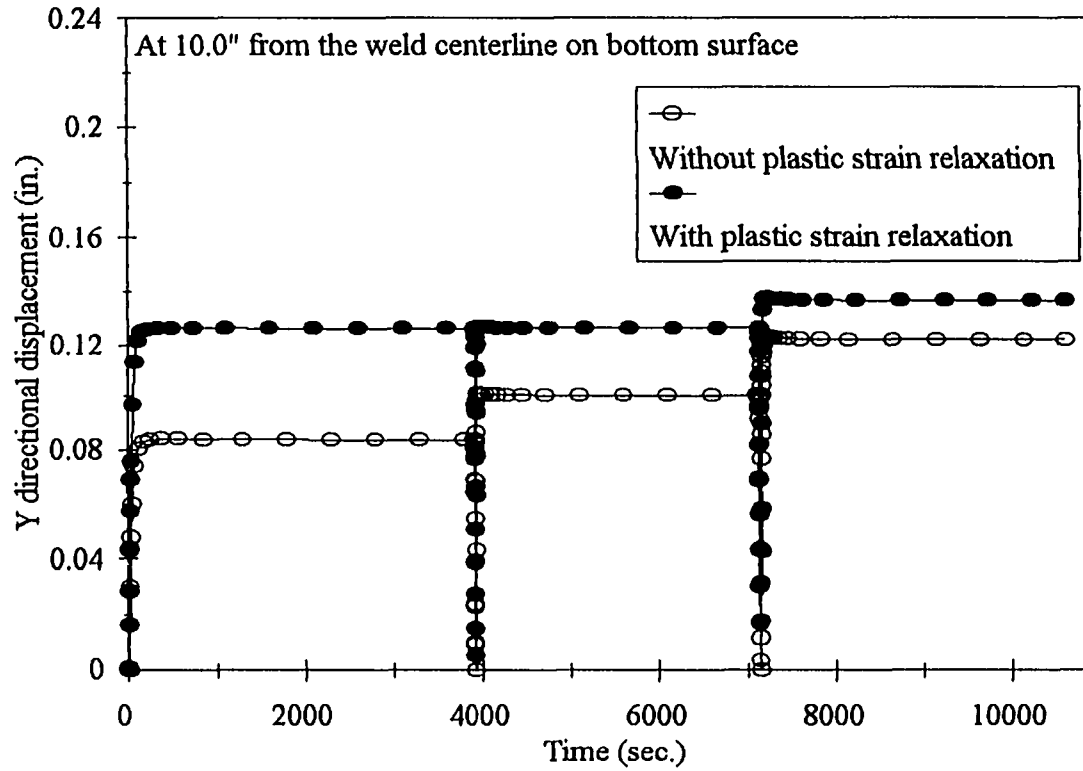


Figure 6.19 Distortion changes at 10" from the weld centerline on bottom surface (a three-pass butt welded plate with a single V groove)

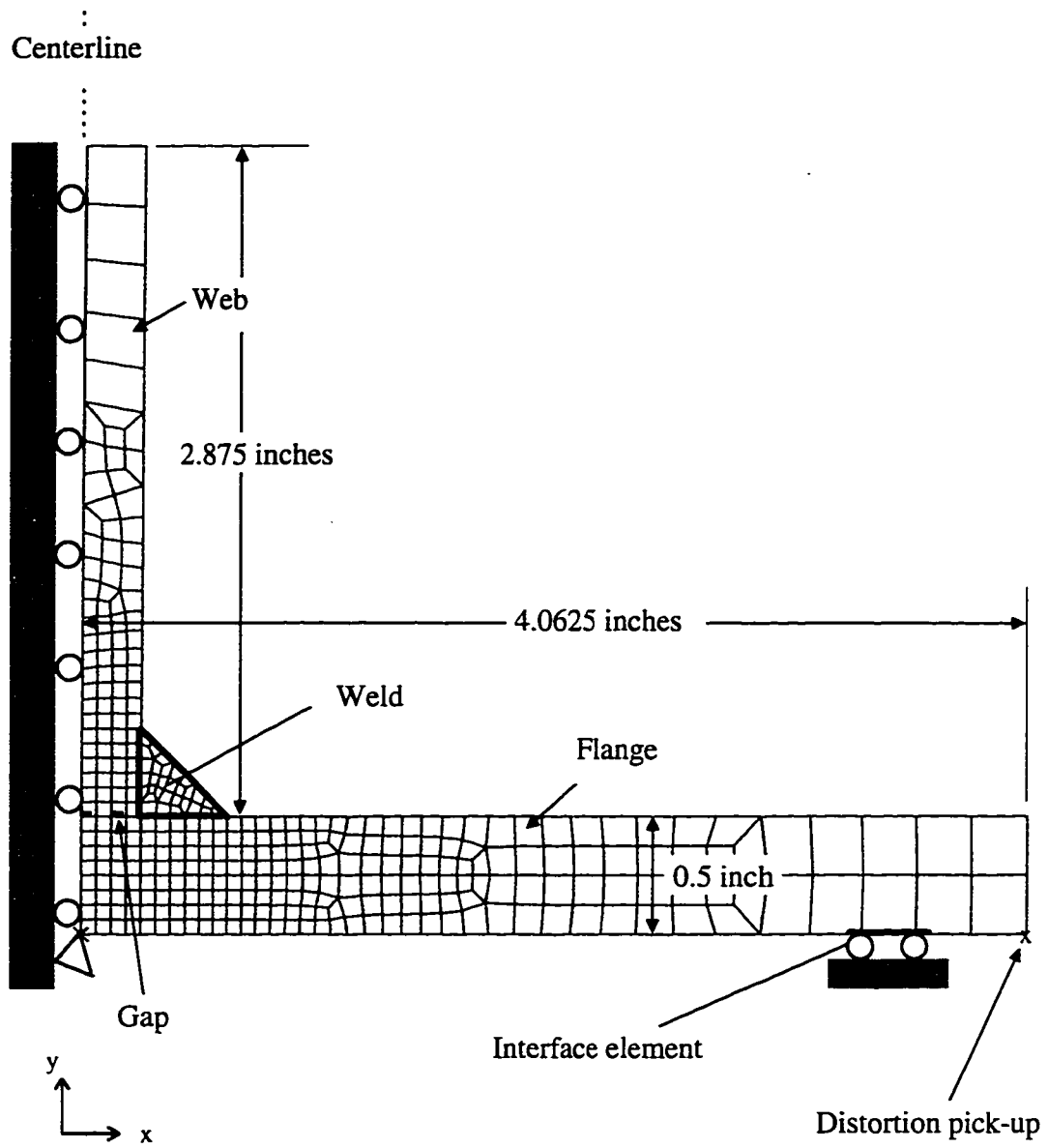
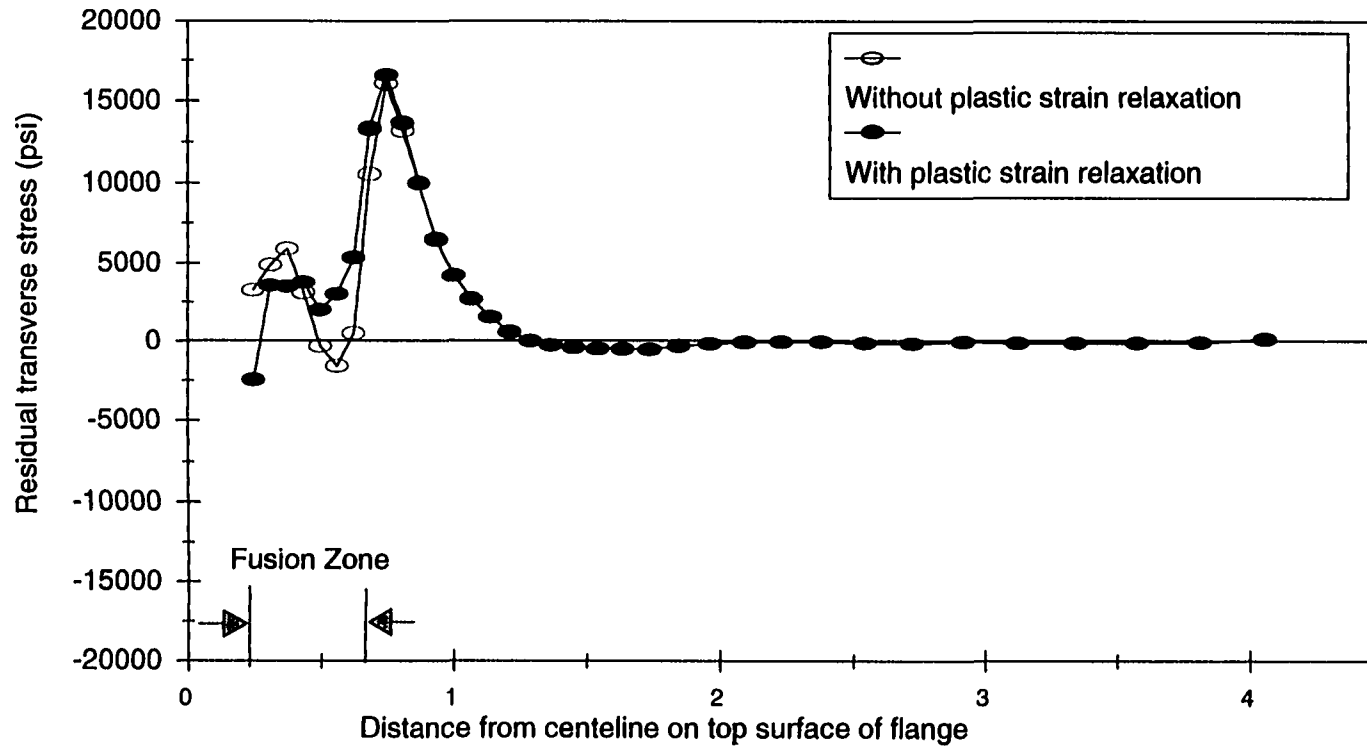


Figure 6.20 Finite element model for a tee-joint with fillet welds



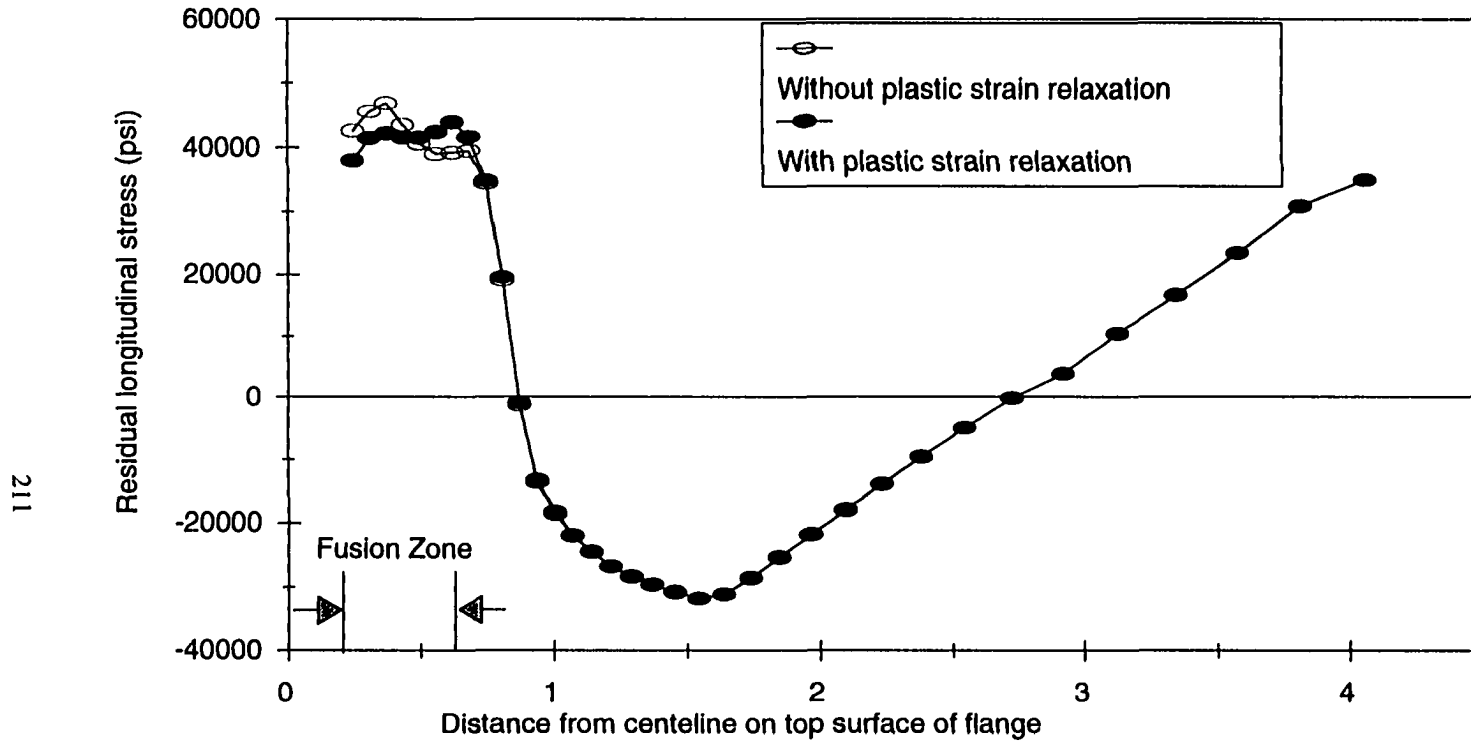
(a)

Figure 6.21 (Continued)

Figure 6.21 Comparison of residual stress distributions with and without considering plastic strain relaxation effect on top surface of the flange (a tee-joint with fillets)

- (a) Transverse stresses
- (b) Longitudinal stresses

Figure 6.21 (Continued)



(b)

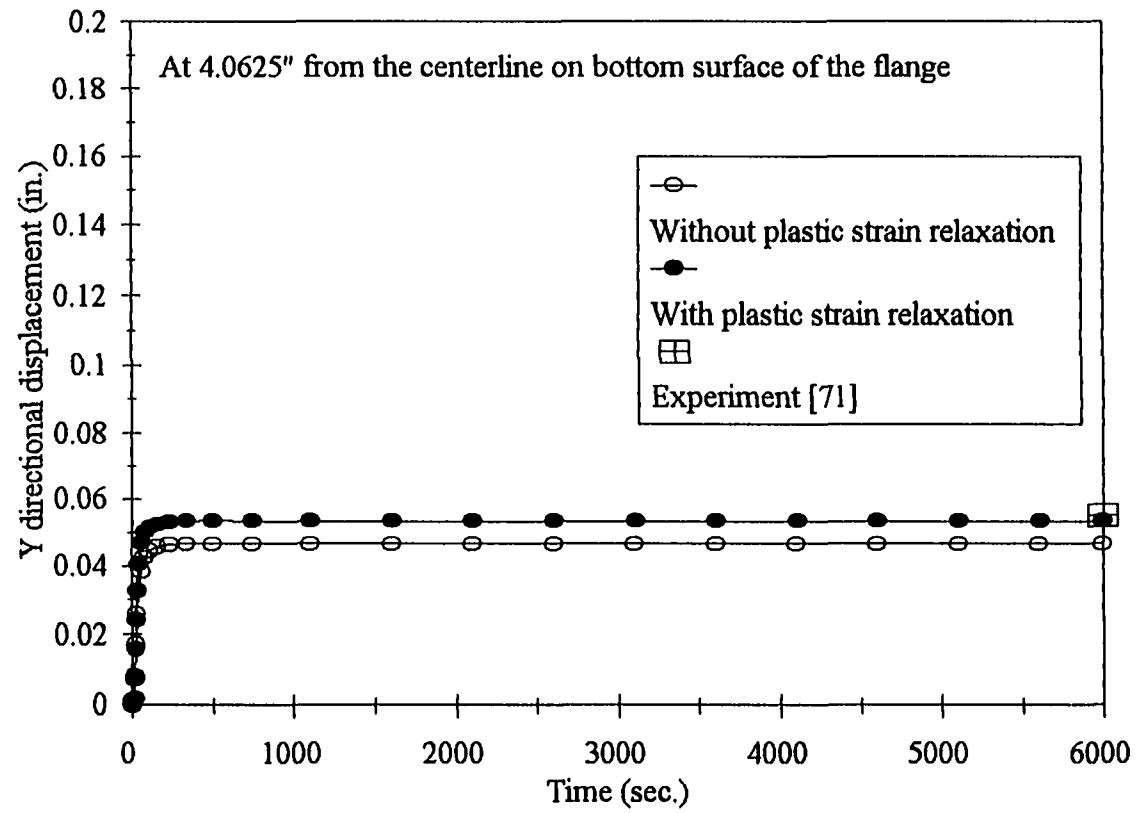


Figure 6.22 Distortion changes at 4.0625" from the centerline on bottom surface of the flange

## CHAPTER 7

### CONCLUSIONS

This dissertation presents the numerical modeling techniques for heat transfer and mechanical (stresses and distortion) analyses related to welding problems. This dissertation is composed of three parts.

The first part of this dissertation deals with the lumping techniques. Through the study of lumping modeling, the FEA procedure is developed and modified for the effective and efficient welding numerical analyses.

From the study of the first part of this dissertation, the following are concluded for the heat transfer and mechanical analyses.

- Heat input should be made of surface heat input and body heat input for numerical analysis. The body heat input is helpful to accommodate the weld shape.
- Initial prescribed temperature of the weld metal seems not to affect final residual stress distributions based on the cases studied.
- The weld zone size and shape determines the final residual stress distributions.
- Residual stresses are not sensitive to the heat input.

The second part of this dissertation deals with the interface element technique including thermal and mechanical mismatch conditions. The interface element technique is developed for multi-pass welding. The following lists the contributions and conclusions:

- The preparation of FE model and input files is cumbersome.
- The interface element technique is good for the prediction of residual stresses, but is not accurate enough for the prediction of distortion.

The third part of this dissertation is related to the plastic strain relaxation effect. The plastic relaxation effect is studied theoretically and compared with the FEA models. A computer program which incorporates the plastic strain relaxation effect is developed. The followings are concluded.

- By using plastic strain relaxation effects, the stress variation becomes small and the stresses are smoothly distributed inside and near fusion zone. This is because the accumulated plastic strains becomes smaller inside and near the fusion zone than those without plastic strain relaxation effect.
- The plastic strain relaxation effect improves the final out-of-plane distortion.
- Incorporating the plastic strain relaxation effect into numerical analyses helps to reduce CPU time in multi-pass weld models.

## LIST OF REFERENCES

- [1] Shim, Y. L., Feng, Z., Lee, S., Kim D., Jaeger J., Papritan, J. C., and Tsai C. L., "Determination of Residual Stresses in Thick-Section Weldments," *Welding Journal*, Vol. 71, No. 9, pp. 305s - 312s, 1992.
- [2] Tsai, C. L., Kim, D. S., Shim, Y. L., Feng, Z., Lee, S., and Jaeger, J., "Determination of Residual Stress and Effects in Thick Section Weldments for Hydraulic Structures," Research Report of Army Corps of Engineers, 1991.
- [3] Tsai, C. L., Feng, Z., Kim, D. S., Jaeger, J. J., Shim, Y. L., and Lee, S. G., "Design Analysis for Welding of Heavy W-Shapes," accepted Jan. 31, 1992, *Welding Journal*.
- [4] Feng, Z., Jaeger, J. J. Kim, D., Lee, S., Papritan, J., Shim, Y. L., and Tsai, C. L., "Finite Element Modeling of Welded thick Plates for Bonneville Navigation Lock," Research Report of Army Corps of Engineers, 1989.
- [5] Tsai, C. L., Lee, S. G., Shim, Y. L., Jaeger, J. J., and Chasten, C., "Experimental Verification of Modeling Techniques of Thermal-Related Welding Problems," The Winter Annual Meeting of the ASME, Orlando, Florida, 1992.
- [6] Shim, Y. L., Feng, Z., Lee, S. G., Kim D. S., Jaeger J. J., and Tsai C. L., "Modeling of Welding Residual Stresses," *Welding and Joining Processes*, pp. 29 - 41, 1991.
- [7] Bertram, L. A. and Ortega, A. R., "Automated Thermomechanical Modeling of Welds Using Interface Elements for 3D Metal Deposition," Manuscript for *Proceedings of ABAQUS User's Conference*, Oxford, England, , Hibbit, Karlsson & Sorensen, Inc., Providence, RI. 1991.
- [8] Das, S., Upadhy, G., Chandra, U., Kleinosky, M. J., and Tims, M. L., "Finite Element Modeling of a Single-Pass GMA Weldment," *Modeling of Casting, Welding and Advanced Solidification Processes VI*, Piwonka, T. S., Voller, V., and Katgerman, L. (eds.), pp. 593 - 600, The Minerals, Metals & Materials Society, 1993.

- [9] Jonsson, M., Karlsson, L., and Lindgren, L.-E., "Deformations and Stresses in Butt-Welding of Large Plates With Special Reference to the Mechanical Material Properties," *Journal of Engineering Materials and Technology*, Vol. 107, pp. 265 - 270, 1985.
- [10] Josefson, B. L., "Prediction of Residual Stresses and Distortions in Welded Structures," *Journal of Offshore Mechanics and Arctic Engineering*, Vol. 115, No. 1, pp. 52 - 57, 1993.
- [11] Josefson, B. L., "Stress Redistribution During Annealing of a Multi-Pass Butt-Welded Pipe," *Journal of Pressure Vessel Technology*, Vol. 105, pp. 165 - 170, 1983.
- [12] Karlsson, L., "Thermal Stresses in Welding," *Thermal Stresses*, Vol. I, R. B. Hetnarski (ed.), North-Holland, Amsterdam, The Netherlands, pp. 300- 389, 1986.
- [13] Goldak, J., "Modeling Thermal Stresses and Distortions in Welds," *Recent Trends in Welding Science and Technology*, David, S. A., and Vitek, I. M. (eds.), ASM International, Material Parks, Ohio, pp. 71 - 82., 1990.
- [14] Josefson, B. L., "Effect of Transformation Plasticity on Welding Residual-Stress Fields in Thin-Walled Pipes and Thin Plates," *Materials Science and Technology*, Vol. 1, pp. 904 - 908, 1985.
- [15] Andersson, B., A., B., "Thermal Stresses in a Submerged-Arc Welded Joint Considering Phase Transformations," *Journal of Engineering Materials and Technology*, Vol. 100, No. 4, pp. 356 - 362, 1978.
- [16] Hibbitt, H. D. and Marcal, P. V., "A Numerical, Thermo-Mechanical Model for the Welding and Subsequent Loading of a Fabricated Structure," *Computer & Structures*, Vol. 3, pp. 1145 - 1174, 1973.
- [17] Argyris, J. H., Szimmat, J., Willam, K. J., "Computational Aspects of Welding Stress Analysis," *Computer Methods in Applied Mechanics and Engineering*, Vol. 33, pp. 635 - 666, 1982.
- [18] Leung C. K., and Pick, R. J., "Finite Element Analysis of Multi-pass Welds," *Welding Research Council Bulletin*, Vol. 356, pp. 11 - 33, 1990.
- [19] ABAQUS User's Manual I & II, Hibbitt, Karlsson & Sorensen, Inc., Providence, RI, 1995, 1996.
- [20] Rosenthal, D., "The Theory of Moving Sources of Heat and Its Application to Metal Treatments," *Transactions of ASME*, Vol. 68, pp. 849 - 865, 1946.

- [21] Myers, P. S., Uyehara, O. A., and Borman, G. L., "Fundamentals of Heat Flow in Welding," *Welding Research Council Bulletin*, Vol. 123, pp. 1 - 46, 1967
- [22] Nippes, E. F., Merrill, L. L., and Savage, W. F., "Cooling Rate in Arc Welds in 1/2-in. Plate," *Welding Journal*, Vol. 28, No. 11, pp. 556s - 564s, 1949.
- [23] Wells, A. A., "Heat Flow in Welding," *Welding Journal*, Vol. 31, No. 5, pp. 263s - 267s, 1952.
- [24] Adams, C. M. Jr., "Cooling Rates and Peak Temperatures in Fusion Welding," *Welding Journal*, Vol. 37, No. 5, pp. 210s - 215s, 1958.
- [25] Jhaveri, P., Moffatt, W. G., and Adams, C. M. Jr., "The Effect of Plate Thickness and Radiation on Heat Flow in Welding and Cutting," *Welding Journal*, Vol. 41, No. 1, pp. 12s - 16s, 1962.
- [26] Christensen, N., Davis, V. de L., and Gjermundsen, K., "Distribution of Temperature in Arc Welding," *British Welding Journal*, Vol. 12, No. 2, pp. 54 - 75, 1965.
- [27] Grosh, R. J., and Trabant, E. A., "Arc-Welding Temperatures." *Welding Journal*, Vol. 35, No. 8, pp. 396s - 400s, 1956.
- [28] Pavelic, V., Tanbakuchi, R., Uyehara, O. A., and Myers, P. S., "Experimental and Computed Temperature Histories in Gas Tungsten-Arc Welding of Thin Plates," *Welding Journal* Vol. 47, No. 7, pp. 295s - 305s, 1969.
- [29] Stoeckinger, G. R., Calabrese, R. A., and Menaul, R. F., "Computerized Prediction of Heat Distribution in Welding Tooling," *Welding Journal*, Vol. 49, No. 1, pp. 14s-26s, 1970.
- [30] Stoeckinger, G. R., Menaul, R. F., and Calabrese, R. A., "Computerized Prediction of Heat Distribution in Welding Tooling - Further Definition," *Welding Journal*, Vol. 49, No. 6, pp. 272s - 277s, 1970.
- [31] Krutz, G. W., and Segerlind, L. J., "Finite Element Analysis of Welded Structures," *Welding Journal*, Vol. 57, No. 7, pp. 211s - 216s, 1978.
- [32] Friedman, E., "Thermomechanical Analysis of the Welding Process Using the Finite Element Method," *Journal of Pressure Vessel Technology*, Vol. 97, pp. 206 - 213, 1975.
- [33] Paley, Z. and Hibbert, P. D., "Computation of Temperatures in Actual Weld Designs," *Welding Journal*, Vol. 54, No. 11, pp. 385s - 392s, 1995.

- [34] Friedman, E., and Glickstein, S. S., "An Investigation of the Thermal Response of Stationary Gas Tungsten Arc Welds," *Welding Journal*, Vol. 55, No. 12, pp. 408s - 420s, 1976.
- [35] Goldak, J., Chakravarti, A. and Bibby, M., "A New Finite Element Model for Welding Heat Sources," *Metallurgical Transactions B*, Vol. 15B, pp. 299 - 305, 1984.
- [36] Goldak, J., Bibby, M., Moore, J., House, R., and Patel, B., "Computer Modeling of Heat Flow in Welds," *Metallurgical Transactions B*, Vol. 17, pp. 587 - 600, 1986.
- [37] Fan, S. J., and Tsai, C. L., "Finite Element Analysis of Welding Thermal Behavior in Transient Conditions," Paper No. 84-HT-80, ASME, 1984.
- [38] Kraus, H. G., "Thermal Finite Element formulation and Solution Versus Experimental Results for Thin-Plate GTA Welding," *Journal of Heat Transfer*, Vol. 108, pp. 591-596, 1986.
- [39] Kannatey-Asibu, E. Jr., Kikuchi, N., and Jallad, A.-R., "Experimental Finite Element Analysis of Temperature Distribution During Arc Welding," *Journal of Engineering Materials and Technology*, Vol. 111, pp. 9 - 18, 1989.
- [40] Tekriwal, P., Stitt, M., and Mazumder, J., "Finite Element Modeling of Heat Transfer for Gas Tungsten Arc Welding," *Metal Construction*, Vol. 19, No. 10, pp. 599R - 606R, 1987.
- [41] Tekriwal, P., and Mazumder, J., "Finite Element Analysis of Three-Dimensional Transient Heat Transfer in GMA Welding," *Welding Journal*, Vol. 67, No. 7, pp. 150s - 156s, 1988.
- [42] Karlsson, C. T., "Finite Element Analysis of Temperatures and Stresses in a Single-Pass Butt-Welded Pipe - Influence of Mesh Density and Material Modelling," *Engineering Computations*, Vol. 6, pp. 133 - 141, 1989.
- [43] Karlsson, R. I., and Josefson, B. L., "Three-Dimensional Finite Element Analysis of Temperatures and Stresses in a Single-Pass Butt-Welded Pipe," *Journal of Pressure Vessel Technology*, Vol. 112, pp. 76 - 84, 1990.
- [44] Boulton, N. S., and Lance Martin, H. E., "Residual Stresses in Arc-Welded Plates," *Proceedings in Institution of Mechanical Engineers*, Vol. 133, pp. 295 - 339, 1936.
- [45] Masubuchi, K., "Analytical Investigation of Residual Stresses and Distortion Due to Welding," *Welding Journal*, Vol. 39, No. 12, pp. 525s - 537s, 1960.

- [46] Tall, I., "Residual Stresses in Welded Plates - A Theoretical Study," *Welding Journal*, Vol. 43, No. 1, pp. 10s - 23s, 1964.
- [47] Muraki, T., Bryan, J. J., and Masubuchi, K., "Analysis of Thermal Stresses and Metal Movements During Welding PART I: Analytical Study," *Journal of Engineering Materials and Technology*, Vol. 97, pp. 81 - 84, 1975.
- [48] Muraki, T., Bryan, J. J., and Masubuchi, K., "Analysis of Thermal Stresses and Metal Movements During Welding PART II: Comparison of Experimental Data and Analytical Results," *Journal of Engineering Materials and Technology*, Vol. 97, pp. 85-91, 1975.
- [49] Rybicki, E. F. and Stonesifer, R. B., "Computation of Residual Stresses due to Multipass Welds in Piping systems," *Journal of Pressure Vessel Technology*, Vol. 101, pp. 149 - 154, 1979.
- [50] Josefson, B. L., "Stress Redistribution During Local Annealing of a Multi-Pass Butt-Welded Pipe," *Journal of pressure Vessel Technology*, Vol. 108, pp. 125 - 130, 1986.
- [51] Free, J. A. and Porter Goff, R. F. D., "Predicted Residual Stresses in Multi-Pass Weldments with the Finite Element Method," *Computer & Structures*, Vol. 32, No. 2, pp. 365 - 378, 1989.
- [52] Mahin, K. W., Winters, W., Holden, T. M., Hosbons, R. R. and McEwen, S. R., "Prediction and Measurement of Residual Elastic Strain Distributions in Gas Tungsten Arc Welds," *Welding Journal*, Vol. 70, No. 9, pp. 245s - 260s, 1991.
- [53] Andersson, M., and Josefson, B. L., "Welding Stress Redistribution in a Butt-Welded Pipe During Later Mechanical and Thermal Loadings," *Journal of Pressure Vessel Technology*, Vol. 110, pp. 402 - 404, 1988.
- [54] Josefson, B. L., and Karlsson, C. T., "FE-Calculated Stresses in a Multi-Pass Butt-Welded-Pipe - A Simplified Approach," *International Journal of Pressure Vessels and Piping*, Vol. 38, pp. 227 - 243, 1989.
- [55] Lindgren, L.-E., and Karlsson, L., "Deformations and Stresses in Welding of Shell Structures," *International Journal for Numerical Methods in Engineering*, Vol. 25, pp. 635-655, 1988.
- [56] Josefson, B. L., and Karlsson, C. T., "Transformation Plasticity Effects on Residual Stresses in a Butt-Welded Pipe," *Journal of Pressure Vessel Technology*, Vol. 114, No. 3, pp. 376 - 378, 1992.
- [57] Farong, Y., and Huadong, S., "Transient Temperature Fields and Residual Stress Fields of Metallic Materials under Welding," *International Conference on*

*Residual Stresses, ICRS-2*, Beck, G., Denis, S., and Simon, A. (eds.), Elsevier Applied Science, London, U. K., pp. 504 - 509, 1989

- [58] Tekriwal, P., and Mazumder, J., "Transient and Residual Thermal Strain-Stress Analysis of Arc Welding Processes," *Modeling of Casting, Welding and Advanced Solidification Processes V*, Rappaz, M., Ozgu, M. R., and Mahin, K. W. (eds.), pp. 211 - 218, The Minerals, Metals & Materials Society, 1991.
- [59] Tekriwal, P., and Mazumder, J., "Transient and Residual Thermal Strain-Stress Analysis of GMAW," *Journal of Engineering Materials and Technology*, Vol. 113, pp. 336 - 343, 1991.
- [60] Ueda, Y., Fukuda, K. and Tanigawa, M., "New Measuring Method of Three Dimensional Residual Stress Based on Theory of Inherent Strain," *Transactions of JWRI*, Vol. 8, No. 2, pp. 89-96, 1979.
- [61] Ueda, Y., Takahashi, E., Fukuda, K., Sakamoto, K., and Nakacho, K., "Multipass Welding Stresses in Very Thick Plates and Their Reduction from Stress Relief Annealing," *Trans. of JWRI*, Vol. 5, No. 2, pp. 179 - 189, 1976.
- [62] Lee, S. G., Modeling of Residual Stress In Thick Section Weldments, Ph. D. Dissertation, The Ohio State University, 1992.
- [63] Josefson, B. L., Jonsson, M., Karlsson, R., Karlsson, C. T., and Lindgren, L.-E., "Transient and Residual Stresses in a Single-Pass Butt-Welded Pipe," *International Conference on Residual Stresses, ICRS-2*, G. Beck, S. Denis, and A. Simon (eds.), Elsevier Applied Science, London, U. K., pp. 497 - 503, 1989.
- [64] Papazoglou, V. J., Analytical Techniques for Determining Temperatures, Thermal Strains, and Residual Stresses, Ph.D. Dissertation, Massachusetts Institute of Technology, 1981.
- [65] Masubuchi, M., *Analysis of Welded Structures*, Pergamon Press, New York, 1980.
- [66] Kumose, T., Yoshida, T., Abbe, T., and Onoue, H., "Prediction of Angular Distortion Caused by One-Pass Fillet Welding," *Welding Journal*, Vol. 33, No. 10, pp. 945 - 956, 1954.
- [67] Guyot, F., "A Note on the Shrinkage and Distortion of Welded Joints," *Welding Journal*, Vol. 26, No. 9, pp. 519s - 529s, 1947.
- [68] Watanabe, M., and Satoh, K., "Effect of Welding Conditions on the Shrinkage Distortion in Welded Structures," *Welding Journal*, Vol. 40, No. 8, pp. 377s - 384s, 1961.

- [69] You, S. Y., Ahn, S. C., and Jo, S. T., "A Study on Weld Distortion in Steel Butt and Fillet Welds Made by Flux Cored Arc Welding," *Recent Trends in Welding Science and Technology*, David, S. A., and Vitek, J. M. (eds.), pp. 119 - 123, ASM International, 1990.
- [70] Brown, S. B., and Song, H., "Implications of Three-Dimensional Numerical Simulations of Welding of Large Structures," *Welding Journal*, Vol. 71, No. 2, pp. 55s - 62s, 1992.
- [71] Penso, J. A., Development of a PC-Based FEM Model to Predict Weld Distortion. M.S. Thesis, The Ohio State University, 1992.
- [72] Cheng, W., Theoretical Development of Spring-Shrinkage Model for Predicting Weld Distortion, M.S. Thesis, The Ohio State University, 1995.
- [73] Karlsson, L., and Lindgren, L.-E., "Combined Heat and Stress-Strain Calculations," *Modeling of Casting, Welding and Advanced Solidification Processes V*, Rappaz, M., Ozgu, M. R., and Mahin, K. W. (eds.), pp. 187 - 202, The Minerals, Metals & Materials Society, 1991.
- [74] Tsai, C. L., Parametric Study on Cooling Phenomena in Underwater Welding, Ph.D. Dissertation, Massachusetts Institute of Technology, 1977.
- [75] Josefson, B. L., "Residual Stresses and Their Redistribution During Annealing of a Girth-Butt Welded Thin-Walled Pipe," *Journal of Pressure Vessel Technology*, Vol. 104, pp. 245 - 250, 1982.
- [76] Lindgren, L.-E., "Temperature Fields in Simulation of Butt-Welding of Large Plates," *Communications in Applied Numerical Methods*, Vol. 2, pp. 155 - 164, 1986.
- [77] Landau, H. G., Weiner, J. H., and Zwicky, E. E., Jr., "Thermal Stress in a Viscoelastic-Plastic Plate with Temperature-Dependent Yield Stress," *Journal of Applied Mechanics*, Vol. 27, No. 2, pp. 297 - 302, 1960.
- [78] Leung C. K., Pick, R. J. and Mok, D. H. B., "Finite Element Modeling of a Single Pass Weld," *Welding Research Council Bulletin*, Vol. 356, pp. 1 - 10, 1990.
- [79] Ueda, Y., and Nakacho, K., "Simplifying Methods for Analysis of Transient and Residual Stresses and Deformations due to Multi-pass Welding," *Trans. of JWRI*, Vol. 11, pp. 95 - 104, 1982.
- [80] Brust, F. W., and Stonesifer R. B., "Effect of Weld Parameters on Residual Stresses in BWR Piping Systems," NP-1747, Final Report by Battelle , Columbus Laboratories to Electric Power Research Institute, March 1981.

- [81] Jhang, J., Dong, P., and Brust, F. W., "A Constitutive Model for Welding Process Simulation Using Finite Element Methods," under preparation, 1996.
- [82] Snyder, M., D., and Bathe, K. J., "A Solution Procedure for Thermo-Elastic-Plastic and Creep Problems," *Nuclear Engineering and Design*, Vol. 64, pp. 49 - 80, 1981.
- [83] Feng, Z., A Methodology for Quantifying The Thermal and Mechanical Conditions for Weld Metal Solidification Cracking, Ph.D. Dissertation, The Ohio State University, 1993.
- [84] Hughes, T. J. R., "Numerical Implementation of Constitutive Models: Rate-Dependent Deviatoric Plasticity," *Theoretical Foundation for Large-Scale Computations of Nonlinear Material Behavior*, Nemat-Nasser, S., Asaro, R. J., and Hegemier, G. A. (eds.), Martinus Nijhoff Publishers, pp. 29 - 63, 1984.